

8-2016

Encapsulated Contrast Agent Markers for MRI-based Post-implant Dosimetry

Tze Yee Lim

Follow this and additional works at: https://digitalcommons.library.tmc.edu/utgsbs_dissertations



Part of the [Medical Biophysics Commons](#)

Recommended Citation

Lim, Tze Yee, "Encapsulated Contrast Agent Markers for MRI-based Post-implant Dosimetry" (2016). *The University of Texas MD Anderson Cancer Center UTHealth Graduate School of Biomedical Sciences Dissertations and Theses (Open Access)*. 691.

https://digitalcommons.library.tmc.edu/utgsbs_dissertations/691

This Dissertation (PhD) is brought to you for free and open access by the The University of Texas MD Anderson Cancer Center UTHealth Graduate School of Biomedical Sciences at DigitalCommons@TMC. It has been accepted for inclusion in The University of Texas MD Anderson Cancer Center UTHealth Graduate School of Biomedical Sciences Dissertations and Theses (Open Access) by an authorized administrator of DigitalCommons@TMC. For more information, please contact digitalcommons@library.tmc.edu.

ENCAPSULATED CONTRAST AGENT MARKERS FOR
MRI-BASED POST-IMPLANT DOSIMETRY

by

Tze Yee Lim, B.Sc.

APPROVED:

Advisor

Rajat J. Kudchadker, Ph.D.

Steven J. Frank, M.D.

Geoffrey S. Ibbott, Ph.D.

Arvind Rao, Ph.D.

R. Jason Stafford, Ph.D.

.....

APPROVED:

Dean, The University of Texas

Graduate School of Biomedical Sciences at Houston

**ENCAPSULATED CONTRAST AGENT MARKERS FOR
MRI-BASED POST-IMPLANT DOSIMETRY**

A
DISSERTATION

Presented to the Faculty of

**The University of Texas
Health Science Center at Houston**

and

**The University of Texas
MD Anderson Cancer Center
Graduate School of Biomedical Sciences**

in Partial Fulfillment
of the Requirements
for the Degree of

DOCTOR OF PHILOSOPHY

by

Tze Yee Lim, B.Sc.

Houston, Texas
August, 2016

© 2016
Tze Yee Lim
All Rights Reserved

Dedicated to my family

Acknowledgments

First and foremost, I am grateful to my advisor, Dr. Rajat Kudchadker, for being a pillar of support, providing much advice and guidance for the past five years. I am also indebted to all my committee members: Dr. Steven Frank for his positive support and continuous optimism, Dr. Jason Stafford for his helpful feedback on all things MRI, Dr. Geoffrey Ibbott for his advice and gracious financial support, and Dr. Arvind Rao for his valuable input on statistical and image analysis.

I would like to express my appreciation to Dr. Jihong Wang for showing me the basics of clinical MRI scanning. I also want to thank the dosimetrists: Teresa Bruno, Mandy Cunningham and Paula Berner who have been instrumental to my understanding of the nuances of MRI-based post-implant dosimetric assessment. I want to thank Dr. Sandeep Dhanesar for being a great partner in the evaluation of the MIM Symphony brachytherapy treatment planning system. I would like to express my gratitude to Christopher MacLellan, Dr. Joshua Yung and Dr. Yao Ding, who helped with phantom MRI scanning, and Dr. Samuel Fahrenholtz for showing me how to make MRI phantoms. I also want to thank Dr. Jingfei Ma for being my first tutorial project advisor who first piqued my interest in MRI and for his feedback on recent MRI protocol development.

Last but certainly not least, I am grateful to my parents, Kheng Kok Lim and Chan Dean Siew, for raising me to be the person I am today and supporting me in all my endeavors unwaveringly. I would also like to thank my little sisters, Tze Min Lim and Tze Xin Lim, for grounding me and inspiring me at the same time, and my boyfriend, Jeremy Wilson, for his never-ending encouragement.

Abstract

Low-dose-rate prostate brachytherapy involves the implantation of tiny radioactive seeds into the prostate to treat prostate cancer. The current standard post-implant imaging modality is computed tomography (CT). On CT images, the radioactive seeds can be distinctively localized but delineation of the prostate and surrounding soft tissue is poor. Magnetic resonance imaging (MRI) provides better prostate and soft tissue delineation, but seed localization is difficult. To aid with seed localization, MRI markers with encapsulated contrast agent that provide positive-contrast on MRI images (Sirius MRI markers; C4 Imaging, Houston, TX) have been proposed to be placed adjacent to the negative-contrast seeds. This dissertation describes the development of the Sirius MRI markers for prostate post-implant dosimetry.

First, I compared the dose-volume histogram and other dosimetry parameters generated by MIM Symphony (a brachytherapy treatment planning system that allow the use of MRI images for treatment planning; MIM Software Inc., Cleveland, OH) and VariSeed (a widely used brachytherapy treatment planning system; Varian Medical Systems, Inc., Palo Alto, CA), and found the dosimetry between both brachytherapy treatment planning systems to be comparable. To gain more insight into the MRI contrast characteristics of the Sirius MRI markers, I measured the Sirius MRI marker contrast agent's spin-lattice and spin-spin relaxivities, and studied the relaxation characteristics' dependence on MRI field strength, temperature, and orientation.

From the Sirius MRI marker's contrast agent relaxation characteristics, I systematically studied the effect of varying MRI scan parameters such as flip angle, number of excitations,

bandwidth, field of view, slice thickness, and encoding steps, on the Sirius MRI markers' signal and contrast, as well as image noise, artifact and scan time. On patients implanted with Sirius MRI markers, I evaluated the visibility of the Sirius MRI markers and image artifacts. Lastly, I semi-automated the localization of markers and seeds to more enable the efficient incorporation of Sirius MRI markers as part of the clinical post-implant workflow.

Ultimately, the Sirius MRI markers may change the paradigm from CT-based to MRI-based post-implant dosimetry, for a more accurate understanding of dose-response relationships in patients undergoing low dose rate prostate brachytherapy.

Contents

Approval Page	i
Title Page	ii
Copyright	iii
Dedication	iv
Acknowledgments	v
Abstract	vi
Contents	viii
List of Acronyms and Symbols	xiii
List of Figures	xv
List of Tables	xix
1 Introduction	1
1.1 Dissertation Scope and Organization	1
1.2 Prostate and Surrounding Structures	5
1.3 Prostate Cancer Incidence and Treatments	7
1.4 Prostate Implant Indications and Outcomes	7
1.5 Prostate Implant General Workflow	11
1.5.1 Pre-implant	11
1.5.2 Implant	13
1.5.3 Post-implant	14
1.6 Post-implant Dosimetry Imaging Modalities	18

1.6.1	Computed Tomography	18
1.6.2	Magnetic Resonance Imaging	20
1.7	Encapsulated Contrast Agent Markers (Sirius MRI Markers)	21
2	Comparison of MIM Symphony and VariSeed treatment planning systems	26
2.1	Background	27
2.1.1	Radioactive Seeds	27
2.1.2	Dose Calculation for Prostate Implants	29
2.1.3	Treatment Planning Systems	32
2.2	Purpose	35
2.3	Methods	35
2.3.1	Evaluation using VariSeed Test Procedures	35
2.3.2	Evaluation on Phantom Images	35
2.3.3	Evaluation on Patient Images	36
2.4	Results and Discussion	38
2.4.1	Evaluation using VariSeed Quality Assurance User Test Procedures .	38
2.4.2	Evaluation on Phantom Images	38
2.4.3	Evaluation on Patient Images	41
2.4.3.1	Comparison of Volume Calculations	41
2.4.3.2	Comparison of DVH Parameter Calculations	45
2.5	Conclusion	48
2.5.1	Summary	48
2.5.2	Limitations	48
2.5.3	Implications	49
3	Relaxation Characteristics of the C4 Contrast Agent	50
3.1	Background	51
3.1.1	Basic MRI Contrast Mechanism	51
3.1.2	Spin-lattice Relaxation Time T_1	51
3.1.3	Spin-spin Relaxation Time T_2	54

3.1.4	Contrast agents	55
3.2	Purpose	55
3.3	Methods	55
3.3.1	Data Collection	55
3.3.2	Measuring Spin-lattice Relaxation Time T_1	57
3.3.3	Measuring Spin-spin Relaxation Time T_2	58
3.3.4	Measuring Relaxivities r_1 and r_2	59
3.4	Results and Discussion	59
3.4.1	Effect of Field Strength	59
3.4.2	Effect of Orientation	62
3.4.3	Effect of Temperature	63
3.5	Conclusion	64
3.5.1	Summary	64
3.5.2	Limitations	66
3.5.3	Implications	66
4	Pulse Sequence Parameter Variations in Phantom	67
4.1	Background	68
4.1.1	Spoiled Gradient Echo Sequences	68
4.1.2	Pulse Sequence Parameters	69
4.2	Purpose	71
4.3	Methods	72
4.3.1	Data Collection	72
4.3.2	Image Processing	73
4.3.3	Statistical Analysis	75
4.4	Results and Discussion	75
4.4.1	Varying Flip Angle	75
4.4.2	Varying Number of Excitations	78
4.4.3	Varying Bandwidth	79
4.4.4	Varying Field-of-view	84

4.4.5	Varying Slice Thickness	88
4.4.6	Varying Encoding Steps	89
4.4.6.1	Varying Frequency Encoding Steps	93
4.4.6.2	Varying Phase Encoding Steps	97
4.5	Conclusion	99
4.5.1	Summary	99
4.5.2	Limitations	99
4.5.3	Implications	101
5	MRI Protocol Development in Patients for Post-implant Dosimetry	102
5.1	Background	103
5.1.1	CT-only post-implant dosimetry	103
5.1.1.1	Advantages	103
5.1.1.2	Disadvantages	104
5.1.2	CT-MRI Fusion-based Post-implant Dosimetry	105
5.1.2.1	Advantages	105
5.1.2.2	Disadvantages	105
5.1.3	MRI-only Post-implant Dosimetry	108
5.1.3.1	Advantages	108
5.1.3.2	Disadvantages	109
5.1.4	Alternatives Solutions (instead of using Sirius MRI Markers) towards MRI-only Post-implant Dosimetry	110
5.2	Purpose	111
5.3	Methods	112
5.3.1	Sirius MRI Markers in the Prostate Implant Workflow	112
5.3.2	Post-implant MRI Protocol	113
5.4	Results and Discussion	115
5.4.1	Visualization of Seeds and Sirius MRI Markers	115
5.4.2	Clinical Challenges	118
5.5	Conclusion	123

5.5.1	Summary	123
5.5.2	Limitations	124
5.5.3	Current status	125
5.5.4	Implications	126
6	Marker-based Seed Localization Algorithms	128
6.1	Introduction	128
6.1.1	Seed Localization Algorithms on CT/CT-MRI Fusion Images	128
6.1.2	Seed Localization Algorithms on MRI Images	129
6.2	Purpose	130
6.3	Methods	131
6.3.1	Data Collection	131
6.3.2	Marker-based Seed Localization Algorithm Workflows	131
6.3.3	Image Processing	131
6.4	Results and Discussion	140
6.4.1	Performance	140
6.5	Conclusion	150
6.5.1	Summary	150
6.5.2	Limitations	150
6.5.3	Implications	150
7	Final Discussion	152
7.1	Overall Summary	152
7.2	Future Directions	153
7.3	Future Implications	155
	Bibliography	157
	Vita	175

List of Acronyms and Symbols

AAPM	American Association of Physicists in Medicine
α	Flip angle
B_0	Magnetic field strength
BW	Receiver bandwidth
CNR	Contrast-to-noise ratio
CT	Computed Tomography
Δz	Slice thickness
DVH	Dose Volume Histogram
DWI	Diffusion weighting imaging
D_x	Minimum dose covering $x\%$ of the volume
FLASH	Fast Low Angle SHot
FN	False negative
FOV	Field of view
FP	False positive
FSE	Fast Spin Echo
FSPGR	Fast Radiofrequency-Spoiled Gradient Recalled Echo
IRON	Inversion Recovery with ON-resonant water suppression
LDR	Low Dose Rate
MRI	Magnetic Resonance Imaging
MRS	Magnetic Resonance Spectroscopy
NEX	Number of excitations

NTCP	Normal tissue complication probability
N_x	Frequency encoding steps
N_y	Phase encoding steps
PSA	Prostate-specific antigen
R_1	Spin-lattice Relaxation Rate
R_2	Spin-spin Relaxation Rate
r_1	Spin-lattice Relaxivity
r_2	Spin-spin Relaxivity
RF	Radiofrequency
ROI	Region of interest
SNR	Signal-to-noise ratio
T_1	Spin-lattice Relaxation Time
T_2	Spin-spin Relaxation Time
TCP	Tumor control probability
TP	True positive
TRUS	Transrectal ultrasound
V_x	Volume receiving $x\%$ of the prescribed dose

List of Figures

1.1	Dissertation context and organization	2
1.2	Pelvic anatomy	5
1.3	Prostate implant	9
1.4	Value framework for prostate implants	10
1.5	Needle configuration	12
1.6	Dose volume histogram showing prostate D90 and V100	15
1.7	Comparison of CT and MRI postimplant images	19
1.8	The C4 contrast agent compared to other paramagnetic and supraparamagnetic contrast agents	22
1.9	First visualization of MRI markers in canine prostate	22
1.10	Dose distribution in water for a radioactive seed adjacent to a Sirius MRI marker	24
2.1	Brachytherapy seed schematic diagrams	28
2.2	Isodose curves produced by common radioactive seeds	29
2.3	Coordinate system used for brachytherapy dosimetry calculations	30
2.4	TRUS images in the VariSeed TPS	32
2.5	TRUS images in the MIM Symphony TPS	33
2.6	MRI images in the MIM Symphony TPS	34
2.7	Dose volume histogram in the MIM Symphony treatment planning system .	37
2.8	Dose point calculation test	39

2.9	Isodose level display functions	39
2.10	Dose volume test	40
2.11	Dose calculation in z-direction test	40
2.12	Differences between the volumes calculations	41
2.13	Comparison of volume calculation methods	43
2.14	Differences between the prostate V100, V150, and V200 calculations	44
2.15	Differences between the bladder V50, V100, and V150 calculations	46
2.16	Differences between the rectum V50, V100, and V150 calculations	47
3.1	T_1 relaxation mechanism	52
3.2	T_1 -weighted contrast mechanism	52
3.3	T_2 relaxation mechanism	53
3.4	T_2 -weighted contrast mechanism	53
3.5	The distinction between T_2 and T_2^*	54
3.6	Vials with increasing concentrations of cobalt dichloride	57
3.7	T_1 and T_2 at different B_0	59
3.8	R_1 and R_2 at different B_0	60
3.9	T_1 and T_2 at different orientations	61
3.10	R_1 and R_2 at different orientations	62
3.11	T_1 and T_2 at different temperatures	63
3.12	R_1 and R_2 at different temperatures	64
4.1	Relative signals of the Sirius MRI marker and prostate for varying TR and TE	69
4.2	Relative signals of the Sirius MRI marker and prostate for varying α	70
4.3	Seeds and Markers in Phantom	73
4.4	The qualitative effect of varying α	75
4.5	The quantitative effect of varying α	76
4.6	The qualitative effect of varying NEX	79
4.7	The quantitative effect of varying NEX	80
4.8	The qualitative effect of varying BW	81
4.9	The quantitative effect of varying BW	82

4.10	Shift artifact at varying BW	83
4.11	The qualitative effect of varying FOV	84
4.12	The quantitative effect of varying FOV	85
4.13	The effect of varying FOV on acquisition pixel size	87
4.14	Wrap artifact at varying FOV	87
4.15	The qualitative effect of varying Δz	90
4.16	The quantitative effect of varying Δz	91
4.17	The appearance of a single marker across consecutive axial slices	92
4.18	Marker visualized in all needle tracks for large Δz	92
4.19	The qualitative effect of varying encoding steps	93
4.20	The quantitative effect of varying $N_x \times N_y$	94
4.21	The effect of varying $N_x \times N_y$ on acquisition pixel size	95
4.22	The qualitative effect of varying N_x	95
4.23	The quantitative effect of varying N_x	96
4.24	The qualitative effect of varying N_y	97
4.25	The quantitative effect of varying N_y	98
5.1	Interobserver variation of prostate contouring on CT	104
5.2	CT-MRI fusion images	106
5.3	Anatomic distortion with endorectal coil magnetic resonance imaging	110
5.4	Seeds and MRI markers	112
5.5	Seeds and markers on CT images	115
5.6	Seeds and markers on 3D T_2 -weighted FSE images	116
5.7	Seeds and markers on 3D FSPGR images	117
5.8	Contour delineation on 3D FSPGR images	119
5.9	Motion artifact	119
5.10	Wrap artifact	120
5.11	Wrap artifact in the phase-encoding = A/P direction	122
5.12	Wrap artifact in the phase-encoding = R/L direction	122
5.13	MRI images with the rigid endorectal coil	126

6.1	Comparison of CT and MRI postimplant images	129
6.2	Marker-based seed-localization algorithm workflows	132
6.3	Preprocess	140
6.4	Threshold	141
6.5	Connected component Analysis	142
6.6	Conversion to physical dimensions	142
6.7	k-means clustering	143
6.8	Extrapolation	143
6.9	Validation	144
6.10	Non-template based seed localization	145
6.11	Pre-implant information	145
6.12	Shift coordinates	146
6.13	Match strands	147
6.14	Comparison of non-template-based and template-based seed localization algorithms	148
6.15	Template-based algorithm	148
6.16	Seed and marker positions identified by the template-based algorithm . . .	149

List of Tables

2.1	Model numbers and characteristics of radioactive isotopes for prostate implants	27
2.2	Volume calculations of known structures	39
2.3	Differences between the prostate D90 calculations	45
3.1	Conversion from weight percentages to millimolar (mM)	56
3.2	Relaxivities r_1 and r_2 for different B_0 , orientations, and temperatures . . .	65
4.1	MRI scan parameters investigated	74
4.2	Recommended range of MRI scan parameters from phantom studies. . . .	99
5.1	Pulse sequences for post-implant dosimetry	114
6.1	Sensitivity, precision and F-score	149

1

Introduction

Contents

1.1	Dissertation Scope and Organization	1
1.2	Prostate and Surrounding Structures	5
1.3	Prostate Cancer Incidence and Treatments	7
1.4	Prostate Implant Indications and Outcomes	7
1.5	Prostate Implant General Workflow	11
1.5.1	Pre-implant	11
1.5.2	Implant	13
1.5.3	Post-implant	14
1.6	Post-implant Dosimetry Imaging Modalities	18
1.6.1	Computed Tomography	18
1.6.2	Magnetic Resonance Imaging	20
1.7	Encapsulated Contrast Agent Markers (Sirius MRI Markers) . .	21

1.1 Dissertation Scope and Organization

The overall narrative and organization of this dissertation is outlined in Figure 1.1. In Chapter 1, the background and motivation of this dissertation work are provided. The *prostate* is surrounded by structures involved in bowel, urinary and sexual functions (Section 1.2). A pathology of the prostate is *prostate cancer*, whereby the treatment options include *radiation* (Section 1.3). In this dissertation, the focus is on a form of radiation therapy, namely low-dose-rate prostate brachytherapy or *prostate implants* (Section 1.4). To assess the

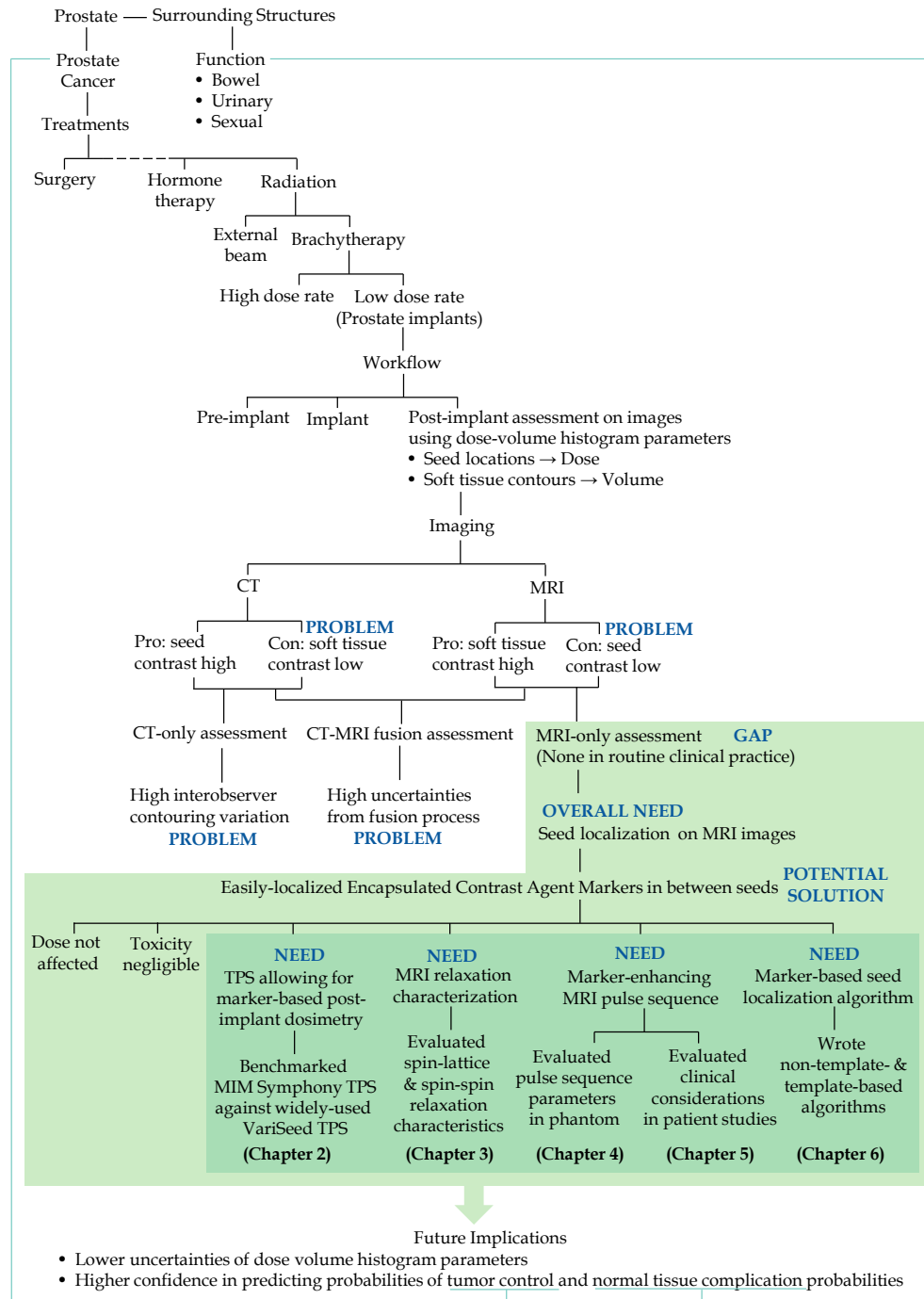


Figure 1.1: The scope of this dissertation is highlighted (dark green box) within the overall framework of prostate implants for the treatment of prostate cancer. The organization of this dissertation is denoted by the chapter numbers under each topic.

efficacy of a prostate implant for local control of prostate cancer and reduced normal tissue complications, *post-implant assessment* of dose-volume histogram parameters is performed on pelvic images acquired after the implant (Section 1.5). On these images, *seed locations* are used to calculate dose, while physician-drawn *soft tissue contours* are used to calculate volume (Section 1.5.3). The post-implant imaging options are mainly computed tomography (CT) and magnetic resonance imaging (MRI) (Section 1.6). On *CT* images, the contrast between the seeds and prostate tissue is high, but soft tissue contrast is low (Section 1.6.1). On *MRI* images, soft tissue contrast is high, but the seeds appear as dark voids that are difficult to localize because the dark voids are also generated by spacers and needle tracks (Section 1.6.2). With these two imaging modalities, the possible options for imaging-based post-implant dosimetric assessment are CT-only assessment, CT-MRI fusion assessment and MRI-only assessment. For *CT-only* assessment, the main problem is the high interobserver variation in contouring of the prostate and surrounding structures (Sections 1.6.1 and 5.1.1). For *CT-MRI fusion-based* assessment, the main problem is the greater uncertainties introduced by the fusion process (Sections 1.6.2 and 5.1.2). *MRI-only* assessment is not routinely used in clinical practice (Section 5.1.3) because seed localization on MRI images is difficult.

A potential solution to enable MRI-only post-implant assessment is to use easily-localized *encapsulated contrast agent markers* (Sirius MRI markers; C4 Imaging, Houston, TX) in between the seeds (Section 1.7). In this dissertation, I present four more components necessary to complete the workflow for incorporating Sirius MRI markers into an MRI-only post-implant dosimetry setting.

1. To enable MRI-only post-implant dosimetry using Sirius MRI markers, a *treatment planning system* (TPS) that will allow for marker-based post-implant dosimetry is needed. The MIM Symphony TPS (MIM Software Inc., Cleveland, OH) was identified as a viable alternative to the VariSeed TPS (Varian Medical Systems, Inc., Palo Alto, CA), which is a TPS widely-used around the world and was used for prostate implant procedures at our institution at the time. In Chapter 2, I benchmarked the MIM Symphony TPS against the VariSeed TPS by evaluating the calculations of

dose (Section 2.4.1), volume (Sections 2.4.2 and 2.4.3.1) and dose-volume histogram parameters (Section 2.4.3.2) of both TPS.

2. To use the Sirius MRI markers, we need to understand the intrinsic *relaxation characteristics* of the *contrast agent* that will be encapsulated in Sirius MRI markers. In Chapter 3, I evaluated the C4 contrast agent’s spin-lattice and spin-spin relaxation times at varying concentrations to obtain the relaxivities for different field strengths (Section 3.4.1), orientations (Section 3.4.2) and temperatures (Section 3.4.3).
3. After determining the relaxation times of the C4 contrast agent, we need to identify a suitable *pulse sequence* that enhances the *encapsulated contrast agent markers*. Chapter 4 describes the effects on the Sirius MRI markers’ signal-to-noise ratio, scan time and resolution *in a prostate phantom* due to variations in user-adjustable pulse sequence parameters, such as flip angle (Section 4.4.1), number of excitations (Section 4.4.2), bandwidth (Section 4.4.3), field of view (Section 4.4.4), slice thickness (Section 4.4.5) and encoding steps (Section 4.4.6). Subsequently, Chapter 5 describes our initial experience visualizing Sirius MRI markers *in patients* using the pulse sequence parameter ranges determined in phantom, as well as the unique challenges of using Sirius MRI markers in the clinical setting.
4. To enable higher efficiency in clinics, the observer-dependent manual seed localization on MRI images needs to be automated. In Chapter 6, I present two approaches of *marker-based seed localization algorithms*. One approach is to find the Sirius MRI markers and directly extrapolate the seed locations, while the other approach is to register marker locations on MRI images to the marker and seed configurations available in the pre-implant template.

Finally, in Chapter 7, I propose future investigations and conclude with a discussion of the *future implications*. MRI-only post-implant dosimetry may eventually enable accurate and consistent characterization of the dose distribution, ultimately allowing for better correlation of the dose received by the prostate and critical structures around the prostate to clinical outcomes. Someday, we may have higher confidence in the prediction of under- or over-dosed

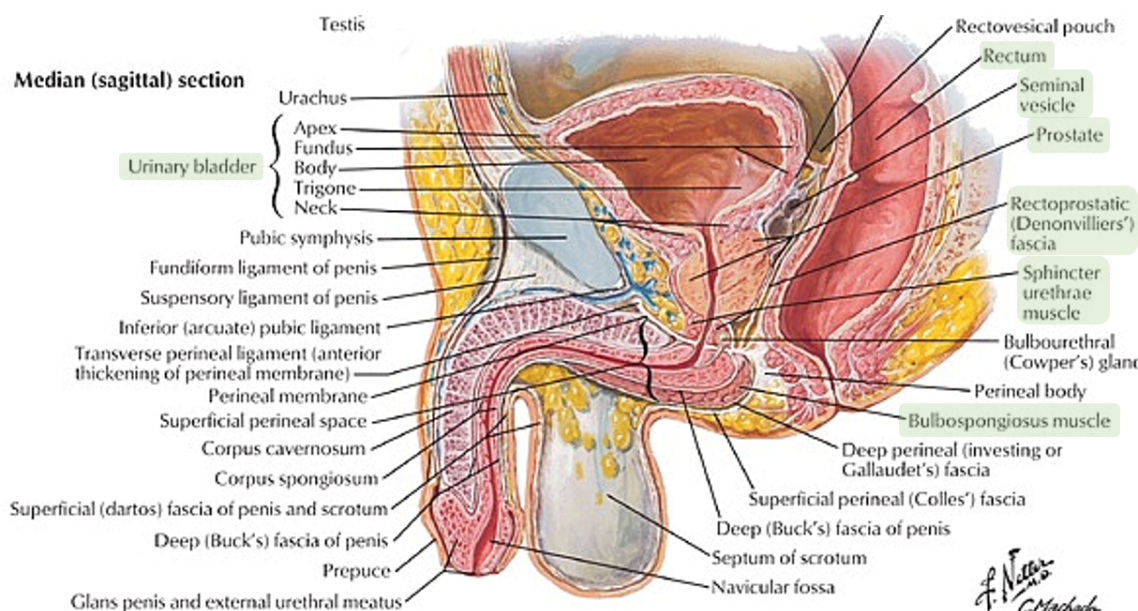


Figure 1.2: Location of the prostate and surrounding critical structures. Reprinted from Frank H. Netter. *Atlas of Human Anatomy*. 5th ed. Philadelphia: W. B. Saunders Co., 2011.³

areas in the prostate for enhanced tumor control, as well as the prediction and management of complications from the dose to normal tissues surrounding the prostate.

1.2 Prostate and Surrounding Structures

The *prostate* is a walnut-shaped gland located in the pelvis that secretes sperm-nourishing fluid.¹ Typical prostate sizes range from 20 cc to 110 cc and the length ranges from 3 cm to 6 cm.² The prostate is surrounded by a dense fibrous capsule containing nerves and veins coated with a fibrous prostatic sheath.¹ The superior aspect of the prostate is the *base* while the inferior aspect is the *apex*.¹ The prostate can be divided into three zones, namely the anterior muscular zone, the central zone and the peripheral zone.¹

Several structures involved in bowel, urinary and sexual functions are in the vicinity of the prostate (Figure 1.2). The functions of these structures are interwoven with the side effects of prostate treatments.*

*See Section 1.4 for a discussion of the side effects of prostate implants.

Bowel function The *rectum* and anal canal are the final parts of the alimentary tract posterior to the prostate that stores feces.¹ The angle between the rectum and anal canal is maintained by the puborectalis muscle at roughly 80° for fecal continence and straightened during defecation.¹ The rectum is directly posterior to the prostate.⁴ The *Denonvilliers' fascia* are fibromuscular layers that separate the prostate from the rectum to about 4.6 cm away.²

Urinary function The *bladder* is a hollow muscular sac superior to the prostate that temporarily stores urine.¹ The bladder neck's muscle fibers are continuous with the prostate base's fibromuscular tissue.¹ The *urethra* is a thin muscular tube running through the prostate that transports urine from the bladder's internal urethral orifice to the penis tip's external urethral orifice.¹ The prostatic urethra length ranges from 3 cm to 6 cm with a 29° bend at about 68% of the prostate length from the bladder neck.² The *internal urethral sphincter* is an involuntary muscle directly inferior to the bladder that prohibits urine release and prevents ejaculate from entering the bladder.¹ The *external urethral sphincter* is a voluntary muscle directly inferior to the prostate that keeps the urethra compressed to maintain urinary continence.¹

Sexual function The *penis* is a roughly-cylindrical organ inferior to the prostate that contains erectile tissue that fills with blood to harden and contains the external urethral orifice.¹ The *urethra*, previously mentioned in terms of urinary function, is also involved in sexual function, namely to deliver semen.¹ The *penile bulb* is the base of the penis and is covered by the *bulbospongiosus muscle* that compresses the penile bulb to discharge remaining urine or semen.¹ The *seminal vesicles* are elongated glands posterosuperior to the prostate between the bladder and rectum that secrete a thick alkaline fluid to form the semen.¹ The *neurovascular bundle* is a network of nerves and blood vessels running along the posterolateral surface of the prostate that supports erectile function. The *internal pudendal artery* is the main blood vessel with branches supplying blood for erectile function.¹ If the internal pudendal artery is obstructed, the penis will receive less blood, subsequently impairing erections.⁵

1.3 Prostate Cancer Incidence and Treatments

According to estimates by the American Cancer Society, prostate cancer has the highest incidence of cancer (180 890 projected new cases in 2016[†]) and second highest mortality rate (26 120 projected deaths in 2016[‡]) in men, apart from skin cancer.⁶ According to the National Comprehensive Cancer Network (NCCN) guidelines,⁷ initial diagnosis of prostate cancer can be made through digital rectal examination (DRE), blood test for the prostate-specific antigen (PSA), and transrectal-ultrasound (TRUS) guided biopsy to evaluate the Gleason score (indicates cancer aggressiveness). Next, depending on the patient's life expectancy and symptomatic status, cancer staging can be done with imaging, including bone scan, pelvic CT or MRI.⁷ The patients are then stratified into risk groups (very low, low, intermediate, high, very high and metastatic), depending on the American Joint Committee on Cancer (AJCC) clinical stage, biopsy Gleason score, and PSA.⁷ The risk groups predict biochemical failure-free survival (using PSA as a prostate cancer indicator),⁸ thereby forming the basis for treatment recommendations.⁷

After risk group stratification, the next course-of-action is either monitoring (active surveillance or inactive observation) or treatment of the prostate cancer. Treatment options include radiation therapy (brachytherapy, external beam photon and proton radiation therapy and radiopharmaceutical therapy), surgery (radical prostatectomy and pelvic lymph node dissection), hormone/androgen deprivation therapy, immunotherapy, and chemotherapy.⁷

1.4 Prostate Implant Indications and Outcomes

Prostate implants, also known as low-dose-rate (LDR) prostate brachytherapy, is of particular interest for the treatment of early-stage prostate cancer. From the definition by the International Commission of Radiation Units and Measurements (ICRU) Report 38,⁹ LDR brachytherapy refers to radiation dose rates of 0.4 Gy/h to 2 Gy/h while high-dose-

[†]Incidence estimates by the American Cancer Society used data collected from the Surveillance, Epidemiology and End Results (SEER) program at the National Cancer Institute (NCI), National Program of Cancer Registries (NPCR) at the Centers for Disease Control and Prevention (CDC), and the North American Association of Central Cancer Registries (NAACCR).⁶

[‡]Mortality estimates by the American Cancer Society used data collected from the National Center for Health Statistics (NCHS).⁶

rate (HDR) brachytherapy refers to dose rates $> 12 \text{ Gy/h}$.[§] According to the American Brachytherapy Society consensus guidelines, prostate implants are indicated as monotherapy for low-risk patients, supplemented with external beam radiotherapy for high risk patients, and case-dependent for intermediate risk patients.¹⁰ Notably, prostate implant as the primary treatment for low-risk patients is accepted by the NCI, NCCN, American Cancer Society (ACR), American Urologic Association (AUA), American Society for Radiation Oncology (ASTRO), American College of Radiology (ACR), European Society for Therapeutic Radiology and Oncology (ESTRO), European Association of Urology (EAU), and European Organization for Research and Treatment of Cancer (EORTC).^{7,10–12}

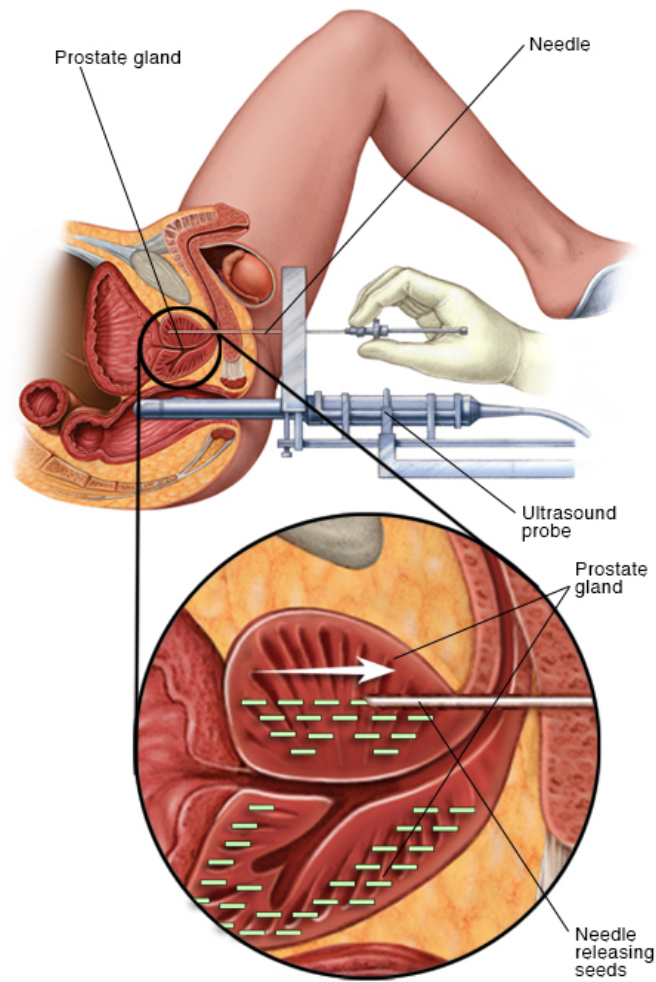
During a prostate implant procedure, numerous small radioactive seeds of a given isotope are permanently implanted into the prostate to deliver localized radiation (Figure 1.3). The seeds may be loose or stranded, and are deposited under transrectal ultrasound (TRUS) and template guidance. As the radioactive isotope decays, the seeds release radiation, damaging the integrity of the nearby cells.¹⁴

Common radioisotopes used for the seeds are Iodine-125, Palladium-103, and Cesium-131.[¶] The seeds typically have a length of 4.5 mm and diameter of 0.8 mm, but the specific geometries depend on the seed manufacturer.¹⁵

Prostate brachytherapy is associated with high survival (biochemical failure-free survival, metastasis-free survival, prostate cancer specific survival, overall survival) and low complications (urinary continence, lack of urinary and bowel bother, preservation of sexual and hormonal function) at low costs (Figure 1.4).¹⁶ Hayes et al.¹⁷ reported that in low-risk patients, compared to radical prostatectomy and intensity modulated radiation therapy (IMRT, a form of external beam radiation therapy that delivers highly conformal dose to the prostate), LDR brachytherapy has the lowest cost and highest quality-adjusted life expectancy. Shah et al.¹⁸ reported no significant differences in survival outcomes among LDR brachytherapy, HDR brachytherapy and IMRT, while LDR brachytherapy cost significantly less to Medicare and health care institutions (\$9938 for LDR brachytherapy, \$17 514 for HDR brachytherapy with 4 fractions and \$29 356 for IMRT).

[§]Gray (Gy) is the SI unit for ionizing radiation dose. $1 \text{ Gy} = 1 \text{ J/kg}$

[¶]See Section 2.1.1 for more information about radioactive sources used for prostate implants.



© MAYO FOUNDATION FOR MEDICAL EDUCATION AND RESEARCH. ALL RIGHTS RESERVED.

Figure 1.3: Permanent prostate brachytherapy involves placing many radioactive seeds within the prostate to treat prostate cancer. During the procedure, an ultrasound probe is placed in the rectum to help guide the placement of seeds. The seeds emit radiation that dissipates over a few weeks or months. Reprinted from *Permanent prostate brachytherapy*. URL: <http://www.mayoclinic.org/tests-procedures/prostate-brachytherapy/multimedia/permanent-prostate-brachytherapy/img-20008710>.¹³

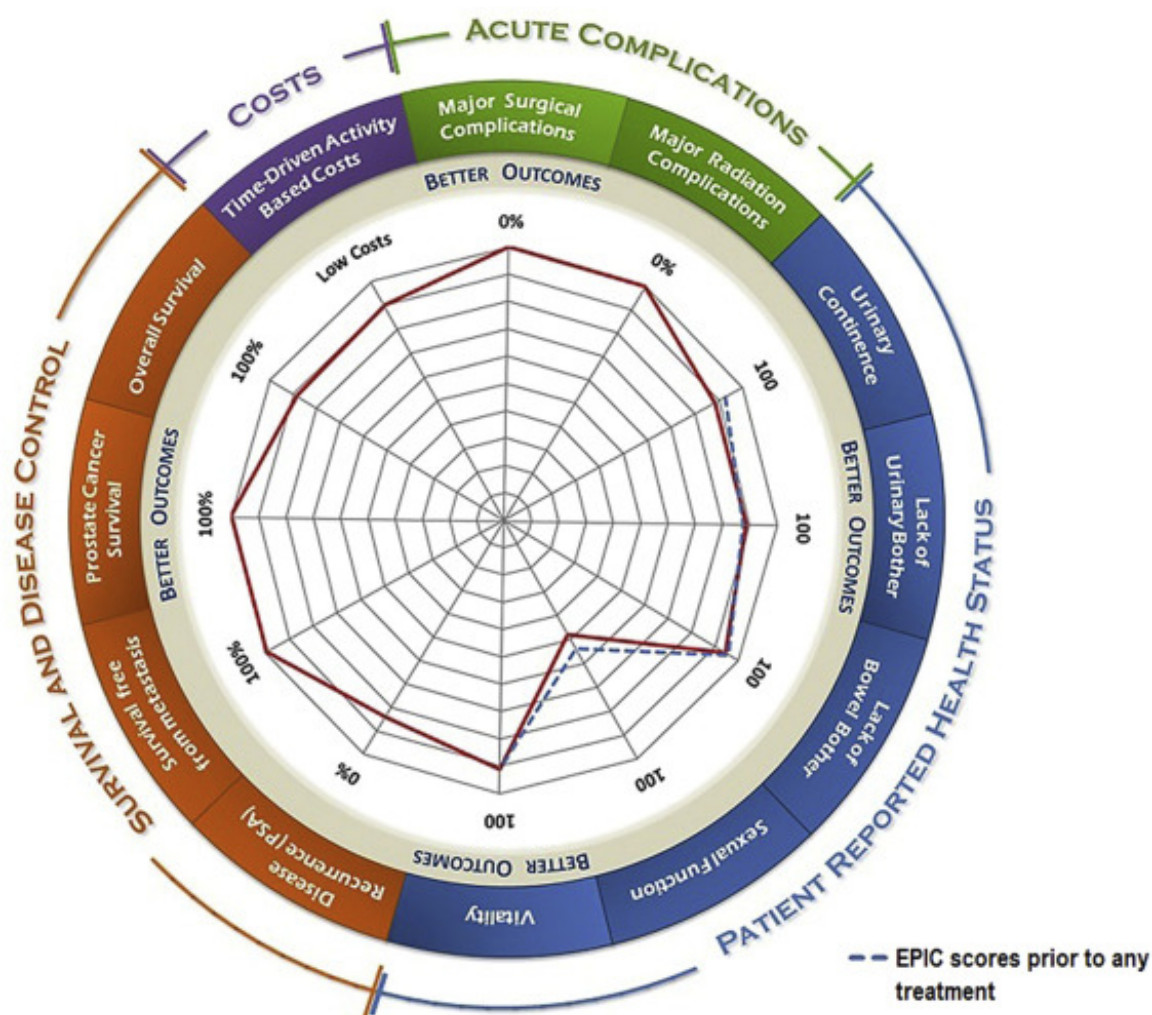


Figure 1.4: Radar chart representing the value framework for prostate implants. The radar chart tool can be used to visualize multiple outcome and costing metrics simultaneously. The chart allows direct visualization of the 6-month complications, 4-year patient-reported outcomes, 10-year survival, and time-driven activity-based costing provider costs at 1 year after implantation. The red line visually connects each numerical outcome or cost value on each axis. The blue dotted line represents the baseline Expanded Prostate Cancer Index Composite (EPIC) scores before prostate implant treatment. Reprinted from N. G. Thaker, T. J. Pugh, U. Mahmood, S. Choi, T. E. Spinks, N. E. Martin, T. T. Sio, R. J. Kudchadker, R. S. Kaplan, D. A. Kuban, D. A. Swanson, P. F. Orio, M. J. Zelefsky, B. W. Cox, L. Potters, T. A. Buchholz, T. W. Feeley, and S. J. Frank. “Defining the value framework for prostate brachytherapy using patient-centered outcome metrics and time-driven activity-based costing”. In: *Brachytherapy* (2016)¹⁶ (license number: 3876101241296).

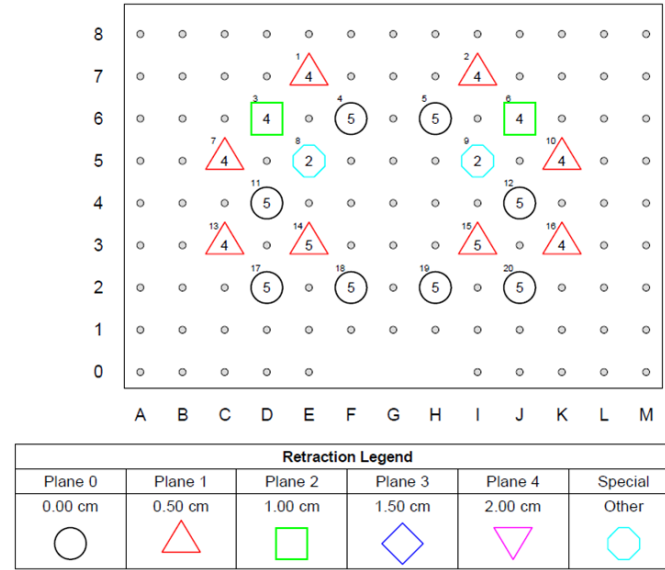
Since prostate implants are associated with low morbidity,¹⁰ consideration of quality-of-life after treatment is imperative. Quality-of-life can be impacted by bowel, urinary and sexual complications, given the adjacency of critical structures described in Section 1.2. For instance, Holmes et al.² reported a mean distance from individual seeds of 1.6 cm to the urethra, and 2.3 cm to the rectum. The Expanded Prostate Cancer Index Composite (EPIC) survey questionnaire can be used to evaluate bowel, urinary and sexual complications. Acute urinary complications, such as urethral stricture, urinary bother, urinary retention, urinary incontinence and painful urination, are common but usually resolve within a year.^{19,20} Also common are bowel complications, such as frequent bowel movements, diarrhea, constipation and rectal fistula.^{20,21} Sexual complications include erectile dysfunction, blood in semen, pain during orgasm and alteration in orgasm intensity.^{5,20,22,23}

1.5 Prostate Implant General Workflow

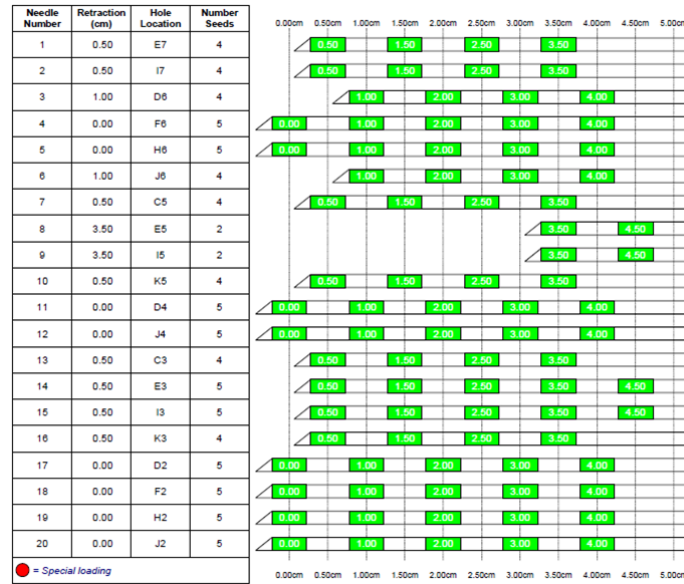
The prostate implant workflow can be broken down into three stages: pre-implant, implant and post-implant.

1.5.1 Pre-implant

Prior to the implant, transrectal ultrasound (TRUS) is the common imaging modality used to assess any potential interference of the needle and pubic arch, as well as obtain images to generate a treatment plan. The physician typically contours the prostate and critical structures (rectum, bladder and urethra) on the TRUS images. The physicist or dosimetrist then plan the seed locations such that the prescribed dose (typically 110 Gy to 160 Gy for monotherapy, depending on the isotope¹⁰) is delivered to as much of the prostate volume while minimizing dose to critical structures. For instance, Figure 1.5 shows a pre-implant plan with a peripheral loading pattern whereby seeds are loaded mostly at the periphery of the prostate, thus reducing dose to the central prostatic urethra.



(a) Peripheral loading pattern



(b) Needle configuration

Figure 1.5: (a) The peripheral loading pattern involves needle placement avoiding the urethra running through the center of the prostate. (b) The needles contain seeds (green) with spacers in between and have different configurations depending on placement of that particular needle in the prostate.

1.5.2 Implant

Current prostate brachytherapy implantation procedures are performed via the transperineal approach using TRUS and template guidance for needle insertion by the physician.²⁴ Depending on the prostate size and radionuclide, the number of seeds implanted typically ranges from 50 to 150.²⁵

This dissertation focuses on the uncertainties related to the evaluation of the quality of the implant. However, the quality of the implant itself can be affected by several uncertainties that are independent of the evaluation process. When reporting outcomes of the evaluation of implant quality, the factors affecting implant quality should be isolated. Explored below are the uncertainties that can affect the quality of the implant, such as varying institution standards, differences due to seed manufacturer, individual variations of the physician performing the implant, the manual process of needle insertion into the prostate, inhomogeneity of disease distribution, and seed migration.

Institution standards Apart from variations of individual physicians, at a higher level, different institutions have varying implant techniques.^{26,27} For instance, some institutions may use more activity per implant and others may have more generous prostatic margins to address extraprostatic disease, resulting in variations in glandular coverage or uniformity due to varying prioritization of biological endpoints.²⁶ Nomograms, used for outcome prediction during treatment selection, may not predict the recurrence after prostate implants depending on institutional variability.²⁸

Seed manufacturer Even for the same radioisotope of the same source strength, different seed manufacturer have variations in dosimetry and visibility on images.^{29||}

Physician implant performance Physician training and experience in performing implants affects the deposited seed distributed and consequently, the implant quality. For instance, some physicians tend to include a more generous margin due to their experience in external beam radiation therapy.²⁷

^{||}See Section 2.1.1 for further details on the impact of seed type on prostate D90 and MRI susceptibility artifacts.

Manual needle insertion There is intrinsic variation of inserting needles manually, with a large contributing factor due to prostate movement during needle insertion. The pre-implant plan assumed dose distribution based on perfectly parallel strands.

Disease distribution An implant with adequate dose coverage of the prostate would not be sufficient if there was undetected microscopic disease at the periphery or outside the prostate.^{30,31} Similarly, inadequate dose coverage of the prostate may still be of good quality for disease control if the underdosing occurred in non-diseased regions in the prostate.³⁰

Seed migration In rare occasions, during needle insertion of the seeds, perforation of the urethra or blood vessels may lead to seed loss via the urethra or seed migration until lodged in small pulmonary vessels.³² Migration is especially common with the use of free seeds. Kunos et al.³³ reported that out of 12 524 seeds implanted in their study cohort, 249 seeds migrated, with 68 to the lungs. The use of stranded seeds compared to loose seeds is associated with a lower incidence of seed migration to the lungs.³⁴ Al-Qaisieh et al.³⁴ observed no evidence of seed migration to the lungs in any of the 238 patients implanted with stranded seeds (RAPIDStrand; GE Healthcare, Arlington Heights, IL).

1.5.3 Post-implant

The patient undergoes a CT pelvic exam typically within 60 days after the implant (usually either on the day of the implant or approximately 30 days later).¹⁰ The physician contours the prostate and critical structures on the CT images. Next, the seed locations are roughly identified with an automated software built-in to the TPS and manually-corrected. The seed locations and structure contours allow for an assessment of the dose delivered to the prostate and critical structures. To assess implant quality, the current standard is to evaluate dose volume histogram (DVH) parameters and isodose line coverage of anatomy on post-implant images. Figure 1.6 illustrates the interpretation of a DVH. Several limits are in place for DVH parameters in LDR prostate brachytherapy, such as D90 (minimum dose covering 90% of the structure), V100 (volume receiving 100% of the prescribed dose), and V150 (volume receiving 150% of the prescribed dose). Lastly, the patient undergoes follow-up care whereby

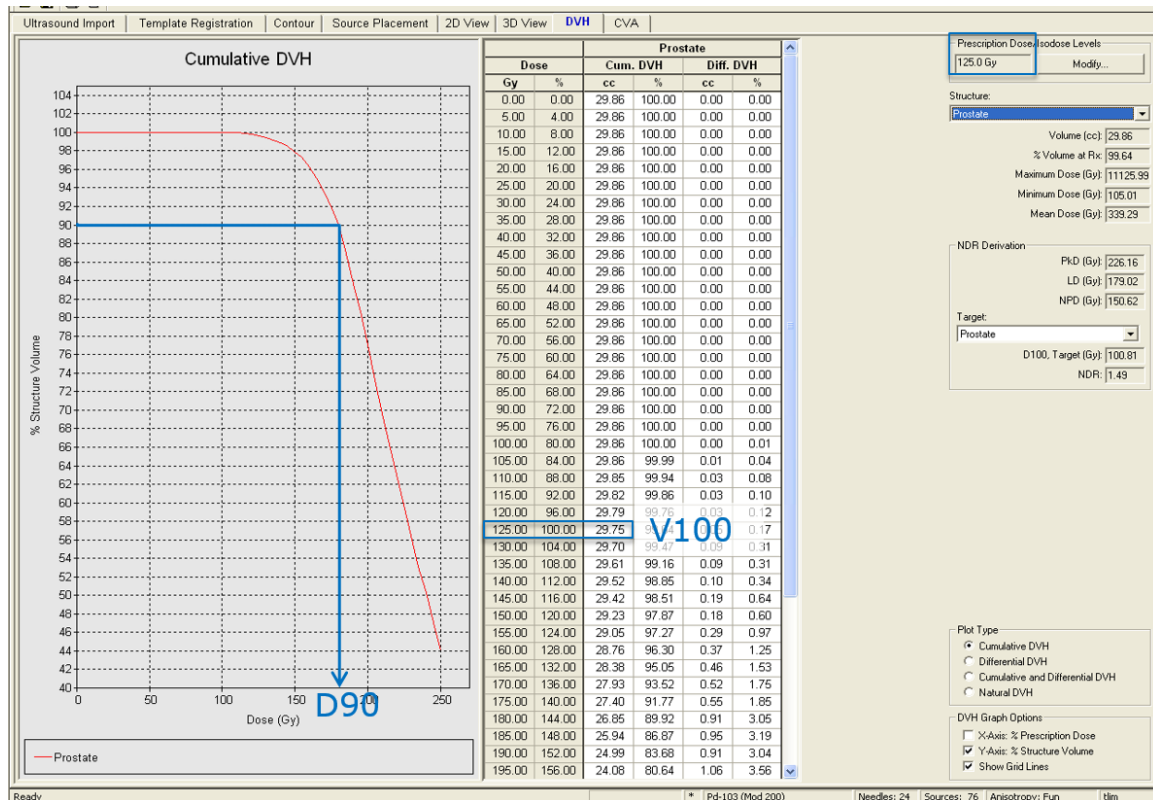


Figure 1.6: A dose-volume histogram (DVH) is a histogram with radiation dose on the x -axis and structure volume on the y -axis. The red line is the DVH for the prostate, as displayed using the VariSeed treatment planning system. The prostate D90 is the minimum dose covering 90% of the prostate volume, as denoted by the blue arrow. The prostate V100 is the volume of the prostate receiving 100% of the prescribed dose, as denoted by the blue box (in this case, the prescription dose was 125 Gy for a Pd-103 implant, as indicated at the top right corner).

the PSA is checked frequently.

The post-implant dosimetric assessment is important for several reasons. Firstly, for day-of-implant dosimetric evaluations, sub-standard implant quality may indicate corrective therapy, such as bringing the patient back to the operating room for implantation of additional seeds into the prostate. Another value of post-implant dosimetry is to serve as feedback to the prostate brachytherapy team for future improvements, such as the physician's needle insertion techniques and the physicist's or dosimetrist's seed loading pattern strategies. Last but most certainly not least, through implant quality evaluation, institutions may better determine dose-response relationships and better establish the correlation between implant strategies to tumor control and normal tissue complications. Implant quality has been linked

to biochemical control and survival.^{30,35–39}

Apart from the uncertainties affecting implant quality described in Section 1.5.2, there are also uncertainties associated with implant quality *evaluation*. Given the importance of implant quality evaluation, we need to be cognizant of the uncertainties of implant quality evaluation, which can affect the perceived implant quality and subsequent clinical management. Since dose is continuously delivered until the radioisotope decays to a negligible level, and patient anatomy during this entire course of treatment is highly variable, the post-implant images only represent a snapshot of the dose distribution in the prostate and nearby critical structures.

Some uncertainties stemming from using DVH parameters obtained from post-implant images as a surrogate for implant quality are elucidated below. These uncertainties of implant quality evaluation stem from varying amounts of bladder and rectal filling, prostate edema, physician contouring, the dose calculation formalism, brachytherapy TPS, and post-implant imaging modality. Of these factors, this dissertation focuses on the uncertainties of implant quality evaluation due to the brachytherapy TPS and post-implant imaging modality.

Bladder and rectal filling at the time of post-implant imaging The bladder and rectum are expandable muscular structures to accommodate storage of urine and feces. The filling of the bladder and rectum changes the location of the prostate in relation to other critical structures. Post-implant imaging at a certain time only offers a snapshot in time of the dose distribution to critical structures nearby.

Extent and resolution of prostate edema Prostate swelling due to needle-induced trauma increases the perceived prostate volume.⁴⁰ Edema also affect the interseed distance and subsequent dose coverage.⁴¹ Furthermore, edema affects seed fixity, leading to seed migration.³² The extent of prostate edema affects the seed distribution in the prostate and in relation to critical structures. Post-implant dosimetric evaluation on the day of the implant results in edema-derived dosimetric errors compared to evaluation at a later stage (optimal timing is 16 ± 4 days for Pd-103 implants and 30 ± 7 days for I-125 implants).¹⁰ Edema can be assessed by comparing the TRUS-defined intraoperative prostate volume

to the post-implant imaging prostate volume. Acher et al.⁴² found mean differences of D90 was 13 Gy using intraoperative TRUS volume to post-operative CT volume, and 17 Gy using intraoperative TRUS volume to post-operative CT-MRI volume.⁴² Ash et al.³⁰ found a significant correlation between D90 and the ratio of CT and TRUS volumes. However, they found that although D90 and PSA control was significant in the low-risk group, it was not significant in the intermediate- and high-risk groups, potentially due to presence of edema distorting the dose-volumes, underdosing occurring in non-diseased areas, or failure occurring outside the prostate. Crook et al.⁴¹ found statistically significant residual edema in 12 % (29 patients) of their study cohort whereby the mean prostate volume was 34.8 cc before the implant but 46.1 cc a month after the implant.

Physician contouring The previous contouring experience, training, bias, stress and fatigue experienced by the physician may affect the subjective delineation of the prostate. Crook et al.⁴³ found that the contouring of the prostate volumes on CT images by inexperienced physicians were significantly smaller than the corresponding volumes on MRI images due to underestimation of prostate edema and overcorrection attempts to exclude the anterior venous plexus and puborectalis muscle. Uncertainties in volume propagate into uncertainties in DVH parameters. Crook et al.⁴³ found that prostate contouring on CT and MRI images resulted in V100 difference of 2.4 % by an experienced physician versus 9.4 % and 4.4 % by 2 inexperienced physicians. Dubois et al.⁴⁴ found that whether prostate volumes contoured on CT and MRI images were significantly different is dependent on the individual observers.

Dose calculation formalism The dose calculation assumes all tissue density to be water-equivalent, according to the American Association of Physicists in Medicine Task Group 43 (AAPM TG-43) report.⁴⁵ Since the dose is delivered at short ranges to tissues with similar electron densities, no electron density corrections are used.¹⁵

Treatment planning system Dose calculation in the TPS introduces uncertainties in implant quality evaluation. Different TPS may adopt different dose calculation input data from literature, especially for newer radioisotopes released after the publication of AAPM

reports concerning brachytherapy dosimetry.^{15,45–48} Different TPS may also calculate volume based on the user-provided contours differently**.

Post-implant imaging modality The choice of imaging modality for post-implant dosimetry is a significant contributor to uncertainties in implant quality evaluation and is the central motivation of this dissertation. The post-implant imaging modality affects the precision of the seed localization,⁴⁹ precision^{27,31,44,50–52} and accuracy^{51,53–55} of prostate delineation, as well as the precision and accuracy of normal tissue contours.^{55,56}

1.6 Post-implant Dosimetry Imaging Modalities

DVH parameters generated from post-implant dosimetric assessment are widely used as metrics to estimate the implant quality. To estimate the extent of the radiation exposure in both the cancerous and normal cells, two main pieces of information are needed from the post-implant images: (1) the radioactive seeds' precise locations; (2) the boundaries of the prostate and normal structures adjacent to the prostate, such as the bladder, urethra, rectum and penile bulb.

The accuracy of localizing the radioactive seeds and contouring the anatomical volumes depends on the post-implant image quality. Therefore, post-implant imaging is crucial for ensuring the quality of the implant. The two main imaging modalities used for post-implant imaging are CT and MRI.

1.6.1 Computed Tomography

The current standard of care is to perform a CT scan after implantation to delineate the anatomy, identify the radioactive seeds, and verify the radiation dose distribution.^{10,58} Contrast on CT images are mainly defined by the object contrast, namely the imaged object's effective atomic number.

The advantage of CT for the purposes of post-implant dosimetry is that the radioactive seeds can be easily visualized on a CT scan (Figure 1.7a). The seeds' high atomic number

**See Chapter 2 for a comparison of calculations of dose, volume and dose-volume histogram parameters by two different TPS

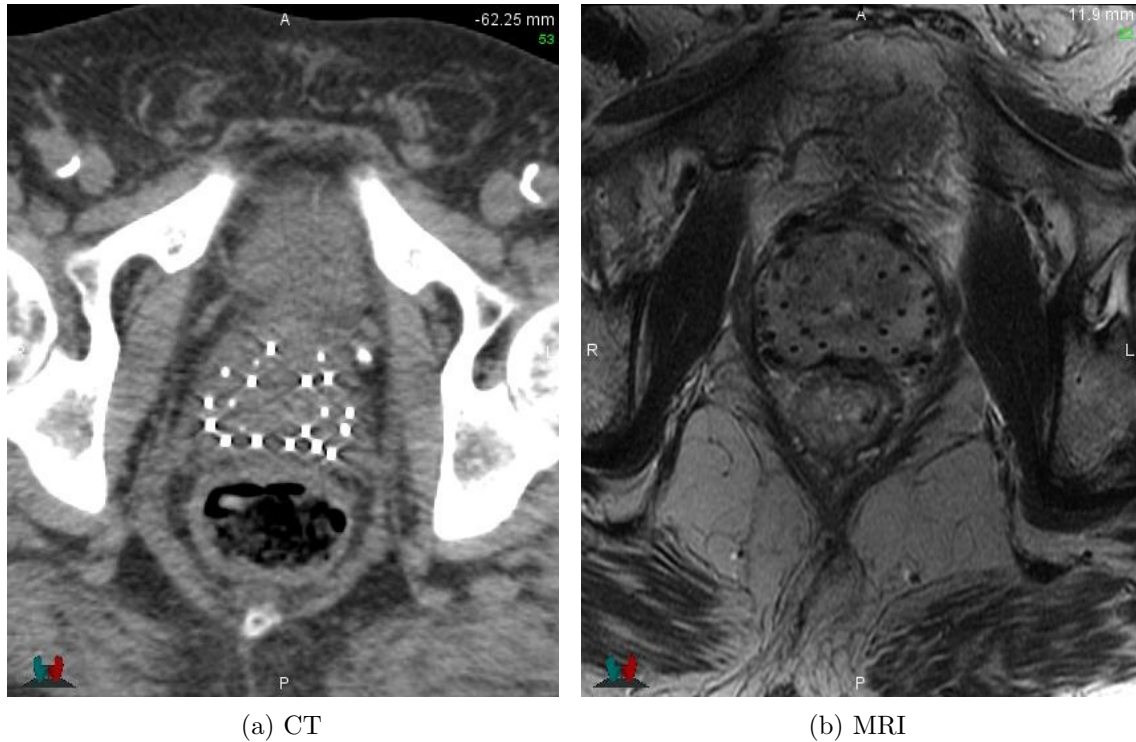


Figure 1.7: Comparison of CT and MRI postimplant images. Brachytherapy seeds can be more definitively identified using CT, but appear as signal voids with MRI. However, the anatomical details of the male pelvis are clearly more visible with MRI. Reprinted from T. Y. Lim, R. J. Stafford, R. J. Kudchadker, M. Sankaranarayanapillai, G. Ibbott, A. Rao, K. S. Martirosyan, and S. J. Frank. “MRI characterization of cobalt dichloride-N-acetyl cysteine (C4) contrast agent marker for prostate brachytherapy”. In: *Phys Med Biol* 59.10 (2014), pp. 2505–16⁵⁷ (©Institute of Physics and Engineering in Medicine. Reproduced by permission of IOP Publishing. All rights reserved).

and density result in high contrast between the seeds and prostatic tissue.

The disadvantage of CT for the purposes of post-implant dosimetry is that poor soft tissue contrast inherent to CT makes it difficult to visualize the prostatic capsule,^{27,51,52} and other tissue may be mistaken for the prostate.⁵⁹ Also, metallic artifacts introduced by the seeds due to the high atomic number of the seed's titanium casing potentially obscures visualization of the prostate boundaries and also confounds definitive seed centroid localization.²⁷

CT-only post-implant dosimetry is common at most institutions, even with uncertainties in the contouring of the prostate and critical soft tissue nearby^{††}.

1.6.2 Magnetic Resonance Imaging

Another post-implant imaging modality is MRI, whereby the hydrogen protons precessing at varying frequencies provide contrast and spatial information[†]. Currently, MRI is the optimum imaging modality for staging of a suspected primary prostate malignancy.^{60–62} Beyersdoff et al.⁶⁰ reported 75% accuracy of prostate cancer staging with MRI.

The advantage of MRI for the purposes of post-implant dosimetry is superior soft-tissue visualization of the prostate and surrounding critical structures.^{61,63–65} A variety of MRI imaging techniques allows for detailed visualization of pelvic anatomy.^{64,66} Improved visualization can be seen on MRI images compared to CT images for intraprostatic zonal detail,⁶³ extraprostatic extension,⁶³ prostate apex and base,²⁰ internal pudendal artery,^{5,20} neurovascular bundles,^{55,63,67,68} penile bulb,^{20,55,68} rectal wall,^{20,55,67} bladder neck,²⁰ urethra⁵⁵ and urinary sphincters.^{5,51,54,56} Anatomical visualization of critical structures is important to potentially correlate the dose delivered to these structures to the treatment complications,²⁰ such as those described in Section 1.4.

The disadvantage of MRI for post-implant dosimetry is that the metallic radioactive seeds and spacers appear as negative voids on MRI images (Figure 1.7b), thus confounding precise detection of seed positions.^{27,49,69–71} The seeds may be mistaken for needle tracks⁷² or blood vessels,^{69,70} or obscured by other inhomogeneities such as hemorrhage, calcifications, or air

^{††}See Section 5.1.1 for further discussion of the advantages and disadvantages of CT-only post-implant dosimetry.

[†]See Section 3.1.1 for more details about the contrast mechanism on MRI images.

bubbles.⁷³ Definitive seed localization remains the main challenge, preventing widespread use of MRI as a single-imaging modality for post-implant dosimetry.^{20,74}

Due to the excellent soft tissue contrast on MRI images and high seed visibility on CT images, CT-MRI fusion-based post-implant dosimetry is the post-implant dosimetry approach recommended by the American Brachytherapy Society¹⁰ and regarded as the gold-standard for prostate edge identification.⁴³ However, CT-MRI fusion-based post-implant dosimetry requires acquisition of two sets of images, thereby introducing further uncertainties from the fusion process as well as logistical issues[†]. MRI-only post-implant dosimetry is not done as part of the routine clinical workflow of any institutions, but there are many ongoing investigations into the possibility of MRI-only post-implant dosimetry[§]

1.7 Encapsulated Contrast Agent Markers (Sirius MRI Markers)

To enable MRI-only post-implant assessment, encapsulated contrast agent markers have been proposed as a potential solution.²⁰ The encapsulated contrast agent markers, also known as Sirius MRI markers, contain cobalt dichloride N-acetyl cysteine ($\text{CoCl}_2\text{-NAC}$; C4 contrast agent) encapsulated in a polyetheretherketone (PEEK) casing. These Sirius MRI markers are hyperintense on MRI images and are designed to be placed adjacent to hypointense seeds.

Frank et al.²⁰ first identified the $\text{CoCl}_2\text{-glycine}$ contrast agent to have the greatest signal when compared to various contrast agents, namely Omniscan (Gadodiamide), L-PG-Bz-DTPA-Gd, Feridex IV, colloidal nanoparticle solutions of Fe_3O_4 , CoFe_2O_4 , Mn-Zn and Ni-Zn ferrites (Figure 1.8). Frank et al.²⁰ also first visualized the C4 contrast agent encapsulated in marker stranded with nonradioactive seeds implanted into a canine prostate (Figure 1.9).

Furthermore, the Sirius MRI markers do not alter the radiation dose distribution.^{75,76} Frank et al.⁷⁵ reported that the Sirius MRI markers adjacent to the radioactive seed did not

[†]See Section 5.1.2 for further discussion of the advantages and disadvantages of CT-MRI fusion-based post-implant dosimetry.

[§]See Section 5.1.3 for further discussion of the advantages and disadvantages of MRI-only post-implant dosimetry.

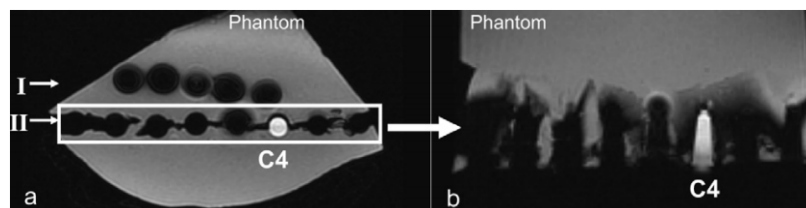


Figure 1.8: Novel C4 agent with positive contrast in 1.5 T magnetic resonance imaging T_1 -weighted sequence. (a) Coronal and (b) sagittal images. I indicates manufactured titanium seeds with paramagnetic and supraparamagnetic contrast agents. "Blooming" susceptibility artifact of titanium seeds shown. II indicates various paramagnetic and supraparamagnetic contrast agents in plastic vials, with C4 agent showing positive magnetic resonance imaging contrast. Reprinted from S. J. Frank, R. J. Stafford, J. A. Bankson, C. Li, D. A. Swanson, R. J. Kudchadker, and K. S. Martirosyan. "A novel MRI marker for prostate brachytherapy". In: *Int J Radiat Oncol Biol Phys* 71.1 (2008), pp. 5–8²⁰ (license number: 3876101018346).

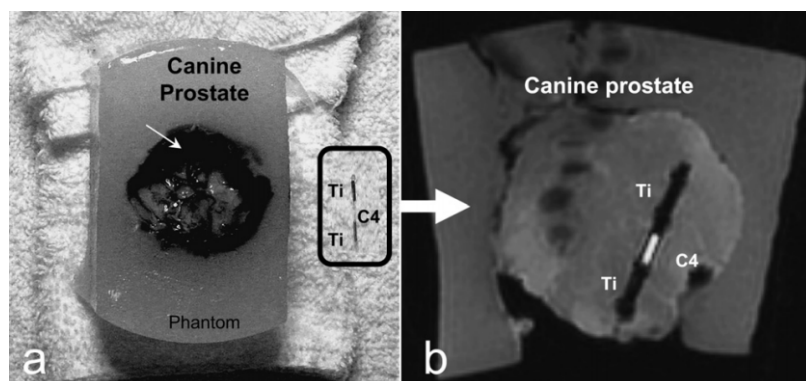


Figure 1.9: Imaging of standard titanium seeds with embedded encapsulated contrast agent marker in canine prostate incorporated into phantom. (a) Canine prostate embedded in agarose gel phantom and strand of standard titanium seeds and encapsulated contrast agent marker with C4 agent between seeds. (b) Sagittal, 1.5 T T_1 -weighted magnetic resonance image of canine prostate with strand of standard titanium seeds containing encapsulated contrast agent marker with C4 agent, permitting accurate identification of seeds. Reprinted from S. J. Frank, R. J. Stafford, J. A. Bankson, C. Li, D. A. Swanson, R. J. Kudchadker, and K. S. Martirosyan. "A novel MRI marker for prostate brachytherapy". In: *Int J Radiat Oncol Biol Phys* 71.1 (2008), pp. 5–8²⁰ (license number: 3876101018346).

significantly affect the seed's 2D anisotropy function $F(r, \theta)$ or 1D anisotropy function $\phi(r)$ as measured by thermoluminescent dosimeters in a water phantom[¶]. Frank et al.⁷⁵ also verified that the Sirius MRI markers can still be visualized by MRI after being irradiated with a dose equivalent to the cumulative dose in a month for a typical prostate implant. The Monte Carlo evaluation of the dosimetric influence of Sirius MRI markers (Figure 1.10) by Melhus et al.⁷⁶ found no significant impact on DVH parameters due to the 1% cobalt chloride concentration marker (chelated with glycine) placed next to I-125, Pd-103 and Cs-131 seeds.

N-acetyl-cysteine (NAC, $C_5H_9NO_3S$) was later used as the chelate instead of glycine ($C_2H_5NO_2$), as NAC increased urinary and fecal cobalt excretion and lowered liver and spleen cobalt levels.⁷⁷ To evaluate the effect of potential leakage of the Sirius MRI markers, Frank et al.⁷⁷ evaluated the biodistribution and toxicity of $CoCl_2$ -NAC by directly injecting the contrast agent into rats, and found no systemic toxicity with dual renal-hepatic elimination at the dose and volume consistent with a volumetric prostate implant.

Nevertheless, use of the Sirius MRI markers is associated with some limitations. A caveat of using Sirius MRI markers is the indirect correspondence between hyperintense signals on MRI images and seed positions. Since the Sirius MRI markers are placed next to the seeds, contrary to conventional CT images, the bright signals do not represent the seeds themselves, but represent the markers instead.

Another limitation from the use of Sirius MRI markers is the restriction to stranded (not loose) seeds. Since the markers need to be placed at a fixed distance adjacent to the seeds, the markers and seeds must be stranded together. Furthermore, migrated seeds would be difficult to localize. Marker-based seed localization depends on the proximity of a Sirius MRI marker to definitively localize a seed. A migrated seed then would be difficult to localize. However, compared to loose seeds, stranded seeds rarely migrate.^{33,34} Moreover, from our institution's experience,⁷⁸ lower overall activity is required for treatment using stranded seeds instead of loose seeds, resulting in greater implant efficiency and improved dose homogeneity.

[¶]See Section 2.1.2 for the description of these anisotropy functions and the TG-43 dose calculation formalism.

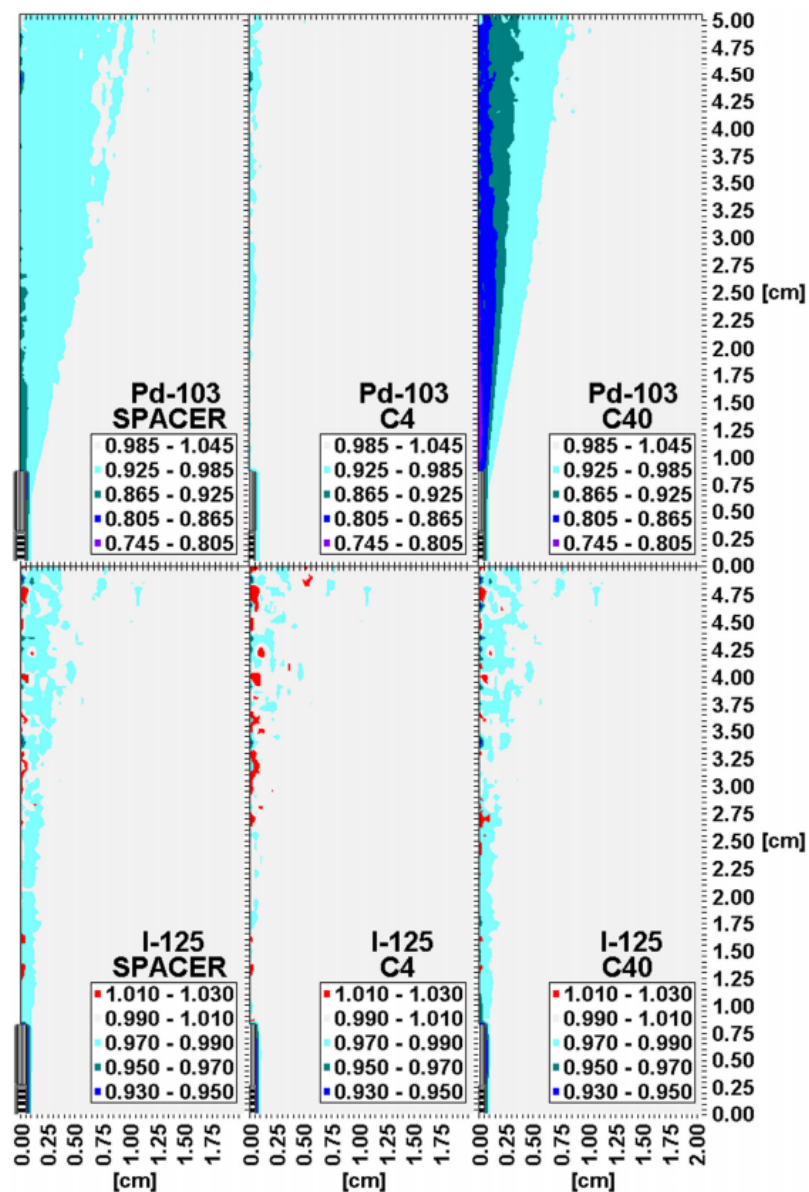


Figure 1.10: The relative dose distributions for Pd-103 (upper panels, with 3% bin width) and I-125 (lower panels, with 2% bin width) for a source in homogeneous water and a source with adjacent spacer for the model 6711 I-125 source and three different spacers. In the lower left corner of each panel, the bold horizontal striped object represents the upper half of the source, and the vertically striped object represents the spacer. Reprinted from C. S. Melhus, J. K. Mikell, S. J. Frank, F. Mourtada, and M. J. Rivard. “Dosimetric influence of seed spacers and end-weld thickness for permanent prostate brachytherapy”. In: *Brachytherapy* (2013)⁷⁶ (license number: 3876101458418).

Apart from limitations intrinsic to the design of the Sirius MRI markers, other limitations for the practical adoption of Sirius MRI markers in the clinical setting are addressed in this dissertation, namely a TPS allowing for MRI-based brachytherapy, Sirius MRI marker relaxation characterization, a pulse sequence to visualize the Sirius MRI markers, and manual seed localization.

This chapter is adapted from S. K. Dhanesar, T. Y. Lim, W. Du, T. L. Bruno, S. J. Frank, and R. J. Kudchadker. "Evaluation of the MIM Symphony treatment planning system for low-dose-rate prostate brachytherapy". In: J Appl Clin Med Phys 16.5 (2015), pp. 62–75⁷⁹ (licensed under a Creative Commons Attribution 3.0 License).

2

Comparison of MIM Symphony and VariSeed treatment planning systems

Contents

2.1	Background	27
2.1.1	Radioactive Seeds	27
2.1.2	Dose Calculation for Prostate Implants	29
2.1.3	Treatment Planning Systems	32
2.2	Purpose	35
2.3	Methods	35
2.3.1	Evaluation using VariSeed Test Procedures	35
2.3.2	Evaluation on Phantom Images	35
2.3.3	Evaluation on Patient Images	36
2.4	Results and Discussion	38
2.4.1	Evaluation using VariSeed Quality Assurance User Test Procedures	38
2.4.2	Evaluation on Phantom Images	38
2.4.3	Evaluation on Patient Images	41
2.5	Conclusion	48
2.5.1	Summary	48
2.5.2	Limitations	48
2.5.3	Implications	49

2.1 Background

2.1.1 Radioactive Seeds

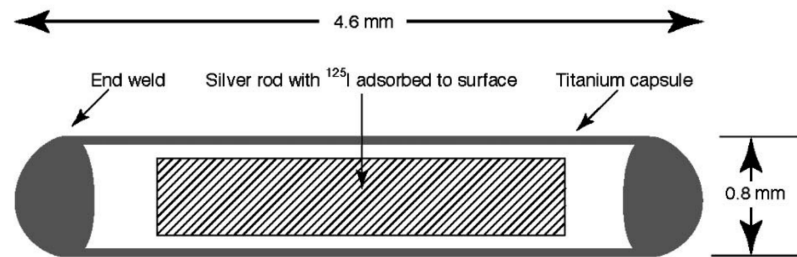
For permanent prostate implants, radioactive seeds with low dose rate (< 2 Gy/h) are used.⁹ To perform dose calculations, clinical brachytherapy treatment planning systems store various constants associated with these seeds for various types of radionuclides and manufacturers. The dose calculation constants and dose calculation formalism will be described in the next section.

Commonly used radionuclides are Iodine-125, Pd-103 and Cs-131 (Table 2.1). Due to differences in half-life and dose rate, the radionuclide chosen dictates the treatment dose prescribed to the planning target volume (PTV).¹⁰ For I-125 monotherapy, the prescription dose to the PTV ranges between 140 Gy to 160 Gy, while for Pd-103 monotherapy, the prescription dose to the PTV ranges between 110 Gy to 125 Gy.¹⁰

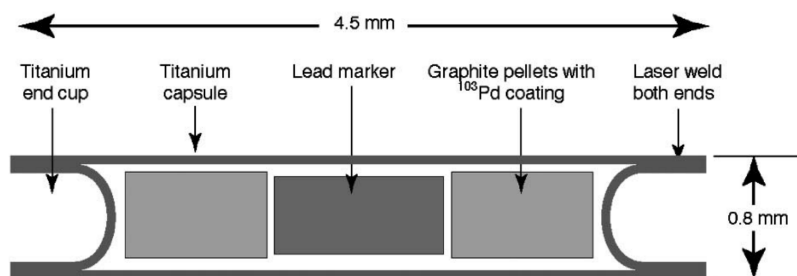
Table 2.1: Model numbers and characteristics of radioactive sources. Reprinted from S. K. Dhanesar, T. Y. Lim, W. Du, T. L. Bruno, S. J. Frank, and R. J. Kudchadker. “Evaluation of the MIM Symphony treatment planning system for low-dose-rate prostate brachytherapy”. In: *J Appl Clin Med Phys* 16.5 (2015), pp. 62–75⁷⁹ (licensed under a Creative Commons Attribution 3.0 License).

	I-125	I-125	Pd-103	Cs-131
Model number	IAI-125A	6711	200	Cs-1
Dose rate constant Λ (cGy/h/U)	0.981	0.965	0.686	1.059
Half-life (days)	59.399	59.399	16.991	9.689
Length (cm)	0.45	0.456	0.45	0.45

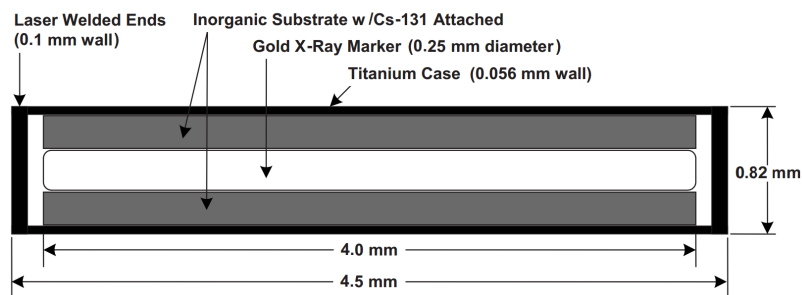
The construction of the seed depends on the seed manufacturer, resulting in differences in capsule thickness, weld thickness, weld material, radioactivity carrier material, radio-opaque material shapes, and other seed variations (Figure 2.1).¹⁵ Al-Qaisieh et al.²⁹ found statistically significant differences in prostate D90 from five different manufacturers’ I-125 seeds placed at the same locations. They also found that although visibility on CT images were similar, one of the source types (IBT Intersource 1251L) has a significantly larger susceptibility artifact on MRI images that could impede contouring.²⁹



(a) I-125 (model 6711)



(b) Pd-103 (model 200)



(c) Cs-131 (model Cs-1)

Figure 2.1: Different seed manufacturers have different seed geometries and internal construction. (a) I-125 and (b) Pd-103 seed schematic diagrams adapted from Mark J. Rivard, Bert M. Coursey, Larry A. DeWerd, William F. Hanson, M. Saiful Huq, Geoffrey S. Ibbott, Michael G. Mitch, Ravinder Nath, and Jeffrey F. Williamson. “Update of AAPM Task Group No. 43 Report: A revised AAPM protocol for brachytherapy dose calculations”. In: *Medical Physics* 31.3 (2004), pp. 633–674¹⁵ (with permission from the American Association of Physicists in Medicine). (c) Cs-131 seed schematic diagram adapted from R. Tailor, G. Ibbott, S. Lampe, W. B. Warren, and N. Tolani. “Dosimetric characterization of a Cs131Cs131 brachytherapy source by thermoluminescence dosimetry in liquid water”. In: 35.12 (2008), pp. 5861–8⁸⁰ (with permission from the American Association of Physicists in Medicine.)

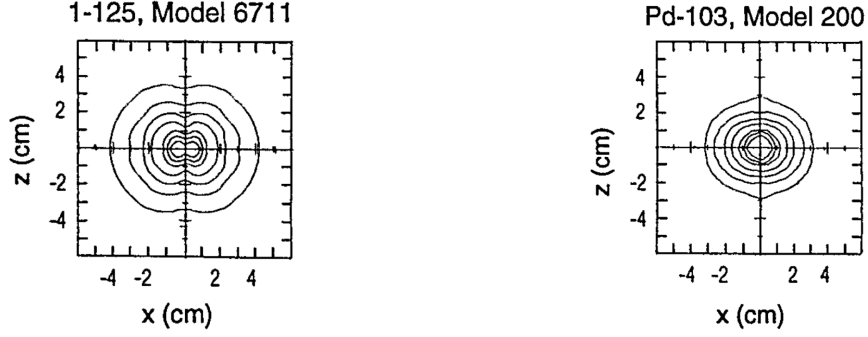


Figure 2.2: The isodose curves produced by I-125 and Pd-103 sources with air kerma strength of 100 U. The dose rates for the isodose curves starting from the outside were 2, 5, 10, 20, 50, 100 and 200 cGy/h. Adapted from Ravinder Nath, Lowell L Anderson, Gary Luxton, Keith A Weaver, Jeffrey F Williamson, and Ali S Meigooni. “Dosimetry of interstitial brachytherapy sources: Recommendations”. In: *Medical physics* 22.2 (1995), pp. 209–234⁴⁵ (with permission from the American Association of Physicists in Medicine).

2.1.2 Dose Calculation for Prostate Implants

Brachytherapy treatment planning systems calculate dose using the formalism recommended by AAPM TG-43.⁴⁵ Prior to the AAPM TG-43 report,⁴⁵ calculation of 2D dose distribution can be accomplished for a point isotropic source, but not for actual brachytherapy seeds with considerable anisotropy (Figure 2.2). To overcome this problem, the AAPM TG-43 formalism used measurements of dose distributions generated by actual brachytherapy seeds.⁴⁵

Using the 2D dose calculation formalism, the dose rate $\dot{D}(r, \theta)$ for a brachytherapy seed at a point (r, θ) in water is

$$\dot{D}(r, \theta) = S_k \cdot \Lambda \cdot \frac{G(r, \theta)}{G(r_0, \theta_0)} \cdot g(r) \cdot F(r, \theta) \quad (2.1)$$

where S_k is the air kerma strength, Λ is the dose rate constant, $G(r, \theta)$ is the geometry function, $G(r_0, \theta_0)$ is the geometry function at the reference point, $g(r)$ is the radial dose function, and $F(r, \theta)$ is the 2D anisotropy function.⁴⁵ From Figure 2.3, r denotes the distance from the center of the active source to the point of interest, r_0 denotes the reference distance of 1 cm, θ denotes the polar angle specifying the point of interest relative to the source longitudinal axis, and the reference polar angle θ_0 defines the source transverse plane which is specified to be 90° or $\pi/2$ radians.⁴⁵

The air kerma strength S_k of a brachytherapy seed characterizes the dose delivered to

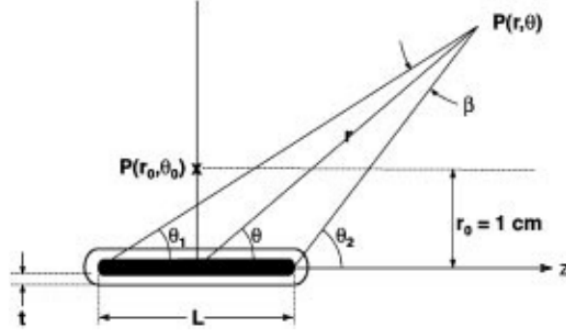


Figure 2.3: Coordinate system used for brachytherapy dosimetry calculations. Reprinted from Mark J. Rivard, Bert M. Coursey, Larry A. DeWerd, William F. Hanson, M. Saiful Huq, Geoffrey S. Ibbott, Michael G. Mitch, Ravinder Nath, and Jeffrey F. Williamson. “Update of AAPM Task Group No. 43 Report: A revised AAPM protocol for brachytherapy dose calculations”. In: *Medical Physics* 31.3 (2004), pp. 633–674¹⁵ (with permission from the American Association of Physicists in Medicine).

air along the transverse plane (Unit: U, where $1 \text{ U} = 1 \text{ cGycm}^2/\text{h}$).⁴⁵

The dose rate constant Λ defines the dose rate to water at $r = 1 \text{ cm}$ along the seed’s perpendicular bisector from a 1 U seed (Unit: cGy/h/U).⁴⁵ Λ includes the effect of seed geometry, spatial distribution of radiation in the seed, encapsulation, self-filtration, and scattering in water.⁴⁵

The geometry function $G(r, \theta)$ accounts for dose variation due to the spatial distribution of activity in the seed. For the line source approximation, where L is the active length of the source, the geometry function is

$$G_L(r, \theta) = \begin{cases} \beta / (Lr \sin \theta) & \text{if } \theta \neq 0^\circ \\ (r^2 - L^2/4)^{-1} & \text{if } \theta = 0^\circ \end{cases} \quad (2.2)$$

At larger distances ($r \gg L$), the radiation dose from a brachytherapy seed can be approximated as a point source and the geometry function can be written as

$$G_P(r) = r^{-2} \quad (2.3)$$

In the equation for dose rate calculation (Equation 2.1), the geometry function $G(r, \theta)$ is normalized to a reference point at $r = 1 \text{ cm}$ along a perpendicular bisector (Figure 2.3).

The radial dose function $g(r)$ characterizes the dose rate fall-off along the seed's transverse axis due to scatter and absorption in the medium (Unit: dimensionless).

The 2D anisotropy function $F(r, \theta)$ characterizes the angular dose rate variation around the source due to self-absorption, attenuation by the capsule, and other unaccounted dosimetric factors (Unit: dimensionless).

The values for the radial dose function $g(r)$ and the 2D anisotropy function $F(r, \theta)$ are source-specific, and can be obtained from AAPM reports⁴⁵ for certain source models* or from the manufacturer directly.

Finally, using Equation 2.1 and the half-life ($T_{1/2}$) for an isotope, the dose $D(r, \theta)$ at a point (r, θ) can be calculated as

$$D(r, \theta) = \ln 2 \cdot T_{1/2} \cdot \dot{D}(r, \theta) \quad (2.4)$$

The 2D dose calculation formalism can be applied to brachytherapy seeds with known L and orientations. To simplify seed localization procedures¹⁵ or if too many implanted seeds are randomly oriented,⁴⁵ the 1D dose calculation formalism¹⁵ can be used to calculate dose rate

$$\dot{D}(r) = S_k \cdot \Lambda \cdot \frac{G_L(r, \theta_0)}{G_L(r_0, \theta_0)} \cdot g_L(r) \cdot \phi_{an}(r) \quad (2.5)$$

where, the subscript L is for line source approximation, P for point source approximation, and $\phi_{an}(r)$ is the 1D anisotropy function.⁴⁵ The 1D anisotropy function $\phi_{an}(r)$ defines the ratio of dose rate at r averaged by the solid angle, to the dose rate at r on the transverse plane.⁴⁵

Although Equation 2.5 is the recommended¹⁵ implementation for 1D dose calculation formalism, most TPS use

$$\dot{D}(r) = S_k \cdot \Lambda \cdot (r_0/r)^2 \cdot g_P(r) \cdot \phi_{an}(r) \quad (2.6)$$

*The values reported were consensus values from several sources obtained by measurements, verified by Monte Carlo simulations, and can be found in figures and tables relevant to the source-of-interest.

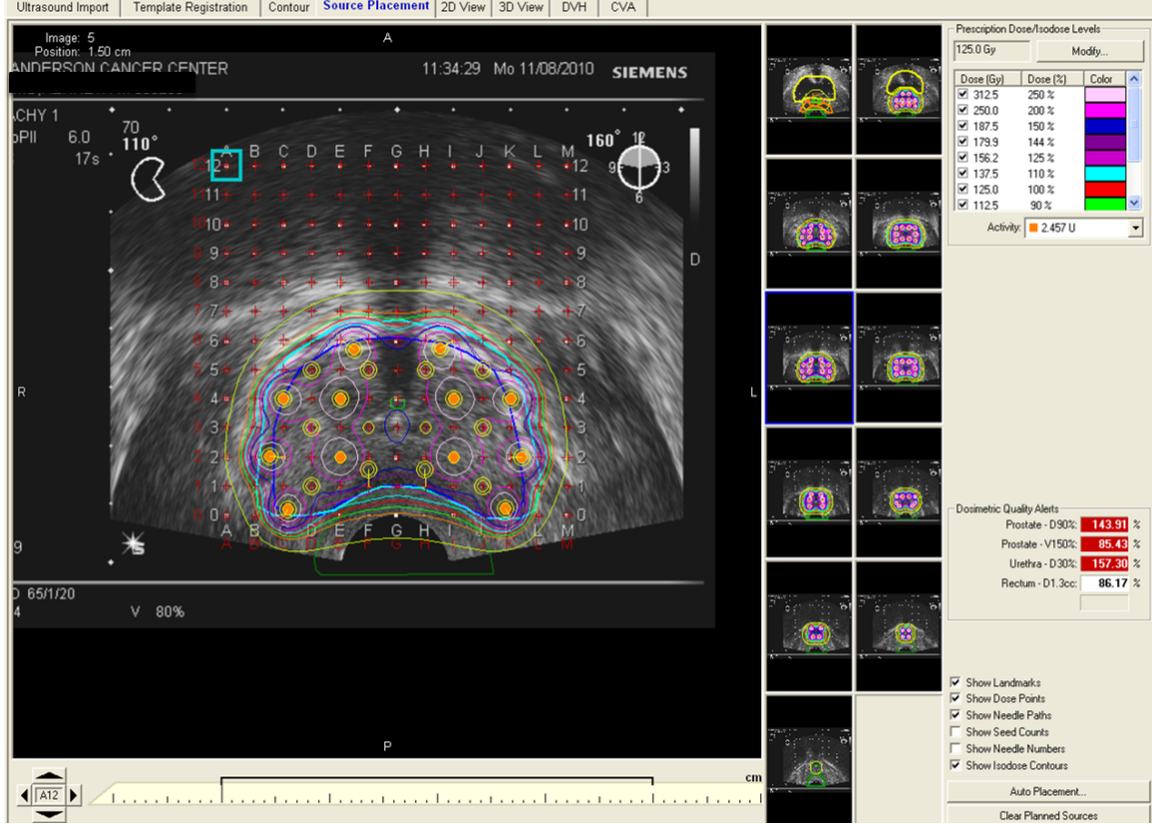


Figure 2.4: Treatment planning in the VariSeed brachytherapy TPS with TRUS images.

2.1.3 Treatment Planning Systems

VariSeed 8.0 was the prostate implant brachytherapy TPS previously used at our institution (Figure 2.4). VariSeed is commonly used for TRUS- and CT-based treatment planning. Recently, interest in MRI-based treatment planning has considerably increased owing to the ability of MRI to provide superior delineation of soft tissue. Particularly, the American Brachytherapy Society recommended fusion of CT and MRI images as useful (but not mandatory) for post-implant dosimetry.¹⁰ At the time of investigation, the VariSeed TPS has limited flexibility in incorporating MRI images.

The MIM Symphony LDR prostate brachytherapy TPS has recently been introduced into the market (Figure 2.5). MIM Symphony provides better tools for TRUS-MRI fusion, CT-MRI fusion, and MRI-only treatment planning. MIM Symphony has several advantages compared to VariSeed: multimodality treatment planning available based on CT, TRUS and MRI (Figure 2.6), compared to CT and TRUS capabilities only in VariSeed; enhanced

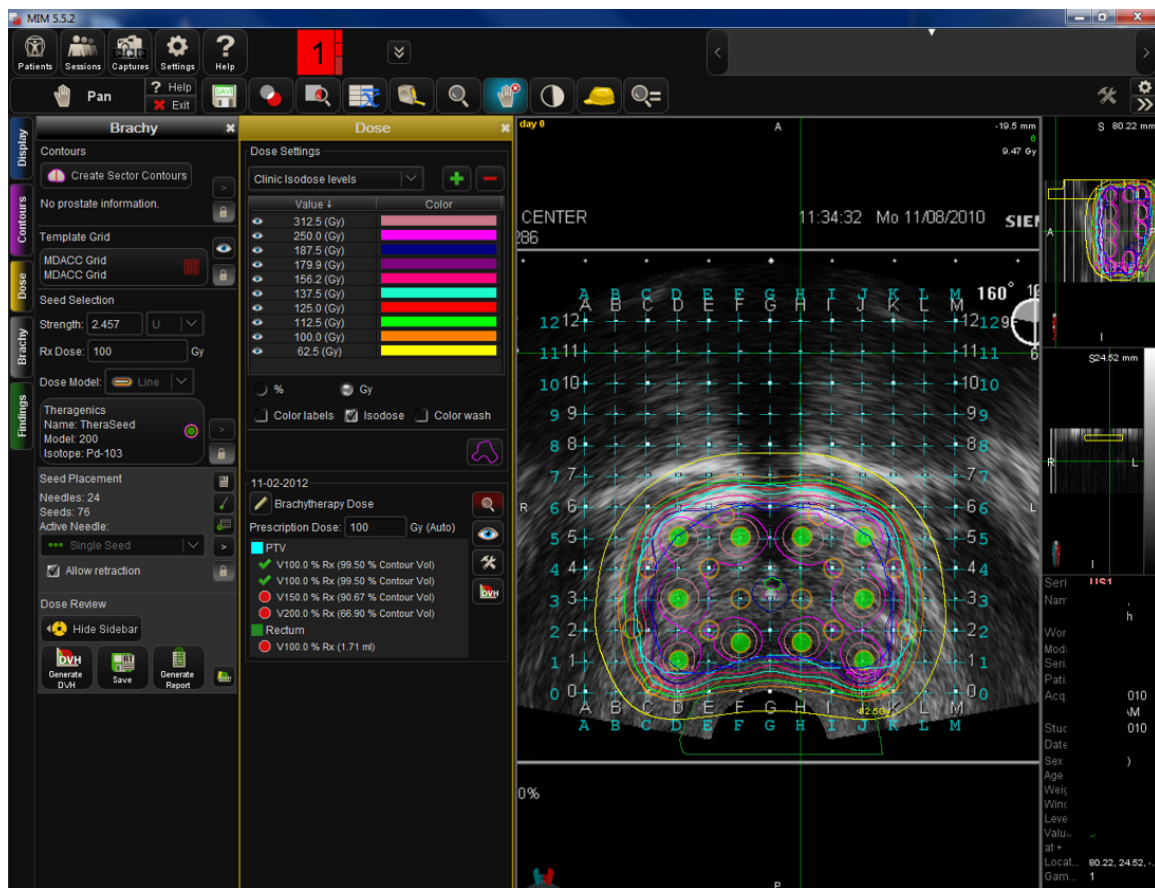


Figure 2.5: Treatment planning in the MIM Symphony brachytherapy TPS with TRUS images.

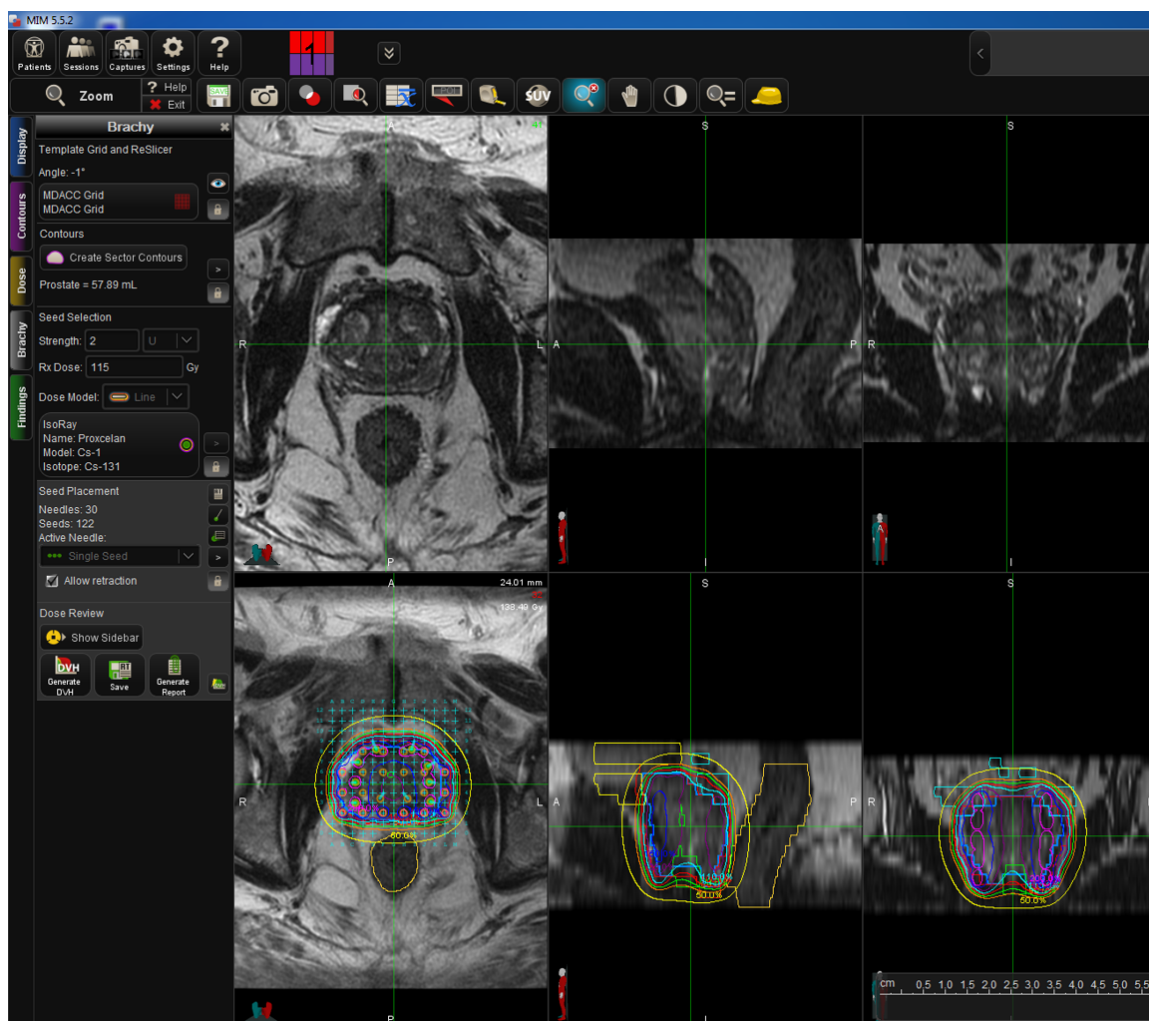


Figure 2.6: MIM Symphony allows treatment planning based on MRI images, apart from CT and TRUS images. The top row shows imported MRI images, while the bottom row shows the contours and planned seed locations.

MRI, CT and US fusion capability; algorithm for auto-contouring of anatomical structures; plan library available for faster treatment planning; improved intraop dosimetry with needle shifts and deflections; dose summation with other plans (external beam and brachytherapy); plans from multiple TPS can be imported (VariSeed requires a VariSeed-specific format); Matlab and Java codes can be run as extensions within the MIM Symphony TPS.

The disadvantage of MIM Symphony compared to VariSeed is that it is a relatively new TPS in the market so it is not as widely used in clinics nationwide. Therefore, available information related to the dosimetric and treatment planning validation of this TPS was limited. The only other available study that compared VariSeed TPS with MIM Symphony

was by Gossman et al.⁸¹ who evaluated DVH parameters for I-125 (Model 6711). In this chapter, I describe further comparisons of the dosimetric accuracy of MIM Symphony TPS to VariSeed TPS.

2.2 Purpose

The ultimate goal of Sirius MRI markers is to enable MRI-only post-implant dosimetry for better evaluation of dose-response relationships. The VariSeed TPS previously used at our institution for LDR prostate brachytherapy treatment planning did not allow for an MRI-only LDR prostate brachytherapy workflow. Conversely, the MIM Symphony TPS, which has better tools for incorporating MRI into the workflow was a new TPS with few documentation in literature. These two TPS may integrate different volume or dose calculation formalisms. Therefore, in this chapter, I evaluate the volume and dose calculations of these two TPS, as well as the subsequent dose-volume histogram parameters generated that may impact evaluation of implant quality.

2.3 Methods

2.3.1 Evaluation using VariSeed Test Procedures

As a preliminary evaluation of the MIM Symphony TPS, I compared the MIM Symphony TPS to the VariSeed TPS using the VariSeed Test Procedures⁸² and Test Data for I-125 (Model 6711).⁸³ Briefly, the tests verify dose calculations (within- and through-plane), display of isodose levels, and dose volume calculations.

2.3.2 Evaluation on Phantom Images

A QA phantom (CIRS Brachytherapy QA Phantom Model 045 SN#D7210-3) which has three ellipsoid objects with certified volumes was imaged using CT and MRI. The images were imported into MIM Symphony and VariSeed and then contoured independently. The auto-contouring tools of MIM Symphony TPS were used.

2.3.3 Evaluation on Patient Images

VariSeed TPS was previously used at our institution for LDR prostate brachytherapy treatment planning. As part of our institution’s clinical workflow, three treatment plans are generated for each patient during the course of the treatment. The pre-implant plan is generated prior to treatment and is based on ultrasound images; this plan is used to determine the number of seeds, needles, and loading patterns needed for treatment. For the pre-implant plan, sonographic images of the prostate are acquired at 5 mm intervals using the Sonoline G20 ultrasound unit (Siemens Medical Solutions, Mountain View, CA), and the images are then transferred to the VariSeed TPS. The radiation oncologist contours the prostate, bladder, rectum, urethra, and seminal vesicles. A PTV of 3 mm around the prostate volume is generated, except at the posterior aspect of the prostate along the rectum, where no margin is added. To determine the quality of the implantation, a CT scan is performed immediately following the implantation and used to generate the Day 0 post-implant plan. After the prostate edema has resolved in approximately a month, another CT scan is performed to generate the Day 30 post-implant plan.

To compare the dosimetric calculation of the VariSeed TPS and MIM Symphony TPS, I evaluated 100 plans in each of the two TPS. I evaluated 25 pre-implant plans and 25 post-implant (Day 30) patient plans for two commonly used seed models at our institution, namely I-125 (Oncoseed Model 6711, GE Healthcare, Arlington Heights, IL) and Pd-103 (Theracore Model 200, Theragenics Corporation, Buford, GA). The seed characteristics were provided in Table 2.1. In this study, I compared the volumes and DVH parameters of the prostate, bladder, and rectum. For the prostate, the DVH parameters examined were D90, V100, V150 and V200. For the bladder, the DVH parameters examined were V50, V100, and V150. Similarly, for the rectum, the DVH parameters examined were V50, V100, and V150.

Considering that VariSeed was our institution’s routine clinical TPS, the DVH and volume values for this TPS were directly reported from clinical plans. For the MIM Symphony TPS, the seed locations and contours were exported from the VariSeed TPS to the MIM Symphony TPS. From these 2D contours and seed coordinates, the volume and dose were calculated. The line model was specified for dose calculations in both TPS.

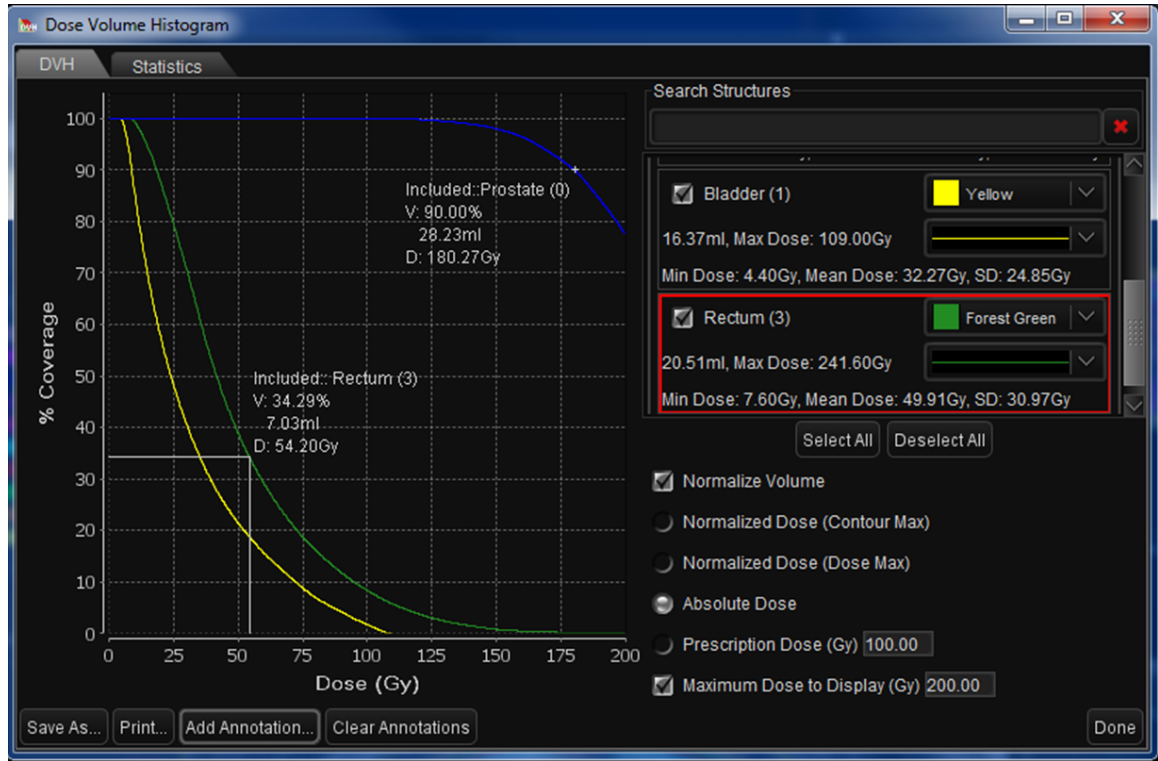


Figure 2.7: The dose volume histogram (DVH) displayed in the MIM Symphony treatment planning system. A fixed annotation was made on the prostate DVH (blue line) for D90 (the minimum dose covering 90% of the prostate volume). With the rectum selected as the structure of interest, moving the cursor shifts the white lines connecting the rectum DVH (green line) to the axes and updates the accompanying annotation, thus allowing for interrogation of the relation between any desired dose or volume.

In VariSeed, the dose resolution was specified to be $1\text{ mm} \times 1\text{ mm} \times 5\text{ mm}$ for pre-implant plans, and $1\text{ mm} \times 1\text{ mm} \times 2.5\text{ mm}$ for post-implant plans. In MIM, the dose resolution was specified to be $1\text{ mm} \times 1\text{ mm} \times 5\text{ mm}$ for pre-implant plans, and $1\text{ mm} \times 1\text{ mm} \times 1.67\text{ mm}$ for post-implant plans. In the VariSeed TPS, the DVH parameter and volume values were obtained from the the plan alerts or interpolated from the DVH tables (Figure 1.6). In the MIM Symphony TPS, the DVH parameter and volume values were obtained directly from annotations made on the DVH itself (Figure 2.7).

Both TPS had the same information for calculation of dose and volume since the defined anatomical contours and seed locations were transferred from VariSeed to MIM. Any differences in the calculated DVH parameters then arise from differences in dose and volume calculation performed by the two TPS. For each DVH parameter evaluated, the difference was calculated between the values from MIM Symphony and VariSeed. A positive difference

indicated that MIM Symphony calculated a greater value than VariSeed, and a negative difference indicated that VariSeed calculated a greater value than MIM Symphony.

2.4 Results and Discussion

2.4.1 Evaluation using VariSeed Quality Assurance User Test Procedures

The VariSeed quality assurance user test procedures were used during the preliminary phase of evaluating the MIM Symphony TPS. Using the VariSeed quality assurance user test procedures, the dose calculated by VariSeed and MIM Symphony were not significantly different (Figures 2.8, 2.9, 2.10 and 2.11).

Using finer distance increments, Dhanesar et al.⁷⁹ tabulated the percentage dose differences between MIM Symphony TPS, VariSeed TPS and TG-43 calculations for Cs-131 (Proxcelan Model Cs-1, IsoRay Medical Inc., Richmond, WA), Pd-103 (Therased Model 200, Theragenics Corporation, Buford, GA), and two models of I-125 sources (Oncoseed Model 6711, GE Healthcare, Arlington Heights, IL; and Advantage Model IAI-125A, Isoaid, LLC, Port Richey, FL). Using the 2D dose calculation formalism, dose calculations by the MIM Symphony TPS, VariSeed TPS and the TG-43 formalism agreed within 0.5% for $r > 1$ cm.⁷⁹ Using the 1D dose calculation formalism, the dose calculations by the MIM Symphony TPS was within 1.4% to dose calculations using the TG-43 formalism, and within 1% compared to dose calculations by the VariSeed TPS, for $r > 1$ cm.⁷⁹

2.4.2 Evaluation on Phantom Images

The evaluation on phantom images was of the volume calculations performed by MIM Symphony versus VariSeed. The structures were contoured using the auto-contouring tool on MIM Symphony and manually contoured on VariSeed. Comparisons using phantom images yielded less than 1 % difference between the volume calculated by MIM Symphony and the actual volume of the phantom. Comparisons were also made to the volumes calculated by VariSeed. Table 2.2 summarizes the results for different structures.

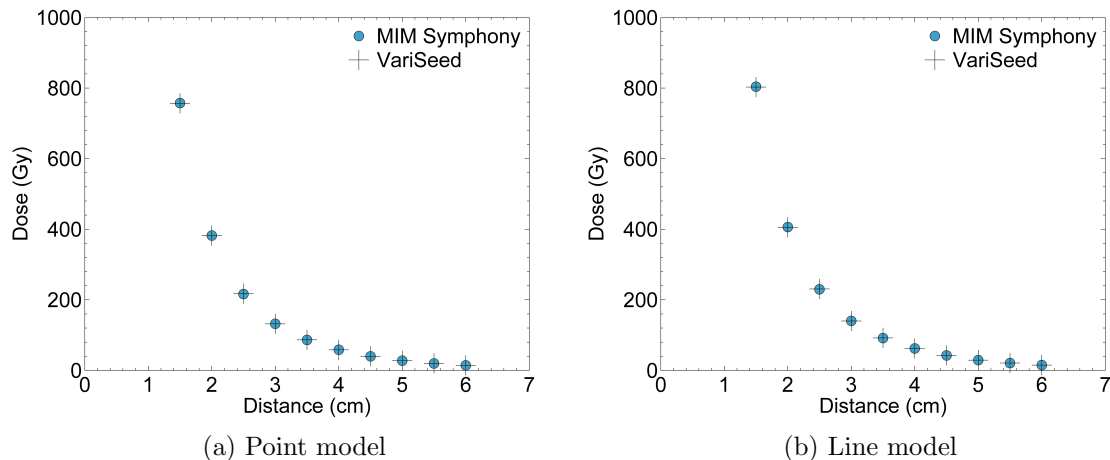


Figure 2.8: Comparison of dose point calculation test results. VariSeed values obtained from User Test Data tables. Distances were specified in the y-direction.

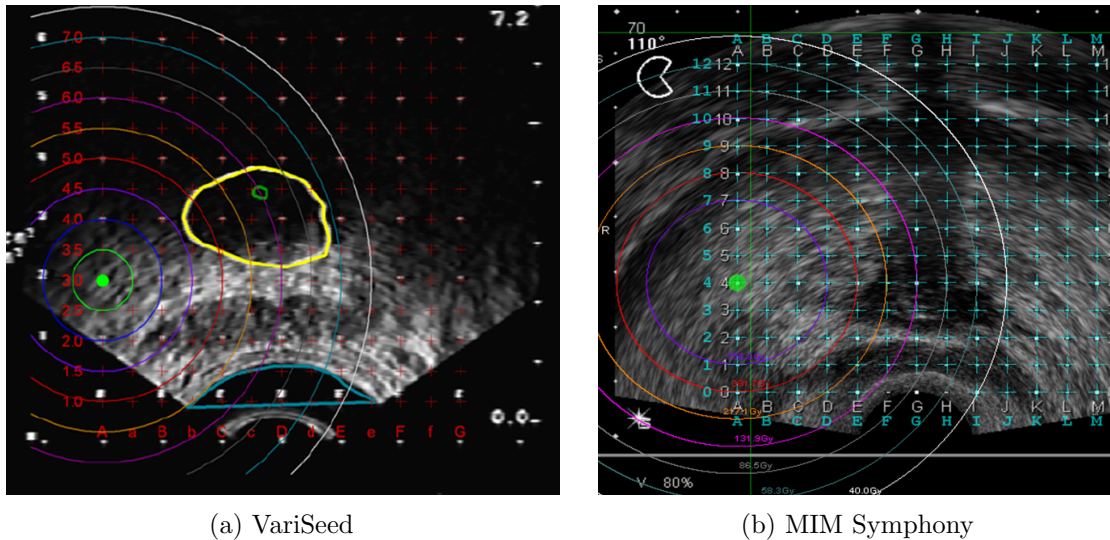


Figure 2.9: Comparison of isodose level display functions. The isodose lines should intersect each crosshair of the same row as the source.

Table 2.2: Volume calculations of known structures by MIM Symphony and VariSeed. Reprinted from S. K. Dhanesar, T. Y. Lim, W. Du, T. L. Bruno, S. J. Frank, and R. J. Kudchadker. “Evaluation of the MIM Symphony treatment planning system for low-dose-rate prostate brachytherapy”. In: *J Appl Clin Med Phys* 16.5 (2015), pp. 62–75⁷⁹ (licensed under a Creative Commons Attribution 3.0 License).

	Volumes (cm ³)			Volume Difference (%)	
	Actual	MIM Symphony	VariSeed	MIM Symphony vs. Actual	VariSeed vs. Actual
Small	3.45	3.43	3.47	-0.6	0.6
Medium	8.51	8.57	8.45	0.7	-0.7
Large	19.78	19.89	20.06	0.6	1.4

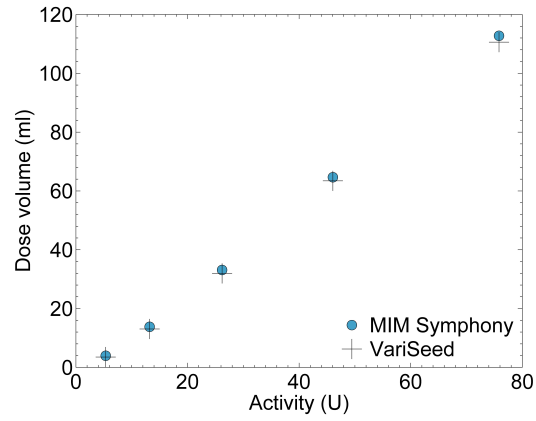


Figure 2.10: Comparison of dose volume test results. Activity was calculated using the anisotropy factor for a point source.

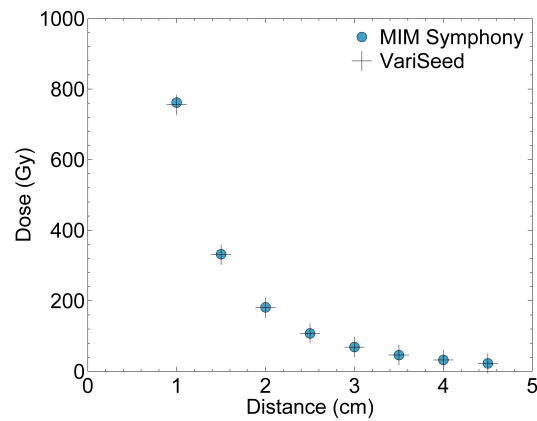


Figure 2.11: Comparison of dose calculations in z-direction.

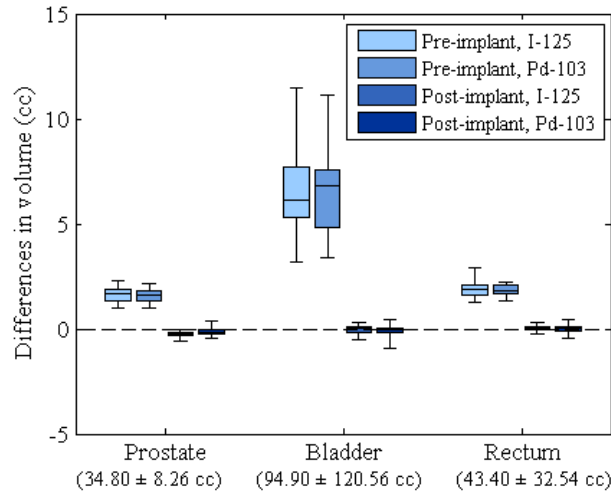


Figure 2.12: Differences between the volumes calculated in MIM Symphony and those calculated in VariSeed for the prostate, bladder, and rectum. Dose volume histogram data for iodine-125 (I-125; Model 6711) and palladium-103 (Pd-103; Model 200) are shown. The bottom and top of each box are the first and third quartiles, the line inside the box indicates the median, and the ends of the whiskers indicate the minimum and maximum values. Total volumes are shown as mean \pm standard deviation. Reprinted from S. K. Dhanesar, T. Y. Lim, W. Du, T. L. Bruno, S. J. Frank, and R. J. Kudchadker. “Evaluation of the MIM Symphony treatment planning system for low-dose-rate prostate brachytherapy”. In: *J Appl Clin Med Phys* 16.5 (2015), pp. 62–75⁷⁹ (licensed under a Creative Commons Attribution 3.0 License).

2.4.3 Evaluation on Patient Images

The evaluation on phantom images were of the volume and dose-volume histogram parameter calculations performed by MIM Symphony versus VariSeed.

2.4.3.1 Comparison of Volume Calculations

The volume calculations for the prostate and rectum did not differ substantially (Figure 2.12). The bladder showed higher volume differences between MIM Symphony and VariSeed than the other two structures in the pre-implant plans (Figure 2.12). These differences may be due to the large Z direction resolution (5 mm used in both MIM Symphony and VariSeed), large contoured areas, partial contouring (bladder contours on a few slices only) and interpolation of VariSeed data.

The greater volume differences calculated on *pre-implant* plans compared with *post-implant* plans are attributable to resolution differences between the pre-implant ultrasound

images and the finer-resolution post-implant CT images. On the other hand, as noted above, the Z resolution for the post-implant plans in MIM Symphony was 1.67 mm compared with 2.5 mm in VariSeed. This resolution discrepancy may have caused differences in post-implant comparisons between the two systems.

To further investigate the volume calculations of the two TPS, volumes generated from rectangular contours drawn on 2 slices (Case A), 4 slices (Case B), 6 slices (Case C) and 8 slices (Case D) were calculated. Volumes calculated on VariSeed were based on the volumes defined from the topmost contour to the bottommost contour. On the other hand, volume calculated on MIM were based on volumes defined with half-slice extrapolations from the topmost and bottommost contours (Figure 2.13).

This finding is consistent with a previous study by Gossman et al..⁸¹ They contoured $0.5\text{ cm} \times 5\text{ cm}$ over 3 slices (2.5 mm slice thickness) and found the resulting volume was 1.875 cm^3 in MIM Symphony.

Determination of the more accurate TPS' volume calculation method is dependent on the contoured structure. For instance, for rounded structures such as the prostate, the half-slice extrapolations round-up the base and apex of the prostate, thus giving a more accurate representation of true anatomy. However, if the physician is unaware of these extrapolations intrinsically performed by the MIM Symphony TPS, overcontouring may ensue. In that case, the what-you-contour-is-what-you-get approach of the VariSeed TPS may lead to more accurate structure definition.

This observed difference in volume calculation methods may have accounted for the greater volume differences found in pre-implant plans compared to post-implant plans. For instance, due to the bladder not fully encompassed in the imaging FOV, contouring of the bladder was partial, resulting in a large area on the topmost slice of the bladder contour. Since the pre-implant TRUS images were acquired at lower slice resolution compared to the post-implant CT images, the effect of half-slice extrapolations performed by MIM Symphony was enhanced, and greater calculated volume differences were observed (Figure 2.12).

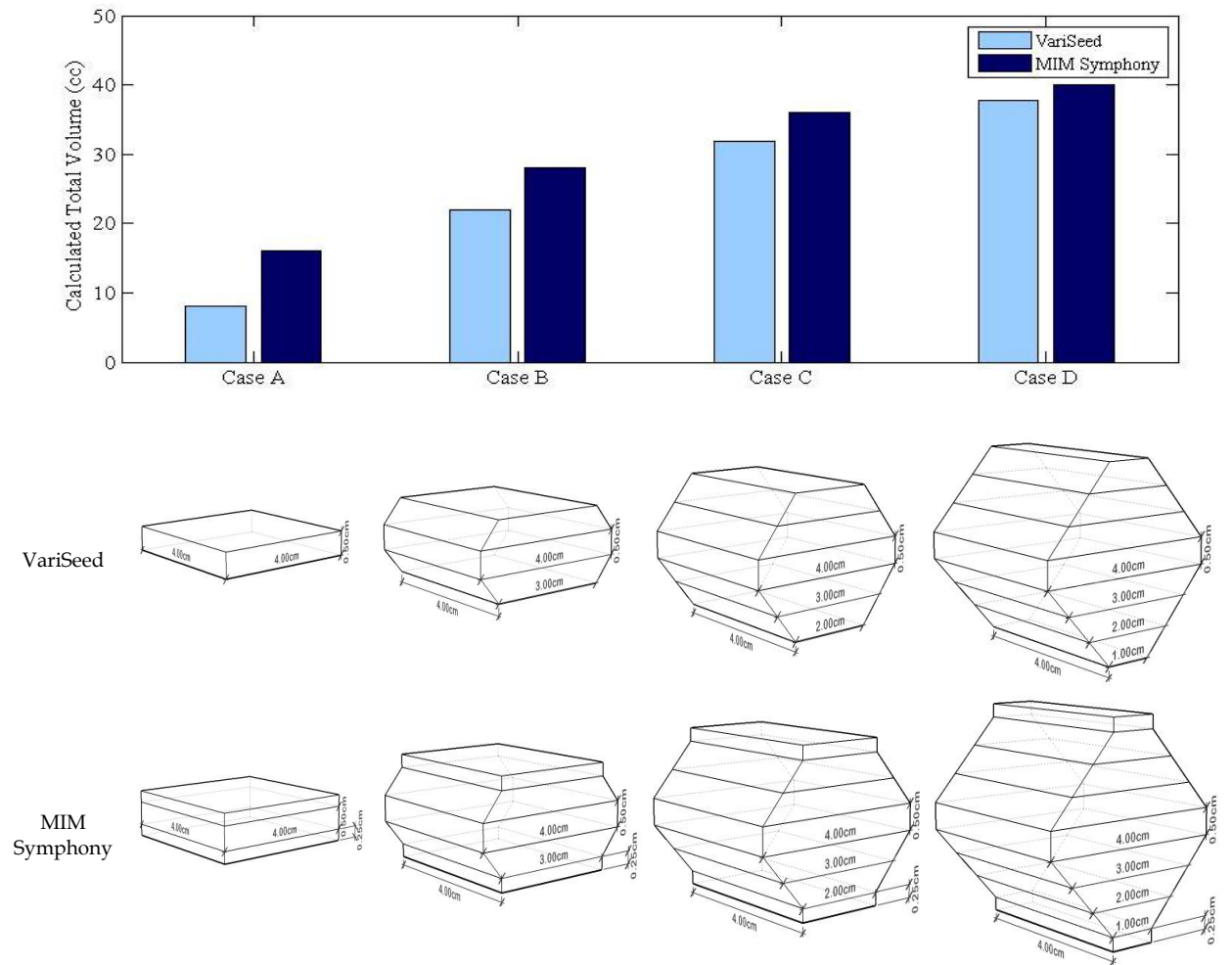


Figure 2.13: Comparison of volume calculation methods in VariSeed and MIM Symphony using rectangular contours drawn on 2, 4, 6 and 8 slices for the volume calculation.

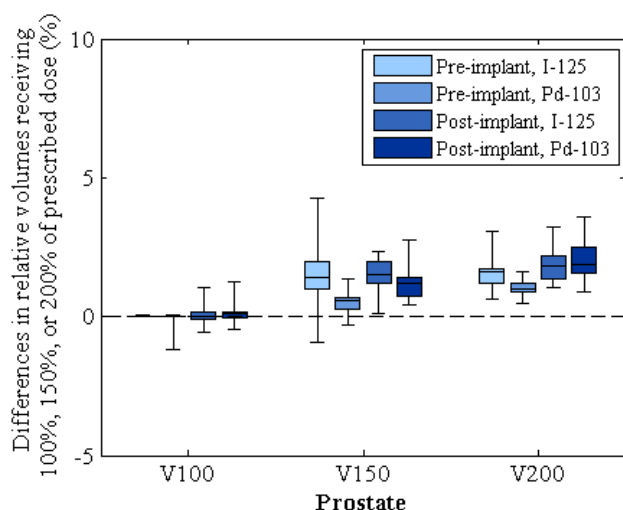


Figure 2.14: Differences between the prostate V100, V150, and V200 calculations in MIM Symphony and those in VariSeed. V_x = portion of the total prostate volume receiving $x\%$ of the prescribed dose. Dose volume histogram data for iodine-125 (I-125; Model 6711) and palladium-103 (Pd-103; Model 200) are shown. The bottom and top of each box are the first and third quartiles, the line inside the box indicates the median, and the ends of the whiskers indicate the minimum and maximum values. Reprinted from S. K. Dhanesar, T. Y. Lim, W. Du, T. L. Bruno, S. J. Frank, and R. J. Kudchadker. “Evaluation of the MIM Symphony treatment planning system for low-dose-rate prostate brachytherapy”. In: *J Appl Clin Med Phys* 16.5 (2015), pp. 62–75⁷⁹ (licensed under a Creative Commons Attribution 3.0 License).

Table 2.3: Differences between the prostate D90 calculations in MIM Symphony and those in VariSeed. Reprinted from S. K. Dhanesar, T. Y. Lim, W. Du, T. L. Bruno, S. J. Frank, and R. J. Kudchadker. “Evaluation of the MIM Symphony treatment planning system for low-dose-rate prostate brachytherapy”. In: *J Appl Clin Med Phys* 16.5 (2015), pp. 62–75⁷⁹ (licensed under a Creative Commons Attribution 3.0 License).

	Differences in prostate D90 (Gy)			
	Pre-implant		Post-implant	
	I-125	Pd-103	I-125	Pd-103
Mean	0.73	0.18	1.46	1.99
Standard deviation	0.64	0.68	1.40	1.29
Minimum	-1.35	-2.52	-0.32	-0.23
Maximum	2.70	0.85	6.80	5.75

2.4.3.2 Comparison of DVH Parameter Calculations

Prostate DVH Parameters The differences between the prostate V100, V150, and V200 values calculated in MIM Symphony and those calculated in VariSeed is shown in Figure 2.14. Because the prostate V100, V150, and V200 values were recorded as percentages of the total prostate volume, the differences in these values are reported in percentages as well. Mean differences in prostate V100, V150, and V200 values were within 2 % (Figure 2.14). Table 2.3 shows the mean, standard deviation, and minimum and maximum differences in prostate D90 values.

Bladder DVH Parameters The differences in the V50, V100, and V150 values calculated by the two TPS for the bladder did not differ substantially (Figures 2.15). Mean differences in bladder V50, V100, and V150 values were within 2 cc (Figure 2.15). The differences in bladder V50 values were slightly higher. This may be due to the differences in volume calculations as described in Section 2.4.3.1.

Rectum DVH Parameters The differences in the V50, V100, and V150 values calculated by the two TPS for the rectum did not differ substantially (Figure 2.16). Mean differences in rectum V50, V100 and V150 values were within 0.5 cc (Figure 2.16).

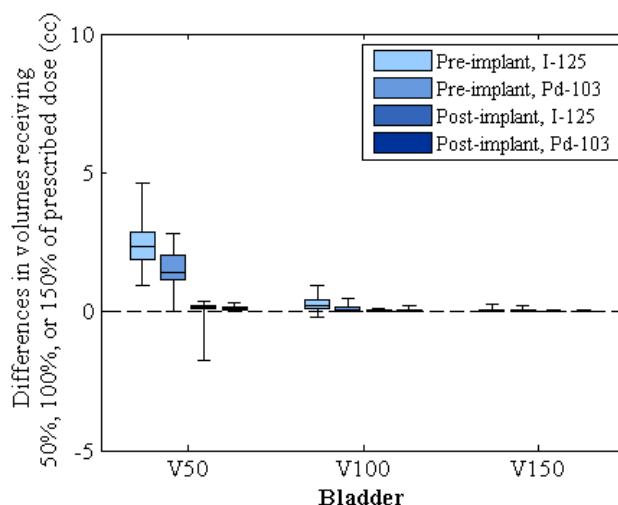


Figure 2.15: Differences between the bladder V50, V100, and V150 calculations in MIM Symphony and those in VariSeed. V_x = portion of the bladder volume receiving $x\%$ of the prescribed dose. Dose volume histogram data for iodine-125 (I-125; Model 6711) and palladium-103 (Pd-103; Model 200) are shown. The bottom and top of each box are the first and third quartiles, the line inside the box indicates the median, and the ends of the whiskers indicate the minimum and maximum values. Reprinted from S. K. Dhanesar, T. Y. Lim, W. Du, T. L. Bruno, S. J. Frank, and R. J. Kudchadker. “Evaluation of the MIM Symphony treatment planning system for low-dose-rate prostate brachytherapy”. In: *J Appl Clin Med Phys* 16.5 (2015), pp. 62–75⁷⁹ (licensed under a Creative Commons Attribution 3.0 License).

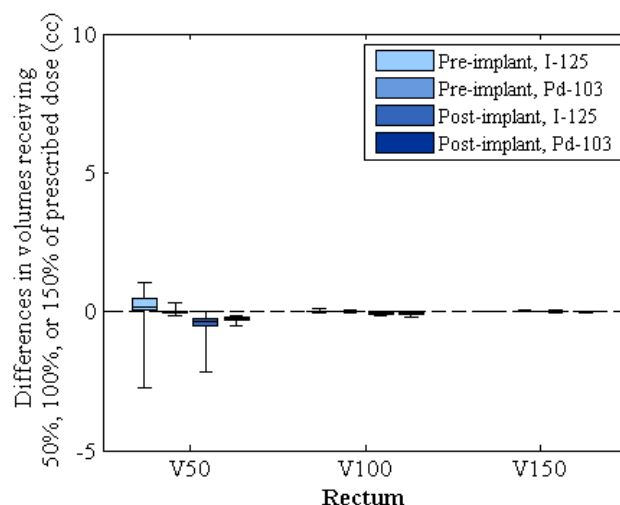


Figure 2.16: Differences between the rectum V50, V100, and V150 calculations in MIM Symphony and those in VariSeed. V_x = portion of the rectal volume receiving $x\%$ of the prescribed dose. Dose volume histogram data for iodine-125 (I-125; Model 6711) and palladium-103 (Pd-103; Model 200) are shown. The bottom and top of each box are the first and third quartiles, the line inside the box indicates the median, and the ends of the whiskers indicate the minimum and maximum values. Reprinted from S. K. Dhanesar, T. Y. Lim, W. Du, T. L. Bruno, S. J. Frank, and R. J. Kudchadker. “Evaluation of the MIM Symphony treatment planning system for low-dose-rate prostate brachytherapy”. In: *J Appl Clin Med Phys* 16.5 (2015), pp. 62–75⁷⁹ (licensed under a Creative Commons Attribution 3.0 License).

2.5 Conclusion

2.5.1 Summary

This chapter described the comparison of two LDR prostate brachytherapy TPS, namely Varian VariSeed 8.0 and MIM Symphony 5.4. Overall, the differences in the DVH parameters evaluated in this work do not disqualify MIM Symphony from clinical treatment planning.

2.5.2 Limitations

A limitation of this study was that the Z resolution for dose calculations for post-implant plans is different for VariSeed and MIM. Both VariSeed and MIM Symphony only allowed specific numeric settings for the dose resolution in Z, namely 0.5 mm, 0.625 mm, 0.833 mm, 1.25 mm, 1.25 mm or 2.5 mm in VariSeed, and 1 mm, 1.67 mm and 5 mm in MIM Symphony. Generally, the Z resolution is set to match the through-plane resolution of the acquired images, that is, 2.5 mm CT slice thicknesses for post-implant plans. In this study, since I wanted to compare MIM Symphony to our clinical standard at that time (VariSeed with 2.5 mm Z resolution), the closest Z resolution (1.67 mm) was used in MIM Symphony. Nevertheless, for general use of MIM Symphony, I recommend the Z resolution to be at the smallest available setting, that is, 1 mm, for greater calculation accuracy.

Another limitation is that unlike the prostate, the bladder and rectum are partially contoured because these anatomical structures are not fully covered in the imaging field of view on the ultrasound imaging system. This amplified the volume calculation differences between VariSeed and MIM Symphony. Therefore, if importing plans from VariSeed, I caution users to carefully evaluate the contours. The contour issues will not be present if the entire treatment planning is done with the MIM Symphony TPS.

Also, note that the bladder was evaluated instead of the urethra. For prediction of urinary complications, the urethra is a better indicator.⁵⁶ A foley catheter is generally used to visualize the urethra on CT images due to the lack of soft tissue contrast between the urethra and the prostate. However, apart from causing discomfort to patients, the placement of the foley catheter in the urethra can distort dose distribution artificially.⁸⁴ Therefore, unless specifically indicated, a foley catheter is not used for Day 30 post-implant imaging.

Since urethra contours were not available for most patients, bladder contours were used for evaluation in this study.

2.5.3 Implications

MIM Symphony can be used as an alternative to VariSeed for the clinical treatment planning of LDR prostate brachytherapy and for post-implant dosimetric evaluation. Specifically for our purposes, MIM Symphony allows the import of MRI images of patients implanted with the Sirius MRI markers. In Chapters 3 to 5, I present the various components involved in MRI image acquisition for post-implant dosimetry.

This chapter is adapted from T. Y. Lim, R. J. Stafford, R. J. Kudchadker, M. Sankaranarayanapillai, G. Ibbott, A. Rao, K. S. Martirosyan, and S. J. Frank. “MRI characterization of cobalt dichloride-N-acetyl cysteine (C4) contrast agent marker for prostate brachytherapy”. In: *Phys Med Biol* 59.10 (2014), pp. 2505–16⁵⁷ (©Institute of Physics and Engineering in Medicine. By permission of IOP Publishing. All rights reserved).

3

Relaxation Characteristics of the C4 Contrast Agent

Contents

3.1	Background	51
3.1.1	Basic MRI Contrast Mechanism	51
3.1.2	Spin-lattice Relaxation Time T_1	51
3.1.3	Spin-spin Relaxation Time T_2	54
3.1.4	Contrast agents	55
3.2	Purpose	55
3.3	Methods	55
3.3.1	Data Collection	55
3.3.2	Measuring Spin-lattice Relaxation Time T_1	57
3.3.3	Measuring Spin-spin Relaxation Time T_2	58
3.3.4	Measuring Relaxivities r_1 and r_2	59
3.4	Results and Discussion	59
3.4.1	Effect of Field Strength	59
3.4.2	Effect of Orientation	62
3.4.3	Effect of Temperature	63
3.5	Conclusion	64
3.5.1	Summary	64
3.5.2	Limitations	66
3.5.3	Implications	66

3.1 Background

3.1.1 Basic MRI Contrast Mechanism

Contrast on MRI images is generated through the magnetic resonance of hydrogen atoms in different tissues of the body.⁸⁵ A hydrogen atom, with only one proton, has a non-zero net magnetic moment.⁸⁵ When in an external magnetic field B_0 , the hydrogen precess at the Larmor frequency ω_0 according to the Larmor equation

$$\omega_0 = \gamma B_0 \quad (3.1)$$

where γ is the gyromagnetic ratio ($\gamma = 42.58 \text{ MHz/T}$ for hydrogen).⁸⁵ Each hydrogen atom will either precess along or opposite to B_0 (defined in the z-direction), but more hydrogen atoms will align along B_0 since this is a lower energy state.⁸⁵ The sum of all the hydrogen atoms' alignment vectors, or net magnetization vector, at equilibrium is M_0 .⁸⁵ Different tissues have different signal intensities on MRI images because of the varying hydrogen contents of the tissues.⁸⁵ To probe this, a radiofrequency (RF) pulse is applied to move the magnetization vector M away from B_0 .⁸⁵ However, M recovers to M_0 to the equilibrium state over time.⁸⁵ This timing is governed by spin-lattice relaxation time T_1 and spin-spin relaxation time T_2 .⁸⁵

3.1.2 Spin-lattice Relaxation Time T_1

As depicted by Figure 3.1, the spin-lattice relaxation is when the longitudinal component of the magnetization vector, M_z recovers towards equilibrium with its surroundings (lattice) according to

$$M_z(t) = M_0(1 - \exp(-t/T_1)) \quad (3.2)$$

Image contrast can be generated by emphasizing the differences in T_1 of various tissues, by adjusting scan parameters, such as repetition time (TR) and echo time (TE) that control image weighting.⁸⁵ For instance, a conventional T_1 -weighted spin echo sequence will have short TR and short TE (Figure 3.2).

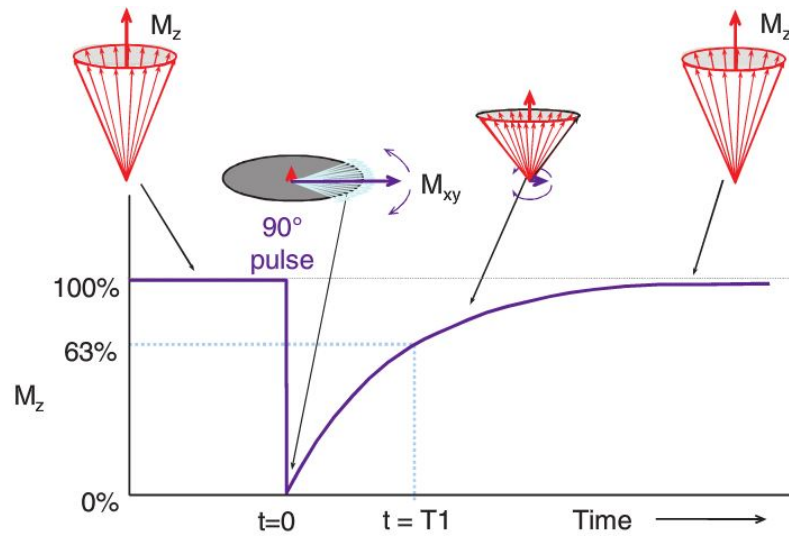


Figure 3.1: After a 90-degree pulse, M_z is converted from a maximum value at equilibrium to $M_z = 0$. Return of M_z to equilibrium occurs exponentially and is characterized by the spin-lattice T_1 relaxation constant. After an elapsed time equal to T_1 , 63 % of the longitudinal magnetization is recovered. Spin-lattice recovery takes longer than spin-spin decay (T_2). Reprinted from Jerrold T. Bushberg. *The essential physics of medical imaging*. 3rd ed. Philadelphia: Lippincott Williams and Wilkins, 2012⁸⁵ (license number: 3876590155681).

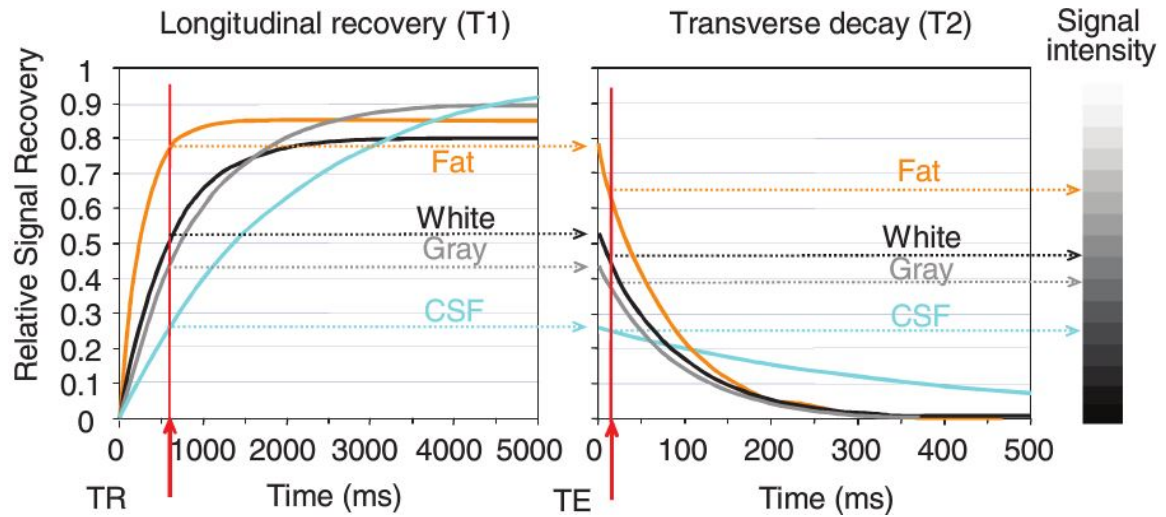


Figure 3.2: T_1 -weighted contrast: Longitudinal recovery (left) and transverse decay (right) diagrams (note the values of the x-axis time scales) show four brain tissues and T_1 and T_2 relaxation constants. T_1 -weighted contrast requires the selection of a TR that emphasizes the differences in the T_1 characteristics of the tissues (e.g., TR = ~ 500 ms), and reduces the T_2 characteristics by using a short TE so that transverse decay is reduced (e.g., TE ≤ 15 ms). Reprinted from Jerrold T. Bushberg. *The essential physics of medical imaging*. 3rd ed. Philadelphia: Lippincott Williams and Wilkins, 2012⁸⁵ (license number: 3876590155681).

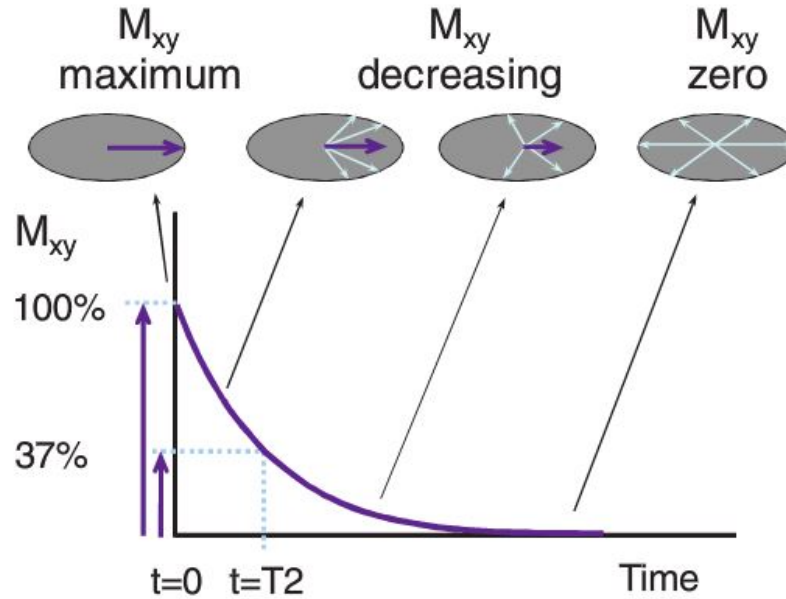


Figure 3.3: The loss of M_{xy} phase coherence occurs exponentially caused by intrinsic spin-spin interactions in the tissues and extrinsic magnetic field inhomogeneities. The exponential decay constant, T_2 is the time over which the signal decays to 37% of the initial transverse magnetization (e.g., after a 90-degree pulse). Reprinted from Jerrold T. Bushberg. *The essential physics of medical imaging*. 3rd ed. Philadelphia: Lippincott Williams and Wilkins, 2012⁸⁵ (license number: 3876590155681).

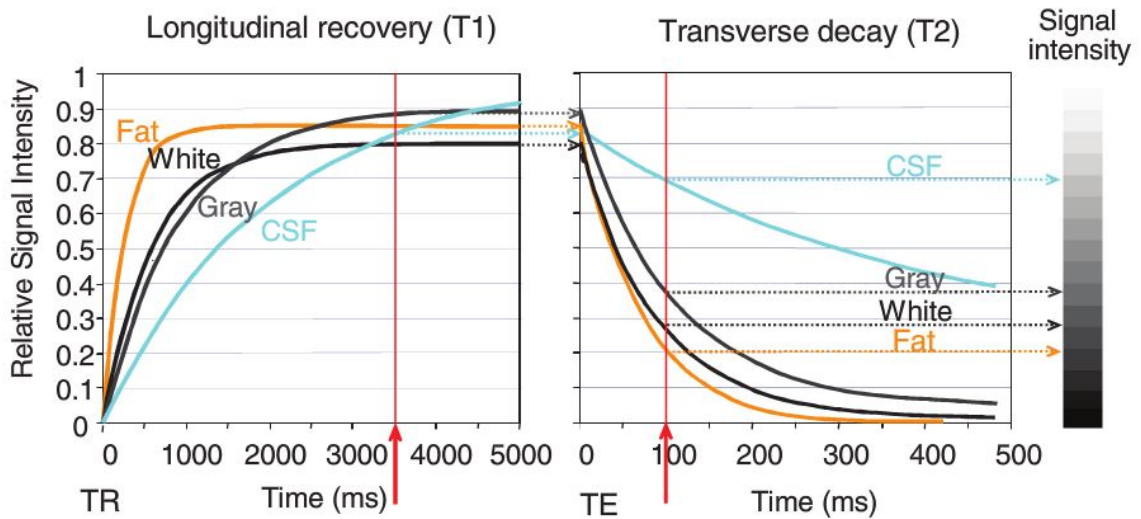


Figure 3.4: T_2 weighted contrast requires the use of a long TR (e.g., greater than 2000 ms) to reduce T_1 influences, and a long TE (e.g., greater than 80 ms) to allow for T_2 decay to evolve. Compared to the proton density weighting, the difference is with longer TE. Reprinted from Jerrold T. Bushberg. *The essential physics of medical imaging*. 3rd ed. Philadelphia: Lippincott Williams and Wilkins, 2012⁸⁵ (license number: 3876590155681).

3.1.3 Spin-spin Relaxation Time T_2

As depicted by Figure 3.3, the spin-spin relaxation is when the transverse component of the magnetization vector M_{xy} decays towards equilibrium. Usually the RF pulse used flips the magnetization vector M 90° into the x-y plane. M_{xy} decays exponentially due to loss of phase coherence due to spin-spin interactions according to

$$M_{xy}(t) = M_{xy}(0) \exp(-t/T_2) \quad (3.3)$$

where $M_{xy}(0)$ is the net transverse magnetization immediately after the RF pulse.

Image contrast can also be generated by emphasizing the differences in T_2 of various tissues, by adjusting scan parameters, such as TR and TE.⁸⁵ For instance, a conventional T_2 -weighted spin echo sequence will have long TR and long TE (Figure 3.4).

Another factor for the loss of phase coherence is due to B_0 inhomogeneities, ΔB_i . Therefore, the observed decay of transverse magnetization would be faster than predicted by T_2 effects alone (Figure 3.5). This observed T_2 is denoted T_2^* , whereby

$$\frac{1}{T_2^*} = \frac{1}{T_2} + \frac{1}{\gamma \Delta B_i} \quad (3.4)$$

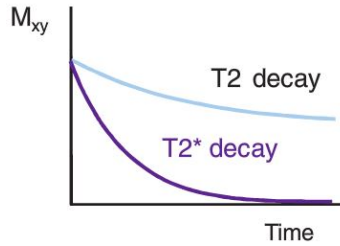


Figure 3.5: T_2 is the decay time resulting from *intrinsic* magnetic properties of the sample. T_2^* is the decay time resulting from *both intrinsic and extrinsic magnetic field variations*. T_2 is always longer than T_2^* . Reprinted from Jerrold T. Bushberg. *The essential physics of medical imaging*. 3rd ed. Philadelphia: Lippincott Williams and Wilkins, 2012⁸⁵ (license number: 3876590155681).

3.1.4 Contrast agents

Contrast agents can be used when the generated MRI images have insufficient contrast.⁶⁵ The ions in contrast agents relax nearby water protons, thereby affecting T_1 and T_2 .²⁵ Positive contrast agents shorten the T_1 of these water protons, leading to more rapid magnetization recovery and higher signal. For example, following injection of a gadolinium into the body, the gadolinium travels along blood vessels and if the blood-brain-barrier is compromised, the gadolinium leaks into and enhances (by T_1 -shortening) the tissue it accumulates in.⁸⁶ Conversely, negative contrast agents shorten the T_2 , leading to increased dephasing of the transverse signal and lower signal. The capacity of contrast agents to shorten the relaxation times of bulk water protons is defined as relaxivity.⁸⁷

3.2 Purpose

Intrinsic parameters (such as T_1 , T_2 and T_2^*) and scan parameters (such as TR and TE) affect the signal on MRI images, hence knowing these parameters is crucial for developing an appropriate post-implant MRI protocol.^{88,89} The improved soft tissue contrast on MRI compared to CT is provided by the variations in T_1 and T_2 , compared to x-ray attenuation.⁹⁰ The Sirius MRI marker introduced in Section 1.7 contains the C4 contrast agent. Previously, the C4 contrast agent's MRI relaxation characteristics had not been characterized. In this chapter, I describe the determination of the relaxation characteristics of the C4 contrast agent. Using common imaging sequences, I measured relaxation times, relaxation rates, and relaxivities at two standard clinical field strengths (1.5 T and 3.0 T), for three conventional scan planes (coronal, sagittal, and axial), and at two temperatures (room temperature and body temperature).

3.3 Methods

3.3.1 Data Collection

In the current study, the C4 contrast agent was obtained by dissolving $\text{CoCl}_2 \cdot 6\text{H}_2\text{O}$ (cobalt dichloride hexahydrate) and NAC (N-acetyl-L-cysteine) in water. Keeping the concentration

Table 3.1: Conversion from weight percentages to millimolar (mM) for various concentrations of cobalt dichloride. Reproduced from T. Y. Lim, R. J. Stafford, R. J. Kudchadker, M. Sankaranarayanapillai, G. Ibbott, A. Rao, K. S. Martirosyan, and S. J. Frank. “MRI characterization of cobalt dichloride-N-acetyl cysteine (C4) contrast agent marker for prostate brachytherapy”. In: *Phys Med Biol* 59.10 (2014), pp. 2505–16⁵⁷ (©Institute of Physics and Engineering in Medicine. Reproduced by permission of IOP Publishing. All rights reserved).

Weight Percentage (%)	Concentration (mM)
0.0	0.00
0.1	4.229
0.2	8.458
0.5	21.145
1.0	42.290
1.5	63.435
2.0	84.580
5.0	211.450

of NAC in the solution fixed at 2 %, the concentration of cobalt dichloride was varied to be 0.1 %, 0.2 %, 0.5 %, 1.0 %, 1.5 %, 2.0 %, or 5.0 %*. To match the standard unit for relaxivity ($\text{mM}^{-1} \text{s}^{-1}$), the weight percentages were converted into millimolar (mM), presented in Table 3.1.

The solutions were separated by cobalt dichloride concentration into seven cylindrical glass vials. Two additional vials, one filled only with water and another filled only with 2.0 % NAC, were used as controls. The nine vials were placed in a thin transparent plastic cup and arranged as shown in Figure 3.6. The plastic cup was then affixed to the center of a cylindrical plastic container. Water was poured into the space between the plastic cup and the container to reduce susceptibility artifacts. The container with the nine samples was then centered in a receive-only head array for reception with the body coil used for excitation.

I investigated the dependence of relaxation on three parameters: field strength, orientation, and temperature. For field strength dependence measurements, the samples were scanned using a 1.5 T and a 3.0 T clinical MRI scanner (Excite HDxt and Discovery MR750 respectively; GE Healthcare, Waukesha, WI). For orientation dependence measurements, the samples were positioned such that the base of the vials were parallel to the chosen scan plane (coronal, sagittal, or axial). For temperature dependence measurements, the samples

*All stated percentages are weight percentages

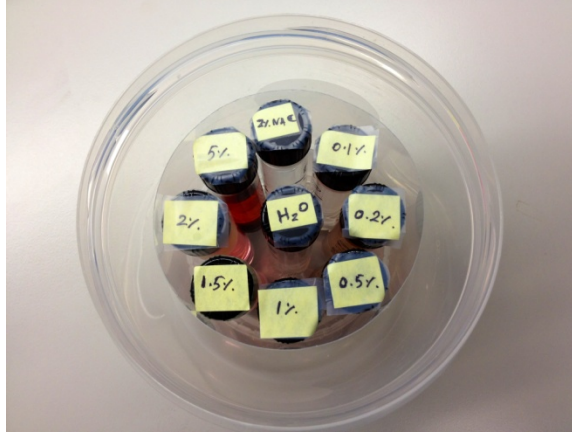


Figure 3.6: Nine glass vials with increasing concentrations of cobalt dichloride, arranged in a clockwise fashion. The center vial contained water only and the top vial contained 2.0 % N-acetyl-L-cysteine (NAC) only; the remaining vials contained 2 % NAC and 0.1 %, 0.2 %, 0.5 %, 1.0 %, 1.5 %, 2.0 %, or 5.0 % cobalt dichloride. Reproduced from T. Y. Lim, R. J. Stafford, R. J. Kudchadker, M. Sankaranarayananpillai, G. Ibbott, A. Rao, K. S. Martirosyan, and S. J. Frank. “MRI characterization of cobalt dichloride-N-acetyl cysteine (C4) contrast agent marker for prostate brachytherapy”. In: *Phys Med Biol* 59.10 (2014), pp. 2505–16⁵⁷ (©Institute of Physics and Engineering in Medicine. Reproduced by permission of IOP Publishing. All rights reserved).

were placed in a water bath at room temperature (20.3 °C as denoted on the console) or body temperature (37 ± 1 °C).

Analysis was performed offline using Matlab 7.9.0. (The MathWorks, Inc., Natick, MA). A square 7-pixel \times 7-pixel region-of-interest (ROI) was defined in the center of each vial on the image, away from the vial edges to prevent signal inhomogeneity. The mean and standard deviation of the signal within the ROI were recorded at each time point.

3.3.2 Measuring Spin-lattice Relaxation Time T_1

T_1 measurements were obtained using a single-slice inversion recovery spin echo sequence, which is the pulse sequence most commonly used for T_1 determination. At 1.5 T, I used the following parameters: TI = 50 ms, 100 ms, 200 ms, 400 ms, 800 ms, 1600 ms, 3200 ms; matrix size = 128×128 ; FOV = 16 cm; TR/TE = 5000/10 ms; bandwidth = ± 122.109 kHz; NEX = 0.5; and slice thickness = 10 mm. At 3.0 T, I used the following parameters: TI = 50 ms, 100 ms, 200 ms, 400 ms, 800 ms, 1600 ms, 3200 ms; matrix size = 256×256 ; FOV = 16 cm; TR/TE = 5000/10 ms; bandwidth = ± 62.50 kHz; NEX = 5.0; and slice thickness = 5 mm.

The signal for inversion recovery is typically expressed as

$$S = M_0(1 - 2 \exp(-TI/T_1) + \exp(-TR/T_1)) \quad (3.5)$$

where M_0 is the equilibrium magnetization, TI denotes inversion time, and TR denotes repetition time. For a given concentration, at each TI, the signal was represented by the mean signal in the ROI and the standard deviation was used to estimate uncertainty. Because TR and M_0 were fixed, I estimated T_1 using the Levenberg-Marquardt least-squares algorithm.^{91,92} For each ROI defined in each vial, I used the time point with the lowest signal as our initial estimate for T_1 , which ideally should be close to the null point. However, T_1 was expected to be extremely close to 0 at higher concentrations (1.5 %, 2.0 % and 5.0 % for 1.5 T, and 5 % for 3.0 T), so to ensure stability for these points, I used 10 ms for some of the initial estimates for T_1 .

3.3.3 Measuring Spin-spin Relaxation Time T_2

T_2 measurements were obtained using a 2D spin-echo sequence. At 1.5 T, I used the following parameters: TR = 1000 ms; TE = 10 ms, 20 ms, 30 ms, 40 ms, 50 ms, 60 ms, 70 ms, 80 ms, 90 ms, 100 ms, 150 ms, 200 ms, 250 ms, 300 ms, 350 ms, 400 ms, 500 ms, 600 ms; matrix size = 128×128 ; bandwidth = ± 122.109 kHz; FOV = 16 cm; NEX = 0.5; and slice thickness = 10 mm. At 3.0 T, I used the following parameters: TR = 5000 ms; TE = 10 ms, 20 ms, 30 ms, 40 ms, 50 ms, 60 ms, 70 ms, 80 ms; matrix size = 256×128 ; bandwidth = ± 62.5 kHz; FOV = 6 cm; NEX = 1; and slice thickness = 10 mm.

I fit the measured echo amplitudes to

$$S = M_0 \exp(-TE/T_2) \quad (3.6)$$

For each ROI, a first-degree polynomial fitting was performed on the spin echo signals plotted against time to obtain the initial estimate for T_2 .

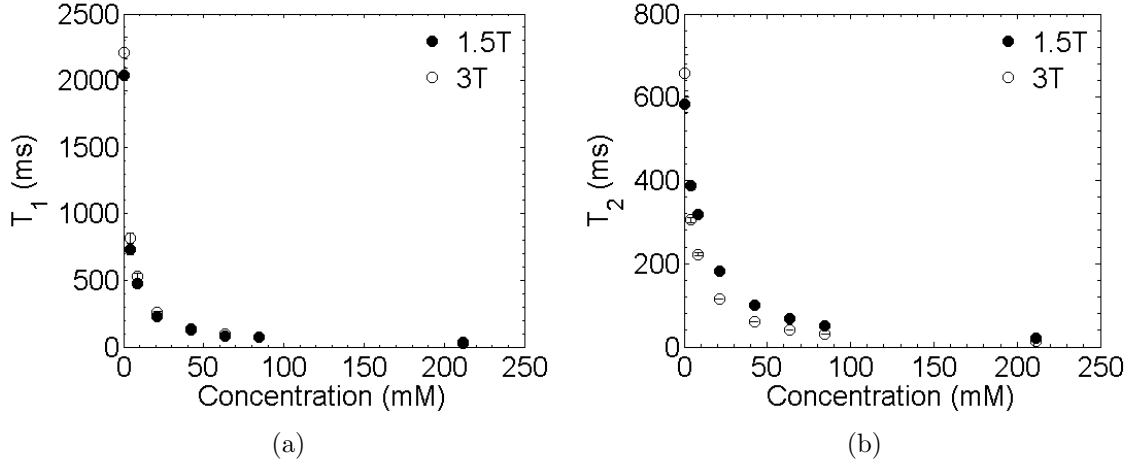


Figure 3.7: Spin-lattice relaxation time, T_1 , and spin-spin relaxation time, T_2 , at 1.5 T and 3.0 T, for various cobalt dichloride concentrations. Reproduced from T. Y. Lim, R. J. Stafford, R. J. Kudchadker, M. Sankaranarayananpillai, G. Ibbott, A. Rao, K. S. Martirosyan, and S. J. Frank. “MRI characterization of cobalt dichloride-N-acetyl cysteine (C4) contrast agent marker for prostate brachytherapy”. In: *Phys Med Biol* 59.10 (2014), pp. 2505–16⁵⁷ (©Institute of Physics and Engineering in Medicine. Reproduced by permission of IOP Publishing. All rights reserved).

3.3.4 Measuring Relaxivities r_1 and r_2

Starting with the initial T_1 and T_2 estimates, I applied nonlinear regression to the signal plotted against each inversion/echo time and iteratively applied the least-squares method to estimate T_1 and T_2 . Relaxivity was defined as the change in relaxation rate of bulk water per unit concentration of cobalt dichloride. The relaxation rates were calculated and plotted against cobalt dichloride concentration. Thus, the slopes from the linear fit to this plot result in relaxivity values r_1 and r_2 .

3.4 Results and Discussion

3.4.1 Effect of Field Strength

T_1 and T_2 values measured at 1.5 T and 3.0 T, for cobalt dichloride concentrations ranging from 0 mM to 211.45 mM, are shown in Figure 3.7. Corresponding relaxation rates are shown in Figure 3.8.

The T_1 values were similar at both field strengths, even across different cobalt dichloride

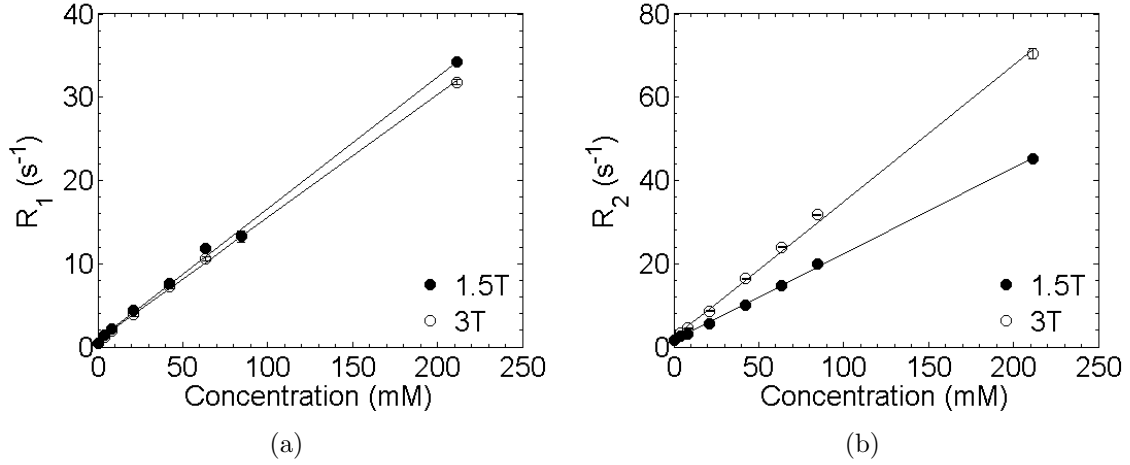


Figure 3.8: Spin-lattice relaxation rate $R_1 = 1/T_1$ and spin-spin relaxation rate $R_2 = 1/T_2$ at 1.5 T and 3.0 T, for various cobalt dichloride concentrations. The relaxivity ($\text{mM}^{-1} \text{s}^{-1}$) was determined by the slope from a linear fit of relaxation rate (s^{-1}) plotted against cobalt dichloride concentration (mM). Reproduced from T. Y. Lim, R. J. Stafford, R. J. Kudchadker, M. Sankaranarayananpillai, G. Ibbott, A. Rao, K. S. Martirosyan, and S. J. Frank. “MRI characterization of cobalt dichloride-N-acetyl cysteine (C4) contrast agent marker for prostate brachytherapy”. In: *Phys Med Biol* 59.10 (2014), pp. 2505–16⁵⁷ (©Institute of Physics and Engineering in Medicine. Reproduced by permission of IOP Publishing. All rights reserved).

concentrations. As field strength increases, the corresponding Larmor frequency increases; hence the energy transfer to the lattice is less efficient. Thus, increased T_1 values are expected at high field strengths, and I did observe this slight increase in T_1 at the lower concentrations of cobalt dichloride. However, the T_1 values at the two field strengths agreed well overall. Hence, the C4 contrast agent’s r_1 relaxivity values obtained at the two different field strengths were similar, suggesting that r_1 is not dependent on field strength.

However, the T_2 values of the C4 contrast agent at 3.0 T were slightly lower than at 1.5 T, translating to consistently higher spin-spin relaxation rates. In other words, the T_2 values at 3.0 T decreased at a greater rate with increasing concentration compared with that at 1.5 T. Therefore, the value of the slope, which corresponds directly to the r_2 of C4 contrast agent, was higher at 3.0 T than at 1.5 T, suggesting that r_2 is dependent on field strength and that T_2 is likely to decrease with increasing field strengths. Although the spin-spin relaxivity (r_2) is higher at 3.0 T than at 1.5 T, the MRI signal intensity is still dependent on the pulse sequence chosen. The higher r_2 values at higher field strengths simply reaffirm the increased

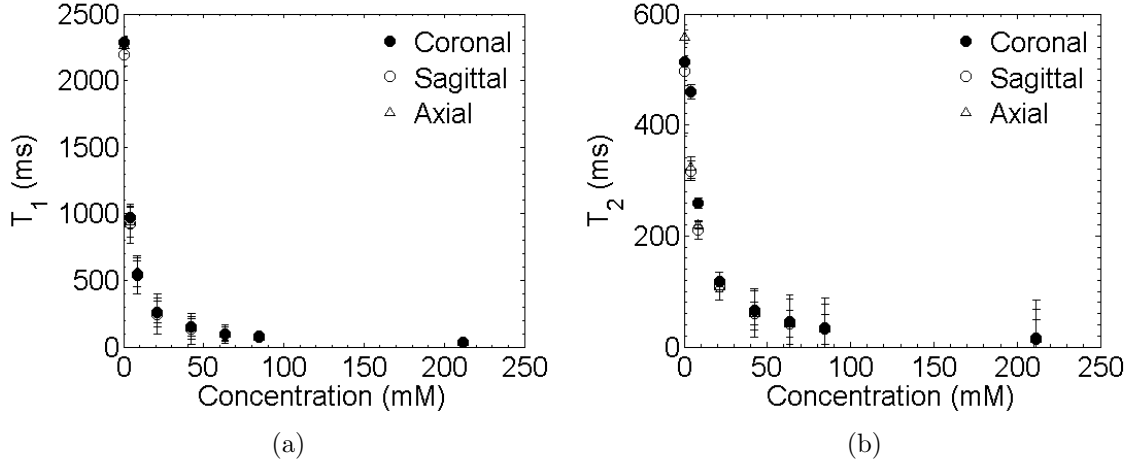


Figure 3.9: Spin-lattice relaxation time, T_1 , and spin-spin relaxation time, T_2 , at three different vial orientations, for various cobalt dichloride concentrations. Reproduced from T. Y. Lim, R. J. Stafford, R. J. Kudchadker, M. Sankaranarayanapillai, G. Ibbott, A. Rao, K. S. Martirosyan, and S. J. Frank. “MRI characterization of cobalt dichloride-N-acetyl cysteine (C4) contrast agent marker for prostate brachytherapy”. In: *Phys Med Biol* 59.10 (2014), pp. 2505–16⁵⁷ (©Institute of Physics and Engineering in Medicine. Reproduced by permission of IOP Publishing. All rights reserved).

T_2 -lowering ability, with the same considerations as stated before. Overall, because r_1 is not dependent on field strength, the increase in r_2 with field strength increases the relaxivity ratio r_2/r_1 .

For cobalt dichloride concentrations $< 1\%$ (42.49 mM), simply increasing the concentration to enhance the signal is not feasible because the shorter T_2 values at 3.0 T reduces the effect of T_1 -shortening. For cobalt dichloride concentrations $> 1\%$, increasing the concentration further offers little gain because the T_1 -shortening effect plateaus. Thus, the concentration of 1% cobalt dichloride offered a reasonable compromise of the T_1 and T_2 changes at the two clinically relevant field strengths to generate a strong signal. The 10% cobalt dichloride marker placed adjacent to the radioactive seed was shown to result in greater radiation dose perturbations (Figure 1.10), and subsequently greater impact on DVH parameter, compared to the 1% marker and a conventional spacer (this study was performed using the glycine instead of NAC as the chelator). Both 1% and 10% cobalt dichloride in the C4 contrast agent is a low concentration that has been shown to be safe for clinical use.⁷⁷

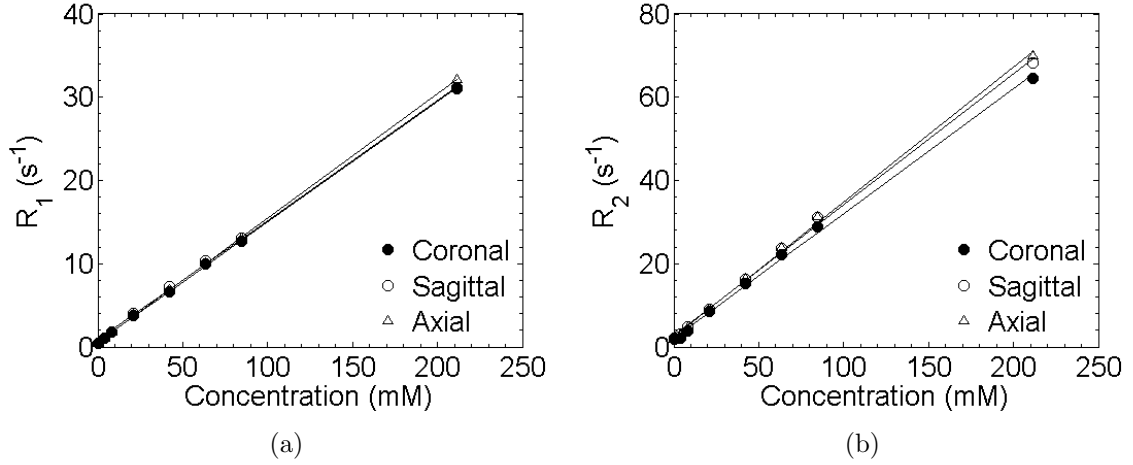


Figure 3.10: Spin-lattice relaxation rate $R_1 = 1/T_1$ and spin-spin relaxation rate $R_2 = 1/T_2$ at three different vial orientations, for various cobalt dichloride concentrations. The relaxivity ($\text{mM}^{-1} \text{s}^{-1}$) was determined by the slope from a linear fit of relaxation rate (s^{-1}) plotted against cobalt dichloride concentration (mM). Reproduced from T. Y. Lim, R. J. Stafford, R. J. Kudchadker, M. Sankaranarayanapillai, G. Ibbott, A. Rao, K. S. Martirosyan, and S. J. Frank. “MRI characterization of cobalt dichloride-N-acetyl cysteine (C4) contrast agent marker for prostate brachytherapy”. In: *Phys Med Biol* 59.10 (2014), pp. 2505–16⁵⁷ (©Institute of Physics and Engineering in Medicine. Reproduced by permission of IOP Publishing. All rights reserved).

3.4.2 Effect of Orientation

The T_1 and T_2 values measured at coronal, sagittal, and axial orientations are shown in Figure 3.9, and Figure 3.10 shows the relaxation rates across different cobalt dichloride concentrations. No significant differences in relaxation measurements were observed across different orientations of the vial with respect to the main magnetic field.

Brachytherapy seeds have been shown to have artifacts that are dependent on the seeds’ orientation with respect to the main magnetic field.⁹³ The main purpose of studying the effects of orientation on the relaxation characteristics of the C4 contrast agent is to detect any possible MR artifacts. When the Sirius MRI marker encapsulating the C4 contrast agent is implanted into the prostate, the Sirius MRI markers could potentially tilt in any direction. In the present study, the relaxation times, relaxation rates, and relaxivities, which are intrinsic to the cobalt dichloride complex, were similar for all three orientations. Therefore, when imaging the Sirius MRI marker, the investigation of the origin of any detected artifacts would be best directed toward scrutinizing extrinsic parameters.

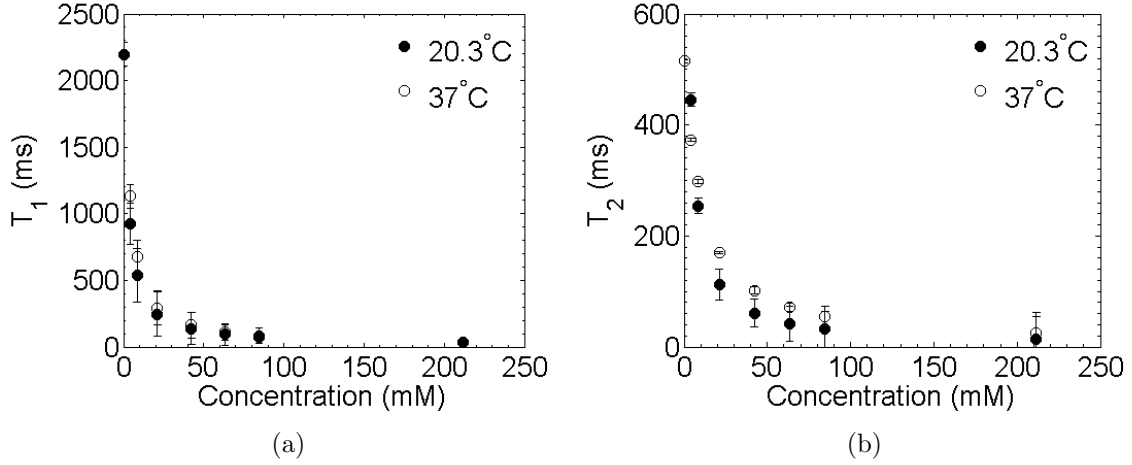


Figure 3.11: Spin-lattice relaxation time, T_1 , and spin-spin relaxation time, T_2 , at room temperature and body temperature, for various cobalt dichloride concentrations. Reproduced from T. Y. Lim, R. J. Stafford, R. J. Kudchadker, M. Sankaranarayananpillai, G. Ibbott, A. Rao, K. S. Martirosyan, and S. J. Frank. “MRI characterization of cobalt dichloride-N-acetyl cysteine (C4) contrast agent marker for prostate brachytherapy”. In: *Phys Med Biol* 59.10 (2014), pp. 2505–16⁵⁷ (©Institute of Physics and Engineering in Medicine. Reproduced by permission of IOP Publishing. All rights reserved).

3.4.3 Effect of Temperature

Figure 3.11 shows the T_1 and T_2 measured at room temperature and body temperature, and Figure 3.12 shows the corresponding relaxation rates across different cobalt dichloride concentrations. T_1 was similar at both room temperature and body temperature for all cobalt dichloride concentrations investigated. Therefore, the corresponding relaxation rates were similar for the two temperatures as well, suggesting that r_1 is not dependent on temperature.

Conversely, the T_2 of the C4 contrast agent at body temperature was slightly higher than at room temperature, translating to lower spin-spin relaxation rates. Therefore, the value of the slope, which corresponds directly to the r_2 of the C4 contrast agent, was lower at body temperature than at room temperature. These temperature data sets suggest that r_2 is dependent on temperature and that T_2 is likely to increase with increasing temperature. Because r_1 is not dependent on temperature, the decrease in r_2 with temperature decreases the relaxivity ratio r_2/r_1 .

Theoretically, as temperature increases, the correlation time for the interaction decreases, requiring longer relaxation times and causing relaxation rates to lower, thereby resulting

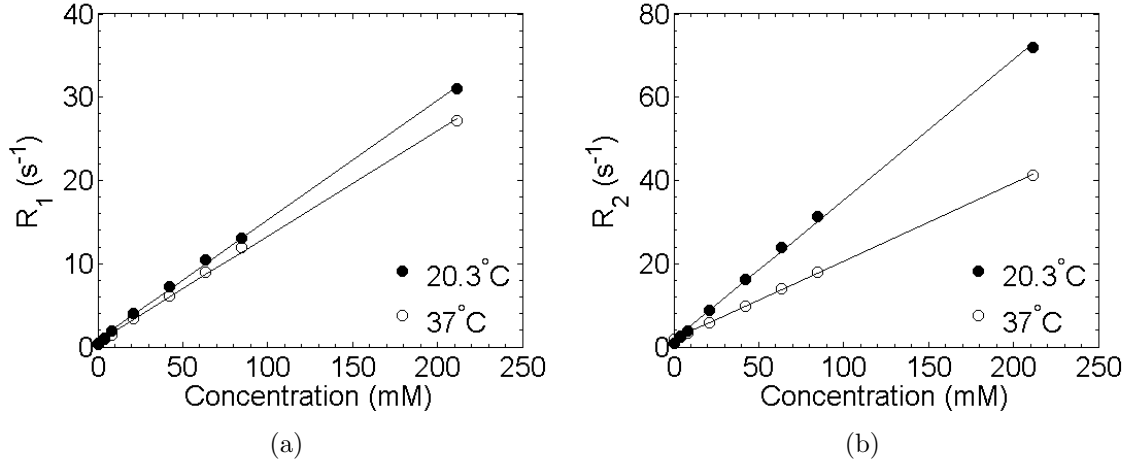


Figure 3.12: Spin-lattice relaxation rate $R_1 = 1/T_1$ and spin-spin relaxation rate $R_2 = 1/T_2$ at room temperature and body temperature, for various cobalt dichloride concentrations. The relaxivity (mM⁻¹s⁻¹) was determined by the slope from a linear fit of relaxation rate (s⁻¹) plotted against cobalt dichloride concentration (mM). Reproduced from T. Y. Lim, R. J. Stafford, R. J. Kudchadker, M. Sankaranarayananpillai, G. Ibbott, A. Rao, K. S. Martirosyan, and S. J. Frank. “MRI characterization of cobalt dichloride-N-acetyl cysteine (C4) contrast agent marker for prostate brachytherapy”. In: *Phys Med Biol* 59.10 (2014), pp. 2505–16⁵⁷ (©Institute of Physics and Engineering in Medicine. Reproduced by permission of IOP Publishing. All rights reserved).

in a decrease in relaxivity.⁹⁴ In this study, for cobalt dichloride concentration of 1 %, the change in T_1 was not significant, whereas T_2 was slightly longer at body temperature.

3.5 Conclusion

3.5.1 Summary

Relaxivity measurements of the C4 contrast agent at different field strengths, orientations and temperatures are presented in Table 3.2.

T_1 and T_2 values can be affected by the presence of positive contrast agents. The greater the concentration of cobalt dichloride ions, the smaller the T_1 and T_2 relaxation times. Consistent with our expectations from previous investigations,²⁰ the T_1 -shortening effect of the C4 contrast agent was very dominant; therefore, a very high signal (positive enhancement) from the C4 contrast agent against the prostatic background was expected. Because of the innate fast transverse relaxation of prostate tissue, the T_2 shortening effect was not as strong as the T_1 shortening effect.

Table 3.2: Relaxivities r_1 and r_2 for different field strengths, orientations, and temperatures. Reprinted from T. Y. Lim, R. J. Stafford, R. J. Kudchadker, M. Sankaranarayananpillai, G. Ibbott, A. Rao, K. S. Martirosyan, and S. J. Frank. “MRI characterization of cobalt dichloride-N-acetyl cysteine (C4) contrast agent marker for prostate brachytherapy”. In: *Phys Med Biol* 59.10 (2014), pp. 2505–16⁵⁷ (©Institute of Physics and Engineering in Medicine. Reproduced by permission of IOP Publishing. All rights reserved).

	r_1 (mM ⁻¹ s ⁻¹)	r_2 (mM ⁻¹ s ⁻¹)
Field Strength		
1.5 T	0.158 ± 0.003	0.208 ± 0.002
3.0 T	0.148 ± 0.002	0.328 ± 0.006
Orientation		
Coronal	0.145 ± 0.001	0.300 ± 0.005
Sagittal	0.144 ± 0.002	0.315 ± 0.006
Axial	0.149 ± 0.001	0.324 ± 0.005
Temperature		
20.3 °C	0.144 ± 0.002	0.337 ± 0.005
37.0 °C	0.127 ± 0.002	0.186 ± 0.001

Gadolinium-based contrast agents are the most commonly used contrast agents.⁹⁵ At 1.5 T and 3.0 T, the measured relaxivities in water for gadolinium-based contrast agents range from 3 mM⁻¹ s⁻¹ to 5 mM⁻¹ s⁻¹.⁹⁵ The relaxivities measured for the C4 contrast agent ranged from 0.1 mM⁻¹ s⁻¹ to 0.4 mM⁻¹ s⁻¹, implying a weaker efficiency in influencing tissue relaxation rates compared with gadolinium-based contrast agents. Cobalt has three unpaired electrons, whereas gadolinium has seven unpaired electrons. Therefore, a higher concentration of cobalt is needed to achieve the same influence as gadolinium. However, the C4 contrast agent remains in the polymer casing with no tissue uptake, because the main indication for the Sirius MRI marker is an encapsulated C4 contrast agent marker to enable more accurate localization of brachytherapy seeds. Moreover, the C4 contrast agent is associated with negligible toxicity,⁷⁷ enabling the use of very high concentrations to reach sufficient T_1 -shortening effects and induce positive contrast. The concentration of gadolinium is limited by the potential for inducing toxicity, such as nephrogenic systemic fibrosis in patients with impaired renal function. Similar to gadolinium-based contrast agents, the spin-lattice and spin-spin relaxivities for the C4 contrast agent are approximately the same, suggesting the same T_1 - or T_2 -shortening capability. Hence, the C4 contrast agent could potentially be used as both a positive and a negative contrast agent.

3.5.2 Limitations

A limitation of this study is that I evaluated the effects of only two different temperatures on relaxation: room temperature and the more clinically relevant body temperature. Any extrapolation of our findings to storage ambient temperature concerns or non-medical use warrants further investigation.

3.5.3 Implications

The relaxation values obtained indicate that the C4 contrast agent is promising for encapsulation as the contrast agent in Sirius MRI markers that may allow MRI-only post-implant dosimetry.

Using specific pulse sequences, such as T_1 -weighted or T_2 -weighted sequences, can enhance the differences in signal intensities of various tissues. With knowledge of the relaxation times of the desired contrast agent concentration, I can adjust pulse sequence parameters to provide greater contrast between the Sirius MRI marker and surrounding tissue. In the next chapter, I will describe a phantom investigation into the effects of scan parameter variations on the visibility of Sirius MRI markers.

This chapter is adapted from T. Y. Lim, R. J. Kudchadker, J. Wang, R. J. Stafford, C. J. MacLellan, A. Rao, G. Ibbott, and S. J. Frank. “Effect of pulse sequence parameter selection on signal strength in positive-contrast MRI markers for MRI-based prostate post-implant assessment”. In: *Med Phys* 43.7 (2016)⁹⁶ (with permission from the American Association of Physicists in Medicine).

4

Pulse Sequence Parameter Variations in Phantom

Contents

4.1	Background	68
4.1.1	Spoiled Gradient Echo Sequences	68
4.1.2	Pulse Sequence Parameters	69
4.2	Purpose	71
4.3	Methods	72
4.3.1	Data Collection	72
4.3.2	Image Processing	73
4.3.3	Statistical Analysis	75
4.4	Results and Discussion	75
4.4.1	Varying Flip Angle	75
4.4.2	Varying Number of Excitations	78
4.4.3	Varying Bandwidth	79
4.4.4	Varying Field-of-view	84
4.4.5	Varying Slice Thickness	88
4.4.6	Varying Encoding Steps	89
4.5	Conclusion	99
4.5.1	Summary	99
4.5.2	Limitations	99
4.5.3	Implications	101

4.1 Background

4.1.1 Spoiled Gradient Echo Sequences

A pulse sequence is a sequence of RF and gradient pulses with predefined pulse lengths and amplitudes that affect signal generation and reception. A pulse sequence with the optimal combination of pulse sequence parameters needs to be defined to obtain high marker visibility while balancing against other conflicting factors (such as image acquisition time, spatial resolution, and image artifacts) to provide the best images for post-implant dosimetry, given the significant time and cost associated with MRI.

Two main classes of pulse sequences are the spin echo sequence⁹⁷ and the gradient echo sequence. Spin echoes are produced by two RF pulses, but gradient echoes are produced with a single RF pulse together with gradient manipulation.⁹⁸ Using a gradient echo pulse sequence enables shorter TR and TE values, therefore reducing image acquisition time. The commonly cited drawback of gradient echo pulse sequences is increased susceptibility artifacts; but for post-implant dosimetry, the susceptibility artifact from the seeds result in a characteristic dumbbell appearance that could potentially be used to more definitively locate the seeds based on the distinct susceptibility patterns*. T_1 -weighted gradient echo sequences have been reported to yield the best seed visibility.²⁷

Spoiled gradient echo sequences are gradient echo sequences with a spoiling mechanism (such as radiofrequency-spoiled) that disrupts transverse coherences that previously persisted, thereby ensuring no transverse coherences immediately before each RF pulse. Different scanner manufacturers have different terms for this sequence: GE = radiofrequency-spoiled gradient recalled echo (SPGR), Siemens = Fast Low Angle SHot (FLASH) while Philips = Fast Field Echo (T1-FFE).

The spoiled gradient echo signal equation is

$$\hat{\rho} = \rho_0 \sin \alpha \frac{1 - \exp(-TR/T_1)}{1 - \exp(-TR/T_1) \cos \alpha} \exp(-TE/T_2^*) \quad (4.1)$$

*See Section 5.1.4 on other pulse sequences that take advantage of the seed susceptibility artifact for seed localization.

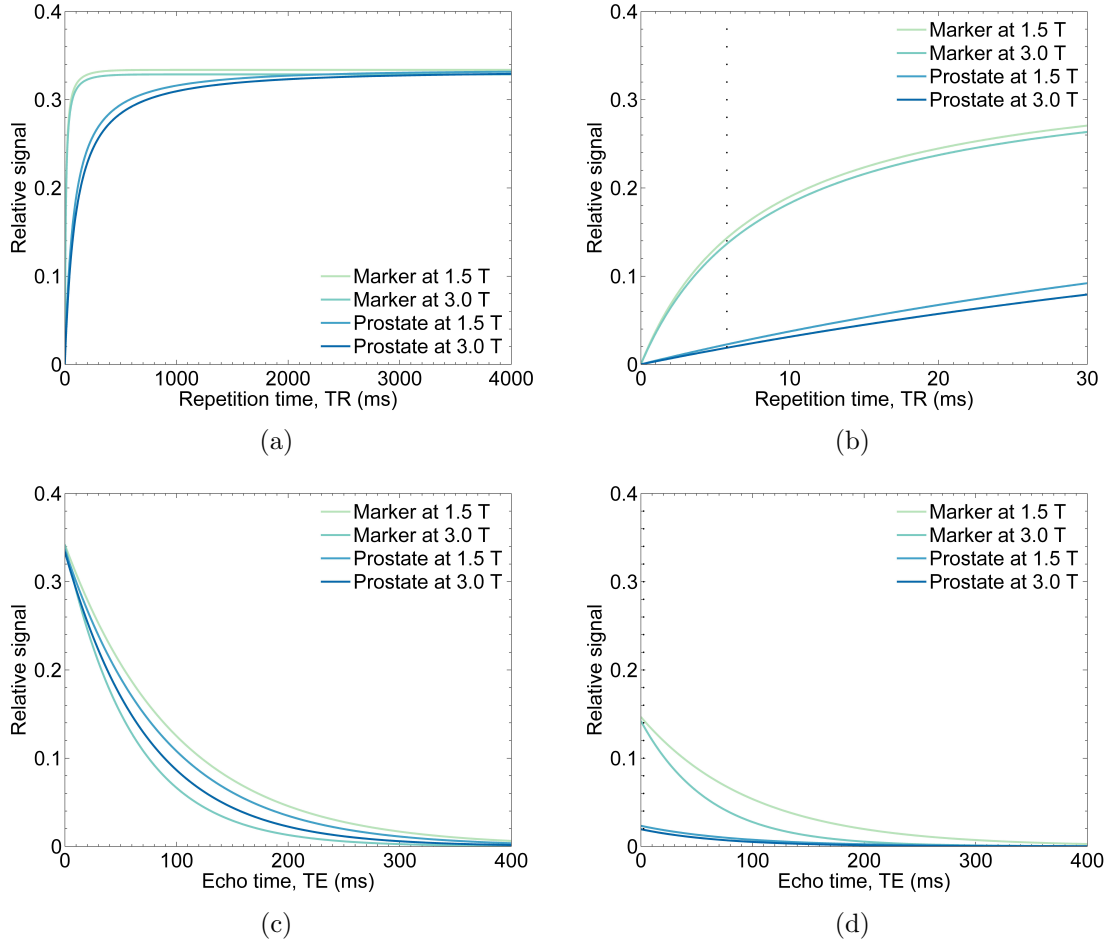


Figure 4.1: Signal trends predicted from Equation 4.1. (a) Relative signals of the Sirius MRI marker and prostate for varying TR, and (b) zoomed view illustrates the signal difference between Sirius MRI marker and prostate using short TR, (c) relative signals of the Sirius MRI marker and prostate for varying TE given *very long* TR, and (d) relative signals of the Sirius MRI marker and prostate for varying TE given *short* TR.

4.1.2 Pulse Sequence Parameters

Repetition Time The repetition time is the time from the application of an RF excitation pulse to the repeated application of the RF excitation pulse.⁸⁵ When imaging at 3.0 T, at sufficiently long TR (> 3600 ms given Sirius MRI marker and prostate estimated relaxation times[57, 99]), the estimated Sirius MRI marker signal becomes lower than the estimated prostate signal (Figures 4.1a and 4.1c), which would result in the markers appearing hypointense against the prostatic tissue. For T_1 -weighted sequences using short TR (Figure 4.1b) and short TE (Figure 4.1d), the differences in T_1 would be emphasized.

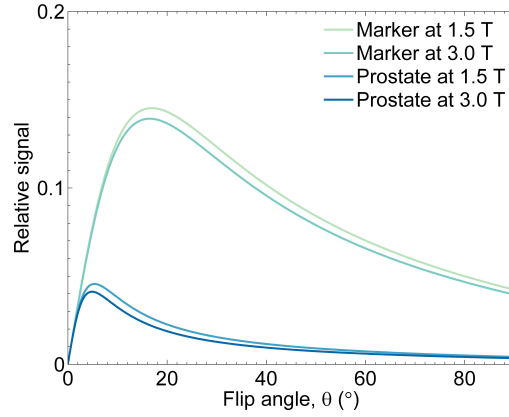


Figure 4.2: Signal trends of the Sirius MRI marker and prostate for varying flip angle, predicted from Equation 4.1.

Echo Time The echo time is the time from the application of an RF excitation pulse to the peak of the echo.⁸⁵ Shown in Figure 4.1 are the signal trends predicted from Equation 4.1 given the Sirius MRI marker and prostate estimated relaxation times^{57,99} (using T_2 instead of T_2^*). When imaging at 3.0 T, due to the relatively short T_2 , the TE used must be sufficiently short ($< 8.3 \text{ ms}^\dagger$ given Sirius MRI marker and prostate estimated relaxation times^{57,99}), else the estimated Sirius MRI marker signal becomes lower than the estimated prostate signal, which would result in the markers appearing hypointense against the prostatic tissue.

Flip angle The flip angle (α) is the angle at which the magnetization vector is flipped from the longitudinal axis of the main magnetic field. Using relaxation times for the Sirius MRI marker's contrast agent⁵⁷ and for prostate⁹⁹ to estimate the signal trend according to Equation 4.1, the contrast separation is highest in the proximity of $\alpha = 16 \text{ deg}$ to 20 deg (Figure 4.2).

Number of Excitations The number of excitations (NEX) is the number of times the scan is repeated and the repeated signals averaged.¹⁰⁰

Bandwidth The receiver bandwidth (BW) is the signal sampling rate, so the faster the signal is sampled, the wider the bandwidth.¹⁰⁰

[†]The actual TE required would be much shorter because the estimated TE value was calculated using T_2 instead of T_2^* , so the TE required would be much shorter.

Field of view The field of view (FOV) is the area from which the signal is sampled in the defined scan plane. It may be specified in the frequency- and phase-encoding directions on the image. In this study, the FOV refers to a square FOV (full phase FOV). For limited gradient strength G_x and the proportional relationship between frequency and field strength via the Larmor equation (Equation 3.1), FOV is directly proportional to BW via

$$FOV_x = BW/(\gamma G_x) \quad (4.2)$$

When the FOV decreases, the distance between the image's edges decrease. Therefore, for fixed BW (range of frequencies from one edge to the other edge of the image), decreasing the FOV requires a stronger gradient.¹⁰⁰

Slice thickness The slice thickness (Δz) defines the through-plane resolution.

Encoding steps The frequency-encoding steps (N_x) and phase-encoding steps (N_y) can be transformed to the x and y dimensions, as spatial locations are encoded by varying frequency and phase across the volume.¹⁰⁰ Generally, encoding steps relates directly to the number of acquisition pixels in the x and y directions, and defines the in-plane resolution.

4.2 Purpose

In the last chapter, the T_1 and T_2 of the C4 contrast agent was determined. The Sirius MRI markers containing the C4 contrast agent can be visualized using the 3D FSPGR sequence. However, the effects on the Sirius MRI marker due to pulse sequence parameter variations should be quantified to allow the appropriate discernment in setting pulse sequence parameters. To obtain the desired image contrast, the MRI user has the capability to adjust several parameters of a pulse sequence, depending on the suitability to the specified pulse sequence template file, variations in imaging technique implementation and hardware performance limits.

To determine which parameters yield the most consistent and high-signal visualization of the markers, I investigated several user-adjustable scan parameters of the 3D FSPGR sequence

on a GE 3.0 T scanner in normal scanning mode. All markers were detected on images acquired using the scan parameter combinations examined, but the extent of the marker visibility and conspicuity varied depending on the selected scan parameter combinations. I also reported the trends of scan times for varying pulse sequence parameters, as short image acquisition time is a priority, sometimes even at the expense of spatial resolution and contrast, to minimize patient motion artifacts. The pulse sequence parameters should be chosen based on evaluating the trade-offs between marker visibility, scan time, resolution and artifacts. I investigated the effects of varying α , NEX, BW, FOV, Δz and $N_x \times N_y$ on the marker's signal strength, image noise level, signal-to-noise ratio (SNR) and spatial resolution. In addition, I noted relevant conflicting factors that may advise against using the parameter value optimized for highest marker signal. A comprehensive and practical understanding of the impact of scan parameter adjustments on image quality is important for the acquisition of high-quality post-implant MRI scans for accurate dosimetric assessment.

4.3 Methods

4.3.1 Data Collection

A multi-modality prostate phantom Model 053-MM for ultrasound, CT and MRI (CIRS, Norfolk, VA) was implanted with 66 MRI markers (Sirius; C4 Imaging, Houston, TX) and 86 dummy (non-radioactive) seeds in stranded seed-marker combination using 20 needles (Figure 4.3). The phantom was imaged using a 3.0 T MRI scanner (GE Discovery MR750 with 50 mT/m amplitude and 200 T/m/s slew rate; GE, Waukesha, WI) and an 8-channel torso coil (GE, Waukesha, WI) with a 3D FSPGR sequence, under various combinations of scan parameters. The scan parameters varied here were α , NEX, BW, FOV, Δz and $N_x \times N_y$. Echo time (TE) was optimized as the minimum achievable TE to acquire a full echo in the frequency-encoding direction and repetition time (TR) was automatically minimized. The marker signal as a function of each parameter of interest was systematically studied by keeping all other parameters constant at baseline values (Table 4.1).

Image resolution refers to the pixel size of the output image. In-plane spatial resolution depends on the FOV and number of encoding steps, while through-plane spatial resolution

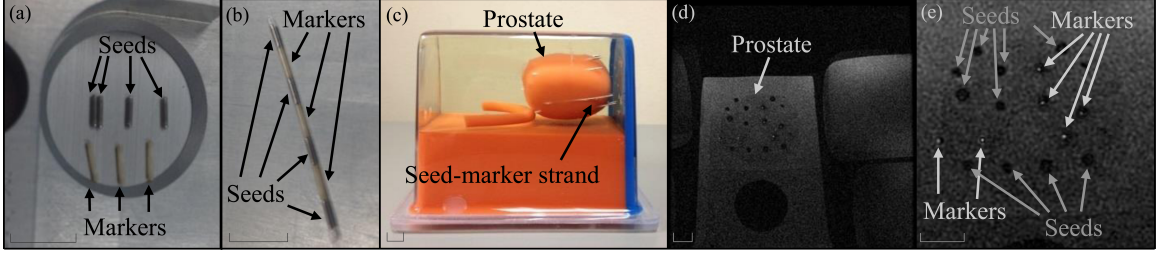


Figure 4.3: Materials used in the study. (a) Dummy seeds and MRI markers. (b) Seed-marker strand. (c) Implanted CIRS multi-modality prostate phantom. (d) MRI scan of the prostate phantom acquired with baseline scan parameters. (e) Zoomed-in view of the prostate. The seeds appear as hypointense voids while markers appear as hyperintense spots. (Scale denotes 1 cm.) Reprinted from T. Y. Lim, R. J. Kudchadker, J. Wang, R. J. Stafford, C. J. MacLellan, A. Rao, G. Ibbott, and S. J. Frank. “Effect of pulse sequence parameter selection on signal strength in positive-contrast MRI markers for MRI-based prostate post-implant assessment”. In: *Med Phys* 43.7 (2016)⁹⁶ (with permission from the American Association of Physicists in Medicine).

depends on the slice thickness.

4.3.2 Image Processing

Image processing was performed in Matlab 8.1.0 (The Mathworks, Inc., Natick, MA). On the magnitude reconstructed images, I recorded the maximum signal intensities for each of the 66 markers to calculate the average and standard deviation of the marker signal intensity. I plotted average marker signal against the various scan parameters, with error bars denoting the marker signal standard deviation. I also recorded the standard deviation of a 50×50 (2500 pixels) rectangular region-of-interest without artifacts in air, per the National Electrical Manufacturers Association (NEMA)¹⁰¹ image noise evaluation method 4. The SNR was calculated as the ratio of average marker signal intensity to the standard deviation in air. I plotted marker SNR against the various scan parameters, with error bars denoting propagated uncertainty from the marker signal. All signal, noise or SNR values were normalized to the signal, noise or SNR values obtained using baseline imaging parameters. I also plotted the (non-normalized) contrast-to-noise ratio (CNR) between the average marker signal intensity to average prostate signal intensity, for various scan parameters.

Table 4.1: Scan parameters investigated (baseline values are bolded). Reprinted from T. Y. Lim, R. J. Kudchadker, J. Wang, R. J. Stafford, C. J. MacLellan, A. Rao, G. Ibbott, and S. J. Frank. “Effect of pulse sequence parameter selection on signal strength in positive-contrast MRI markers for MRI-based prostate post-implant assessment”. In: *Med Phys* 43.7 (2016)⁹⁶ (with permission from the American Association of Physicists in Medicine).

Scan Parameters	Range of Values
α ($^\circ$)	4, 8, 12, 14, 16, 18, 20 , 22, 30, 40, 50, 60
NEX ^a	1, 2, 3, 4, 5, 6, 7, 8 , 9, 10, 15, 20, 25
BW (\pm kHz)	19.23, 31.25, 41.67, 50.00, 62.50, 83.33 , 90.91, 100.00, 111.10, 125.00, 142.86
FOV (cm) ^b	8, 10, 12, 14 , 16, 18, 20
Δz (mm) ^c	1.0, 1.2, 1.4, 1.6, 2.0 , 3.0, 4.0, 5.0, 6.0, 7.0, 8.0, 9.0, 10.0
$N_x \times N_y$ ^d	140×140 , 160×160 , 160×256 , 192×192 , 224×224 , 256×160 , 256×192 , 256×224 , 256×256 , 320×320 , 320×256 , 384×256 , 384×384 , 512×256 , 512×512
TE ms	2.3
TR ms	5.9
Scan time min	7.3

^a Halved due to phase oversampling

^b Square FOV

^c Interpolated to half the specified Δz

^d Interpolated to 512×512

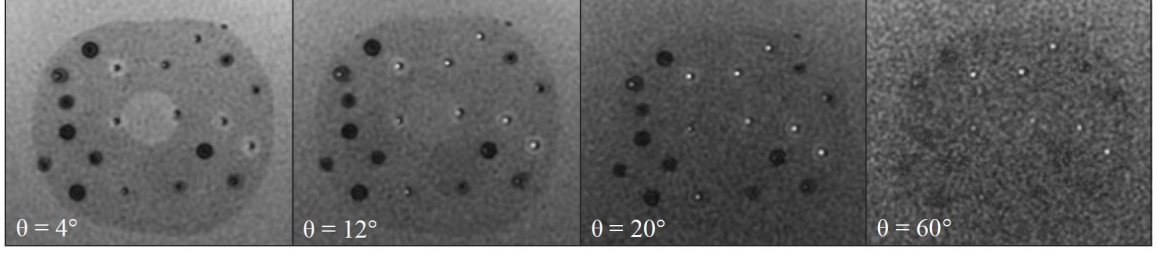


Figure 4.4: The effect of varying flip angle on the visual appearance of images. Reprinted from T. Y. Lim, R. J. Kudchadker, J. Wang, R. J. Stafford, C. J. MacLellan, A. Rao, G. Ibbott, and S. J. Frank. “Effect of pulse sequence parameter selection on signal strength in positive-contrast MRI markers for MRI-based prostate post-implant assessment”. In: *Med Phys* 43.7 (2016)⁹⁶ (with permission from the American Association of Physicists in Medicine).

4.3.3 Statistical Analysis

To determine whether there was a significant relationship between a certain scan parameter versus signal, noise or SNR, I performed a linear regression t-test at significance level = 0.01 with the null hypothesis that the slope parameter of a simple linear regression model was zero against the alternative hypothesis that the slope was not zero. The assumptions made were that signal, noise, or SNR has a linear relationship to a certain scan parameter, independent of the scan parameter, has the same probability distribution standard deviation, and roughly normally distributed.

4.4 Results and Discussion

4.4.1 Varying Flip Angle

At very small and very large α , the Sirius MRI marker’s visibility was reduced, but appeared more hyperintense at certain α (Figure 4.4). In the following sections, the effect of α on several image quality considerations for post-implant dosimetry purposes is illustrated.

Signal The signal of the Sirius MRI marker is strongly dependent on α , following the trend predicted by the spoiled gradient recalled echo sequence equation (Equation 4.1). The α that provided the highest marker signal was 14° (Figure 4.5a). The signals acquired at $\alpha = 12^\circ$ (angle providing greatest signal) and $\alpha = 14^\circ$ (angle providing greatest SNR)

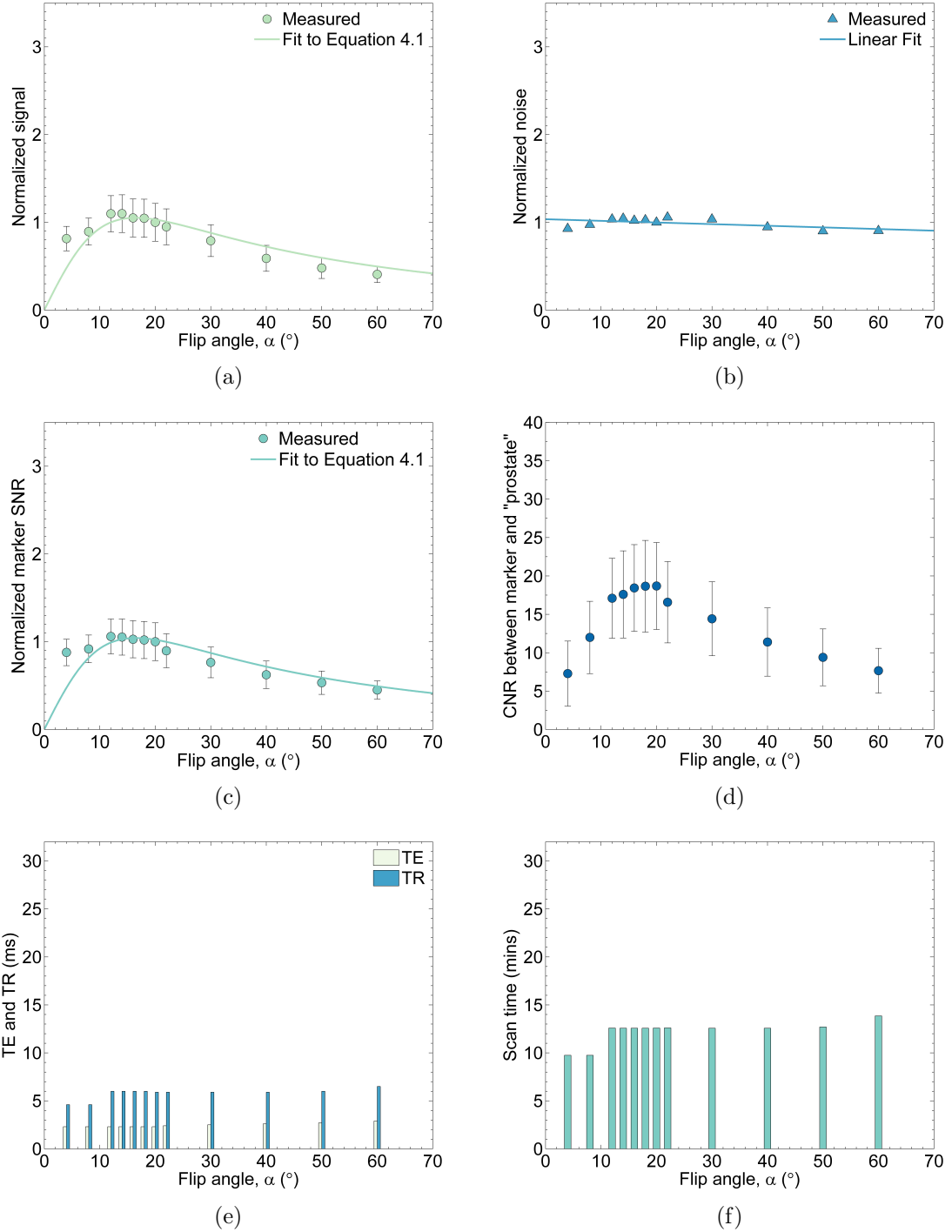


Figure 4.5: The effect of varying flip angle α on: (a) normalized Sirius MRI marker signal, (b) normalized image noise, (c) normalized Sirius MRI marker signal-to-noise ratio (SNR), (d) contrast-to-noise ratio (CNR) between the Sirius MRI marker and the prostate in phantom, (e) echo time TE and repetition time TR, (e) scan times. Adapted from T. Y. Lim, R. J. Kudchadker, J. Wang, R. J. Stafford, C. J. MacLellan, A. Rao, G. Ibbott, and S. J. Frank. "Effect of pulse sequence parameter selection on signal strength in positive-contrast MRI markers for MRI-based prostate post-implant assessment". In: *Med Phys* 43.7 (2016)⁹⁶ (with permission from the American Association of Physicists in Medicine).

were not significantly different ($p = 0.4799$). The measured α that provided the greatest signal was not significantly lower than the theoretical $\alpha_E = (16.48 \pm 1.08)^\circ$ ($p = 0.2538$). The lower signal measurements (Figure 2a) may be due to non-uniform excitation, that is, radiofrequency field inhomogeneity leading to spatial variation of the flip angle.

Noise Noise was not significantly affected by α (slope = -0.0019, $p = 0.0554$) (Figure 4.5b).

Signal-to-noise ratio Owing to the constancy in noise levels across varying α , the marker's SNR reflects the measured marker signal, and the α that provided the highest marker SNR was 12° (Figure 4.5c).

Contrast-to noise-ratio The trend of the CNR between Sirius MRI marker and “prostate” is similar to the trend of SNR for Sirius MRI markers because the signal of the Sirius MRI marker is much greater than the signal of the “prostate” (Figure 4.5d).

Timing TE, TR, and scan time were longer at larger α (Figure 4.5f). Smaller α , characteristic of gradient echo sequences, allows for shorter TR and thus shorter scan times (Figure 4.5f).

Contrast agents, such as that encapsulated in the marker, interact with nearby hydrogen protons, facilitating the magnetization recovery of the hydrogen protons and shortening the T_1 of the material, resulting in a bright appearance on T_1 -weighted images.¹⁰² Together with TR and the intrinsic T_1 , α affects the extent of T_1 -weighting. For $\alpha < 12^\circ$, the marker signal falls off very quickly, and becomes similar in signal intensity to the prostate, making the markers less conspicuous (Figure 4.4); hence I do not recommend using $\alpha < 12^\circ$. Conversely, for $\alpha > 12^\circ$, the reduced regrowth of the longitudinal magnetization may have reduced the signal, but even at very large flip angles, the marker signal remained higher than the prostate signal such that the markers can still be visualized (Figure 4.4). Since noise and scan time are similar across the range of α investigated, the selection of a suitable α is mainly motivated by increasing Sirius MRI marker signal. Therefore, for mean signal reduction of no more than 10 % of the maximum Sirius MRI marker signal, I recommend not using $\alpha >$

20°.

4.4.2 Varying Number of Excitations

With increasing NEX, the Sirius MRI marker’s visibility increased and the image appeared less noisy (Figure 4.6). In the following, the effect of NEX on several image quality considerations for post-implant dosimetry purposes is illustrated.

Signal The average signal was not significantly affected by varying NEX (slope = -0.0022, $p = 0.0188$), except at NEX = 1 where the signal was lower (Figure 4.7a). However, since I selected the phase-oversampling option (doubled N_y to reduce wrap artifact[‡]), NEX was reduced by half to preserve scan time. The signal drop at NEX = 1 (Figure 4.7a) was most likely due to phase-oversampling requiring the use of fractional NEX imaging where only about half of k-space was sampled.

Noise The average noise was reduced by $1/\sqrt{\text{NEX}}$ (Figure 4.7b), except at NEX = 1 (most likely due to phase-oversampling). Noise reduction with greater NEX is consistent with theory.¹⁰⁰

Signal-to-noise ratio SNR was thus improved by $\sqrt{\text{NEX}}$ (Figure 4.7c). SNR increase with greater NEX is consistent with theory.¹⁰⁰

Contrast-to noise-ratio The trend of the CNR between Sirius MRI marker and “prostate” is similar to the trend of SNR for Sirius MRI markers because the signal of the Sirius MRI marker is much greater than the signal of the “prostate” (Figure 4.7d).

Timing Varying NEX did not affect TE and TR (Figure 4.7f). However, since NEX is the number of times the scan is repeated, scan time proportionally increases with NEX (Figure 4.7f).

[‡]See Section 4.4.4 and 4.14 for discussion of the wrap artifact

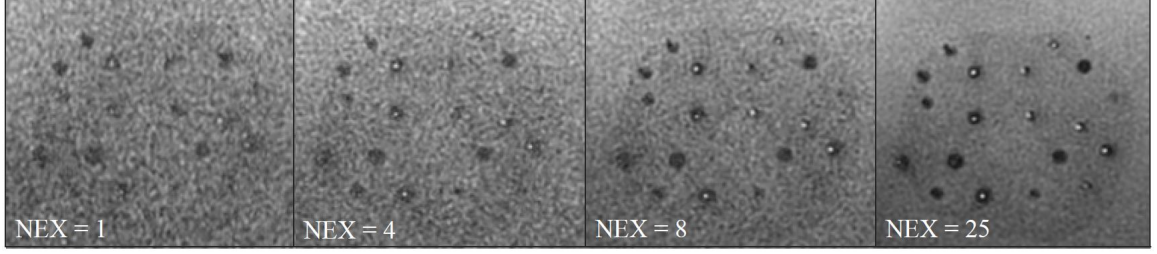


Figure 4.6: The effect of varying number of excitations on the visual appearance of images. Reprinted from T. Y. Lim, R. J. Kudchadker, J. Wang, R. J. Stafford, C. J. MacLellan, A. Rao, G. Ibbott, and S. J. Frank. “Effect of pulse sequence parameter selection on signal strength in positive-contrast MRI markers for MRI-based prostate post-implant assessment”. In: *Med Phys* 43.7 (2016)⁹⁶ (with permission from the American Association of Physicists in Medicine).

Artifacts Even though the signal using more NEX is greater, it may not be clinically feasible, as the lengthened scan time increases the likelihood of patient *motion artifacts*.

Very high NEX ($\text{NEX} \geq 15$) has diminishing returns, whereby further increases in NEX did not yield significant gain in SNR but scan time still scaled proportionally. Limiting to scan times under 10 minutes, I recommend using $\text{NEX} \leq 10$.

4.4.3 Varying Bandwidth

At narrower BW, the image appeared less noisy and the Sirius MRI marker is more visible albeit shifted (Figure 4.8). In the following, the effect of BW on several image quality considerations for post-implant dosimetry purposes is illustrated.

Signal For $\text{BW} \geq 244.14 \text{ Hz/pixel}$, the signal increased with $\sqrt{\text{BW}}$; for $\text{BW} < 244.14 \text{ Hz/pixel}$, the measured signal was greater than expected, with increasing signal at smaller BW until 162.77 Hz/pixel , then decreasing signal at smaller BW (Figure 4a). For narrow BW ($\text{BW} < 162.77 \text{ Hz/pixel}$), the sampling time was longer and the TE required was longer (Figure 4c), resulting in more T_2 decay and the subsequent drop in signal (Figure 4.9a). Theoretically,¹⁰⁰ signal increases with $\sqrt{\text{BW}}$. Since bandwidth is the signal sampling rate, at smaller bandwidth, the sampling time is longer, and the TE required is longer, resulting in more T_2 decay, hence lower signal. However, for $\text{BW} < 244.14 \text{ Hz/pixel}$, the measured signal being

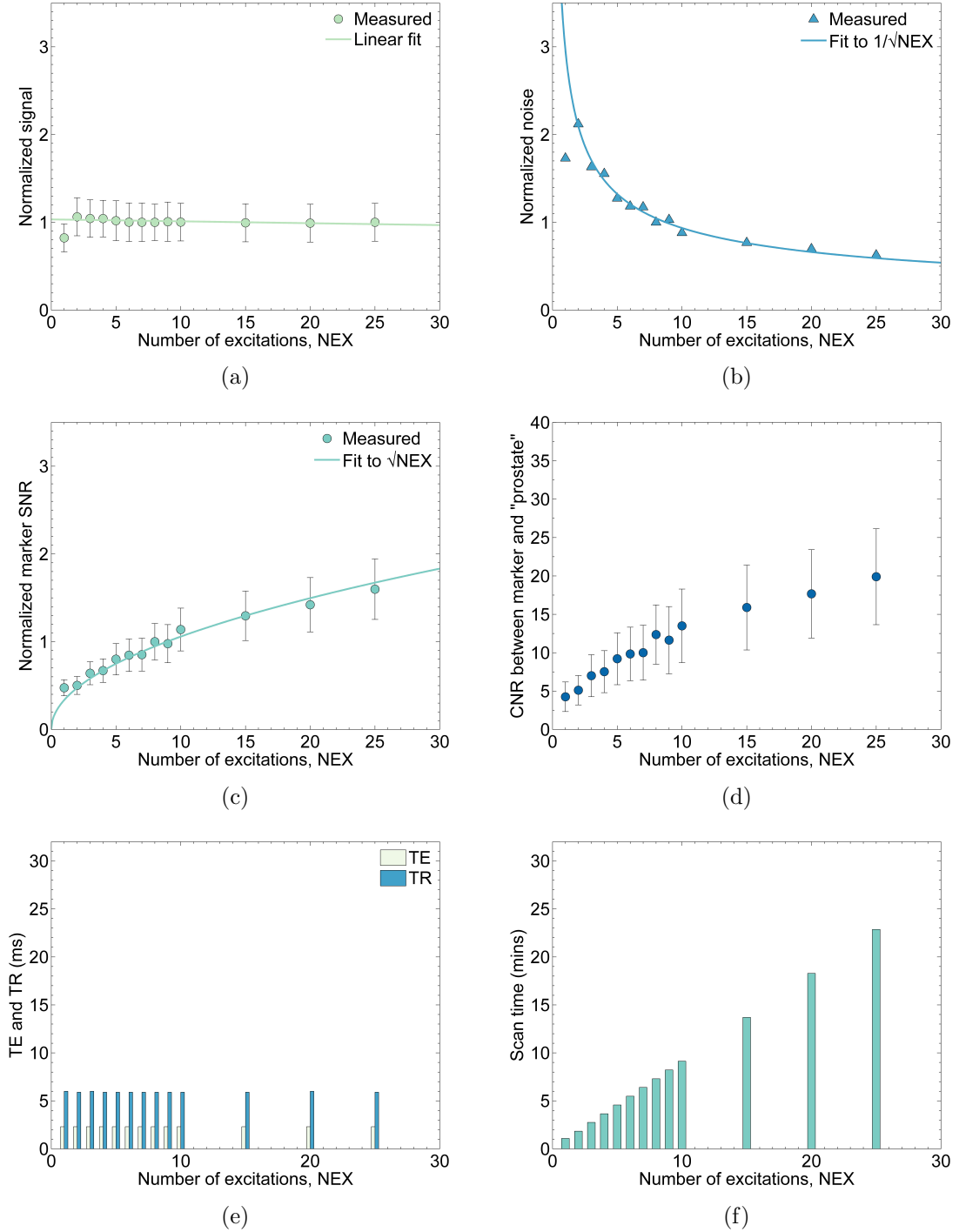


Figure 4.7: The effect of varying number of excitations on: (a) normalized Sirius MRI marker signal, (b) normalized image noise, (c) normalized Sirius MRI marker signal-to-noise ratio (SNR), (d) contrast-to-noise ratio (CNR) between the Sirius MRI marker and the prostate in phantom, (e) echo time TE and repetition time TR, (e) scan times. Adapted from T. Y. Lim, R. J. Kudchadker, J. Wang, R. J. Stafford, C. J. MacLellan, A. Rao, G. Ibbott, and S. J. Frank. "Effect of pulse sequence parameter selection on signal strength in positive-contrast MRI markers for MRI-based prostate post-implant assessment". In: *Med Phys* 43.7 (2016)⁹⁶ (with permission from the American Association of Physicists in Medicine).

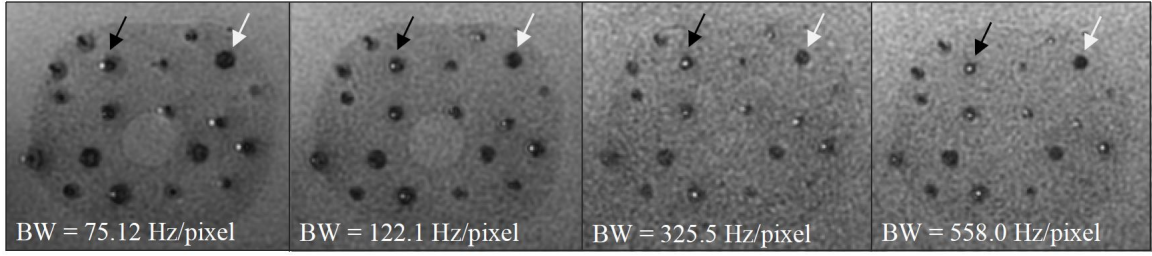


Figure 4.8: The effect of varying bandwidth on the visual appearance of images. Both the chemical shift artifact (black arrows) and seed susceptibility artifact (white arrows) were reduced with increasing bandwidth. Reprinted from T. Y. Lim, R. J. Kudchadker, J. Wang, R. J. Stafford, C. J. MacLellan, A. Rao, G. Ibbott, and S. J. Frank. “Effect of pulse sequence parameter selection on signal strength in positive-contrast MRI markers for MRI-based prostate post-implant assessment”. In: *Med Phys* 43.7 (2016)⁹⁶ (with permission from the American Association of Physicists in Medicine).

greater than the theoretical prediction (Figure 4.9a) may be due to increased TR (Figure 4.9f).

Noise Narrower BW was associated with lower noise (Figure 4.9b). This is consistent with the theory¹⁰⁰ that narrower bandwidths allow less noise to pass through.

Signal-to-noise ratio SNR decreased with increasing BW and then leveled off starting at 244.14 Hz/pixel (Figure 4.9c). Theoretically,¹⁰⁰ SNR is proportional to $1/\sqrt{BW}$. However, the measured SNR did not strictly follow the trendline depicted as the trendline did not include variations in TE and TR at different BW. SNR was improved at narrower BW (Figure 4.9c) mainly due to reduced noise, the effects of which may outweigh that of increased T_2 decay.

Contrast-to noise-ratio The trend of the CNR between Sirius MRI marker and “prostate” is similar to the trend of SNR for Sirius MRI markers because the signal of the Sirius MRI marker is much greater than the signal of the “prostate” (Figure 4.9d).

Timing At $BW < 162.77$ Hz/pixel, increasing BW decreased TE (Figure 4.9f). At $BW < 244.14$ Hz/pixel, increasing BW decreased TR and scan times, while at $BW \geq 244.14$ Hz/pixel, increasing BW increased TR and scan times. Images acquired with narrow BW had high SNR (Figure 4.9c), but long scan times (Figure 4.9f). Scan times were < 10 minutes for

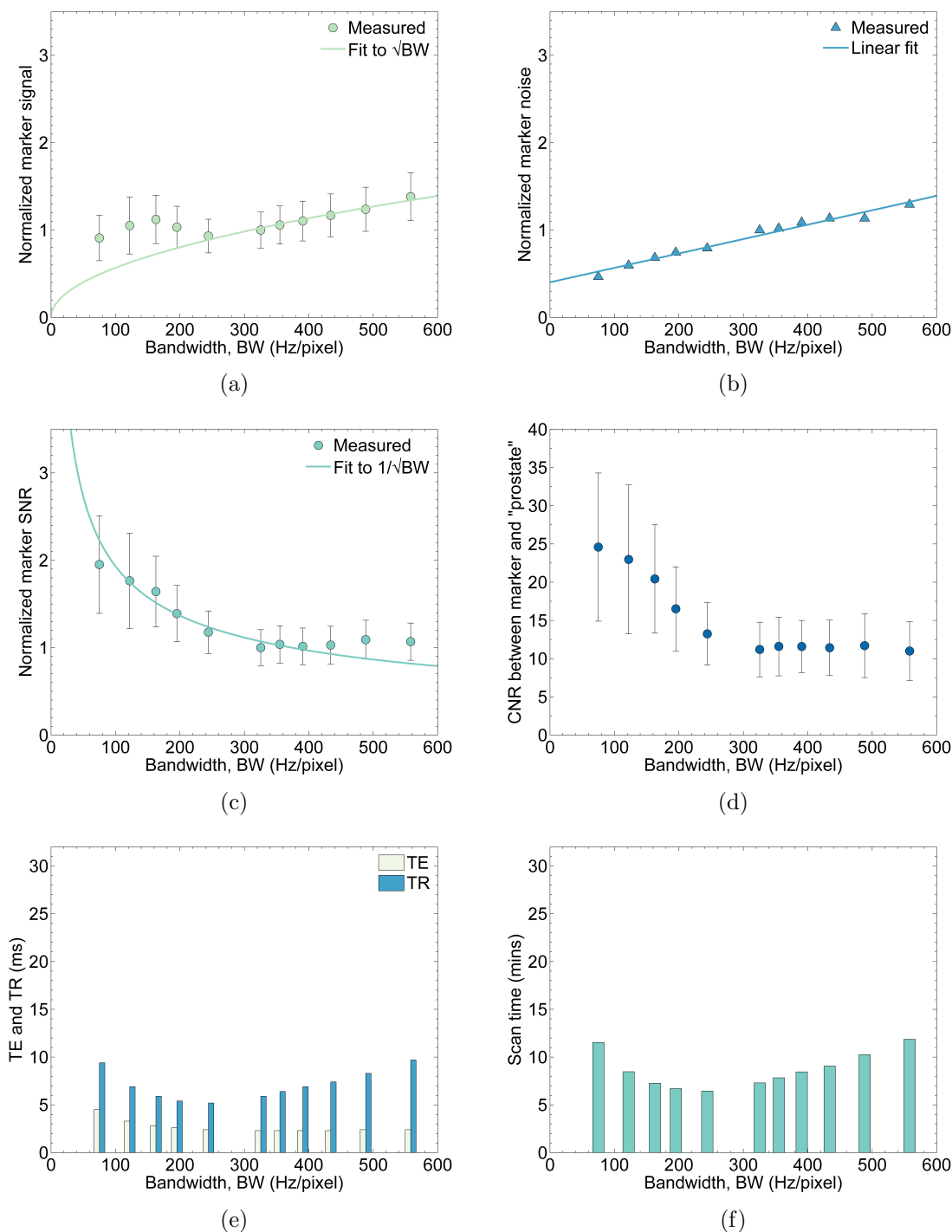


Figure 4.9: The effect of varying bandwidth on: (a) normalized Sirius MRI marker signal, (b) normalized image noise, (c) normalized Sirius MRI marker signal-to-noise ratio (SNR), (d) contrast-to-noise ratio (CNR) between the Sirius MRI marker and the prostate in phantom, (e) echo time TE and repetition time TR, (e) scan times. Adapted from T. Y. Lim, R. J. Kudchadker, J. Wang, R. J. Stafford, C. J. MacLellan, A. Rao, G. Ibbott, and S. J. Frank. "Effect of pulse sequence parameter selection on signal strength in positive-contrast MRI markers for MRI-based prostate post-implant assessment". In: *Med Phys* 43.7 (2016)⁹⁶ (with permission from the American Association of Physicists in Medicine).

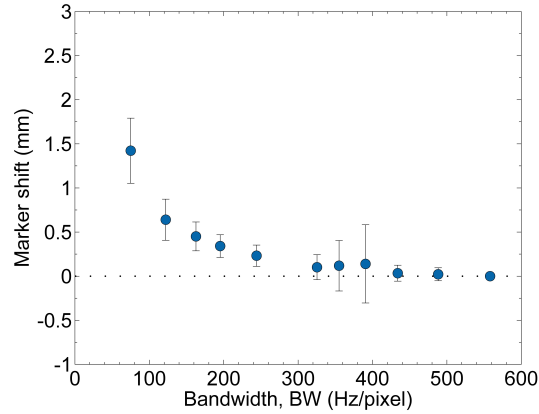


Figure 4.10: Shift artifact. At narrower bandwidths, the marker shift in the frequency-encoding direction due to the chemical shift artifact is greater. Reprinted from T. Y. Lim, R. J. Kudchadker, J. Wang, R. J. Stafford, C. J. MacLellan, A. Rao, G. Ibbott, and S. J. Frank. “Effect of pulse sequence parameter selection on signal strength in positive-contrast MRI markers for MRI-based prostate post-implant assessment”. In: *Med Phys* 43.7 (2016)⁹⁶ (with permission from the American Association of Physicists in Medicine).

$122.07 \text{ Hz/pixel} \leq \text{BW} \leq 433.98 \text{ Hz/pixel}$ (Figure 4.9f).

Artifacts At very narrow BW, I observed reduced seed *susceptibility artifact* and prominent shift of the Sirius MRI marker in the frequency-encoding direction, potentially due to a *chemical shift artifact*[§] (Figure 4.8 and Figure 4.10). At narrower BW, the shift artifact observed in the frequency-encoding direction was greater (Figure 4.8). For $\text{BW} \geq 122.07 \text{ Hz/pixel}$, the mean marker shifts were $< 1 \text{ mm}$; for $\text{BW} \geq 325.51 \text{ Hz/pixel}$, the mean shifts of the Sirius MRI markers were $< 0.2 \text{ mm}$ (Figure 4.10). At wider BW, Sirius MRI marker chemical shift and seed susceptibility artifacts were reduced. The impact of the Sirius MRI markers’ shift artifact on dosimetry depends on the seed localization method. The shift extent must be accounted for if the marker locations are used to extrapolate to the seed locations. On the other hand, the shift artifact would be less consequential if the markers were simply used to confirm that the negative-contrast voids adjacent to positive-contrast markers are seeds (for instance, during manual seed localization). Furthermore, although the Sirius MRI marker shift is distinct on phantom images, it may be difficult to distinguish

[§]The chemical shift artifact arises when a compound’s protons resonates at a slightly higher or lower frequency than is expected of water protons at the same location. Since spatial information on MRI images is encoded based on frequencies, the different frequency emitted by the compound’s protons result in a location offset.

the Sirius MRI marker if its signal is shifted into the prostatic stroma.

At narrower BW, there was less noise and higher SNR, while at wider BW, there was less susceptibility artifacts and chemical shift artifacts.¹⁰² For the highest SNR with scan time < 10 minutes and mean marker shift < 0.2 mm, I recommend using $BW = 325.51$ Hz/pixel (± 83.33 kHz).

4.4.4 Varying Field-of-view

At smaller FOV, the Sirius MRI marker is more distinctive (Figure 4.11). In the following, the effect of FOV on several image quality considerations for post-implant dosimetry purposes is illustrated.

Signal Smaller FOV was associated with increased signal (Figure 4.12a) due to the longer TR and partial volume artifact. As FOV decreases, the BW (the signal sampling *rate*) decreases (Equation 4.2), hence the signal sampling *time* increases, resulting in longer TR (Figure 4.12e), contributing to higher signal, but also longer scan times (Figure 4.12f).

Noise Smaller FOV was associated with increased noise (Figure 4.12b).

Signal-to-noise ratio SNR was slightly higher at smaller FOV (Figure 4.12c).

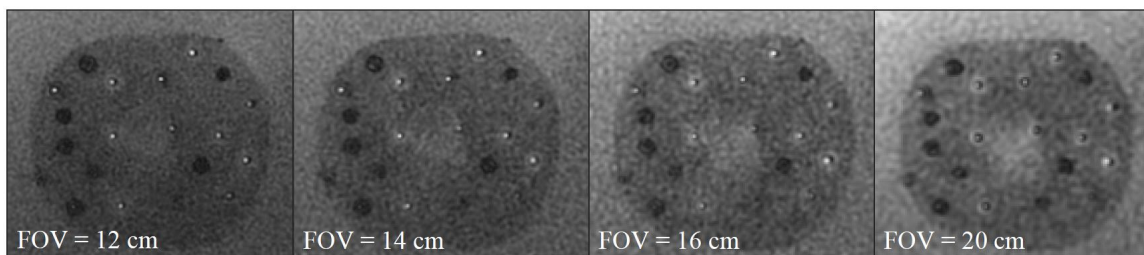


Figure 4.11: The effect of varying field of view on the visual appearance of images. Reprinted from T. Y. Lim, R. J. Kudchadker, J. Wang, R. J. Stafford, C. J. MacLellan, A. Rao, G. Ibbott, and S. J. Frank. “Effect of pulse sequence parameter selection on signal strength in positive-contrast MRI markers for MRI-based prostate post-implant assessment”. In: *Med Phys* 43.7 (2016)⁹⁶ (with permission from the American Association of Physicists in Medicine).

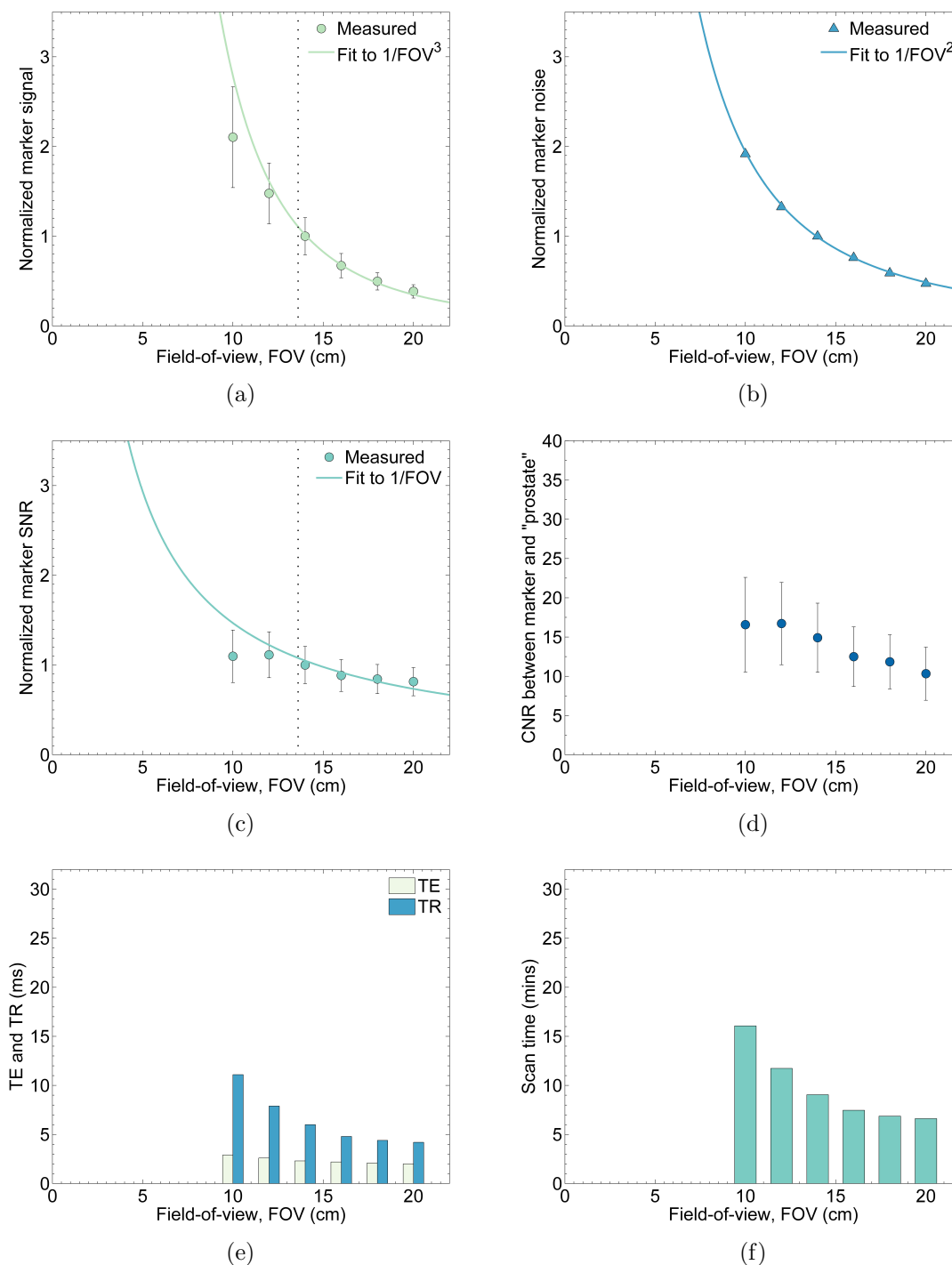


Figure 4.12: The effect of varying field-of-view on: (a) normalized Sirius MRI marker signal, (b) normalized image noise, (c) normalized Sirius MRI marker signal-to-noise ratio (SNR), (d) contrast-to-noise ratio (CNR) between the Sirius MRI marker and the prostate in phantom, (e) echo time TE and repetition time TR, (e) scan times. The dotted vertical lines denote the FOV giving the active cross-sectional area of the Sirius MRI markers; hence the acquisition pixel sizes of points to the left of the dotted line were less than the marker's active cross-sectional and were least subjected to partial volume averaging artifacts. Adapted from T. Y. Lim, R. J. Kudchadker, J. Wang, R. J. Stafford, C. J. MacLellan, A. Rao, G. Ibbott, and S. J. Frank. "Effect of pulse sequence parameter selection on signal strength in positive-contrast MRI markers for MRI-based prostate post-implant assessment". In: *Med Phys* 43.7 (2016)⁹⁶ (with permission from the American Association of Physicists in Medicine).

Contrast-to noise-ratio The trend of the CNR between Sirius MRI marker and “prostate” is similar to the trend of SNR for Sirius MRI markers because the signal of the Sirius MRI marker is much greater than the signal of the “prostate” (Figure 4.9d).

Timing At smaller FOV, the TR and scan times are longer (Figure 4.12f).

Resolution At smaller FOV, in-plane resolution was better and the markers were more conspicuous (Figure 4.13).

Artifacts The use of a small FOV corresponded to small voxel sizes. Theoretically, smaller voxel sizes have less spins in the voxel resulting in lower signal. However, I observed higher signal (Figure 4.12a) and SNR (Figure 4.12c) at smaller FOV. This is most likely due to the small size of the markers causing the *partial volume averaging artifact* to dominate, whereby higher resolution images allow partial volume objects that are smaller than the voxel size to be visible¹⁰² (see Figure 4.13 for the resolution at varying FOV.) Smaller voxels were more likely to contain signal from the marker only, resulting in higher signal; larger voxels succumbed to the partial volume averaging artifact whereby marker and non-marker signals were averaged out, resulting in lower signal (Figure 4.12a) and lower visibility of the marker (Figure 4.11). The acquisition pixel sizes using FOV = 10 cm and FOV = 12 cm were less than the marker’s active cross-sectional area (left of dotted line in Figure 4.12a), and thus may be least subjected to the partial volume artifact. Smaller FOV resulted in less partial volume artifact, but was more susceptible to the aliasing/wraparound artifact observed in the phase-encoding direction (Figure 4.14). Phase-oversampling only oversamples one-half of the FOV at each end in the phase-encoding direction, hence signals outside these limits may still wrap into the FOV. To prevent the wrap artifact, larger FOV could be used. However, if a smaller FOV is desired, the use of an endorectal coil may render the wrap artifact less prominent by conforming signal reception in a smaller area.

At smaller FOV, the scan time is longer and the wrap artifact is more prominent; at larger FOV, the partial volume averaging artifact may impair accurate marker localization. For scan times < 10 min, I recommend a mid-range FOV of 14 cm to 16 cm.

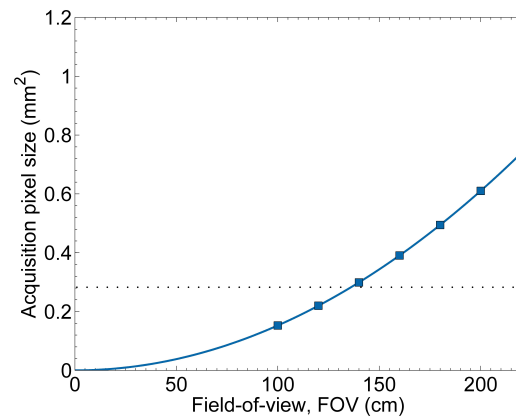


Figure 4.13: The effect of varying field-of-view on acquisition pixel size. The smaller the pixel size, the greater the image spatial resolution. The dotted horizontal line denotes the markers active cross-sectional area; hence points above the dotted line are subjected to partial volume artifacts.

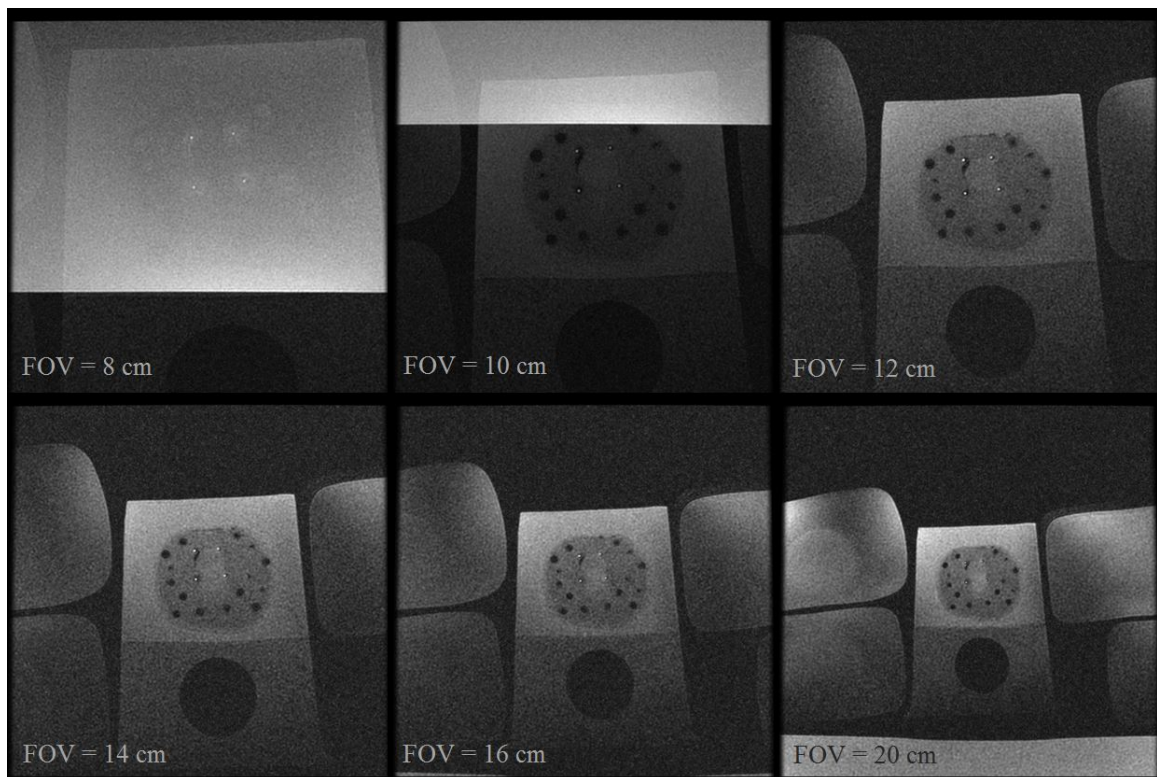


Figure 4.14: Images acquired at varying field-of-view (FOV) values and the associated wrap artifact in the phase-encoding direction. Note that the wrap artifact is more severe at smaller FOVs. The image set acquired with FOV = 8 cm were excluded from SNR measurements because of the severe wrap artifact.

4.4.5 Varying Slice Thickness

The images appeared noisier at thinner Δz but the Sirius MRI markers cannot be reliably localized at thicker Δz (Figure 4.15). In the following, the effect of Δz on several image quality considerations for post-implant dosimetry purposes is illustrated.

Signal Using smaller Δz , the signal was higher (Figure 4.16a).

Noise The noise was higher at smaller Δz (Figure 4.16b).

Signal-to-noise ratio Therefore, over varying effective $\Delta z \leq 1.5$ mm (reconstructed marker's active length), there was no significant change in SNR (slope = -0.0376, $p = 0.2707$) (Figure 4.16c).

Contrast-to noise-ratio The trend of the CNR between Sirius MRI marker and “prostate” is similar to the trend of SNR for Sirius MRI markers because the signal of the Sirius MRI marker is much greater than the signal of the “prostate” (Figure 4.16d).

Timing Using thin slices did not affect TE and TR, but to cover the same volume, more slices and longer scan times were needed (Figure 4.16f).

Resolution At smaller Δz , the through-plane resolution is better and the ends of the Sirius MRI maker can be better visualized (Figure 4.15).

Artifacts At larger Δz , the *partial volume averaging artifact* was more severe (Figure 4.15 and 4.18). Images with effective $\Delta z = 1.5$ mm were interpolated from images acquired with input $\Delta z = 3.0$ mm, which is the filled length of the marker. This may be why there was no significant change in the SNR for varying effective $\Delta z \leq 1.5$ mm (Figure 4.16c), but the SNR for effective $\Delta z > 1.5$ mm were statistically significantly lower due to the partial volume averaging artifact. At smaller Δz , the same marker could be seen traversing across more slices and appeared brighter because the voxels with marker contain mostly signal from the marker. At very thin Δz (effective $\Delta z < 0.7$ mm), the through-plane resolution was improved, but much longer scan time was required to cover the same volume (Figure 4.16f)

and miniscule bubbles in the marker may cause a *disjointed artifact* that can potentially confound accurate marker localization. Conversely, very thick Δz resulted in the inability to discern marker versus seed due to low through-plane resolution. Extreme partial volume averaging artifact was observed for effective $\Delta z > 2.5$ mm, hence I did not report on the signal, noise, or SNR of the marker on those images. In fact, on most slices of the scan acquired with $\Delta z = 5.0$ mm, all the needle tracks contained a hyperintense signal (Figure 4.18). This is because each needle track contained a seed-marker strand, where the marker signal overwhelmed the voxels. Figure 4.17 illustrates the marker appearance across axial slices for varying Δz [¶].

To minimize the disjointed artifact, partial volume averaging artifact and for scan time < 10 minutes, I recommend effective Δz of 0.7 mm to 1.5 mm. Adequately thin image slices may allow us to obtain the orientation of the marker. Orientation information from the marker can be coupled with the seed's dumbbell artifact to estimate the seed's orientation, such that treatment planning systems may incorporate seed anisotropy calculations to generate more accurate dose distributions.

4.4.6 Varying Encoding Steps

At lower $N_x \times N_y$, the Sirius MRI markers cannot be reliably localized (Figure 4.19). In the following, the effect of $N_x \times N_y$ on several image quality considerations for post-implant dosimetry purposes is illustrated.

Signal Theoretically, larger voxel sizes are associated with higher SNR, but in the measurements I observed higher SNR using smaller voxel sizes, most likely owing to dominance

[¶]Looking down the column of effective $\Delta z = 1.0$ mm, the topmost slice showed the hypointense seed void, followed by slices with the hyperintense markers, ending with the bottommost slice showing the beginning of the hypointense void of the next seed. However, if the marker was not perfectly filled with the contrast agent, using very small Δz would result in a disjointed artifact. On the other hand, looking down the column of effective $\Delta z = 0.5$ mm, in the middle of the marker there was no hyperintense signal characteristic of the marker, most likely owing to the presence of a tiny air bubble. For effective $\Delta z > 0.5$ mm, the partial volume averaging artifact helped reduce the appearance of the bubble, at the expense of lowered signal since the voxel contained air as well. Hence, at very small Δz , the through-plane resolution was improved, but miniscule bubbles in the marker may cause a disjointed artifact. Last but not least, looking down the column of effective $\Delta z = 5.0$ mm, the hyperintense signal in the middle of the needle track could be seen on both slices.

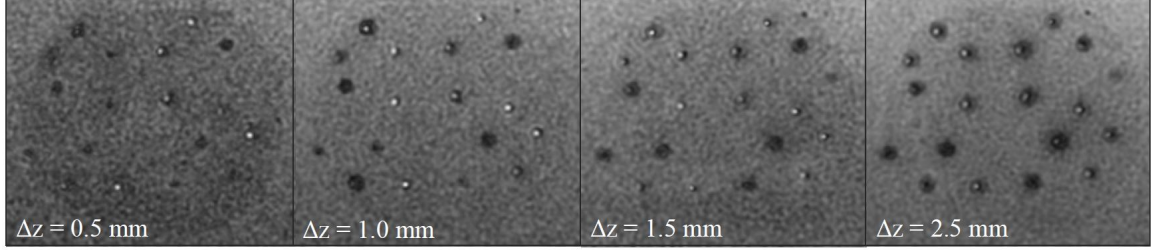


Figure 4.15: The effect of varying slice thickness on the visual appearance of images. Reprinted from T. Y. Lim, R. J. Kudchadker, J. Wang, R. J. Stafford, C. J. MacLellan, A. Rao, G. Ibbott, and S. J. Frank. “Effect of pulse sequence parameter selection on signal strength in positive-contrast MRI markers for MRI-based prostate post-implant assessment”. In: *Med Phys* 43.7 (2016)⁹⁶ (with permission from the American Association of Physicists in Medicine).

of the partial volume averaging artifact. (See Figures 4.21 for the acquisition pixel sizes in relation to the marker’s active cross-sectional area.)

Noise At higher $N_x \times N_y$, the signal was higher (Figure 4.20a), but the noise was also higher (Figure 4.20b).

Signal-to-noise ratio The SNR increased with $N_x \times N_y$, but leveled off beyond 320×320 , where the acquisition pixel size is smaller than the marker’s active cross-section, which is associated with minimal partial volume averaging artifacts (Figure 4.20c). For images acquired with encoding steps $\geq 320 \times 320$, there was no statistically significant difference in SNR (Figure 4.20c).

Contrast-to noise-ratio The trend of the CNR between Sirius MRI marker and “prostate” is similar to the trend of SNR for Sirius MRI markers because the signal of the Sirius MRI marker is much greater than the signal of the “prostate” (Figure 4.20d).

Timing With higher $N_x \times N_y$, scan time was longer (Figure 4.20f). The zero filling process^{||} can be used to reduce scanning time without too much SNR loss. Higher $N_x \times N_y$ required longer TR, and scan time increased proportionally (Figure 4.20f).

^{||}Zero filling was used to allow for lower acquisition resolution but increased apparent displayed resolution. Since extra zeroes contain no signal or noise, zero filling should not affect SNR.

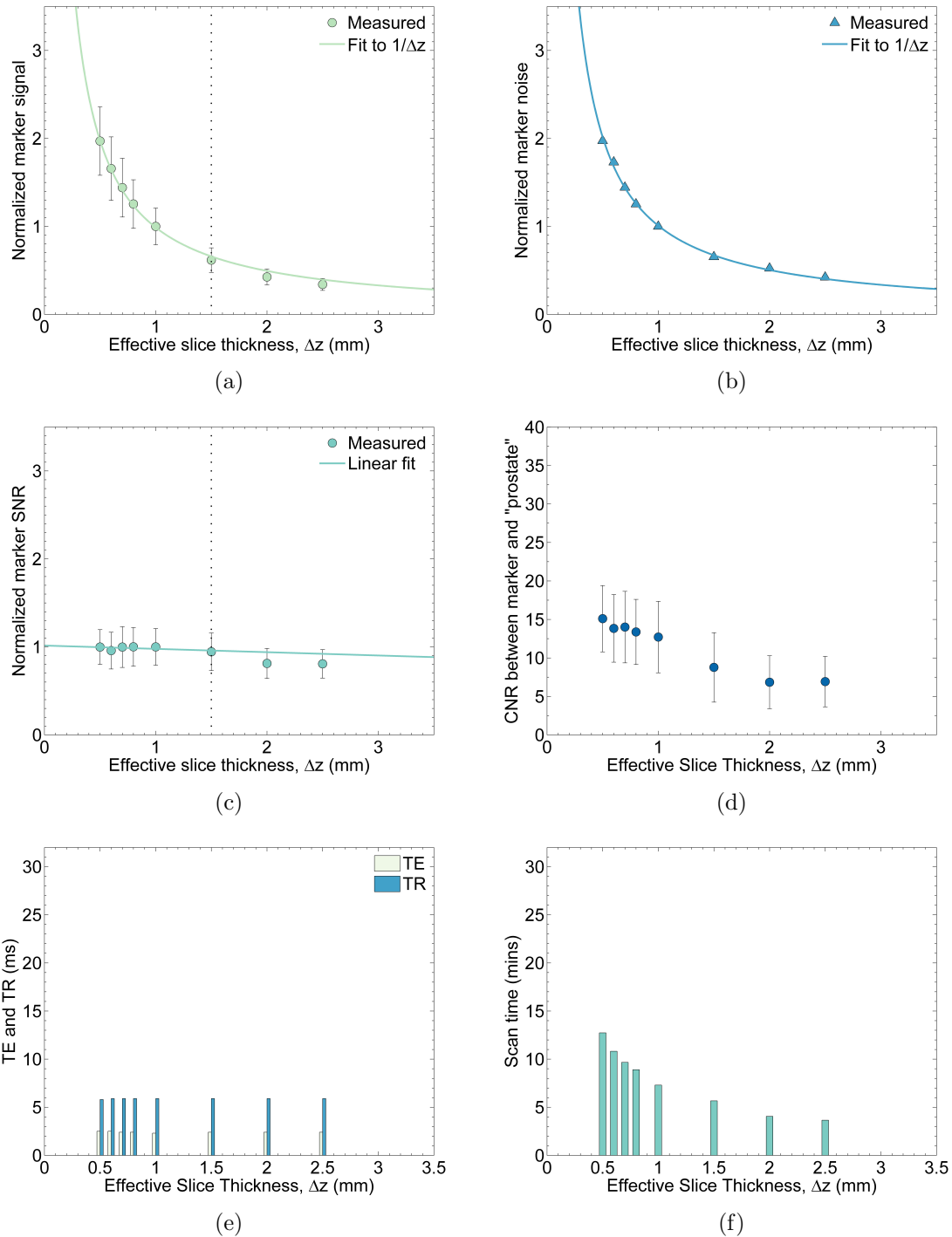


Figure 4.16: The effect of varying slice thickness on: (a) normalized Sirius MRI marker signal, (b) normalized image noise, (c) normalized Sirius MRI marker signal-to-noise ratio (SNR), (d) contrast-to-noise ratio (CNR) between the Sirius MRI marker and the prostate in phantom, (e) echo time TE and repetition time TR, (e) scan times. The dotted vertical lines denotes the markers reconstructed active length; hence the points to the right of the line are subjected to more partial volume averaging artifacts. Adapted from T. Y. Lim, R. J. Kudchadker, J. Wang, R. J. Stafford, C. J. MacLellan, A. Rao, G. Ibbott, and S. J. Frank. "Effect of pulse sequence parameter selection on signal strength in positive-contrast MRI markers for MRI-based prostate post-implant assessment". In: *Med Phys* 43.7 (2016)⁹⁶ (with permission from the American Association of Physicists in Medicine).

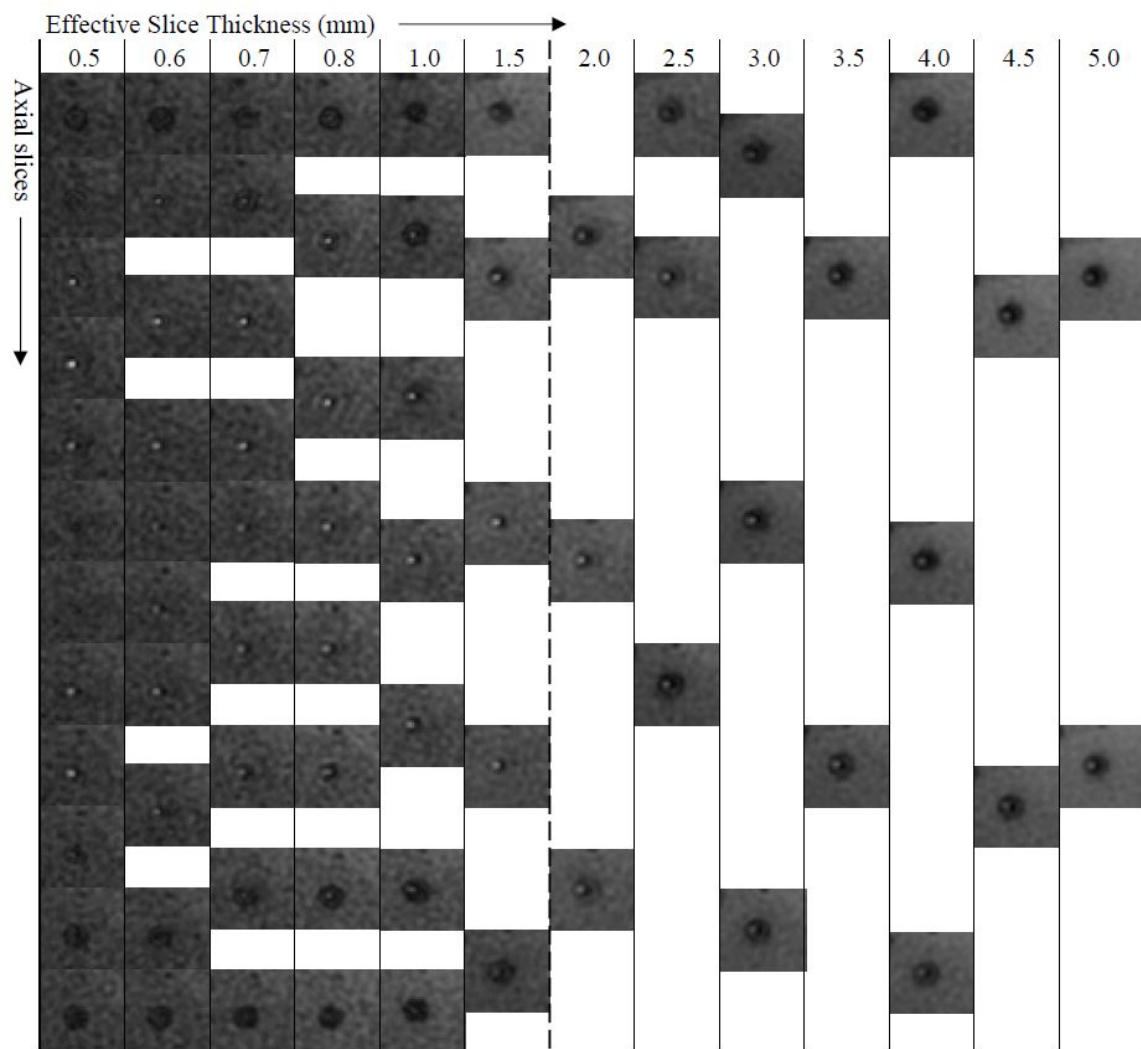


Figure 4.17: The appearance of a single marker across consecutive axial slices (vertical) for images acquired with varying slice thicknesses, Δz (horizontal). The displayed images are arranged as axially-linked to the axial slices of the first column, that is, scrolling through the 12 axial slice images shown in the column of effective $\Delta z = 0.5$ mm is equivalent in location to scrolling through the 3 axial slice images of the column of effective $\Delta z = 2.0$ mm. The dotted vertical line denotes the markers reconstructed active length.

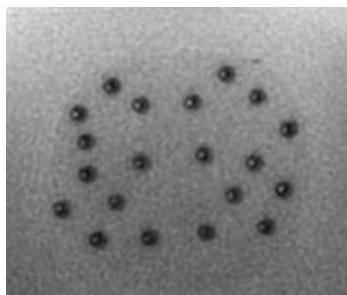


Figure 4.18: On most slices of the scan acquired with $\Delta z = 5.0$ mm, all the needle tracks contained a hyperintense signal.

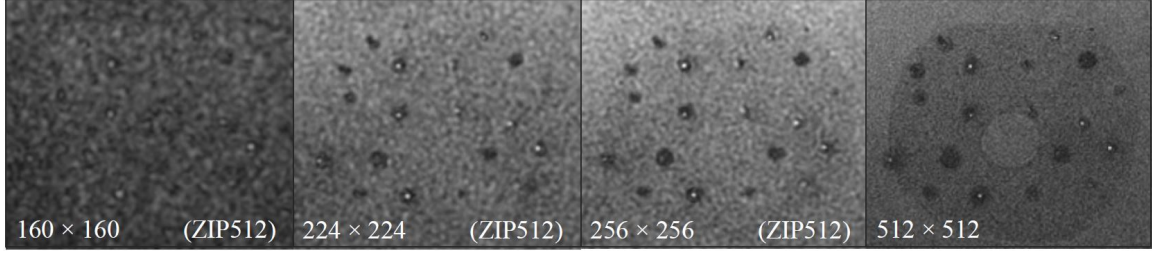


Figure 4.19: The effect of varying encoding steps on the visual appearance of images. Reprinted from T. Y. Lim, R. J. Kudchadker, J. Wang, R. J. Stafford, C. J. MacLellan, A. Rao, G. Ibbott, and S. J. Frank. “Effect of pulse sequence parameter selection on signal strength in positive-contrast MRI markers for MRI-based prostate post-implant assessment”. In: *Med Phys* 43.7 (2016)⁹⁶ (with permission from the American Association of Physicists in Medicine).

Resolution The in-plane resolution is better with higher $N_x \times N_y$ (Figure 4.21).

Artifacts At lower $N_x \times N_y$, the *partial volume averaging artifact* was more prominent as a single voxel was more likely to contain signals from disparate objects, such as the Sirius MRI marker, needle track and “prostate”.

For the highest in-plane resolution with scan time < 10 minutes, I recommend a square 256×256 acquisition matrix (interpolated to 512×512). To examine the effect of varying $N_x \times N_y$ on signal, noise and SNR, I examined the effects of varying N_x and N_y separately.

4.4.6.1 Varying Frequency Encoding Steps

Increasing N_x increased the signal (Figure 4.23a), but the noise increased as well (Figure 4.23b). SNR increased with increasing N_x , but leveled off beyond 320×320 , where the acquisition pixel size was smaller than the marker’s active cross-section and the partial volume artifact was minimal (Figure 4.23c). The trends of signal, noise and SNR were inferred from examining the trends of varying N_y only and varying $N_x \times N_y$. Scan time increased proportionally with increasing N_x (Figure 4.23f). Since the frequency-encoding gradient is on during echo sampling, increasing the number of N_x (while keeping BW and sampling interval constant) increases the sampling time, thereby increasing TE, TR and scan time (Figure 4.23f). The markers were still visible at low N_x , but image resolution was poor (Figure 4.22). Although scan time can be shortened by lowering N_x (Figure 4.23f),

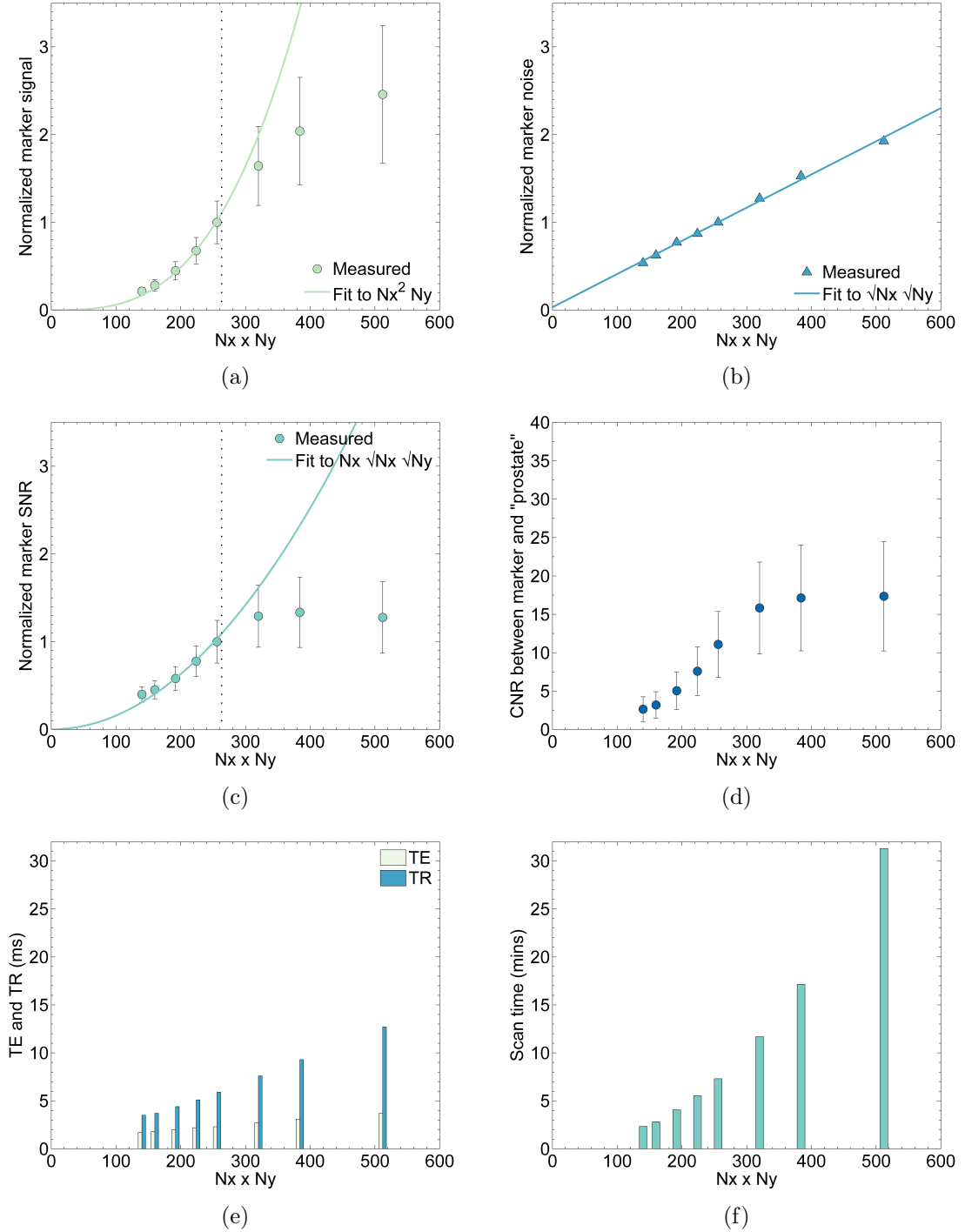


Figure 4.20: The effect of varying encoding steps on: (a) normalized Sirius MRI marker signal, (b) normalized image noise, (c) normalized Sirius MRI marker signal-to-noise ratio (SNR), (d) contrast-to-noise ratio (CNR) between the Sirius MRI marker and the prostate in phantom, (e) echo time TE and repetition time TR, (e) scan times. The dotted vertical line denotes the encoding steps resulting in an acquisition pixel size corresponding to the active cross-sectional area of the Sirius MRI markers; hence points to the left of the line are subjected to partial volume averaging artifacts. Adapted from T. Y. Lim, R. J. Kudchadker, J. Wang, R. J. Stafford, C. J. MacLellan, A. Rao, G. Ibbott, and S. J. Frank. "Effect of pulse sequence parameter selection on signal strength in positive-contrast MRI markers for MRI-based prostate post-implant assessment". In: *Med Phys* 43.7 (2016)⁹⁶ (with permission from the American Association of Physicists in Medicine).

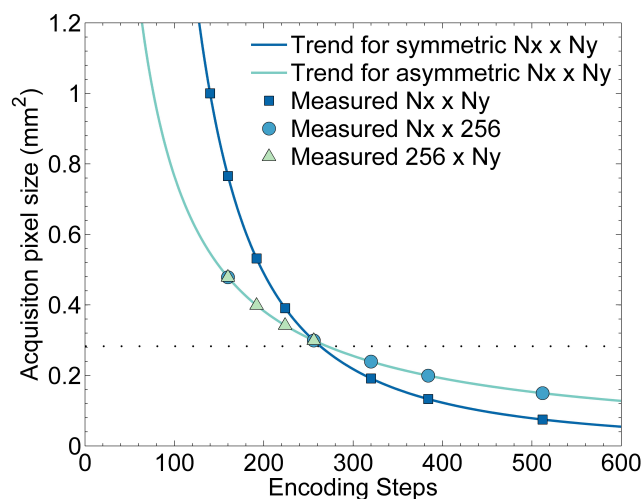


Figure 4.21: The effect of varying encoding steps on acquisition pixel size. The smaller the pixel size, the greater the image spatial resolution. The dotted horizontal line denotes the active cross-sectional area of the Sirius MRI markers; hence points above the dotted line are subjected to partial volume averaging artifacts.

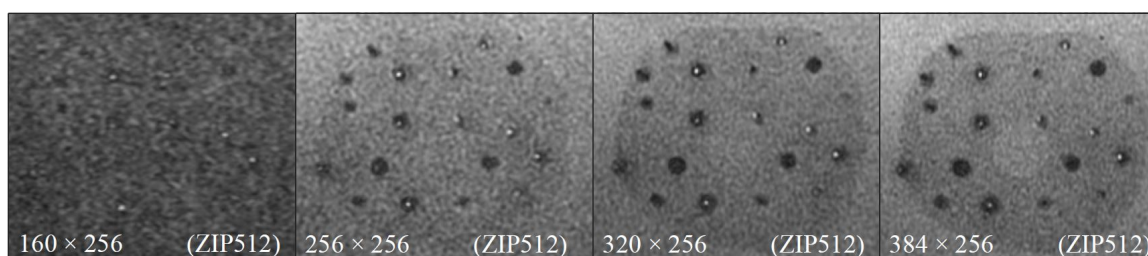


Figure 4.22: The effect of varying frequency encoding steps on the visual appearance of images. Reprinted from T. Y. Lim, R. J. Kudchadker, J. Wang, R. J. Stafford, C. J. MacLellan, A. Rao, G. Ibbott, and S. J. Frank. “Effect of pulse sequence parameter selection on signal strength in positive-contrast MRI markers for MRI-based prostate post-implant assessment”. In: *Med Phys* 43.7 (2016)⁹⁶ (with permission from the American Association of Physicists in Medicine).

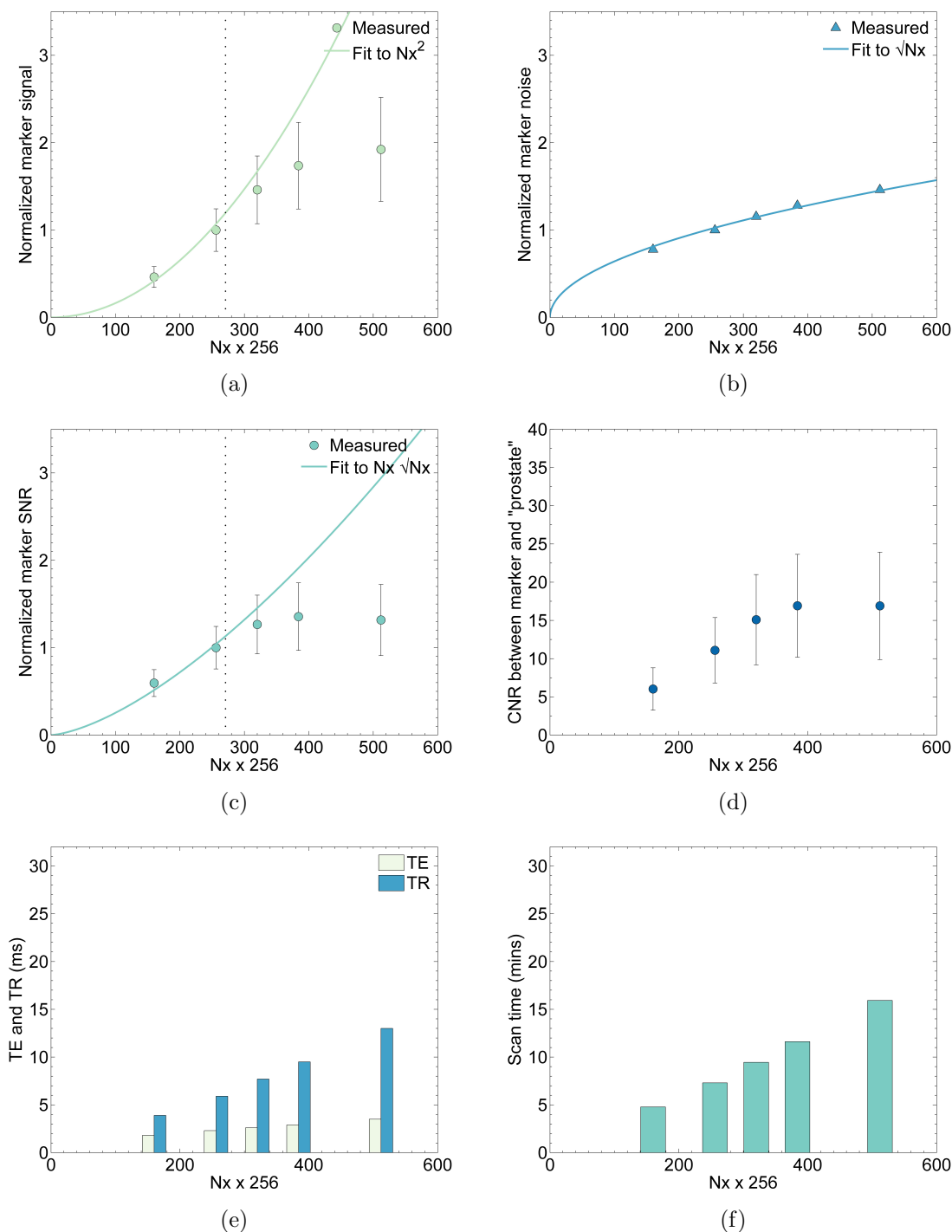


Figure 4.23: The effect of varying frequency encoding steps on: (a) normalized Sirius MRI marker signal, (b) normalized image noise, (c) normalized Sirius MRI marker signal-to-noise ratio (SNR), (d) contrast-to-noise ratio (CNR) between the Sirius MRI marker and the prostate in phantom, (e) echo time TE and repetition time TR, (e) scan times. The dotted vertical line denotes the encoding steps resulting in an acquisition pixel size corresponding to the active cross-sectional area of the Sirius MRI markers; hence points to the left of the line are subjected to partial volume averaging artifacts. Adapted from T. Y. Lim, R. J. Kudchadker, J. Wang, R. J. Stafford, C. J. MacLellan, A. Rao, G. Ibbott, and S. J. Frank. "Effect of pulse sequence parameter selection on signal strength in positive-contrast MRI markers for MRI-based prostate post-implant assessment". In: *Med Phys* 43.7 (2016)⁹⁶ (with permission from the American Association of Physicists in Medicine).

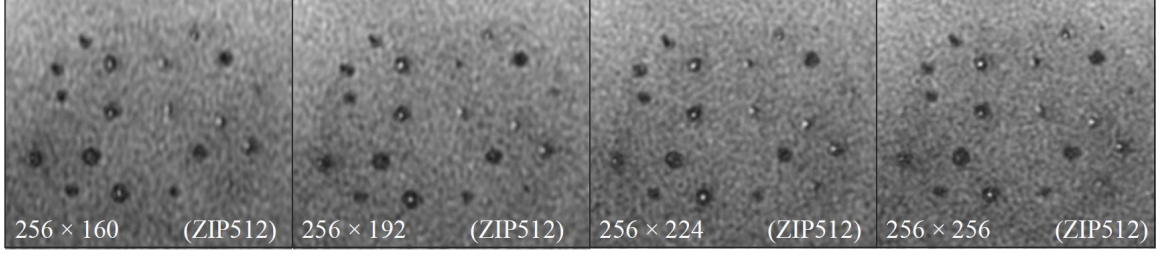


Figure 4.24: The effect of varying phase encoding steps on the visual appearance of images. Reprinted from T. Y. Lim, R. J. Kudchadker, J. Wang, R. J. Stafford, C. J. MacLellan, A. Rao, G. Ibbott, and S. J. Frank. “Effect of pulse sequence parameter selection on signal strength in positive-contrast MRI markers for MRI-based prostate post-implant assessment”. In: *Med Phys* 43.7 (2016)⁹⁶ (with permission from the American Association of Physicists in Medicine).

SNR (Figure 8b) and in-plane resolution (Figure 4.22) would be reduced due to partial volume averaging effects.

4.4.6.2 Varying Phase Encoding Steps

Increasing N_y increased the signal proportionally (Figure 4.25a) and increased the noise by $\sqrt{N_y}$ (Figure 4.25b), resulting in a net $\sqrt{N_y}$ increase in SNR (Figure 4.25c), at the expense of proportional increase in scan time (Figure 4.25f). Theoretically,¹⁰⁰ increasing N_y decreases the voxel size thus decreasing the SNR by $1/\sqrt{N_y}$. However, from the measurements, increasing N_y resulted in an increase in SNR by $\sqrt{N_y}$ (Figure 4.25c). I postulate that the trends in signal, noise and SNR observed for varying N_y were heavily determined by the partial volume averaging artifact, whereby smaller voxel sizes contain a greater percentage of marker signals. For the measurements of varying N_y , all the acquisition pixel sizes were greater than the marker’s active cross-sectional area; hence all these measurements were subjected to partial volume averaging artifacts. The 256×256 acquisition matrix yielded acquisition pixel size similar to the marker’s active cross-sectional area. The in-plane resolution at high N_y was better (Figure 4.24). Reducing N_y is a common technique to reduce scan time (Figure 4.25f). Although lower N_y shortened scan time (Figure 4.25f), SNR (Figure 4.25c) and in-plane resolution (Figure 4.24) were reduced due to partial volume averaging artifacts.

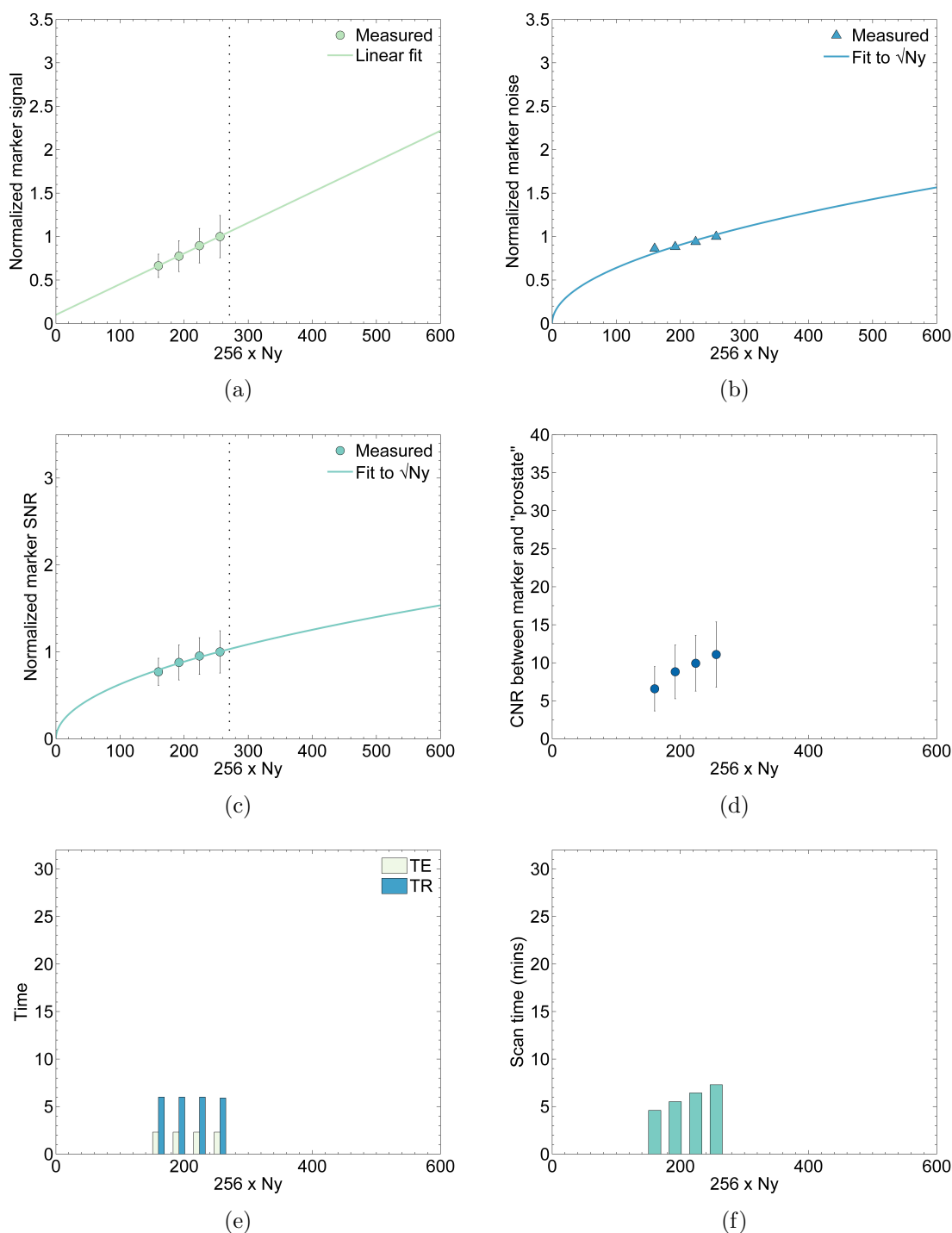


Figure 4.25: The effect of varying phase encoding steps on: (a) normalized Sirius MRI marker signal, (b) normalized image noise, (c) normalized Sirius MRI marker signal-to-noise ratio (SNR), (d) contrast-to-noise ratio (CNR) between the Sirius MRI marker and the prostate in phantom, (e) echo time TE and repetition time TR, (e) scan times. The dotted vertical line denotes the encoding steps resulting in an acquisition pixel size corresponding to the active cross-sectional area of the Sirius MRI markers; hence points to the left of the line are subjected to partial volume averaging artifacts. Adapted from T. Y. Lim, R. J. Kudchadker, J. Wang, R. J. Stafford, C. J. MacLellan, A. Rao, G. Ibbott, and S. J. Frank. "Effect of pulse sequence parameter selection on signal strength in positive-contrast MRI markers for MRI-based prostate post-implant assessment". In: *Med Phys* 43.7 (2016)⁹⁶ (with permission from the American Association of Physicists in Medicine).

Table 4.2: Recommended scan parameters for high visualization of MRI markers, accounting for scan time, in-plane and through-plane resolution, and artifacts. Reprinted from T. Y. Lim, R. J. Kudchadker, J. Wang, R. J. Stafford, C. J. MacLellan, A. Rao, G. Ibbott, and S. J. Frank. “Effect of pulse sequence parameter selection on signal strength in positive-contrast MRI markers for MRI-based prostate post-implant assessment”. In: *Med Phys* 43.7 (2016)⁹⁶ (with permission from the American Association of Physicists in Medicine).

Scan Parameters	Values
α	12° to 20°
NEX	2 to 10 (halved due to phase oversampling)
BW	± 83.33 kHz
FOV	14 cm to 16 cm
Δz	1.4 mm to 3.0 mm (interpolated to 0.7 mm to 1.5 mm)
$N_x \times N_y$	256×256 (interpolated to 512×512)

4.5 Conclusion

4.5.1 Summary

In this study, the impact of varying scan parameters on marker visualization were presented, and the scan parameters that led to best marker visualization were defined. From the range of investigated values, the highest MRI marker SNR were independently given by $\alpha = 12^\circ$, NEX = 25 (scan time = 22.9 minutes), BW = ± 19.23 kHz (shift = 1.42 ± 0.37 mm), FOV = 12 cm and 384×384 . However, the scan parameters that provided the highest MRI marker SNR may not be the best choice from a practical standpoint. Taking into consideration SNR, scan time, resolution and artifacts, the recommended scan parameters based on this phantom study are listed in Table 4.2. This phantom study provides a practical understanding on the impact of pulse sequence parameter adjustments on marker visibility, image quality, and scan time, thus allowing for a more directed effort to be made for marker evaluation in patients.

4.5.2 Limitations

The main limitation of this study is that not every possible combination of all the scan parameters was covered because it would be extremely laborious to acquire images and

perform analysis for all possible scan parameter combinations**. Nevertheless, I presented all signal, noise and SNR values normalized to that acquired using baseline scan parameters (bold font in Table 4.1), so that different plots can be studied together to estimate gains/losses in signal, noise, and SNR for the desired combination of scan parameters. However, this estimation needs to account for the interactions between the pulse sequence parameters.

Another limitation of the study is that the metric used was signal instead of contrast, because this study is a phantom study, but contrast is dependent on the prostate and other tissues in the imaging volume. Measuring true contrast between marker and prostate is problematic due to inter-patient variation, intra-patient variation, scan time, and ethical considerations. Inter-patient variation owing to differences in prostate T_1 and T_2 from patient to patient compels all measurements to be done in a single patient to be able to isolate the effect of scan parameter variation from inter-patient variation. However, there is also intra-patient variation, because different prostate zones exhibit different contrast and the presence of edema enhances regions within the prostate, resulting in the contrast measurements being affected by the marker position within the prostate. Statistics aside, looking at only a single marker in a specified location within the prostate for a single patient, the total continuous scan time of more than 11 hours would raise patient discomfort, motion, and tissue heating concerns. The systematic evaluation of the effects on MRI marker signal for 70 different scan parameter combinations in this phantom study guided the next chapter's in-vivo studies of the MRI marker visibility.

The scan parameter values affect the actual TE and TR used on the GE scanner used for this study. For instance, when changing only the BW at the scanner console in normal scanning mode, any change in signal was not due solely to the change of BW because the TE and TR changed as well (Figure 4.9f), thus confounding direct prediction of signal behavior from equations and necessitating actual measurement of the signal, as was done in this study. On other scanner manufacturer platforms, the TE and TR may be better controlled even in clinical mode.

Moreover, the phantom images of the Sirius MRI markers were acquired at room

**From just the discrete number of values for each of the 6 scan parameters studied, there are $12 \times 13 \times 11 \times 7 \times 13 \times 15 = 2342340$ possible combinations.

temperature, but the indication for the Sirius MRI markers is for implantation into the human body. However, since at body temperature the T_2 is longer, I expect that the Sirius MRI marker signal would be higher in patient studies compared to this phantom study.

4.5.3 Implications

I have evaluated the effects of α , NEX, BW, FOV, Δz and $N_x \times N_y$ on Sirius MRI marker SNR, scan time, resolution and artifacts in a prostate brachytherapy phantom on a GE 3.0 T scanner. The findings of this study may be used to guide MRI protocol development for high marker visibility to obtain useful post-implant dosimetry images in patients. In the next chapter, I investigate the visibility of Sirius MRI markers on patient images generated from various pulse sequences, specifically the 3D FSPGR sequence.

This chapter is adapted from T. Y. Lim, R. J. Kudchadker, J. Wang, T. Bathala, J. Szklaruk, T. J. Pugh, U. Mahmood, G. S. Ibbott, and S. J. Frank. “Development of an MRI protocol to visualize encapsulated contrast agent markers in prostate brachytherapy recipients: Initial patient experience”. In: J Contemp Brachytherapy 8.3 (2016)¹⁰³ (licensed under Creative Commons Attribution-NonCommercial-ShareAlike 4.0 International License).

5

MRI Protocol Development in Patients for Post-implant Dosimetry

Contents

5.1	Background	103
5.1.1	CT-only post-implant dosimetry	103
5.1.2	CT-MRI Fusion-based Post-implant Dosimetry	105
5.1.3	MRI-only Post-implant Dosimetry	108
5.1.4	Alternatives Solutions (instead of using Sirius MRI Markers) towards MRI-only Post-implant Dosimetry	110
5.2	Purpose	111
5.3	Methods	112
5.3.1	Sirius MRI Markers in the Prostate Implant Workflow	112
5.3.2	Post-implant MRI Protocol	113
5.4	Results and Discussion	115
5.4.1	Visualization of Seeds and Sirius MRI Markers	115
5.4.2	Clinical Challenges	118
5.5	Conclusion	123
5.5.1	Summary	123
5.5.2	Limitations	124
5.5.3	Current status	125
5.5.4	Implications	126

5.1 Background

Post-implant quality assessment is important to ensure that the radiation dose distribution from the brachytherapy seeds adequately covers the prostate and is acceptable in nearby critical structures. Implant quality can be represented by DVH parameters, which correlate with biochemical control.^{30,35} For the calculation of DVH parameters, 2 vital pieces of information are needed: dose information from the seed locations, and volume information using the boundaries of the prostate and surrounding critical structures. Seed localization and anatomical delineation are dependent on the post-implant imaging modality.

5.1.1 CT-only post-implant dosimetry

5.1.1.1 Advantages

Consistent seed localization The main advantage of CT-only post-implant dosimetry is consistent seed localization due to the high visibility of the seeds.^{27,49,71} In a CT- and MRI-compatible-phantom study, De Brabandere et al.⁴⁹ found smaller mean seed localization errors on CT images (0.9 ± 0.6 mm) compared to MRI images acquired using FSE sequences on Philips (2.1 ± 1.4 mm) and Siemens 1.5 T (2.3 ± 0.8 mm). In a subsequent patient study, De Brabandere et al.²⁷ reported the impact of seed localization variability on the standard deviation of D90 to be 2% for CT-based seed localization, compared to 7% for MRI-based seed localization. In a separate study, De Brabandere et al.⁷¹ further reported D90 variability of 1.5% using CT compared to 6.6% using MRI-based seed localization.

Time savings CT scans generally takes less time compared to MRI scans, because the weak MRI signal can be hidden by electronic noise, requiring repetition for each projection.¹⁰⁴ A non-contrast CT scan takes approximately 5 to 10 minutes, while a non-contrast MRI scan takes approximately 30 minutes.

Cost savings The cost for a CT scan is usually less than the cost for an MRI scan. According to the Healthcare Blue Book,¹⁰⁵ a pelvic CT costs \$634 while a pelvic MRI costs \$1209.

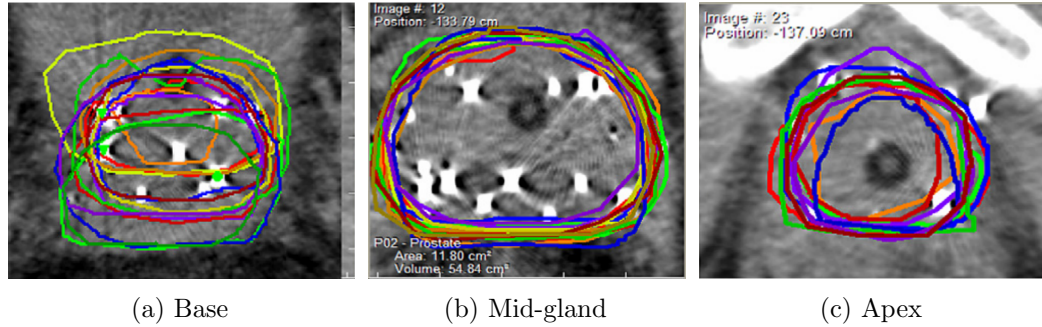


Figure 5.1: Superimposed contours on CT images generated by 15 physicians experienced in brachytherapy and prostate contouring during a workshop aimed at examining prostate contouring variability. Reprinted from J. Crook, N. Patil, C. Ma, M. McLean, and J. Borg. “Magnetic resonance imaging-defined treatment margins in iodine-125 prostate brachytherapy”. In: *Int J Radiat Oncol Biol Phys* 77.4 (2010), pp. 1079–84³¹ (license number: 3876100661790).

5.1.1.2 Disadvantages

Poor soft tissue contrast The main disadvantage of using CT images for post-implant dosimetry are poor soft tissue contrast and seed streak artifacts, leading to compromised anatomical contours.

Low precision of prostate contours Prostate delineation on CT is associated with low precision of prostate contours, that is, high interobserver variability.^{27,31,43,50} Figure 5.1 depicts the variability in prostate contouring by 15 experienced physicians. Crook et al.⁴³ found that contours and DVH parameters were not reproducible due to interobserver variation in prostate contouring. De Brabandere et al.²⁷ found that the standard deviation of prostate delineation by eight physicians was 23% using CT images, compared to 17% using MRI images. Dubois et al.⁴⁴ reported significant interobserver and intraobserver differences of prostate volumes derived using CT images (insignificant differences using MRI images). Han et al.²⁵ reported interobserver variability (standard deviation) in prostate volumes delineated on CT images to range from 9% to 29%, resulting in inadequate implants for 14% of the implants judged by V100 and 24% judged by D90. In a study of CT-based post-implant dosimetry at 28 Japanese institutions, Aoki et al.⁵⁰ found significant interobserver variability in prostate volume and subsequent D90.

Low accuracy of prostate contours Prostate delineation on CT is also associated with low accuracy of prostate contours, as prostate volumes can be overestimated on CT images.^{51,53,54,59} Petrik et al.⁵⁹ reported that in their study cohort of 75 patients, the mean prostate volume was 38.3cc on CT images compared to 33.3cc on MRI images. Normal tissue being incorrectly contoured as part of the prostate on CT images may delay necessary corrective therapy (implantation of additional seeds) or cause unnecessary treatment complications.

Low accuracy and precision of normal tissue contours Delineation of the critical structures near the prostate is challenging, thus limiting management of acute or late radiation effects as the radiation dose to these critical structures cannot be determined.

High variability in DVH parameter reporting Due to the variability in anatomical contours, the resultant DVH parameters have high variability,²⁷ thereby obscuring dose-response relationships.⁴³

5.1.2 CT-MRI Fusion-based Post-implant Dosimetry

5.1.2.1 Advantages

Simultaneous consistent seed localization and excellent anatomical visualization Amdur et al.¹⁰⁶ first proposed CT-MRI fusion to capitalize on seed visualization on CT images, while still benefiting from soft tissue delineation on MRI scans. On CT-MRI fusion images (Figure 5.2), seed localization is performed on the hyperintense seeds visible on CT images.

5.1.2.2 Disadvantages

Registration technique uncertainties The uncertainties during registration affects the precision and accuracy of CT-MRI fusion. Registration technique variation include differences in registration landmarks. The landmarks used to guide fusion of the CT and MRI images include the urethra,¹⁰⁶ bladder¹⁰⁶ and bones in the pelvis.⁵³ Amdur et al.¹⁰⁶ performed registration using the urethra and base of bladder, and reported average maximum differences

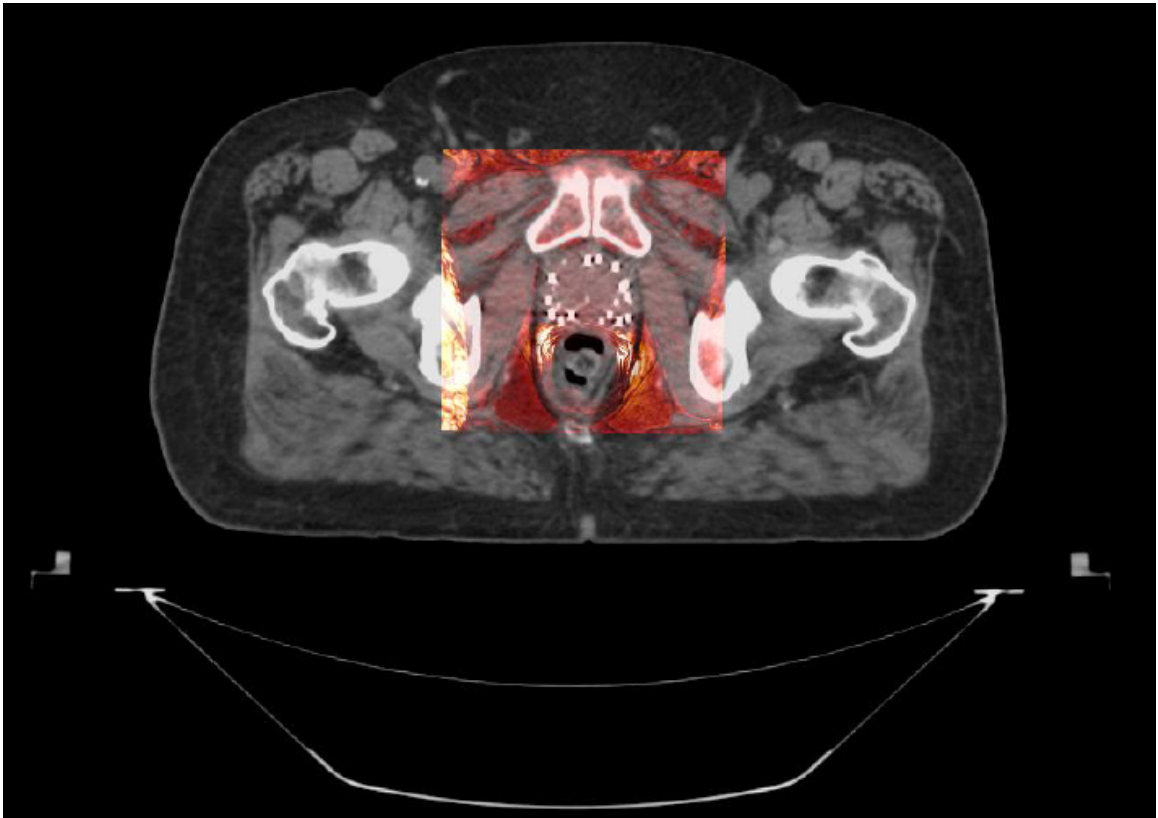


Figure 5.2: Fused MRI-CT scan of the prostate. Grayscale image, CT scan; red color-washed image, MRI scan. The MRI scan (3D FSPGR) was acquired with an endorectal coil but the CT scan was acquired with no rectal distortion, and may lead to misregistration between the MRI and CT scans.

of the urethra of 2.5 ± 0.9 mm. Using bony landmarks, such as pubic arch and femur, to perform image fusion is sensitive to the impact of bladder and rectal filling. Bony landmarks stay stationary even when the prostate location gets shifted due to bladder and rectal filling. The fusion process lends itself to large interobserver variability as small inaccuracies in fusion results in a displacement of the seed cloud with respect to the prostate, leading to substantial uncertainty in DVH parameter evaluation.²⁷ Another registration technique variation is the fusion method,^{107,108} fusion algorithm parameters and fusion software: CT-MRI fusion has been done in the Pinnacle TPS (Philips Radiation Oncology Systems, Fitchburg, WI)¹⁰⁶ and the MIM Symphony TPS.⁷⁹ Fusion of CT and T_2 -weighted images can be more precisely performed using T_1 -weighted images as an intermediate dataset.²⁷ De Brabandere et al.²⁷ reported a large impact of fusion uncertainties on D90 (16%) from the direct fusion of CT and T_2 -weighted images, compared to the indirect fusion with T_1 -weighted images as an intermediate step (7%). Another variation of registration technique is the variation in personnel training and experience. Optimal CT-MRI fusion can be time-consuming, and training of the radiation oncologist, dosimetrist, and/or physicist to identify the relevant anatomical landmarks is required.

Input uncertainties The precision and accuracy of CT-MRI fusion-based post-implant dosimetry depends on the CT and MRI image acquisitions. Variation in the quality of the input data includes differences in pulse sequence and scan parameters (such as slice thickness²⁷). Various pulse sequences^{27,74} have been described to allow for fusion with CT images. Another variation is due to physician experience with contouring. Crook et al.⁴³ found significant differences between the contours made by experienced physicians versus inexperienced ones, resulting in differences in prostate V100 and D90. Other variations in the quality of input data are administered contrast, pelvic tilt, prostate edema, seed orientations, coil types,¹⁰⁹ patient travel between CT and MRI scanners, time lapse between CT and MRI scans, as well as bladder and rectal filling differences on CT and MRI images.

Time and cost Compared to CT-only or MRI-only approaches, the CT-MRI fusion-based approach incurs extra workload and cost due to the addition of another imaging modality.⁷¹

5.1.3 MRI-only Post-implant Dosimetry

5.1.3.1 Advantages

Excellent soft tissue contrast The positive implications of MRI-only post-implant dosimetry include superior visualization of anatomy. Bloch et al.⁶⁷ reported periprostatic seed enumeration and localization not possible using CT images at the neurovascular bundle, seminal vesicles, periurethral, penile bulb, Denonvillier's Fascia/rectal wall and urinary bladder.

High precision of prostate contours Prostate delineation on MRI is associated with less interobserver contouring variability compared to CT.^{27,44,51,52} De Brabandere et al.²⁷ found that although the standard deviation of prostate contours by eight physicians was lower on MRI images compared to CT images, it was still surprisingly large due to variations in inclusion of cranial aspects of the gland and margin generosity, thereby calling into question the increased accuracy of prostate contours on MRI images.

High precision and accuracy of normal tissue contours Consistent quantitation of dose to critical structures, such as the urinary sphincter,⁵⁶ would improve evaluation of dose-response relationships. Buch et al.⁵⁵ reported that MRI promotes a meaningful dosimetric assessment of normal tissue that is not possible using CT, for critical structures such as the urethra, anterior rectal wall, neurovascular bundles and penile bulb.

No ionizing radiation Using the MRI-only post-implant dosimetry approach, no unnecessary dose of ionizing radiation is given, unlike with CT.

Imaging flexibility Multiple contrast types can be obtained to illuminate structural and functional information. For instance, Gillan et al.⁵ reported DVH evaluation to the internal pudendal arteries using time-of-flight MR angiography. Apart from using Sirius MRI markers for MRI-only post-implant dosimetry, other solutions to enable MRI-only have focused on changing the pulse sequence used for post-implant dosimetry.

Time and cost savings Compared to CT-MRI fusion-based post-implant dosimetry, MRI-only post-implant dosimetry saves the time and cost of having to acquire a CT scan.

5.1.3.2 Disadvantages

Seed localization difficulties On MRI images, the brachytherapy seed appear as a negative void that are larger than the seed's physical length, and the interpretation of void's centroid is subjected to observer interpretation.²⁷ De Brabandere et al.⁷¹ found a mean interobserver variability in MRI-based seed localization (using T_1 -weighted gradient echo images) of 3 mm compared to 1.1 mm in CT-based seed localization. The variability in seed localization on MRI images lead to greater variability in DVH parameters compared to CT.^{27,71} However, evaluation of seed localization using DVH parameters only with no spatial information may obscure poor seed localization.⁷¹

Imaging uncertainties The accuracy of prostate and normal tissue contours depends on the MRI imaging technique. If endorectal coils are used, the inflation may significantly distort prostate anatomy (Figure 5.3). Also, a limitation of the other potential solutions to MRI-only post-implant dosimetry is that they were phantom studies and their utility in patients have yet to be investigated.

Time and cost Compared to CT-only post-implant dosimetry, MRI-only post-implant dosimetry takes longer and costs more than CT scans, as mentioned in Section 5.1.1.1.

Logistics MRI-based post-implant dosimetry may be subjected to limited availability of the MRI scanner to the prostate implant team.¹¹⁰ Access to an MRI scanner may be limited due to scheduling difficulties, the MRI scanner being in a different building or belonging to a completely different institution. These logistics difficulties increases scheduling inconveniences to the brachytherapy team and patients themselves.

Complexity MRI is a complex technology and is challenging to learn. Personnel education is a potential barrier to the adoption of MRI for post-implant dosimetry.

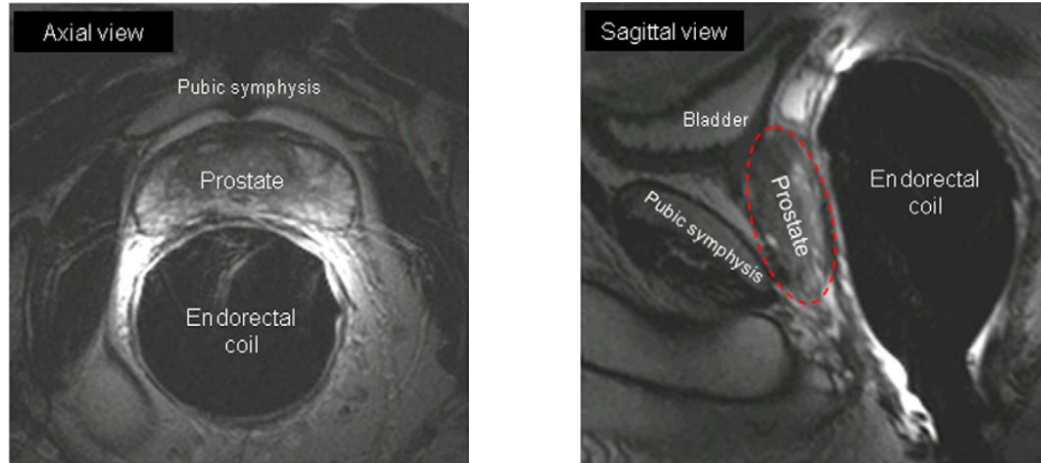


Figure 5.3: T2-weighted axial and sagittal images from a patient demonstrate the significant anatomic distortion caused by introduction of an endorectal coil (red dotted line on the sagittal image highlights the prostate shape). Reprinted from J. M. Albert, D. A. Swanson, T. J. Pugh, M. Zhang, T. L. Bruno, R. J. Kudchadker, and S. J. Frank. “Magnetic resonance imaging-based treatment planning for prostate brachytherapy”. In: *Brachytherapy* 12.1 (2013), pp. 30–7⁶¹ (licensed under a Creative Commons Attribution-NonCommercial-No Derivatives License).

5.1.4 Alternatives Solutions (instead of using Sirius MRI Markers) towards MRI-only Post-implant Dosimetry

Using encapsulated contrast agent markers* is one of the potential solutions to enable MRI-only post-implant dosimetry. Dubois et al.⁷⁰ and Moerland et al.⁶⁹ were the first groups to describe seed localization on MRI images. Dubois et al.⁷⁰ described using a proton-density-weighted fast spin echo (FSE) sequence to visualize the prostate and localize seeds, but lamented the steep learning curve in distinguishing seeds from blood vessels and identification of extraprostatic seeds. Dubois et al.⁷⁰ acquired the images on a GE 1.5 T Signa MRI scanner with the pulse sequence: “TR — 3000 ms, effective TE — 27 ms; 256 × 256 matrix, NEX of 2; 8 kHz bandwidth; 3 mm slice thickness, interleaved, 16 cm FOV, anterior-posterior phase direction, superior saturation band, flow compensation and no phase wrap... performed in a pelvic coil and required no more than 15 min to complete.”

Moerland et al.⁶⁹ used T_1 -weighted spin echo images for seed localization, but reported seed placement inaccuracies when the seeds cluster together. McLaughlin et al.⁵⁴ found that T_2 -weighted images are better than T_1 -weighted images for prostate delineation. However,

*See Section 1.7 for previous description of the Sirius MRI markers.

McLaughlin et al.⁵⁴ concluded that they could not determine an MRI technique that can reliably identify seeds to allow for MRI-only post-implant dosimetry. Tanaka et al.¹¹¹ used a contrast enhanced T_1 -weighted sequence, which yielded more accurate dosimetry compared to CT-based, but overestimated D90, V100 and V150 compared to the CT-MRI fusion-based post-implant dosimetry.

Most of the other solutions to enable MRI-only post-implant dosimetry focus on the seed artifacts for advanced manipulation of the pulse sequence and post-processing. The seeds have distinct susceptibility patterns depending on their orientations to the main magnetic field.^{93,112,113} By taking advantage of the seeds high magnetic susceptibility, recent efforts in seed visualization on MRI images include: the use of an Inversion-Recovery with ON-Resonant Water Suppression (IRON) pre-pulse to spectrally-select off-resonant protons,¹¹⁴ the use of ultrashort-TE sequences to preserve signal before rapid transverse dephasing,⁷³ the post-processing use of homodyne high-pass filters of various sizes,^{115,116} the use of susceptibility gradient mapping using the original resolution (SUMO) by filtering in k-space,¹¹⁷ the use of a kernel deconvolution algorithm with regularized L1 minimization¹¹⁸ (the dipole kernel¹¹⁹ and a nominal seed kernel¹²⁰ has been explored), the use of center-out Radial Sampling with Off-Resonance reception (co-RASOR) that moves the radial signal pile-up to the seeds center (using multiple acquisitions¹²¹ and only a single acquisition¹²²), and the use of multi-echo gradient recalled echo sequences.¹²³ However, imaging susceptibility may be inconsistent across MRI slices, difficult to locate accurately, and more challenging in heterogeneous tissue.¹¹⁶

5.2 Purpose

Sirius MRI markers may allow for the full integration of MRI for post-implant dosimetry by helping to overcome the barrier of seed localization difficulties on MRI images. Visualization of the Sirius MRI markers have been well-characterized in phantom (Figure 5.4) as described in the last chapter, but the feasibility of using these Sirius MRI markers in patients was unknown at the time of study. This chapter describes the initial patient experience in developing an appropriate MRI protocol for Sirius MRI marker visualization, and the process

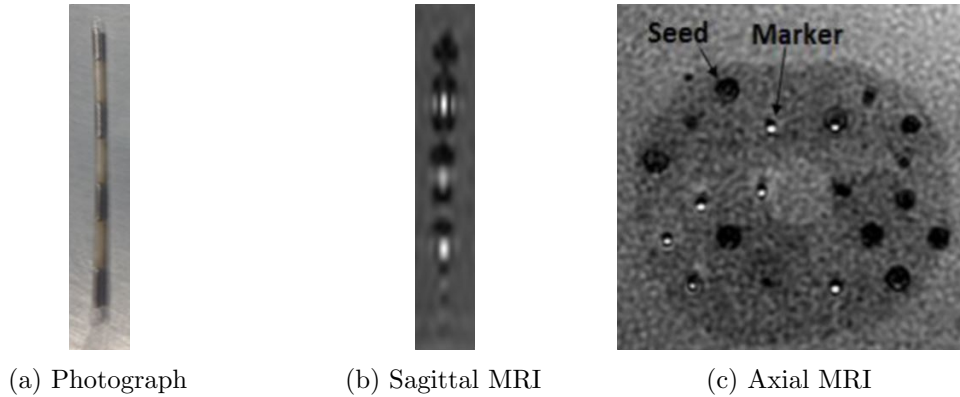


Figure 5.4: (a) Photograph of markers between brachytherapy seeds. (b) The appearance of markers (hyperintense cylinder) between seeds (hypointense dumbbell-shaped voids) in a commercially available prostate phantom. The displayed sagittal slice was obtained at a plane crossing the center of the topmost marker. (c) Axial view in a prostate phantom. Markers appear definitively as hyperintense regions, whereas signal voids may be seeds or needle tracks. Reprinted from T. Y. Lim, R. J. Kudchadker, J. Wang, T. Bathala, J. Szklaruk, T. J. Pugh, U. Mahmood, G. S. Ibbott, and S. J. Frank. “Development of an MRI protocol to visualize encapsulated contrast agent markers in prostate brachytherapy recipients: Initial patient experience”. In: *J Contemp Brachytherapy* 8.3 (2016)¹⁰³ (licensed under Creative Commons Attribution-NonCommercial-ShareAlike 4.0 International License).

of incorporating the markers into our LDR prostate brachytherapy clinical practice.

5.3 Methods

5.3.1 Sirius MRI Markers in the Prostate Implant Workflow

In an institutional process quality improvement protocol, 10 prostate cancer patients selected to undergo LDR prostate brachytherapy were evaluated. Various imaging modalities, such as transrectal ultrasound (TRUS), CT and MRI, were used throughout the implant workflow.

Pre-implant Prior to the implant, TRUS and MRI images were acquired. These pre-implant images were used to generate the treatment plan on MIM Symphony (MIM, Cleveland, OH), which was evaluated in Chapter 2. The treatment plan dictated the ordering of seeds and markers in a unique configuration for each patient. The Sirius MRI markers (C4 Imaging, Houston, TX) contain cobalt dichloride-N-acetyl cysteine encapsulated in a polymer capsule of 5.5 mm length, 0.8 mm diameter, and have been approved by the United States Food and Drug Administration for LDR prostate implants. The seed-marker strands

were ordered depending on the isotope and seed manufacturer (IsoRay Medical, Richland, WA; IsoAid, Port Richey, FL; Theragenics, Buford, GA) with appropriate sterilization of the strands.

Implant The seed-marker strands were implanted in patients under TRUS- and template-guidance in the same manner as seed-spacer strands.

Post-implant After the implant, CT and MRI scans were acquired on the day-of-implant and again approximately a month later. The post-implant CT images were used to perform post-implant dosimetry for all patients according to the current standard of care. The post-implant MRI images were evaluated for marker, seed and prostatic anatomy visibility, as well as artifacts, including marker chemical shift, partial volume averaging, seed susceptibility, motion, and wraparound artifacts.

5.3.2 Post-implant MRI Protocol

Previously, our institution’s post-implant MRI protocol consisted of 3D T_2 -weighted FSE, 2D T_2 -weighted FSE (axial), and 2D T_1 -weighted FSE (axial/sagittal/coronal) sequences. The 3D T_2 -weighted FSE sequence (GE: CUBE; Siemens: SPACE, Sampling Perfection with Application optimized Contrasts using different flip angle Evolution) was routinely used for fusion with CT images.

The *updated* post-implant MRI protocol consists of a 3D fast radiofrequency-spoiled gradient-recalled echo (FSPGR) sequence, with the scan parameters defined based on the phantom studies described in Chapter 4 and repeat 3D FSPGR scans performed to optimize the sequence for post-implant dosimetry (Table 5.1).

MRI scans were acquired using a Signa HDxt 3.0 T scanner (GE, Waukesha, WI) for eight patients, a Signa HDxt 1.5 T scanner (GE, Waukesha, WI) for one patient, and a MAGNETOM Aera 1.5 T scanner (Siemens, Malvern, PA) with the similar fast low angle shot (FLASH) sequence for one patient. Except for the first patient, all patients were imaged with a disposable inflatable endorectal coil (Medrad®; Bayer, Whippany, NJ). Surface Coil Intensity Correction (SCIC) and Phased array UnifoRmity Enhancement (PURE)

Table 5.1: Pulse sequences for post-implant dosimetry. Reprinted from T. Y. Lim, R. J. Kudchadker, J. Wang, T. Bathala, J. Szklaruk, T. J. Pugh, U. Mahmood, G. S. Ibbott, and S. J. Frank. “Development of an MRI protocol to visualize encapsulated contrast agent markers in prostate brachytherapy recipients: Initial patient experience”. In: *J Contemp Brachytherapy* 8.3 (2016)¹⁰³ (licensed under Creative Commons Attribution-NonCommercial-ShareAlike 4.0 International License).

	3D T2W FSE		3D FSPGR	
Scanner manufacturer	GE	GE	GE	Siemens
Field strength (T)	3.0	3.0	1.5	1.5
Scan plane	Axial	Axial	Axial	Axial
TR/TE (ms)	2000/120	8/2	8/3.6	12/2.4
FOV (cm) ^a	14	14	16	14
BW (Hz/pixel)	122	326	244	500
Echo train length	74	-	-	-
θ ($^{\circ}$)	-	20	25	25
Δz (mm)	1	1 ^b	1 ^b	1 ^b
Matrix size ^c	512×512	512×512	512×512	512×512
NEX	1	4	4.5	2
Frequency direction	R/L	A/P	A/P	A/P

^a Square field-of-view

^b Interpolated from 2 mm

^c Interpolated from 256×256

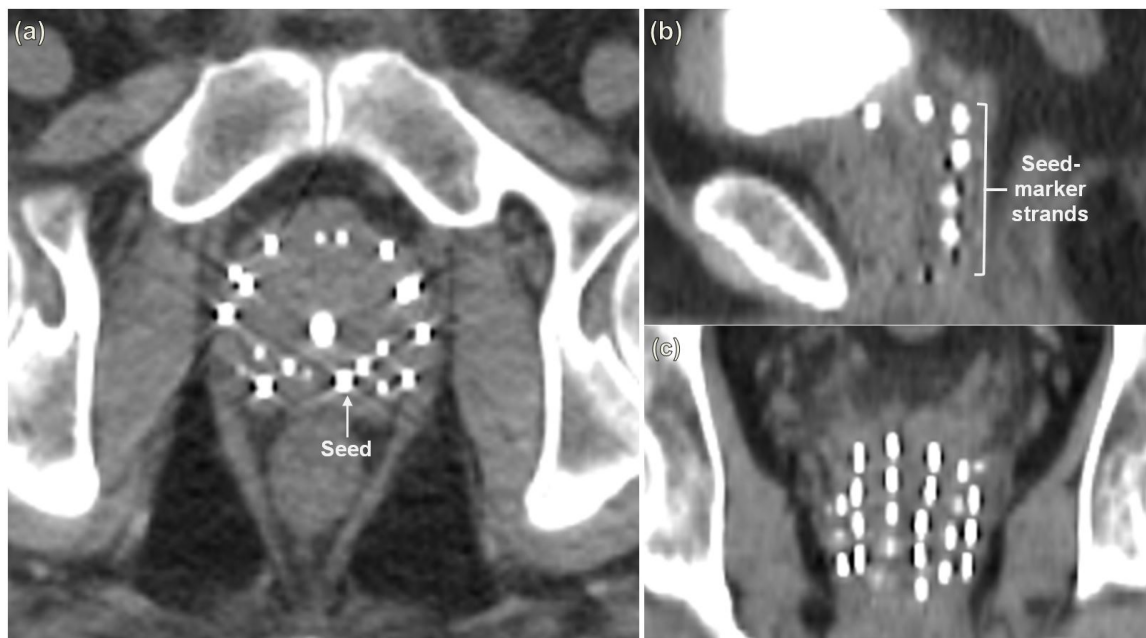


Figure 5.5: Axial (a), sagittal (b) and coronal (c) views of the prostate acquired using CT. Markers could not be visualized. Seeds appeared hyperintense with streak artifacts. Reprinted from T. Y. Lim, R. J. Kudchadker, J. Wang, T. Bathala, J. Szklaruk, T. J. Pugh, U. Mahmood, G. S. Ibbott, and S. J. Frank. “Development of an MRI protocol to visualize encapsulated contrast agent markers in prostate brachytherapy recipients: Initial patient experience”. In: *J Contemp Brachytherapy* 8.3 (2016)¹⁰³ (licensed under Creative Commons Attribution-NonCommercial-ShareAlike 4.0 International License).

post-processing were applied to minimize the high signal intensity proximal to the endorectal coil. All patients were imaged in the supine position.

5.4 Results and Discussion

5.4.1 Visualization of Seeds and Sirius MRI Markers

CT Images On the CT images (Figure 5.5), the markers appeared similar in intensity to the prostate tissue and were obscured by the seeds. On the other hand, the seeds appeared as hyperintense cylinders. The seed positions were confounded by the metal streak artifacts and partial volume averaging artifacts, appearing longer and wider than the seeds’ physical dimensions.

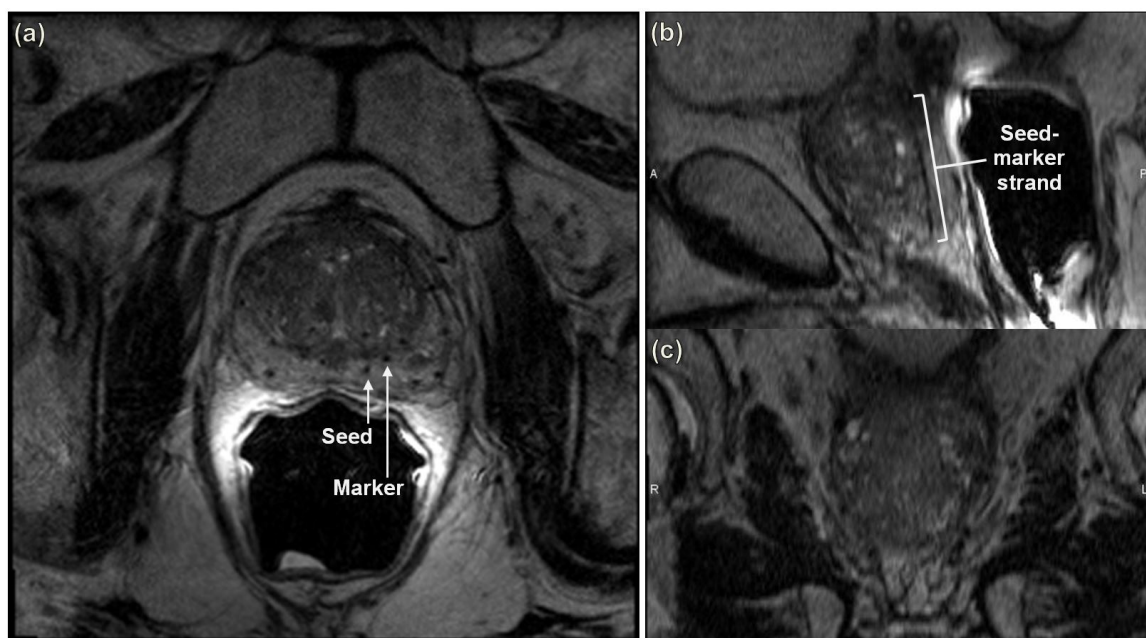


Figure 5.6: Axial (a), sagittal (b) and coronal (c) views of the prostate acquired using a 3D FSE sequence. The hypointense seeds and markers were not clearly distinguishable. Reprinted from T. Y. Lim, R. J. Kudchadker, J. Wang, T. Bathala, J. Szklaruk, T. J. Pugh, U. Mahmood, G. S. Ibbott, and S. J. Frank. “Development of an MRI protocol to visualize encapsulated contrast agent markers in prostate brachytherapy recipients: Initial patient experience”. In: *J Contemp Brachytherapy* 8.3 (2016)¹⁰³ (licensed under Creative Commons Attribution-NonCommercial-ShareAlike 4.0 International License).



Figure 5.7: Axial (a), sagittal (b) and coronal (c) views of the prostate acquired using a 3D FSPGR sequence. Markers appeared as hyperintense cylinders, while seeds appeared as hypointense dumbbell-shaped susceptibility voids. Reprinted from T. Y. Lim, R. J. Kudchadker, J. Wang, T. Bathala, J. Szklaruk, T. J. Pugh, U. Mahmood, G. S. Ibbott, and S. J. Frank. “Development of an MRI protocol to visualize encapsulated contrast agent markers in prostate brachytherapy recipients: Initial patient experience”. In: *J Contemp Brachytherapy* 8.3 (2016)¹⁰³ (licensed under Creative Commons Attribution-NonCommercial-ShareAlike 4.0 International License).

FSE Images On the standard post-implant protocol’s 3D T_2 -weighted FSE images (Figure 5.6), the markers and seeds appeared inconsistently as hypointense cylinders or isointense to prostatic tissue. Unclear distinction between seeds and markers confounded seed localization. Prostate anatomy was better visualized on the 3D T_2 -weighted FSE images. This is consistent with the consensus MRI experts’ opinion (such as from the European Society of Urogenital Radiology¹²⁴) that T_2 -weighted images yield the best visualization of the prostate zones and capsule.

FSPGR Images On the updated protocol’s 3D FSPGR images (Figure 5.7), the markers appeared as hyperintense cylinders within the hypointense needles tracks, giving the characteristic appearance on axial images of bright filled circles with a dark outline. A chemical shift artifact of the marker was pronounced at low BW. The marker chemical shift artifact results from slight differences between the Larmor frequencies of hydrogen spins

in the marker and the prostate, thereby displacing the marker in the frequency-encoding direction. The presence and magnitude of this displacement depends on BW and matrix size. The BW should be high enough for minimal marker displacement but low enough for acceptable noise. To reduce partial volume averaging artifacts due to the small size of the markers, I used $0.27 \text{ mm} \times 0.27 \text{ mm} \times 1 \text{ mm}$ voxels. The number of averages used was relatively high compared to standard sequences to increase the signal-to-noise ratio (SNR).

The seeds appeared as hypointense dumbbell-shapes, with wider ends of the seeds compared to the center. These dumbbell-shaped seed susceptibility artifacts were seen owing to the higher magnetic permeability of the seeds' metallic casing, especially at the end-welding, compared to background prostatic tissue. This causes the magnetic field to be distorted near the seeds, leading to spatial variation in local tissue relaxation times.¹⁰² The seed susceptibility artifact was more pronounced at low BW and more visible on 3D FSPGR images compared to 3D FSE images due to the lack of a 180 pulse that cancels out magnetic field inhomogeneity. The seed susceptibility artifact, along with the markers, enabled easier seed centroid identification.

Intraprostatic detail was not as clearly visualized with the 3D FSPGR sequence (Figure 5.7) as with the 3D T_2 -weighted FSE sequence (Figure 5.6). The prostate demonstrated a homogenous signal intensity and the prostatic zones were not easily discernible. Nevertheless, for post-implant dosimetry purposes, only prostate boundary delineation was needed. Figure 5.8 shows the contouring of relevant structures on the 3D FSPGR sequence images.

5.4.2 Clinical Challenges

Motion artifact Patient motion caused a ripple appearance in the phase-encoding direction due to improper registration of phase information, which obscured prostate margins and impaired seed and marker identification (Figure 5.9). The motion artifact could be expected owing to peristaltic or respiratory motion during the long (>10 minutes) image acquisition. Similar to diagnostic sequences, these motion artifacts should be directed away from the prostate by setting the phase-encoding direction to right/left (R/L) (Figure 5.9b). Motion artifacts can also be minimized by reducing scan time.

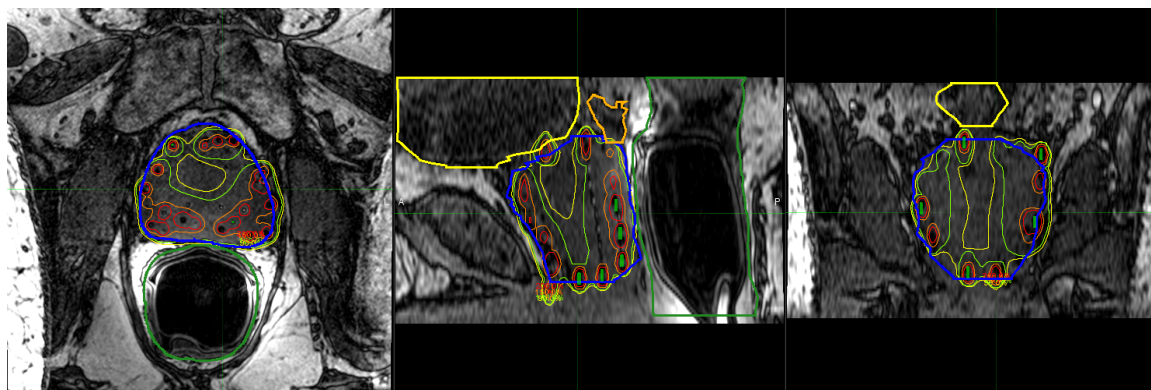
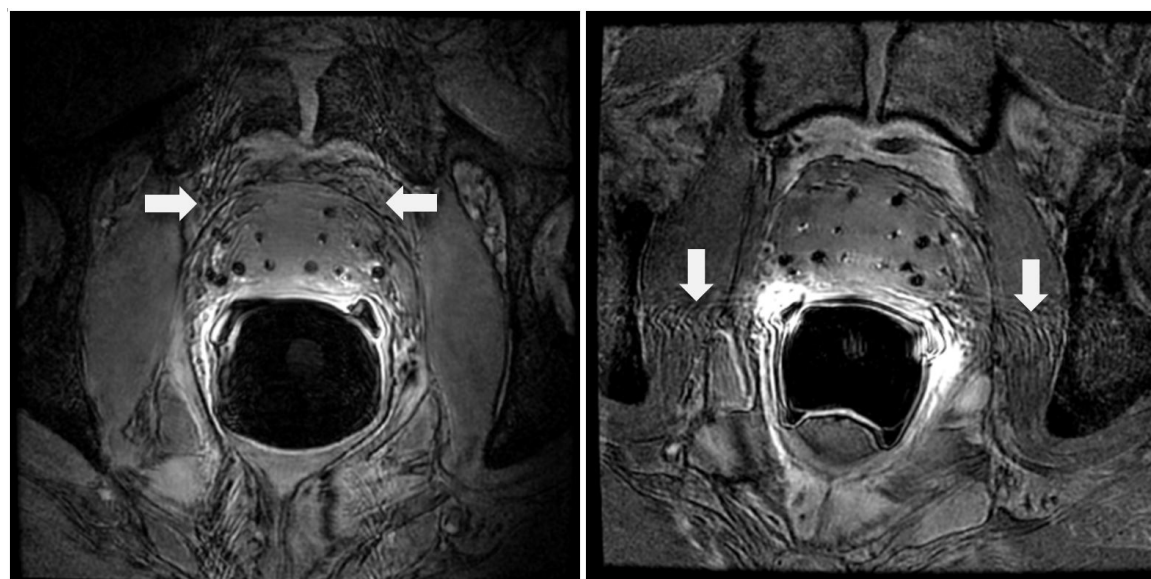


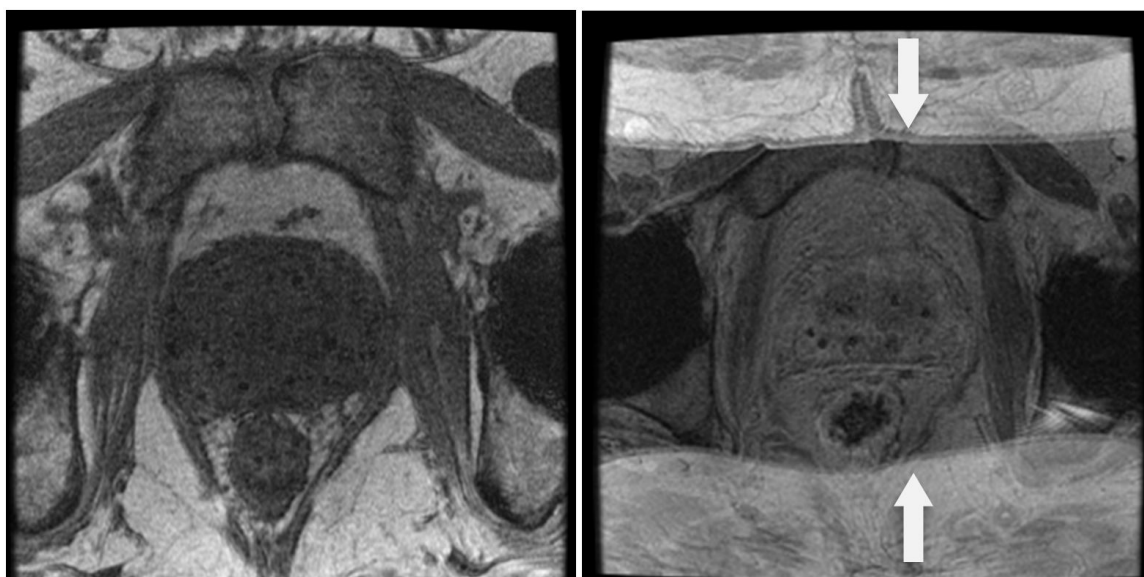
Figure 5.8: Delineation of the contours (prostate, thick blue lines; bladder, thick yellow lines; rectum, thick green lines) and identification of the radioactive seeds assisted by the use of positive-contrast MRI markers (thin lines are isodose lines) in a set of 3D-FSPGR MRI scans (axial, sagittal, and coronal views shown).



(a) Phase-encoding direction = A/P

(b) Phase-encoding direction = R/L

Figure 5.9: Impact of motion artifact on axial views of the prostate acquired using a 3D FSPGR sequence depends on the phase-encoding direction. Reprinted from T. Y. Lim, R. J. Kudchadker, J. Wang, T. Bathala, J. Szklaruk, T. J. Pugh, U. Mahmood, G. S. Ibbott, and S. J. Frank. “Development of an MRI protocol to visualize encapsulated contrast agent markers in prostate brachytherapy recipients: Initial patient experience”. In: *J Contemp Brachytherapy* 8.3 (2016)¹⁰³ (licensed under Creative Commons Attribution-NonCommercial-ShareAlike 4.0 International License).



(a) No wrap artifact

(b) Wrap artifact

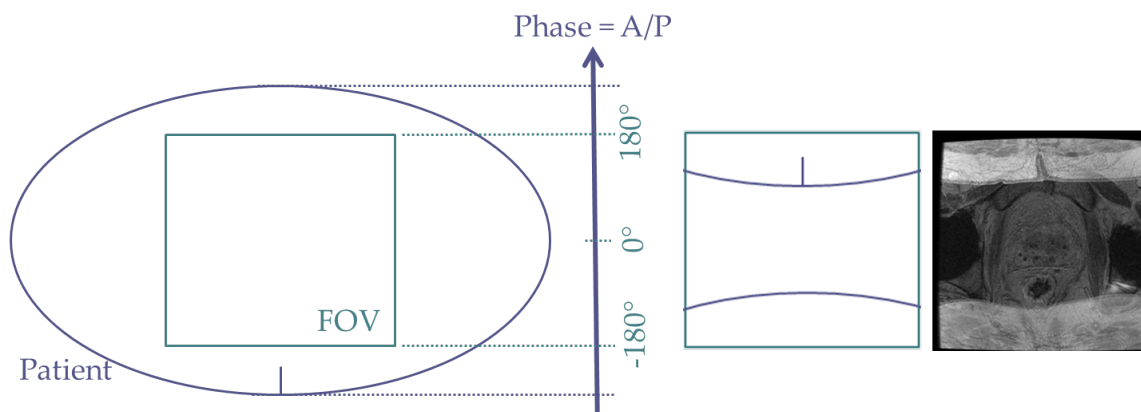
Figure 5.10: Axial views of the prostate acquired using a 3D FSPGR sequence with (a) no wrap artifact versus (b) with wrap artifact. Reprinted from T. Y. Lim, R. J. Kudchadker, J. Wang, T. Bathala, J. Szklaruk, T. J. Pugh, U. Mahmood, G. S. Ibbott, and S. J. Frank. “Development of an MRI protocol to visualize encapsulated contrast agent markers in prostate brachytherapy recipients: Initial patient experience”. In: *J Contemp Brachytherapy* 8.3 (2016)¹⁰³ (licensed under Creative Commons Attribution-NonCommercial-ShareAlike 4.0 International License).

Wraparound artifact The wraparound artifact (Figure 5.10b) was seen in the phase-encoding direction owing to improper assignment of phase-shift information. Depending on the extent of the wrap artifact, marker visibility could be affected. To reduce this artifact, a common technique is to set the phase-encoding direction to anterior/posterior because the anteroposterior width usually has the shortest skin-to-skin distance (Figure 5.11a). However, since the imaging FOV was smaller than the anteroposterior width of most patients, patient anatomy outside the FOV would wrap into the image. In this study, to reduce the wraparound artifact, I oversampled the FOV (Figure 5.11b), used saturation bands to reduce superimposed signal from outside the imaging FOV, and kept the patient's arms away from their sides.

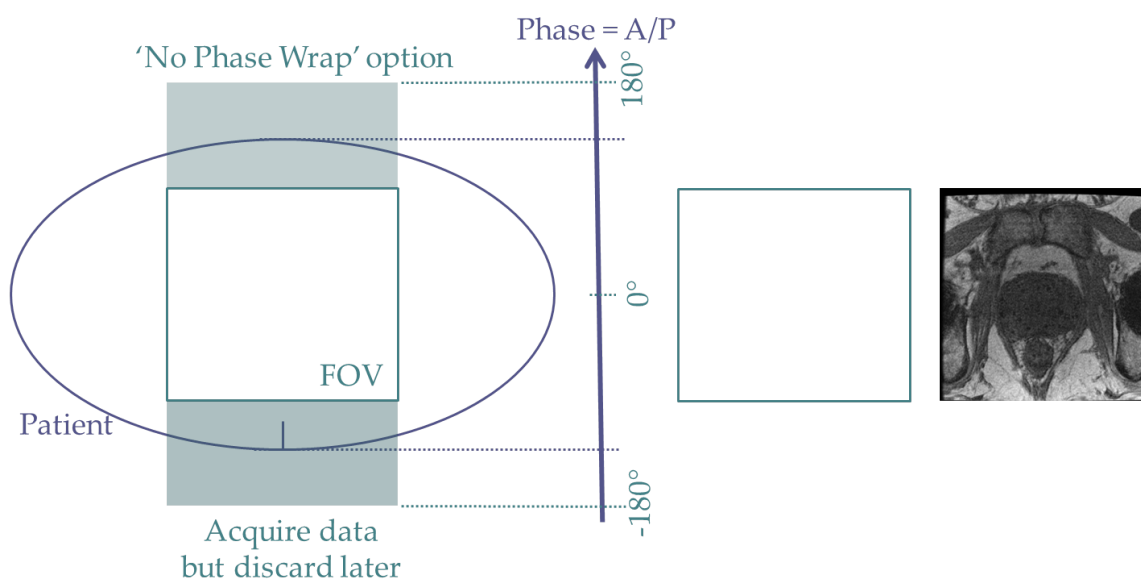
Minimizing the motion artifact and wraparound artifact required the phase-encoding to be set in different directions. Nevertheless, using phase oversampling, the wraparound artifact would not extend into the prostate; hence preventing the motion artifact from impinging into the prostate region could be prioritized to ensure visualization of the prostate boundaries and markers/seeds within the prostate for the purposes of post-implant dosimetric evaluation. Therefore, the phase-encoding direction should be set to R/L. For patients with lateral widths greater than the oversampled FOV (Figure 5.12), the wrap artifact would be observable (hyperintense tissue visible on R/L edges of the axial and coronal views of Figure 5.7).

Biomedical implants Patients' biomedical implants may be contraindicated for 3.0 T MRI, but they may be allowed to be scanned at lower field strengths. A reduction in field strength corresponds to a reduction in power deposition in the patient, relaxation times, susceptibility artifact effect, SNR, and geometric distortion. At 1.5 T, the image quality was reduced compared to 3.0 T images, but the visibility of the markers was not compromised.

Scanner manufacturers Regardless of the MRI scanner manufacturer, consistent and uniform protocols are essential. The MRI markers could be visualized on both GE and Siemens scanner platforms. The convenience of using the clinically-available 3D FSPGR pulse sequence compared to novel pulse sequences for MRI-based post-implant dosimetry



(a) Without phase oversampling



(b) With phase oversampling

Figure 5.11: Wrap artifact in the phase-encoding = A/P direction.

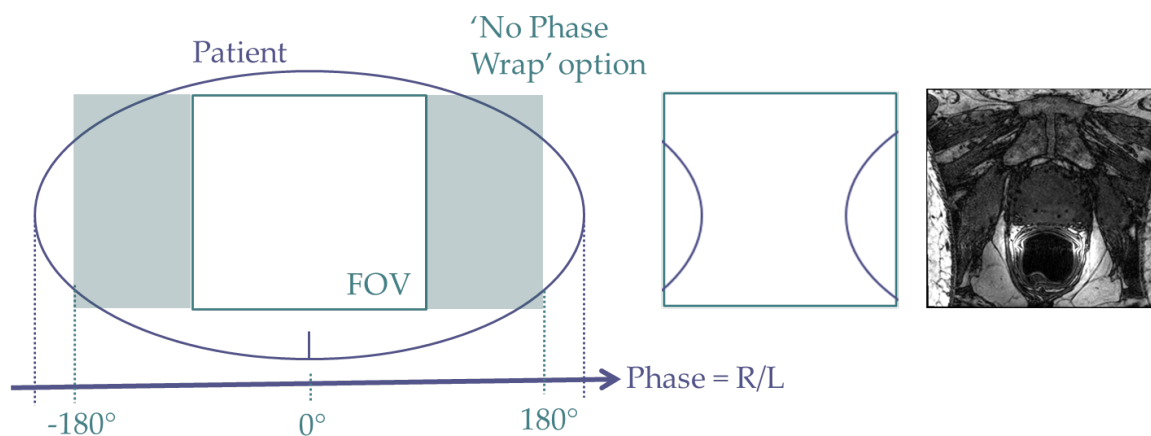


Figure 5.12: Wrap artifact in the phase-encoding = R/L direction.

was that the scan parameters could be matched with similar pulse sequences of different scanner manufacturers.

Coils Endorectal coils are routinely used to enhance the prostate signal for diagnostic sequences, as the prostate is centered in the body while signal from the torso coil falls off away from the skin. However, the endorectal coil is not routinely used in the post-implant setting within the LDR prostate brachytherapy community. Dubois et al.,⁷⁰ who first presented the use of MRI for post-implant dosimetry, recommended the pelvic coil and discouraged the use of the endorectal coil, citing concerns due to distortion of the prostate's posterior edge, the signal gradient artifact proximal to the endorectal coil and patient discomfort. Even for the acquisition of pre-implant images, Albert et al.⁶¹ cautioned against using an endorectal coil due to anatomical distortion. However, identification of the seeds and markers was impossible without the endorectal coil (Figure 5.10a). Depending on the size of the endorectal coil, it may deform the prostate (Figure 5.3), resulting in CT-MRI fusion difficulties and producing unnatural dose distributions. However, the endorectal coil can provide greater consistency towards the ultimate goal of an MRI-only LDR prostate brachytherapy workflow. In this study, to reduce prostate deformation while maintaining coil immobility, the endorectal coil was slightly inflated to only 30 cc instead of maximum inflation. Proper communication with the patient regarding the benefit of the endorectal coil was necessary to ensure patient cooperation.

5.5 Conclusion

5.5.1 Summary

Post-implant dosimetry improves care by allowing for corrective measures to be taken if necessary, and can improve the care of future patients through implant quality feedback to the brachytherapy team. Communication of the methodology and end-points of post-implant dosimetric assessment by the brachytherapy team to the MRI team is crucial to ensure useful images are acquired while maintaining high SNR, minimal artifacts, and reasonable scan time.

This chapter described the development of an MRI protocol for Sirius MRI marker and prostate visualization, and the incorporation of markers into our LDR prostate brachytherapy clinical practice. This is the first study presenting the appearance of MRI markers in human prostate, and the first evaluation of the practical feasibility of using these markers as part of the LDR prostate brachytherapy workflow. The MRI protocol consists of a 3D FSPGR scan for marker visualization, and an optional 3D T_2 -weighted FSE scan for detailed anatomical visualization. The 3D FSPGR scan may be used as the sole image set to identify markers and seeds, and provides adequate prostate edge visualization for contouring. However, CT-MRI fusion can be done using either the 3D FSPGR or 3D FSE scans in our protocol for fusion with CT images, if desired. Especially on the 3D FSPGR images, the markers can be visualized, potentially allowing for greater registration to CT images, as the markers and seeds are interleaved. MRI-MRI fusion post-implant dosimetry can also be straightforwardly done with our protocol's 3D FSPGR and 3D FSE scans, as these scans were acquired consecutively using an endorectal coil with the same scan prescription.

5.5.2 Limitations

A limitation of the study is that the effects of different scan parameters, scan conditions and scanner manufacturers could not be comprehensively studied due to scanner time constraints, patient comfort concerns and the small patient sample size. This chapter illustrates our preliminary findings and experiences with the first ten patients implanted with the Sirius MRI markers. We are currently acquiring MRI images of more patients implanted with the Sirius MRI markers to further optimize the pulse sequence and investigate if there is any clinically significant difference of the DVH parameters between CT-only, CT-MRI fusion-based, and MRI-only post-implant dosimetry.

Compared to the use of CT, a limitation of using MRI is that geometric distortion¹²⁵ may introduce uncertainty in the reconstructed seed positions. Given the current quality assurance methods to test MRI geometric distortion, gradient distortion correction techniques as well as the small size of the prostate, the error of reconstructed seed positions due to geometric distortion can be managed. However, care must be taken when investigating dose distributions to critical structures far from the center on images with large field-of-view.

Conversely, prostate geometrical distortion of another kind can be observed on post-implant CT images due to edema and the inherent indistinct borders can cause the misrepresentation of anatomy. Although current post-implant CT images provide absolute coordinates of the seeds, we are also concerned with the relative distance to critical structures and the distribution of seeds within the prostate volume, thus dose-volume-histograms are used extensively. Methods for correcting geometric distortions evaluated in phantom do not fully represent patient-induced distortions.¹²⁵ Thus, the impact of geometric distortion on dose-volume-histogram parameters of prostate implants can be illuminated in future studies.

Another limitation of this study is that the pulse sequence parameters were derived with the emphasis on high marker signal at the expense of scan time, resulting in motion artifacts when used in patients. The emphasis on high marker signal is to enable threshold-based automated marker identification and seed extrapolation. However, for manual marker and seed identification, if the Sirius MRI marker is not hyperintense and even isointense to the prostatic stroma, the needle tracks still allow distinction between the Sirius MRI marker and prostatic stroma.

The pulse sequence parameters that were derived based on phantom studies have two main limitations, namely temperature and coil. Due to logistical reasons, the phantom was scanned at room temperature instead of at body temperature. The Medrad endorectal coil (Bayer Healthcare LLC, Whippany, NJ) is generally used for patient scans, but this coil does not fit in the prostate phantom, hence the phantom images were acquired using an 8-channel torso coil (GE, Waukesha, WI) typically used for pelvic exams.

5.5.3 Current status

Since the initial experience in the first 10 patients implanted with Sirius MRI markers described in this study, our institution has continued to optimize the post-implant MRI protocol.

Kim et al.¹²⁶ previously compared the inflatable coil (Medrad, as described in this chapter) and a rigid endorectal coil (USA Instruments, Aurora, OH) and found that the inflatable coil caused significantly greater prostate compression in the A/P direction and widening in the R/L direction. To reduce prostate deformation, the current standard for the

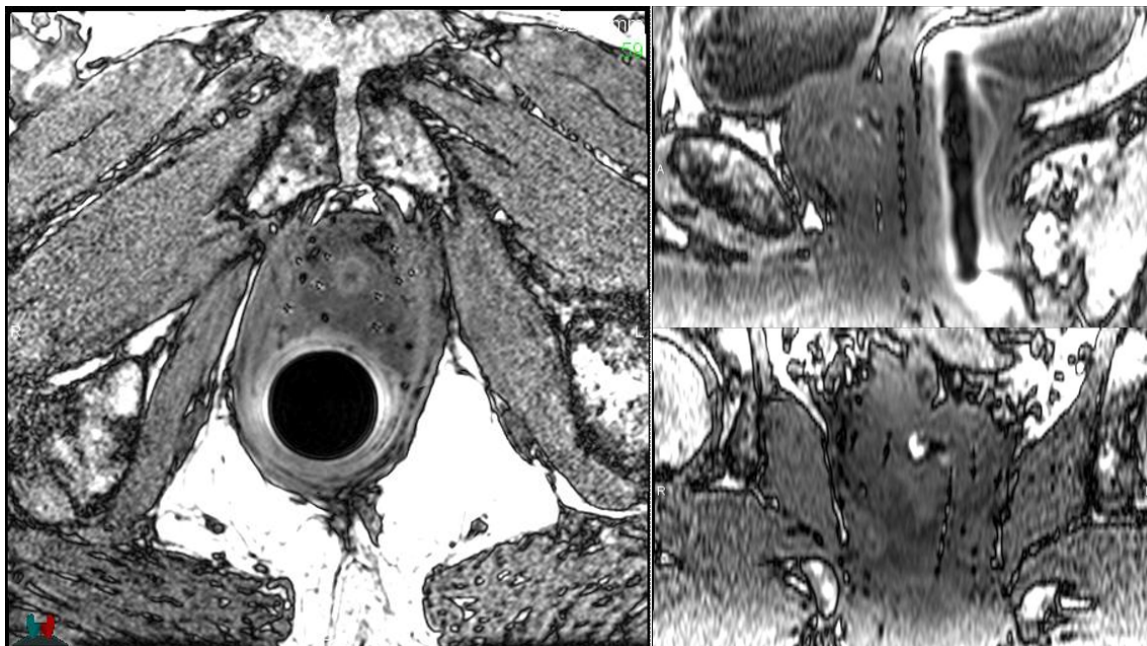


Figure 5.13: Axial, sagittal and coronal views of the prostate acquired with a rigid endorectal coil show less prostate deformation.

coil to be used in the post-implant MRI protocol with Sirius MRI markers at our institution is the Sentinelle endorectal coil (Invivo, Gainesville, FL), which is a rigid smaller-diameter endorectal coil about the size of a TRUS probe. This coil is currently under investigation to reduce prostate deformation while maintaining marker conspicuity (Figure 5.13).

5.5.4 Implications

Use of MRI instead of CT-MRI fusion for post-implant dosimetry can decrease the time and costs required of patients and hospital staff. In clinics utilizing CT-MRI fusion, the use of Sirius MRI markers alleviates the need for an extra CT scan to localize the seeds, thereby eliminating additional ionizing radiation to the patient, reducing uncertainties caused by imprecise registration from CT-MRI fusion, and improving the efficiency of the workflow. In institutions currently only using CT for post-implant dosimetry, better prevention of recurrence and prediction of side effects can improve the overall quality of life for patients, thus offsetting the greater upfront financial cost and time to undergo an MRI exam instead of a CT exam.

The advantages of using marker-based MRI-only post-implant dosimetry are easier

identification of hyperintense markers compared to hypointense seeds, prevention of spacers being incorrectly identified as seeds, and better distinction between needle tracks and blood vessels.

Nevertheless, even with the use of the markers for MRI-based post-implant dosimetry, the true dose distribution may vary between scans due to motion of the internal structures, such as varying amounts of bladder/rectal displacements.¹⁰⁸ This motion artifact can be minimized by the use of glucagon to reduce bowel peristalsis, or by reducing the scanning duration. Ultimately, the advantages of dedicated MRI-only post-implant evaluation are superior soft tissue contrast, no extraneous radiation dose, image-acquisition flexibility and possible integration of functional imaging.

In the next chapter, I present semi-automated marker-seed finding algorithms that could facilitate better integration of the markers into busy brachytherapy clinics.

6

Marker-based Seed Localization Algorithms

Contents

6.1	Introduction	128
6.1.1	Seed Localization Algorithms on CT/CT-MRI Fusion Images	128
6.1.2	Seed Localization Algorithms on MRI Images	129
6.2	Purpose	130
6.3	Methods	131
6.3.1	Data Collection	131
6.3.2	Marker-based Seed Localization Algorithm Workflows	131
6.3.3	Image Processing	131
6.4	Results and Discussion	140
6.4.1	Performance	140
6.5	Conclusion	150
6.5.1	Summary	150
6.5.2	Limitations	150
6.5.3	Implications	150

6.1 Introduction

6.1.1 Seed Localization Algorithms on CT/CT-MRI Fusion Images

Many algorithms have been developed for different types of imaging modalities. On CT images, the seeds are distinctly visible and many automated seed-localization algorithms for CT images have been reported. On CT-MRI fusion images, seed localization is still mainly performed on the hyperintense seeds visible on CT images.

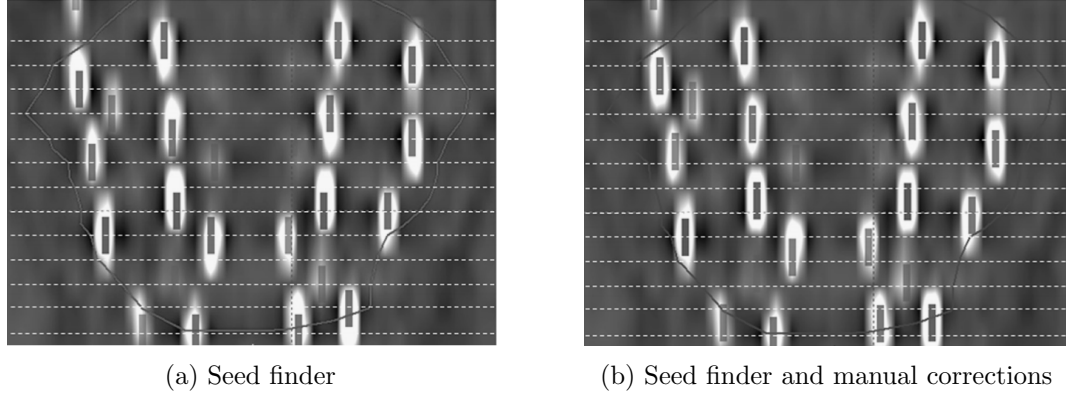


Figure 6.1: Seed positions as localized by the (a) VariSeed seed finder tool and (b) after manual corrections. Reprinted from M. De Brabandere, B. Al-Qaisieh, L. De Wever, K. Haustermans, C. Kirisits, M. A. Moerland, R. Oyen, A. Rijnders, F. Van den Heuvel, and F. A. Siebert. “CT- and MRI-based seed localization in postimplant evaluation after prostate brachytherapy”. In: *Brachytherapy* 12.6 (2013), pp. 580–87⁷¹ (license number: 3876110458254).

In a multi-institutional study, Bice et al.²⁶ described seed localization by first counting the number of seeds on anterior-posterior radiograph images or examining the implant documentation to determine the expected number of seeds, then applying a semi-automated nearest-neighbor approach to reduce the identified seeds to the expected number of seeds. Brinkman et al.¹²⁷ reported an automated algorithm on CT images using a workflow of threshold and connected component analysis. Li et al.¹²⁸ and Lee et al.¹²⁹ also demonstrated similar thresholding-based automated seed localization. Holupka et al.^{130,131} described seed localization using Hough transforms. Tubic et al.¹³² reported automatic seed localization before the generation of CT images, directly on the sinogram (the raw data plot with rays on the x -axis and angles on the y -axis⁸⁵).

Current brachytherapy TPS, such as VariSeed and MIM Symphony, have the seed localization algorithm on CT images built-in to the graphic user interface. The TPS-generated seeds positions usually require some manual corrections (Figure 6.1).

6.1.2 Seed Localization Algorithms on MRI Images

Dubois et al.⁷⁰ described seed localization method similar to that of Bice et al.,²⁶ that is, by manually localizing the seeds on each slice, check abutting slices for any repeated identification of the same seed, then reduce to the expected number of seeds.

Lee et al. (2007)¹²⁹ developed a semi-automated seed localization algorithm on MRI images by examining Day 30 MRI images on six patients who received real-time MRI-guided prostate implants. After cropping to the ROI, a manually-determined threshold was used to remove bony structures and soft tissues, then connected component analysis was performed until the specified number of seeds were identified. The authors reported a unanimous 100% seed identification rate in their 6-patient cohort. However, the pulse sequence used to generate the MRI images used in this study was unclear, as the authors stated that the work was an extension of MRI pulse sequence optimization efforts, citing the work of Dubois et al.⁷⁰ However, the MRI images used for algorithm development were of recipients of real-time MRI-guided prostate implants (citation not provided). D’Amico et al.¹³³ and Cormack et al.¹³⁴ demonstrated real-time MRI-guided prostate implants in a 0.5 T split-bore interventional MR unit with images acquired using T_1 - and T_2 -weighted sequences.

Kuo et al.¹¹⁴ described a Laplacian of a Gaussian blob detection technique on images acquired with an IRON prepulse and reported identification of 62 of 61 seeds (one false positive) on phantom images.

Current brachytherapy TPS do not have the capability to automatically find seeds on MRI images with the click of a button.

6.2 Purpose

Seed localization algorithms for MRI-based post-implant dosimetry based on Sirius MRI markers have not been demonstrated. An asset of CT-based post-implant dosimetry is the availability of automated seed localization tools that enable reproducible seed localization.²⁷ Conversely, De Brabandere et al.²⁷ reported greater interobserver variability of seed localization on T_1 -weighted images compared to CT images as a result of differences in the observers’ interpretations of the seed voids exact locations, especially in the longitudinal direction. Manual seed localization on MRI images, even with the use of Sirius MRI markers, is time-consuming and not clinically-feasible for large volumes of patients. An automated seed localization algorithm may increase the practicality of marker-based MRI-only post-implant dosimetry.

6.3 Methods

6.3.1 Data Collection

A multi-modality prostate phantom (Model 053-MM for ultrasound, CT and MRI; CIRS, Norfolk, VA) was implanted with 66 Sirius MRI markers (C4 Imaging, Houston, TX) and 86 dummy seeds in stranded seed-marker combination using 20 needles. The phantom was imaged using a 3.0 T MRI scanner (Discovery MR750; GE, Waukesha, WI) and an 8-channel torso coil (GE, Waukesha, WI) with a 3D fast radiofrequency-spoiled gradient recalled echo (FSPGR) sequence. The scan parameters used were: $TR/TE = 8/3.6$ ms, $NEX = 8$, $FOV = 14$ cm, $BW = \pm 83.3$ kHz, $\alpha = 14^\circ$, 256×256 (interpolated to 512×512), and frequency-encoding direction = anterior/posterior.

6.3.2 Marker-based Seed Localization Algorithm Workflows

The MRI images were processed using two strategies (Figure 6.2):

1. **Non-template-based:** The MRI image set was first preprocessed to obtain an ROI of the filtered image. Then, a threshold was defined and applied to the image set to obtain regions likely to contain markers. Next, connected component analysis was performed to detect the Sirius MRI marker positions. Lastly, the seed positions were extrapolated from the Sirius MRI marker positions.
2. **Template-based:** The MRI image set was first preprocessed to obtain an ROI of the filtered image. Then, a threshold was defined and applied to the image set to obtain regions likely to contain markers. Next, connected component analysis was performed to detect the Sirius MRI marker positions. Then, instead of directly extrapolating from the detected marker positions, the detected marker positions were registered to the predicted marker positions. The final step then was extrapolating these registered marker positions to the seed positions.

6.3.3 Image Processing

All image processing were performed using Matlab 8.1.0 (The Mathworks, Inc., Natick, MA).

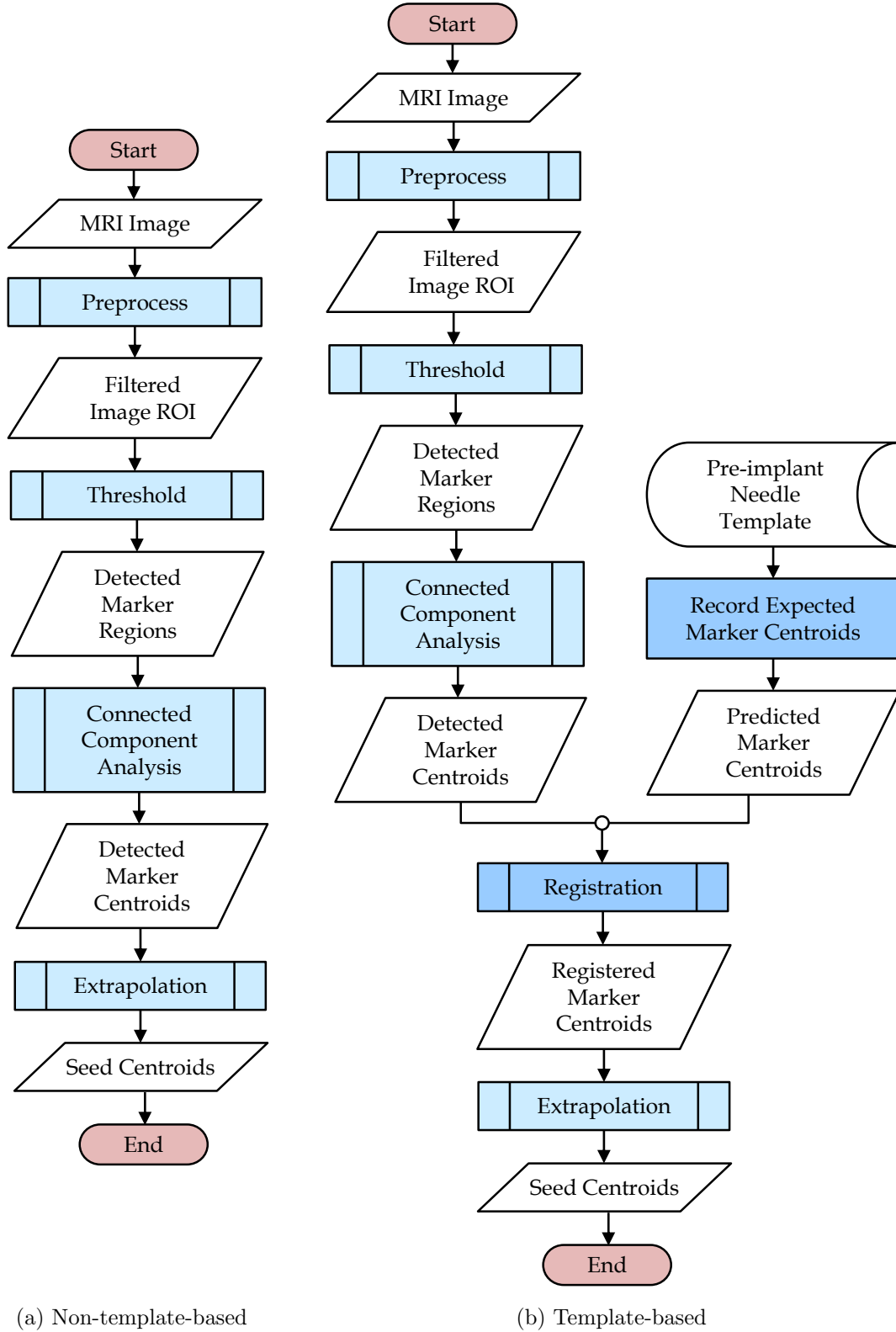


Figure 6.2: Marker-based seed-localization algorithm workflows based on two strategies: (a) non-template-based, and (b) template-based. The difference between the two strategies (highlighted in dark blue) is that pre-implant template information is used for registration in the template-based strategy.

Preprocess The MRI images were first imported into the workspace. The ‘open’ filter, consisting of ‘erode’ and ‘dilate’ operations, was used as the background. The background was subtracted from the original image. The image was then cropped to a rectangular ROI. To standardize the testing process, I set a fixed ROI that sufficiently covers the prostate and includes all markers and seeds. In non-testing settings, the user would be prompted to select a region-of-interest on the image. The filter was applied first before cropping to the region-of-interest such that the structuring element could better sample the edges of the region-of-interest. The downside of filter-then-crop as opposed to crop-then-filter is computation time, but the computation time was not discernible. The pseudocode for the preprocess function is provided in Algorithm 1.

Algorithm 1 Preprocess an MRI image set

```

procedure PREPROCESS(image path, number of slices)
  Read in image set from path
  (Rotate  $x,y$  coordinates of image due to Matlab flipping  $x,y$  axes)
  Background  $\leftarrow$  Morphological open filter (Matlab built-in function)
  Filtered image  $\leftarrow$  Image - Background
  Define ROI containing prostate
  Record pixels of filtered image within defined ROI
end procedure

```

Threshold For each slice in the image set, the image coordinates were recorded if the image intensity at the location was greater than the set threshold. The pseudocode for the preprocess function is provided in Algorithm 2.

Algorithm 2 Threshold an MRI image set

```

procedure THRESHOLD(image intensities, threshold)
  for all pixel intensities on each slice do
    Record the row and column locations where the intensity > threshold
    Record the slice location
  end for
end procedure

```

Connected Component Analysis The limits that define the same marker were defined in all 3 directions. All points were first set to be unique. For each point, if it was unique, distances to all other points were calculated. Extra points were recorded as such and the point was set to be not unique anymore. Then, for each unique point, the average of all the extra points were recorded as the marker location. The image coordinate system was

then converted to physical dimensions in cm. The pseudocode for the preprocess function is provided in Algorithm 3.

Algorithm 3 Connected component analysis

```

procedure CCA(bright coordinates)
  Initialize all bright coordinates to be unique markers
  for all bright coordinates do
    if a coordinate-in-question is a unique marker then
      for all other coordinates do
        if this-other-coordinate is also a unique marker then
          Distance = | coordinate-in-question - this-other-coordinate |
          if Distance < preset marker limits then
            Extra coordinate  $\leftarrow$  this-other-coordinate
            Record that coordinate-in-question is no longer unique
            Record that this-other-coordinate is no longer unique
          end if
        end if
      end for
    if no extra points then
      Store as a marker centroid
    else
      Calculate centroid from coordinate-in-question and extra coordinates
      Store as a marker centroid
    end if
  end if
end for
end procedure

```

Extrapolate To find the unique strands given all the detected locations of the Sirius MRI markers, k-means clustering was performed, which partitions n observations into k clusters by minimizing the within-cluster sum-of-squares. To find markers belonging to the same strand, the n observations are the marker locations while the k clusters are the strand numbers. For each strand, the coordinates of the marker in the strand were recorded. If only one marker was present in the strand, one seed was added above the marker and another seed was added below the marker. For more than one marker in a strand, one seed was added above the first marker, one seed was added after the last marker and seeds were added in between the markers in the strand. The pseudocode for the preprocess function is provided in Algorithm 4.

Registration For the template-based workflow, an additional registration step was taken before extrapolation. Before each implant, a pre-implant plan is always generated to determine the number and locations of the seeds and markers. A priori information from this pre-implant plan can be taken for the registration purposes. From the pre-implant needle

Algorithm 4 Extrapolation

```

procedure EXTRAPOLATION(detected marker coordinates, number of strands)
  Perform k-means clustering using squared Euclidean  $x$  and  $y$  distances
  for each strand do
    Determine this strand's markers  $x, y, z$ 
    if only one marker in this strand then
      Top seed  $x, y \leftarrow$  marker  $x, y$ 
      Top seed  $z \leftarrow$  marker  $z - 0.5$ 
      Bottom seed  $x, y \leftarrow$  marker  $x, y$ 
      Bottom seed  $z \leftarrow$  marker  $z + 0.5$ 
    else
      for each marker in strand do
        if first marker then
          Imaginary marker  $x, y \leftarrow$  marker  $x, y - (\text{next marker } x, y - \text{marker } x, y)$ 
          Top seed  $x, y \leftarrow (\text{marker } x, y + \text{imaginary marker } x, y) / 2$ 
          Top seed  $z \leftarrow$  marker  $z - 0.5$ 
        end if
        if last marker then
          Imaginary marker  $x, y \leftarrow$  marker  $x, y + (\text{marker } x, y - \text{prev marker } x, y)$ 
          Bottom seed  $x, y \leftarrow (\text{marker } x, y + \text{imaginary marker } x, y) / 2$ 
          Bottom seed  $z \leftarrow$  marker  $z + 0.5$ 
        else
          if distance between next marker and this marker  $>$  expected then
            Temp marker  $x, y, z \leftarrow (\text{marker } x, y, z + \text{next marker } x, y, z) / 2$ 
            Seed  $x, y, z \leftarrow (\text{marker } x, y, z + \text{temp marker } x, y, z) / 2$ 
            Next seed  $x, y, z \leftarrow (\text{temp marker } x, y, z + \text{next marker } x, y, z) / 2$ 
          else
            Seed  $x, y, z \leftarrow (\text{marker } x, y, z + \text{next marker } x, y, z) / 2$ 
          end if
        end if
      end for
    end if
    Record this strand's seeds  $x, y, z$ 
  end for
end procedure

```

template, the number of needles, x , y and z (based on retraction) positions of the seeds and markers were recorded, dependent on the loading pattern of each strand. The pseudocode for the preprocess function is provided in Algorithm 5. Then, given all the detected marker locations, k-means clustering was performed to find the unique strands. For each strand, the detected/clustered strand indices were matched to the template strand indices using the nearest neighbor method. For each strand, the registered marker positions were matched to the detected marker positions. For strands with missing markers, a distance matrix was built for each marker in the strand to determine which markers in the strand were visible to enable the correct registration. Once the markers were detected, the seed positions were determined from the marker positions by matching to the pre-implant needle template's defined strand loading pattern. The pseudocode for the preprocess function is provided in Algorithm 6.

Algorithm 5 Get template information

```

procedure GETTEMPLATE
  Input number of needles from needle template
  Input retractions of each needle from needle template
  Input alphabets of each needle from needle template
  Input  $y$  template locations of each needle from needle template
  Input number of seeds in each needle from needle template
  Input number of markers in each needle from needle template
  Number the alphabets according to alphabetical order
  Convert the inputted alphabets to numeric indices of  $x$ 
   $x \leftarrow (x \text{ index} - 1) / 2$  (Subtract to start at 0 and divide to convert to cm)
   $y \leftarrow y \text{ index} / 2$ 
  for each needle do
    for each seed  $s$  in needle do
      Record  $x, y$ 
      Record  $z \leftarrow \text{retraction} + s - 1$ 
      Record the needle number
      if not last seed (place markers) then
        Record  $x, y$ 
        Record  $z \leftarrow \text{retraction} + s - 0.5$ 
        Record number of seeds above this marker
        Record number of seeds below this marker
      end if
    end for
  end for
end procedure

```

Validation To validate the detected marker and seed positions, I manually identified the marker and seed positions on the MRI images. The manually-identified positions were treated as the ground truth. The limits for whether a marker was considered detected were defined in all 3 directions. The distances between each detected marker/seed positions

Algorithm 6 Registration

```

procedure REGISTRATION(detected marker coordinates, template marker coordinates)
  Calculate center-of-mass of template marker coordinates
  Calculate center-of-mass of detected marker coordinates
  Shift template marker positions to match detected marker positions
  Perform k-means clustering using squared Euclidean  $x$  and  $y$  distances of detected markers
  Record number of strands
  Record template strand indices
  for each strand do
    Record shifted template strand centroids
  end for
  for each strand in template do
    for each strand detected on image do
       $\Delta x \leftarrow$  shifted template centroid  $x$  - detected centroid  $x$ 
       $\Delta y \leftarrow$  shifted template centroid  $y$  - detected centroid  $y$ 
      Distance matrix =  $\sqrt{\Delta x^2 + \Delta y^2}$ 
    end for
  end for
  for each strand do
    Determine detected strand indices that correspond to template strand indices by finding the minimum
    distances
  end for
  for each strand do
    Extract shifted template positions
    Extract detected marker positions
    if template and detected marker match then
      Registered marker positions  $\leftarrow$  detected marker positions
    else
      Calculate  $z$  shift to account for unmatching retraction
      for each template marker position do
        template marker position  $\leftarrow$  template marker position -  $z$  shift
      end for
      for each template marker positions do
        for each detected marker position do
           $\Delta x, \Delta y, \Delta z \leftarrow$  template marker  $x, y, z$  - detected centroid  $x, y, z$ 
          Distance matrix =  $\sqrt{\Delta x^2 + \Delta y^2 + \Delta z^2}$ 
        end for
      end for
    for each strand do
      Matched marker index  $\leftarrow$  detected marker index that correspond to template marker index by finding
      the minimum distance
    end for
    for each matched marker do
      for each next matched marker do
        if matched marker index == next matched marker index and matched marker index not 0 then
          if distance between template marker and detected matched marker < distance between next
          template marker and detected matched marker then next matched marker index = 0
          else matched marker index = 0 (marker undetected on image cannot be matched to template-
          predicted marker)
        end if
      end if
    end for
  end for
  Check scenarios according to Algorithm 7
  end if
  Record registered marker coordinates of this strand
end for
for each strand do
  if one marker in strand then
    Add top and bottom seeds
  else
    Add seed before first marker
    Add seeds in between markers
    Add seed after last marker
  end if
  Record seed coordinates
end for
end procedure

```

Algorithm 7 Check scenarios of detected and undetected markers

```

procedure CHECKSCENARIOS
  for each marker in this strand do
    if matched marker index not 0 (no markers undetected on image) then
      marker  $x, y, z \leftarrow$  corresponding detected marker  $x, y, z$ 
    else
      if undetected marker is not 1st or last marker then
        if prev marker also undetected but next marker is detected then
          marker  $x, y \leftarrow$  next marker  $x, y$ 
          marker  $z \leftarrow$  next marker  $z - 1$ 
        else if prev marker detected but next marker also undetected then
          if there is a marker prev to the prev marker then
            if previous-previous marker detected then
              marker  $x, y \leftarrow$  prev marker  $x, y - (\text{prev-prev marker } x, y - \text{prev marker } x, y)$ 
              marker  $z \leftarrow$  prev marker  $z + 1$ 
            end if
          else
            marker  $x, y \leftarrow$  prev marker  $x, y$ 
            marker  $z \leftarrow$  next marker  $z + 1$ 
          end if
        else
          marker  $x, y, z \leftarrow (\text{prev marker } x, y, z + \text{next marker } x, y, z) / 2$ 
        end if
      else if 1st marker undetected then
        if 2nd marker also undetected but 3rd marker detected then
          1st marker  $x, y \leftarrow$  3rd marker  $x, y$ 
          1st marker  $z \leftarrow$  3rd marker  $z - 2$ 
        else if second marker detected but 3rd marker also undetected then
          1st marker  $x, y \leftarrow$  2nd marker  $x, y$ 
          1st marker  $z \leftarrow$  2nd marker  $z - 1$ 
        else(second and third markers detected)
          1st marker  $x, y, z \leftarrow$  2nd marker  $x, y, z - (3\text{rd marker } x, y, z - 2\text{nd marker } x, y, z)$ 
        end if
      else if last marker undetected then
        if 2nd-last marker also undetected but 3rd-last marker detected then
          if there is a 4th-last marker then
            if 4th-last marker is detected then
              Last marker  $x, y \leftarrow$  3rd-last marker  $x, y + 2 \times (3\text{rd-last marker } x, y - 4\text{th-last marker } x, y)$ 
              Last marker  $z \leftarrow$  3rd-last marker  $z + 2$ 
            end if
          else
            Last marker  $x, y \leftarrow$  3rd-last marker  $x, y$ 
            Last marker  $z \leftarrow$  3rd-last marker  $z + 2$ 
          end if
        else if 2nd-last marker detected but 3rd-last marker undetected then
          Last marker  $x, y \leftarrow$  2nd-last marker  $x, y$ 
          Last marker  $z \leftarrow$  2nd-last marker  $z + 1$ 
        else(2nd-last and 3rd-last markers detected)
          Last marker  $x, y, z \leftarrow$  2nd-last marker  $x, y, z + (2\text{nd-last marker } x, y, z - 3\text{rd-last marker } x, y, z)$ 
        end if
      end if
    end if
  end for
end procedure

```

Algorithm 8 Validation of detected seed or marker locations

```

procedure VALIDATION(detected centroids, manually-identified centroids)
  Start with  $n = 0$ 
  for each detected centroid do
    for each manually-identified centroids do
      Distance  $\leftarrow$  | detected centroids - manually-identified centroids |
      if distance  $< 3$  mm in XY and 2 mm in Z then
         $n \leftarrow n + 1$ 
      end if
    end for
  end for
  True positive  $\leftarrow n$ 
  if Number detected -  $n > 0$  then
    False negative  $\leftarrow$  Number detected -  $n$ 
  else
    False negative  $\leftarrow 0$ 
  end if
  Calculate sensitivity according to Equation 6.1
  Calculate precision according to Equation 6.2
  Calculate F-score according to Equation 6.3
end procedure

```

and all the manually-identified marker/seed positions were calculated to determine the number of markers/seeds that were truly detected by the algorithm, which is the number of true positives (TP). The number of false positives (FP) is the number of truly detected markers/seeds subtracted from the number of detected markers/seeds. The number of false negatives (FN) is the number of detected markers/seeds subtracted from the number of manually-identified markers/seeds. To determine the efficacy of the algorithm, sensitivity, precision and the F-score (measure of accuracy) were then calculated.

$$\text{Sensitivity} = \frac{\text{TP}}{\text{TP} + \text{FN}} \quad (6.1)$$

$$\text{Precision} = \frac{\text{TP}}{\text{TP} + \text{FP}} \quad (6.2)$$

$$\text{F-score} = \frac{2 \times \text{Precision} \times \text{Sensitivity}}{\text{Precision} + \text{Sensitivity}} \quad (6.3)$$

6.4 Results and Discussion

6.4.1 Performance

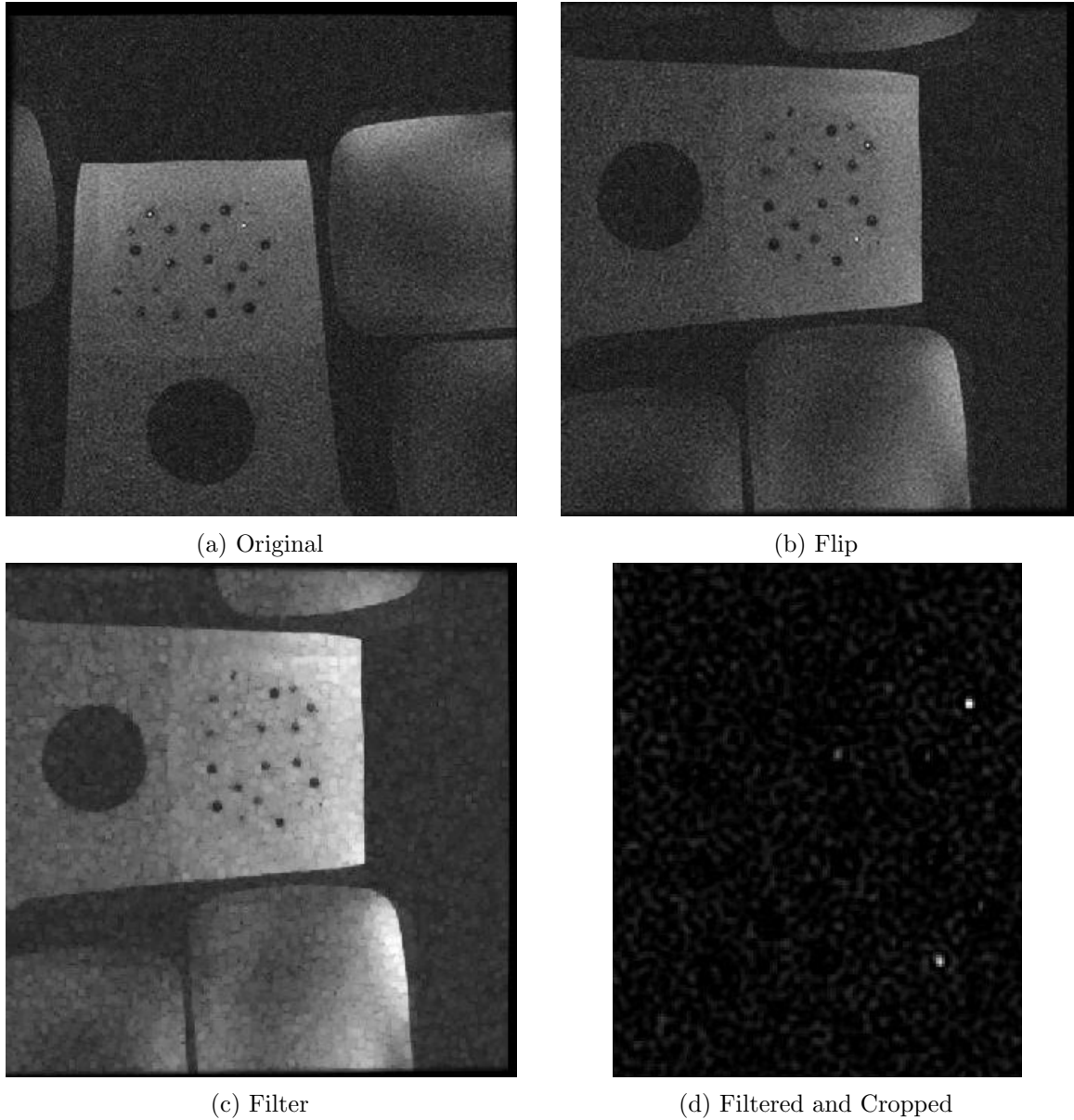


Figure 6.3: The preprocessing function imported the (a) original images, (b) flipped the axes due to Matlab axes definition, (c) applied a filter, then (d) cropped to the ROI containing prostate.

The preprocess function can highlight the relevant pixels containing markers for further image processing. Flipping the image axes to match Matlab's image axes definition (Figure 6.3b) did not affect marker/seed localization. This is because the definition of a coordinate system

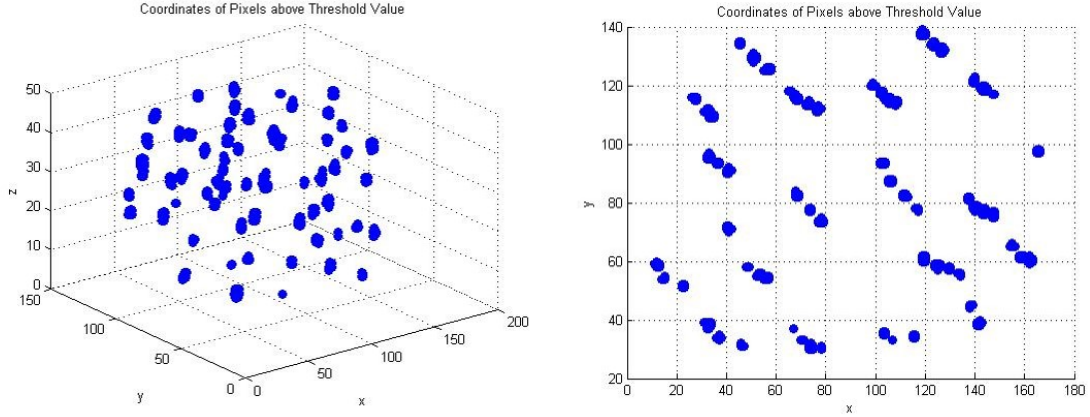


Figure 6.4: Regions of markers after thresholding.

is arbitrary within the prostate and the distance between markers/seeds were preserved in this workflow. Multiple filter types are available on Matlab. The erosion filter (Figure 6.3c), as well as its corresponding structuring element type and size, were selected based on trial-and-error. The defined ROI eliminated extraneous signal from outside the prostate (Figure 6.3d), so that subsequent functions (such as connected component analysis) would not have to process these extraneous signal and can be more efficient.

Figure 6.4 depicts “blobs”, or regions on the image that most likely contain the markers. Since each marker span over multiple pixels in all 3 directions, each marker had multiple coordinates defined, forming a “blob”.

By finding the centroids of the “blobs” of markers, the marker positions can be better defined (Figure 6.5). Multiple studies described in Sections 6.1.1 and 6.1.2 adopt the connected component analysis for seed-finding, that is, by identifying the pixels containing seeds on the images and image slices, then defining seed locations as the centroids of these pixels. For instance, Dubois et al.⁷⁰ and Bice et al.²⁶ referred to the connected component analysis as “nearest-neighbor approach” for processing their manually-identified pixels as seeds, while Kuo et al.¹¹⁴ referred to this connected component analysis as “blob-detection technique” for finding the seeds on MRI images with the IRON prepulse.

Instead of an arbitrary image coordinate system, the marker and seed locations are mapped out in physical dimensions based on pixel sizes (Figure 6.6).

To be able to properly extrapolate the seed locations from the marker locations, the

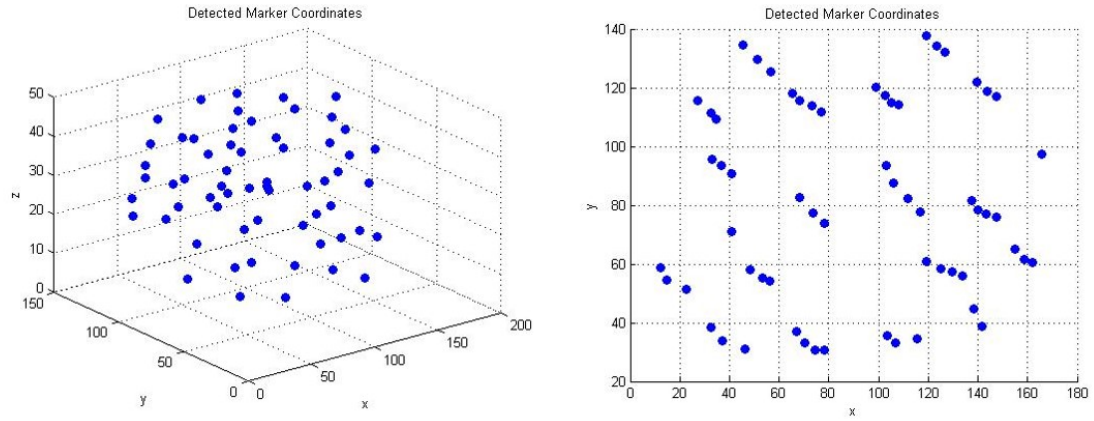


Figure 6.5: Connected component analysis find the marker centroids.

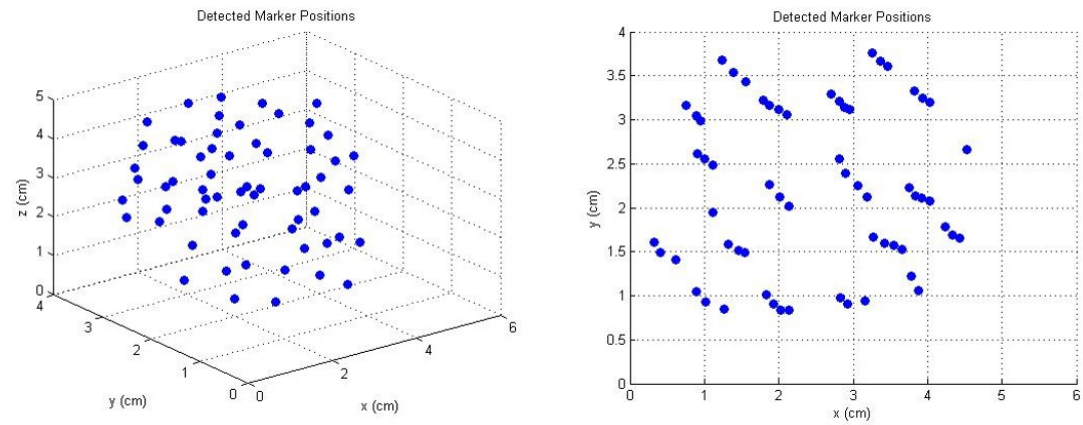


Figure 6.6: Marker centroids in real dimensions.

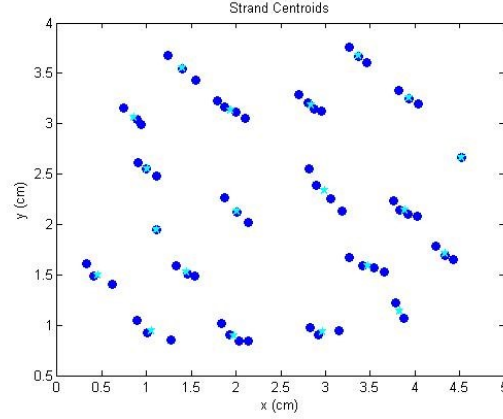


Figure 6.7: k-means clustering was performed to find individual strands (identified with light blue star).

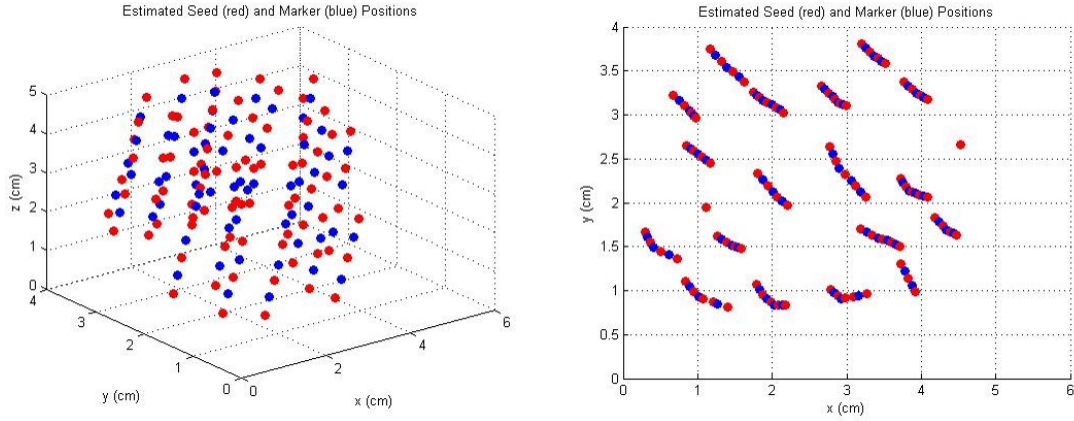


Figure 6.8: Seeds positions (red) extrapolated from marker positions (blue).

markers need to be grouped by their strands. k-means clustering was performed to identify the individual strands (Figure 6.7).

By knowing the strand information of the markers, the seeds can be extrapolated. For instance, if a strand only have two markers, one seed would be extrapolated in between the two markers, and one seed would be extrapolated from the other ends of the two markers as the first and last seeds. For strands with only one marker, first and last seeds are placed directly above the marker. Figure 6.8 depicts the seed and marker positions obtained using the non-template-based seed localization algorithm.

To check whether the seed and marker locations identified on Figure 6.8 were accurate, they must be compared to true seed and marker locations. The true seed and marker

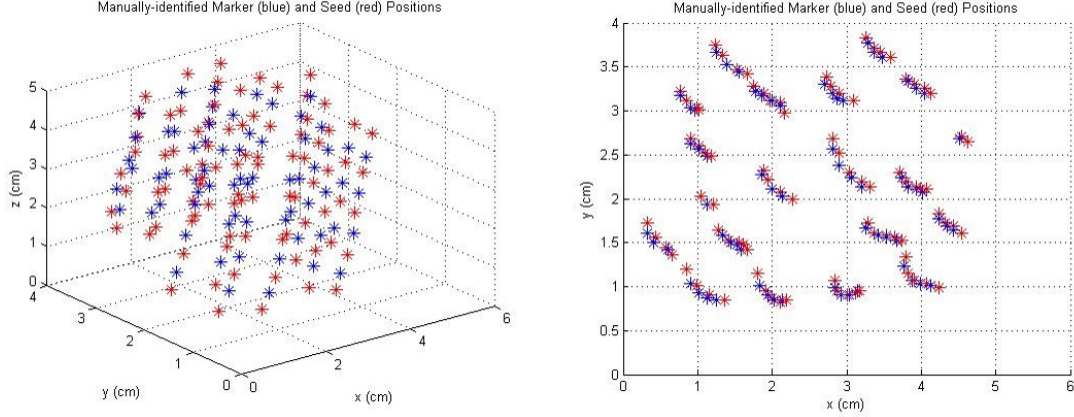


Figure 6.9: Validated marker (blue) and seed (red) positions generated by manual identification.

locations were defined based on seed and marker locations manually-identified directly on the MRI images. Figure 6.9 shows the validated marker and seed positions.

When overlaying the marker and seed positions identified using the non-template-based algorithm over the validated marker and seed positions, we can readily identify false negatives (Figure 6.10). This is due to some marker intensities not meeting the threshold and thus those markers were not identified. The misidentification of markers propagates to seeds not being able to be extrapolated.

A way to overcome the seed false negatives is to incorporate the information about the expected number of markers and seeds in each strand. This information can be obtained from the pre-implant plan that is always generated for each implant. The marker and seed positions obtained from the pre-implant needle template are modeled as perfectly parallel strands (Figure 6.11). The pre-implant marker and seed configurations are currently explicitly recorded based on the needle template (Figure 1.5). However, with the incorporation of the template-based seed localization algorithm into a TPS, the TPS would already have the pre-implant seed and marker configurations in its environment, thus obviating the need to explicitly define marker and seed configurations.

Since the coordinate system is arbitrary, and only the distances between markers/seeds are definitive, the centers-of-mass of the pre-implant coordinate system and the detected marker coordinate system are matched (Figure 6.12).

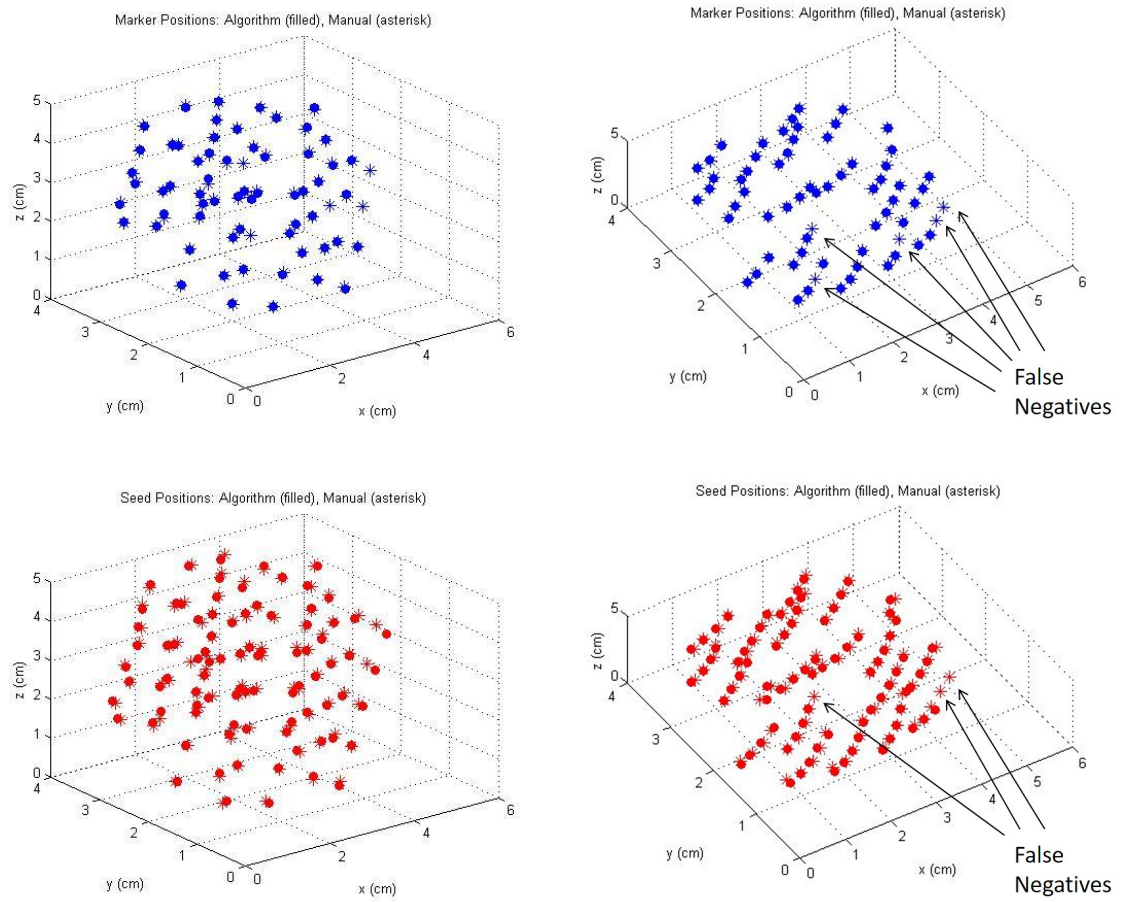


Figure 6.10: Non-template-based localization of (a, b) markers and (c, d) seeds.

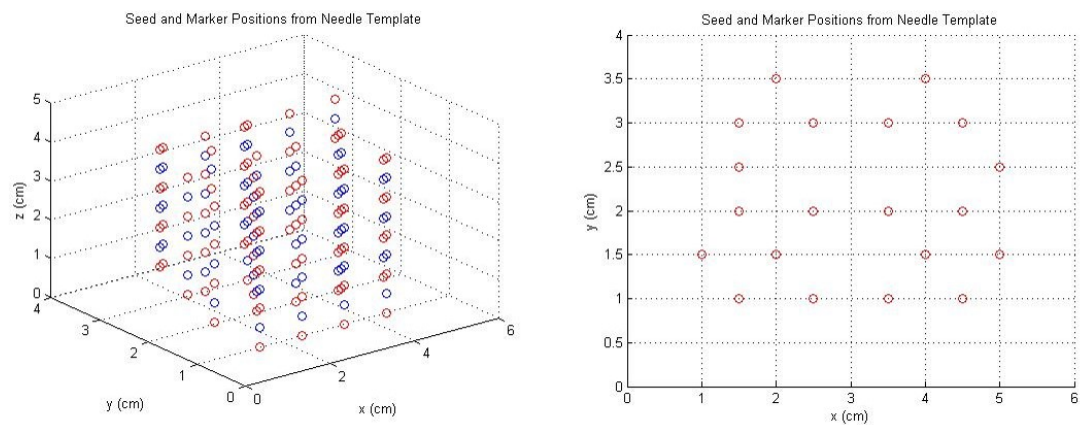


Figure 6.11: Preimplant marker and seed positions generated from pre-implant needle template.

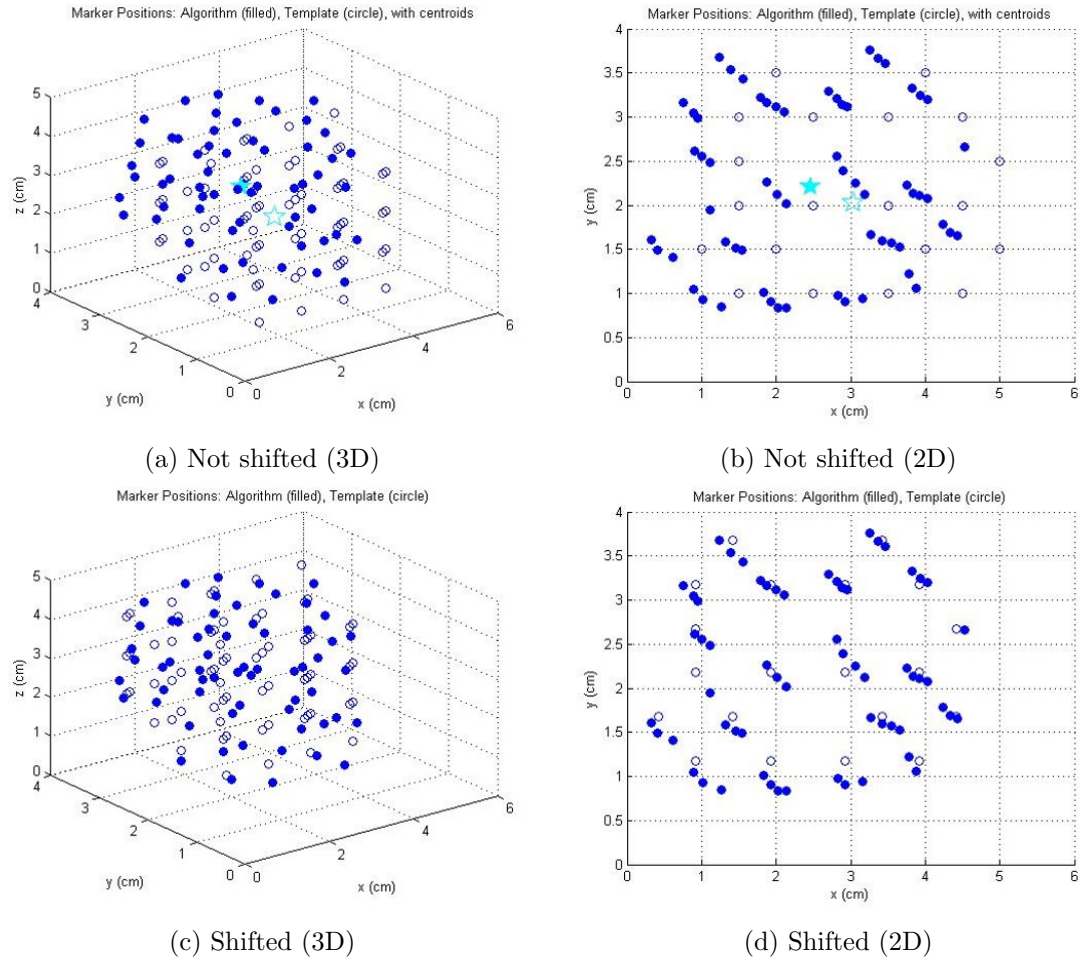


Figure 6.12: Coordinates shifted to match center-of-masses.

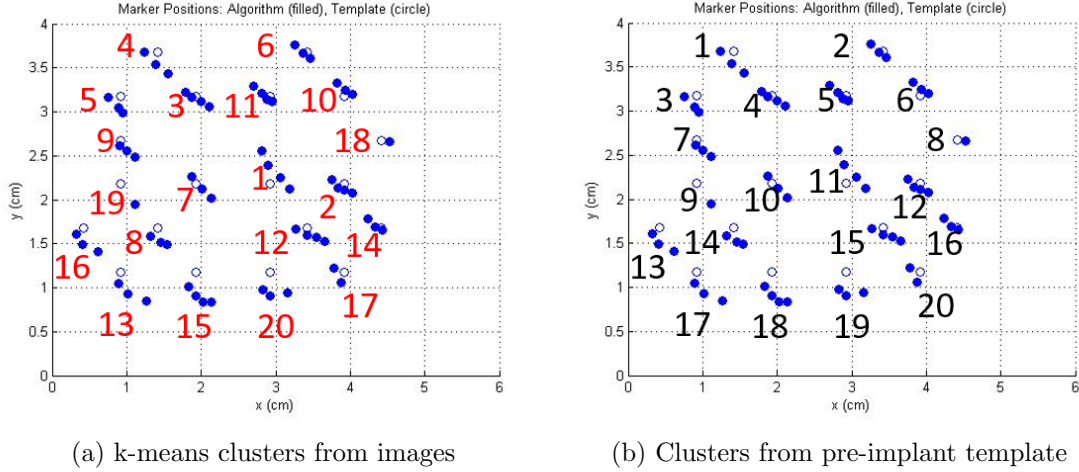


Figure 6.13: To obtain the information on the seed and marker configurations, (a) the strands identified on the images are matched to the corresponding (b) pre-implant needle strands.

The k-means clustering algorithm generated clusters and numbered the strands arbitrarily (Figure 6.13a). The pre-implant template numbers the strands consecutively from left-to-right, top-to-bottom (Figure 6.13b). Therefore, to obtain the information on the seed and marker configurations, the strand numbers were matched (Figure 6.13).

With the pre-implant template information, the template-based algorithm was able to determine the marker locations based on the expected marker configuration in a strand, even when the markers had low signal intensity on MRI images. Compared to the non-template-based algorithm, the template-based algorithm was able to identify more markers (Figure 6.14).

Lastly, as was done with the non-template-based algorithm, the seed locations were extrapolated from the marker locations for the template-based algorithm as well (Figure 6.15).

Figure 6.16 depicts the template-based algorithm's identified seed and marker locations compared to the validated seed and marker locations. Since curvature information is not available from the pre-implant template, curvature could not be accounted for the last strand when some markers in that strand had low signal intensity on MRI images.

The non-template-based and template-based algorithm localized seed and marker positions are shown in Figure 6.10 and 6.16. The sensitivity, precision and F-score acquired

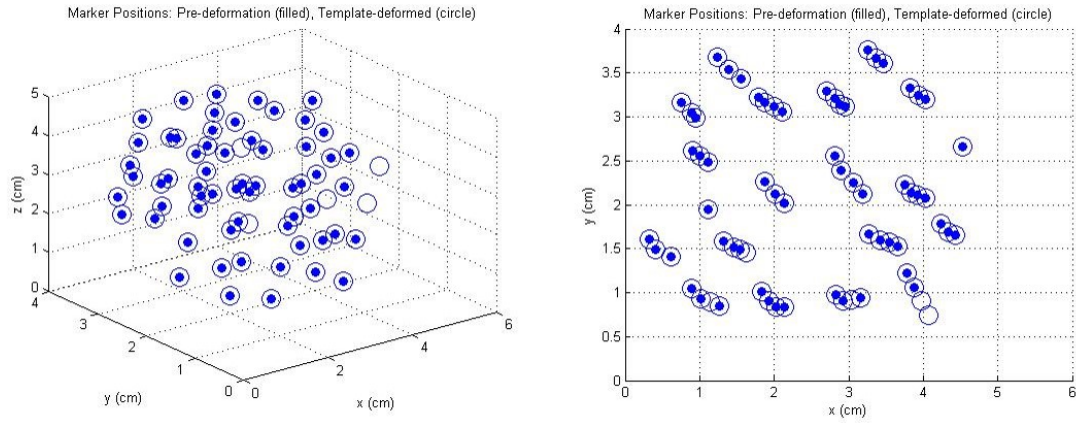


Figure 6.14: Non-template-based (filled circles) versus template-based (circles) marker and seed localization.

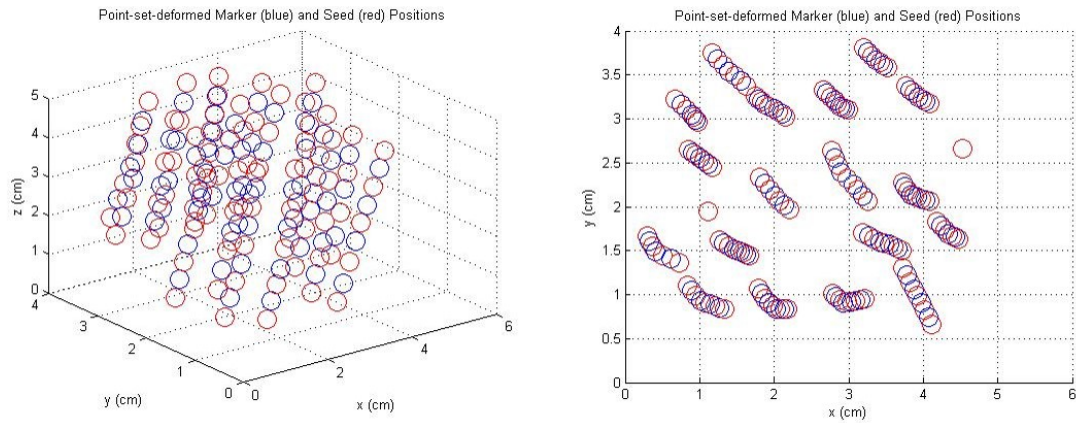


Figure 6.15: Template-based algorithm identified seed (red) and marker (blue) locations.

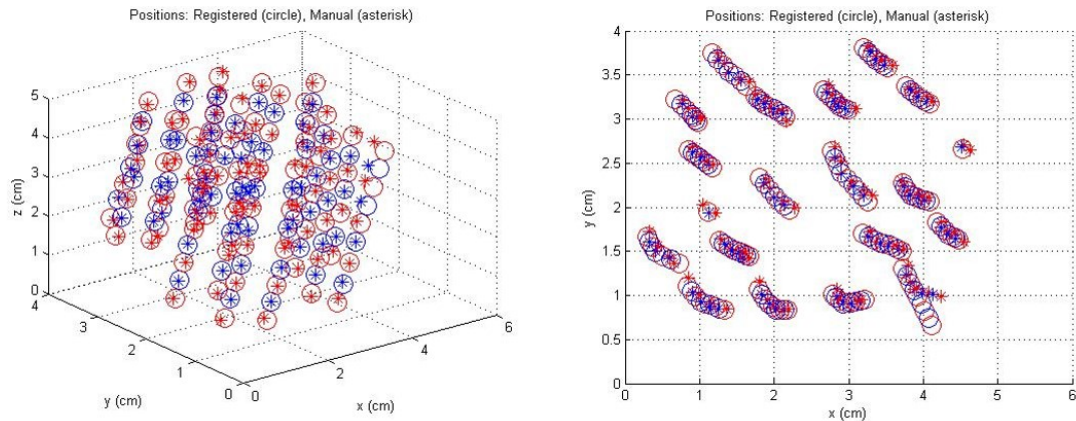


Figure 6.16: Seed (red) and marker (blue) positions identified by the template-based algorithm (circles) compared to seed and marker positions that were manually-identified (asterisks).

Table 6.1: Sensitivity, precision and F-score acquired for the non-template-based and template-based seed-identification algorithms.

	Non-template-based	Template-based
Markers		
Sensitivity	0.9242	0.9242
Precision	1.0000	1.0000
F-score	0.9606	0.9606
Seeds		
Sensitivity	0.9651	0.9884
Precision	1.0000	0.9884
F-score	0.9822	0.9884

for the non-template-based and template-based seed-identification algorithms are listed in Table 6.1. The non-template-based seed identification algorithm was prone to FN, as seed extrapolation would not occur if the adjacent marker was not identified. The template-based seed-identification algorithm was able to identify seeds even when the adjacent markers were not visible.

6.5 Conclusion

6.5.1 Summary

The seed-finding algorithms are flexible for localizing seeds at the ends of the strand. For the extrapolation-based method, the seeds can be detected if the adjacent markers were detected, but would not otherwise. For the template-based method, the seeds can be detected even if the adjacent markers were not detected.

6.5.2 Limitations

A limitation of the seed-localization algorithms outlined in this chapter is that they do not handle seed migration. For the template-based method, even when there is no marker or seed at a location, a marker or seed will be assigned at that location based on the template.

Another limitation of this study is that not all possible combinations of each image processing component were tested. For instance, for preprocessing, various image filters could be used and the order in which they are applied could be varied.

Moreover, the sensitivity and precision were set at certain limits that may under- or over-account for the number of markers and seeds detected. More stringent limits could be set which would result in lower sensitivity and precision.

Furthermore, the algorithms were tested on phantom images. Seed localization on patient images in the clinical scenario would be more challenging, especially with strands that may be more curved due to the manifestation and recession of edema distorting the strands. The marker-based seed-localization algorithms cannot handle curved strands as the seed locations are extrapolated from Sirius MRI marker locations. A vessel enhancement filter¹³⁵ may potentially be used to handle strand curvature. Further optimization and validation for the marker-based seed algorithms on clinical images is needed before routine clinical use.

6.5.3 Implications

The seed-finding algorithm could potentially be incorporated into the MIM Symphony TPS to ensure a smooth post-implant dosimetry workflow. The algorithm for seed-identification based on Sirius MRI markers has been developed. These Sirius MRI markers could potentially

enable more widespread use of MRI for post-implant dosimetry with further testing and optimization.

7

Final Discussion

Contents

7.1 Overall Summary	152
7.2 Future Directions	153
7.3 Future Implications	155

7.1 Overall Summary

The Sirius MRI markers may spur the use of MRI for post-implant dosimetry by helping overcome the barrier of seed localization on MRI images. To enable MRI-only post-implant dosimetry using Sirius MRI markers, a TPS that will allow for marker-based post-implant dosimetry is first needed. The MIM Symphony TPS was identified as a viable alternative to the widely-used VariSeed TPS. In Chapter 6, the calculations of DVH and other dosimetric

parameters by the two TPS were compared and found to be clinically-comparable.

The intrinsic relaxation characteristics of the C4 contrast agent encapsulated in the Sirius MRI markers were evaluated. The C4 contrast agent's spin-lattice and spin-spin relaxivities for different field strengths, orientations and temperatures have been documented in Chapter 3.

From the relaxation characteristics of the C4 contrast agent, a suitable pulse sequence that enhances the Sirius MRI markers was identified. In Chapter 4, the effects on the Sirius MRI markers' SNR, scan time and resolution due to variations in user-adjustable pulse sequence parameters, such as α , NEX, BW, FOV, Δz , and $N_x \times N_y$ were identified in a prostate phantom. Subsequently, the initial experience visualizing Sirius MRI markers in patients using the pulse sequence parameter ranges determined in phantom, as well as the unique challenges of using Sirius MRI markers in the clinical setting, were described in Chapter 5.

To enable higher efficiency in clinics, the observer-dependent manual seed localization on MRI images needs to be automated. Two approaches of marker-based seed localization algorithms, with and without pre-implant template information, were presented in Chapter 6.

7.2 Future Directions

The marker-based seed localization algorithm could be improved. Line detection methods may be incorporated into the algorithm to better handle curved strands. In the future, when more datasets (MRI images of the markers and the marker/seed locations) are available, sophisticated machine learning techniques may be explored for enhanced marker and seed localization. Instead of in-house algorithms operating external to the post-implant dosimetry workflow, the algorithms may be incorporated into the brachytherapy TPS for greater efficiency.

Future clinical trials for the Sirius MRI marker will further illuminate any clinical challenges. Depending on the pulse sequence used and time lapsed since the brachytherapy procedure, the Sirius MRI marker's signal may be obscured or confused with other hyper-

intense sources, such as adipose tissue, cysts, hemorrhage, or edema from infections.⁷² A potential study is to evaluate the post-implant MRI images for image quality, seed and marker visualization, geometric distortion and image blur using a subjective scoring system, similar to the method adopted by Schieda et al.¹²³

Efficacy and feasibility comparisons can also be made against other MRI-only post-implant dosimetric assessment methods that do not require the use of the Sirius MRI marker, such as the techniques^{69,70,73,114–122} described in Section 5.1.4.

Another possible study is the impact of the Sirius MRI markers by comparing DVH parameters generated from CT images, MRI images, and CT-MRI fusion images, given the MRI protocol described in this study. More importantly, the efficacy of using these DVH parameters for the prediction of acute and late effects of LDR prostate brachytherapy could be studied.

There may also be exciting implications for recurrence prediction and management using multiparametric MRI to assess tumor response to treating prostate cancer using prostate implants.¹³⁶ Multiparametric MRI combines anatomic imaging (T_2 -weighted imaging) with functional information from MR spectroscopy (MRS), diffusion-weighted imaging (DWI) and dynamic contrast-enhanced MRI (DCE-MRI). Although T_2 -weighted images have limited utility due to radiation-induced morphologic transformations such as inflammation and fibrosis, MRS, DWI and DCE-MRI may be used for detection of local recurrence.¹³⁷ Pathologic Gleason scores has been correlated with high MRS ratios.^{138–140} Cornud et al.¹⁴¹ reported the relationship between apparent diffusion coefficient from DWI to Gleason score. Future studies can look into the potential of correlating the dose distribution within the prostate on MRI images with additional information obtained using multiparametric MRI to guide the evaluation of the presence of clinically significant disease and the differentiation between recurrent disease or radiation necrosis.¹²⁴ While PSA elevations can be due to local or distant recurrence or even false-positives, MRI with endorectal coil and MRS findings can better correlate with biopsy findings of local tumor extent and aggressiveness, compared to PSA findings.^{66,142}

The incorporation of time-of-flight MR angiography for the visualization of the internal pudendal arteries to improve the management of erectile dysfunction⁵ can enhance marker-

based MRI-only post-implant dosimetry. Gillan et al.⁵ had established the use of time-of-flight MR angiography for Day 30 evaluation with CT-MRI fusion, and further research can be done with MRI-only post-implant dosimetric evaluation to assess the dose-response relationship.

Apart from post-implant dosimetry, the Sirius MRI marker may be used during real-time MRI-guided prostate brachytherapy for rapid intraoperative seed localization. D’Amico et al.¹³³ demonstrated real-time MRI-guided prostate brachytherapy using a 0.5 T intraoperative MRI, whereby each insertion the seed locations and DVH were calculated and adjustments can be made intraoperatively whenever necessary.

Another potential indication for the Sirius MRI marker is to serve as a fiducial marker for a variety of other image guided radiation therapy purposes. The use of both permanent and temporary implantable fiducial markers is standard in many disease sites. For example, fiducial markers are placed in the prostate for daily image-guided radiation treatment, in the cervix for localization and treatment planning, in the breast for tumor localization prior to lumpectomy, and in the lung for tumor tracking during radiation therapy.

7.3 Future Implications

MRI-based post-implant dosimetry may reduce inconsistencies in target delineation and subsequent reporting of DVH parameters. With more accurate DVH parameters, we can better quantify the radiation dose to cancerous and various surrounding normal tissue, such that a more accurate picture of acute and late effects of brachytherapy can be depicted. The dose-response relationship for critical organs and subsequent toxicity can be studied in a more meaningful manner, such that we can better manage the dose delivered to the prostate and surrounding critical structures in the future.

The ultimate objective of the LDR prostate brachytherapy treatment is to have high tumor control probability (TCP) and low normal tissue complication probability (NTCP), hence the current long-term goal would be to correlate the dose received by the prostate and adjacent critical structures to clinical outcomes. Accurate seed positions coupled with clear anatomical delineation on MRI images allows for accurate characterization of the dose distribution and lowers interobserver variation. This enables better prediction and prevention

of acute or late effects, as well as better prediction of underdosed areas in the prostate for enhanced tumor control. Sirius MRI markers may enable MRI-based post-implant dosimetry, and have exciting potential for biologically-based treatment plan evaluation and optimization. Biological evaluation of treatment plans using TCP and NTCP models may improve clinical decision making.¹⁴³ The more accurate dose and volume metrics provided by MRI-based post-implant dosimetry, combined with other considerations (such as age, performance status and patient-reported outcomes) may be used to build more predictive TCP and NTCP models.

Bibliography

- [1] Keith L. Moore, Anne M. Agur, and Arthur F. Dalley. *Essential Clinical Anatomy*. Philadelphia: Lippincott Williams and Wilkins, 2010.
- [2] 3rd Holmes D. R., B. J. Davis, C. C. Goulet, T. M. Wilson, L. A. Mynderse, K. M. Furutani, J. J. Camp, and R. A. Robb. “Shape analysis of the prostate: Establishing imaging specifications for the design of a transurethral imaging device for prostate brachytherapy guidance”. In: *Brachytherapy* 13.5 (2014), pp. 465–70.
- [3] Frank H. Netter. *Atlas of Human Anatomy*. 5th ed. Philadelphia: W. B. Saunders Co., 2011.
- [4] M. Hilts, I. Spadinger, and M. Keyes. “Comparison of methods for calculating rectal dose after (125)I prostate brachytherapy implants”. In: *Int J Radiat Oncol Biol Phys* 53.3 (2002), pp. 775–85.
- [5] C. Gillan, A. Kirilova, A. Landon, I. Yeung, G. Pond, and J. Crook. “Radiation dose to the internal pudendal arteries from permanent-seed prostate brachytherapy as determined by time-of-flight MR angiography”. In: *Int J Radiat Oncol Biol Phys* 65.3 (2006), pp. 688–93.
- [6] Rebecca L. Siegel, Kimberly D. Miller, and Ahmedin Jemal. “Cancer statistics, 2016”. In: *CA: A Cancer Journal for Clinicians* 66.1 (2016), pp. 7–30.
- [7] J. L. Mohler, A. J. Armstrong, R. R. Bahnson, A. V. D’Amico, B. J. Davis, J. A. Eastham, C. A. Enke, T. A. Farrington, C. S. Higano, E. M. Horwitz, M. Hurwitz, C. J. Kane, M. H. Kawachi, M. Kuettel, R. J. Lee, J. J. Meeks, D. F. Penson, E. R.

- Plimack, J. M. Pow-Sang, D. Raben, S. Richey, M. Roach, S. Rosenfeld, E. Schaeffer, T. A. Skolarus, E. J. Small, G. Sonpavde, S. Srinivas, S. A. Strobe, and J. Tward. *NCCN Clinical Practice Guidelines in Oncology: Prostate Cancer*. 2016.
- [8] A. V. D’Amico, R. Whittington, S. B. Malkowicz, J. Fondurulia, M. H. Chen, I. Kaplan, C. J. Beard, J. E. Tomaszewski, AA. Renshaw, A. Wein, and C. N. Coleman. “Pretreatment nomogram for prostate-specific antigen recurrence after radical prostatectomy or external-beam radiation therapy for clinically localized prostate cancer”. In: 17.1 (1999), pp. 168–72.
- [9] *Dose and Volume Specification for Reporting Intracavitary Therapy in Gynecology (Report 38)*. Tech. rep. International Commission on Radiation Units and Measurements, 1985.
- [10] B. J. Davis, E. M. Horwitz, W. R. Lee, J. M. Crook, R. G. Stock, G. S. Merrick, W. M. Butler, P. D. Grimm, N. N. Stone, L. Potters, A. L. Zietman, M. J. Zelefsky, and Society American Brachytherapy. “American Brachytherapy Society consensus guidelines for transrectal ultrasound-guided permanent prostate brachytherapy”. In: *Brachytherapy* 11.1 (2012), pp. 6–19.
- [11] S. A. Rosenthal, N. H. Bittner, D. C. Beyer, D. J. Demanes, B. J. Goldsmith, E. M. Horwitz, G. S. Ibbott, W. R. Lee, S. Nag, W. W. Suh, and L. Potters. “American Society for Radiation Oncology (ASTRO) and American College of Radiology (ACR) practice guideline for the transperineal permanent brachytherapy of prostate cancer”. In: *Int J Radiat Oncol Biol Phys* 79.2 (2011), pp. 335–41.
- [12] D. Ash, A. Flynn, J. Battermann, T. de Reijke, P. Lavagnini, and L. Blank. “ESTRO/EAU/EORTC recommendations on permanent seed implantation for localized prostate cancer”. In: *Radiother Oncol* 57.3 (2000), pp. 315–21.
- [13] *Permanent prostate brachytherapy*. URL: <http://www.mayoclinic.org/tests-procedures/prostate-brachytherapy/multimedia/permanent-prostate-brachytherapy/img-20008710>.

-
- [14] P. Vacha and R. Engenhart-Cabillic. “Radiation Therapy of Prostate Cancer”. In: *Prostate Cancer: Diagnosis and Surgical Treatment*. Ed. by R. Hofmann. Berlin: Springer-Verlag, 2003, pp. 177–83.
- [15] Mark J. Rivard, Bert M. Coursey, Larry A. DeWerd, William F. Hanson, M. Saiful Huq, Geoffrey S. Ibbott, Michael G. Mitch, Ravinder Nath, and Jeffrey F. Williamson. “Update of AAPM Task Group No. 43 Report: A revised AAPM protocol for brachytherapy dose calculations”. In: *Medical Physics* 31.3 (2004), pp. 633–674.
- [16] N. G. Thaker, T. J. Pugh, U. Mahmood, S. Choi, T. E. Spinks, N. E. Martin, T. T. Sio, R. J. Kudchadker, R. S. Kaplan, D. A. Kuban, D. A. Swanson, P. F. Orio, M. J. Zelefsky, B. W. Cox, L. Potters, T. A. Buchholz, T. W. Feeley, and S. J. Frank. “Defining the value framework for prostate brachytherapy using patient-centered outcome metrics and time-driven activity-based costing”. In: *Brachytherapy* (2016).
- [17] J. H. Hayes, D. A. Ollendorf, S. D. Pearson, M. J. Barry, P. W. Kantoff, P. A. Lee, and P. M. McMahon. “Observation Versus Initial Treatment for Men With Localized, Low-Risk Prostate Cancer: A Cost-Effectiveness Analysis”. In: *Ann Intern Med* 158.12 (2013).
- [18] C. Shah, Jr. Lanni T. B., M. I. Ghilezan, G. S. Gustafson, K. S. Marvin, H. Ye, F. A. Vicini, and A. A. Martinez. “Brachytherapy provides comparable outcomes and improved cost-effectiveness in the treatment of low/intermediate prostate cancer”. In: *Brachytherapy* 11.6 (2012), pp. 441–5.
- [19] J. F. Anderson, D. A. Swanson, L. B. Levy, D. A. Kuban, A. K. Lee, R. Kudchadker, J. Phan, T. Bruno, and S. J. Frank. “Urinary side effects and complications after permanent prostate brachytherapy: the MD Anderson Cancer Center experience”. In: *Urology* 74.3 (2009), pp. 601–5.
- [20] S. J. Frank, R. J. Stafford, J. A. Bankson, C. Li, D. A. Swanson, R. J. Kudchadker, and K. S. Martirosyan. “A novel MRI marker for prostate brachytherapy”. In: *Int J Radiat Oncol Biol Phys* 71.1 (2008), pp. 5–8.

-
- [21] J. Phan, D. A. Swanson, L. B. Levy, R. J. Kudchadker, T. L. Bruno, and S. J. Frank. “Late rectal complications after prostate brachytherapy for localized prostate cancer: incidence and management”. In: *Cancer* 115.9 (2009), pp. 1827–39.
- [22] G. S. Merrick, K. Wallner, W. M. Butler, J. H. Lief, and S. Sutlief. “Short-term sexual function after prostate brachytherapy”. In: *Int J Cancer* 96.5 (2001), pp. 313–9.
- [23] J. T. Whaley, L. B. Levy, D. A. Swanson, T. J. Pugh, R. J. Kudchadker, T. L. Bruno, and S. J. Frank. “Sexual function and the use of medical devices or drugs to optimize potency after prostate brachytherapy”. In: *Int J Radiat Oncol Biol Phys* 82.5 (2012), e765–71.
- [24] Y. Yu, L. L. Anderson, Z. Li, D. E. Mellenberg, R. Nath, M. C. Schell, F. M. Waterman, A. Wu, and J. C. Blasko. “Permanent prostate seed implant brachytherapy: report of the American Association of Physicists in Medicine Task Group No. 64”. In: *Med Phys* 26.10 (1999), pp. 2054–76.
- [25] B. H. Han, K. Wallner, G. Merrick, K. Badiozamani, and W. Butler. “The effect of interobserver differences in post-implant prostate CT image interpretation on dosimetric parameters”. In: *Med Phys* 30.6 (2003), pp. 1096–102.
- [26] Jr. Bice W. S., B. R. Prestidge, P. D. Grimm, J. L. Friedland, V. Feygelman, 3rd Roach M., J. J. Prete, D. F. Dubois, and J. C. Blasko. “Centralized multiinstitutional postimplant analysis for interstitial prostate brachytherapy”. In: *Int J Radiat Oncol Biol Phys* 41.4 (1998), pp. 921–7.
- [27] M. De Brabandere, P. Hoskin, K. Haustermans, F. Van den Heuvel, and F. A. Siebert. “Prostate post-implant dosimetry: interobserver variability in seed localisation, contouring and fusion”. In: *Radiother Oncol* 104.2 (2012), pp. 192–8.
- [28] S. J. Frank, L. B. Levy, D. A. Kuban, A. K. Lee, R. J. Kudchadker, T. L. Bruno, M. van Vulpen, and D. A. Swanson. “Prostogram predicted brachytherapy outcomes are not universally accurate: an analysis based on the M. D. Anderson Cancer Center experience with (125)iodine brachytherapy”. In: *J Urol* 181.4 (2009), 1658–63; discussion 1663–4.

-
- [29] B. Al-Qaisieh, D. W. Smith, E. Brearley, S. St Clair, and P. Bownes. “Comprehensive I-125 multi-seed comparison for prostate brachytherapy: dosimetry and visibility analysis”. In: *Radiother Oncol* 84.2 (2007), pp. 140–7.
- [30] D. Ash, B. Al-Qaisieh, D. Bottomley, B. Carey, and J. Joseph. “The correlation between D90 and outcome for I-125 seed implant monotherapy for localised prostate cancer”. In: *Radiother Oncol* 79.2 (2006), pp. 185–9.
- [31] J. Crook, N. Patil, C. Ma, M. McLean, and J. Borg. “Magnetic resonance imaging-defined treatment margins in iodine-125 prostate brachytherapy”. In: *Int J Radiat Oncol Biol Phys* 77.4 (2010), pp. 1079–84.
- [32] Y. Kono, K. Kubota, T. Aruga, A. Ishibashi, M. Morooka, K. Ito, J. Itami, M. Kanemura, S. Minowada, and T. Tanaka. “Swelling of the Prostate Gland by Permanent Brachytherapy May Affect Seed Migration”. In: *Japanese Journal of Clinical Oncology* 40.12 (2010), pp. 1159–65.
- [33] C. A. Kunos, M. I. Resnick, T. J. Kinsella, and R. J. Ellis. “Migration of implanted free radioactive seeds for adenocarcinoma of the prostate using a Mick applicator”. In: *Brachytherapy* 3.2 (2004), pp. 71–7.
- [34] B. Al-Qaisieh, B. Carey, D. Ash, and D. Bottomley. “The use of linked seeds eliminates lung embolization following permanent seed implantation for prostate cancer”. In: *Int J Radiat Oncol Biol Phys* 59.2 (2004), pp. 397–9.
- [35] R. G. Stock, N. N. Stone, A. Tabert, C. Iannuzzi, and J. K. DeWyngaert. “A dose-response study for I-125 prostate implants”. In: *Int J Radiat Oncol Biol Phys* 41.1 (1998), pp. 101–8.
- [36] M. J. Zelefsky, D. A. Kuban, L. B. Levy, L. Potters, D. C. Beyer, J. C. Blasko, B. J. Moran, J. P. Ciezki, A. L. Zietman, T. M. Pisansky, M. Elshaikh, and E. M. Horwitz. “Multi-institutional analysis of long-term outcome for stages T1-T2 prostate cancer treated with permanent seed implantation”. In: *Int J Radiat Oncol Biol Phys* 67.2 (2007), pp. 327–33.

- [37] S. Choi, K. E. Wallner, G. S. Merrick, W. Cavanagh, and W. M. Butler. "Treatment margins predict biochemical outcomes after prostate brachytherapy". In: *Cancer J* 10.3 (2004), pp. 175–80.
- [38] L. Potters, C. Morgenstern, E. Calugaru, P. Fearn, A. Jassal, J. Presser, and E. Mullen. "12-year outcomes following permanent prostate brachytherapy in patients with clinically localized prostate cancer". In: *J Urol* 179.5 Suppl (2008), S20–4.
- [39] N. N. Stone, L. Potters, B. J. Davis, J. P. Ciezki, M. J. Zelefsky, M. Roach, K. Shinohara, P. A. Fearn, M. W. Kattan, and R. G. Stock. "Multicenter analysis of effect of high biologic effective dose on biochemical failure and survival outcomes in patients with Gleason score 7-10 prostate cancer treated with permanent prostate brachytherapy". In: *Int J Radiat Oncol Biol Phys* 73.2 (2009), pp. 341–6.
- [40] O. Tanaka, S. Hayashi, M. Matsuo, M. Nakano, H. Uno, K. Ohtakara, T. Miyoshi, T. Deguchi, and H. Hoshi. "Effect of edema on postimplant dosimetry in prostate brachytherapy using CT/MRI fusion". In: *Int J Radiat Oncol Biol Phys* 69.2 (2007), pp. 614–8.
- [41] J. Crook, M. McLean, I. Yeung, T. Williams, and G. Lockwood. "MRI-CT fusion to assess postbrachytherapy prostate volume and the effects of prolonged edema on dosimetry following transperineal interstitial permanent prostate brachytherapy". In: *Brachytherapy* 3.2 (2004), pp. 55–60.
- [42] P. Acher, S. Puttagunta, K. Rhode, S. Morris, J. Kinsella, A. Gaya, P. Dasgupta, C. Deehan, R. Beaney, R. Popert, and S. Keevil. "An analysis of intraoperative versus post-operative dosimetry with CT, CT-MRI fusion and XMR for the evaluation of permanent prostate brachytherapy implants". In: *Radiother Oncol* 96.2 (2010), pp. 166–71.
- [43] J. Crook, M. Milosevic, P. Catton, I. Yeung, T. Haycocks, T. Tran, C. Catton, M. McLean, T. Panzarella, and M. A. Haider. "Interobserver variation in postimplant computed tomography contouring affects quality assessment of prostate brachytherapy". In: *Brachytherapy* 1.2 (2002), pp. 66–73.

-
- [44] D. F. Dubois, B. R. Prestidge, L. A. Hotchkiss, J. J. Prete, and Jr. Bice W. S. “Intraobserver and interobserver variability of MR imaging- and CT-derived prostate volumes after transperineal interstitial permanent prostate brachytherapy”. In: *Radiology* 207.3 (1998), pp. 785–9.
- [45] Ravinder Nath, Lowell L Anderson, Gary Luxton, Keith A Weaver, Jeffrey F Williamson, and Ali S Meigooni. “Dosimetry of interstitial brachytherapy sources: Recommendations”. In: *Medical physics* 22.2 (1995), pp. 209–234.
- [46] Mark J. Rivard, Wayne M. Butler, Larry A. DeWerd, M. Saiful Huq, Geoffrey S. Ibbott, Zuofeng Li, Michael G. Mitch, Ravinder Nath, and Jeffrey F. Williamson. “Erratum: Update of AAPM Task Group No. 43 Report: A revised AAPM protocol for brachytherapy dose calculations”. In: *Medical Physics* 31.12 (2004), pp. 3532–3533.
- [47] Mark J. Rivard, Wayne M. Butler, Larry A. DeWerd, M. Saiful Huq, Geoffrey S. Ibbott, Ali S. Meigooni, Christopher S. Melhus, Michael G. Mitch, Ravinder Nath, and Jeffrey F. Williamson. “Supplement to the 2004 update of the AAPM Task Group No. 43 Report”. In: *Medical Physics* 34.6 (2007), p. 2187.
- [48] Mark J. Rivard, Wayne M. Butler, Larry A. DeWerd, Geoffrey S. Ibbott, Ali S. Meigooni, Christopher S. Melhus, Michael G. Mitch, and Ravinder Nath. “Erratum: Supplement to the 2004 update of the AAPM Task Group No. 43 Report”. In: *Medical Physics* 37.5 (2010), p. 2396.
- [49] M. De Brabandere, C. Kirisits, R. Peeters, K. Haustermans, and F. Van den Heuvel. “Accuracy of seed reconstruction in prostate postplanning studied with a CT- and MRI-compatible phantom”. In: *Radiother Oncol* 79.2 (2006), pp. 190–7.
- [50] M. Aoki, A. Yorozu, and T. Dokiya. “Results of a dummy run of postimplant dosimetry between multi-institutional centers in prostate brachytherapy with ^{125}I seeds”. In: *Jpn J Radiol* 27.10 (2009), pp. 410–5.
- [51] W. L. Smith, C. Lewis, G. Bauman, G. Rodrigues, D. D’Souza, R. Ash, D. Ho, V. Venkatesan, D. Downey, and A. Fenster. “Prostate volume contouring: a 3D analysis

- of segmentation using 3DTRUS, CT, and MR”. In: *Int J Radiat Oncol Biol Phys* 67.4 (2007), pp. 1238–47.
- [52] N. Usmani, R. Sloboda, W. Kamal, S. Ghosh, N. Pervez, J. Pedersen, D. Yee, B. Danielson, A. Murtha, J. Amanie, and T. Monajemi. “Can images obtained with high field strength magnetic resonance imaging reduce contouring variability of the prostate?” In: *Int J Radiat Oncol Biol Phys* 80.3 (2011), pp. 728–34.
- [53] C. Rasch, I. Barillot, P. Remeijer, A. Touw, M. van Herk, and J. V. Lebesque. “Definition of the prostate in CT and MRI: a multi-observer study”. In: *Int J Radiat Oncol Biol Phys* 43.1 (1999), pp. 57–66.
- [54] P. W. McLaughlin, V. Narayana, D. G. Drake, B. M. Miller, L. Marsh, J. Chan, Jr. Gonda R., R. J. Winfield, and P. L. Roberson. “Comparison of MRI pulse sequences in defining prostate volume after permanent implantation”. In: *Int J Radiat Oncol Biol Phys* 54.3 (2002), pp. 703–11.
- [55] K. Buch, T. Morancy, I. Kaplan, M. M. Qureshi, A. E. Hirsch, N. M. Rofksy, E. Holupka, R. Oismueller, R. Hawliczek, T. H. Helbich, and B. N. Bloch. “Improved dosimetry in prostate brachytherapy using high resolution contrast enhanced magnetic resonance imaging: a feasibility study”. In: *J Contemp Brachytherapy* 6.4 (2015), pp. 337–43.
- [56] S. P. Register, R. J. Kudchadker, L. B. Levy, D. A. Swanson, T. J. Pugh, T. L. Bruno, and S. J. Frank. “An MRI-based dose-response analysis of urinary sphincter dose and urinary morbidity after brachytherapy for prostate cancer in a phase II prospective trial”. In: *Brachytherapy* 12.3 (2013), pp. 210–6.
- [57] T. Y. Lim, R. J. Stafford, R. J. Kudchadker, M. Sankaranarayananpillai, G. Ibbott, A. Rao, K. S. Martirosyan, and S. J. Frank. “MRI characterization of cobalt dichloride-N-acetyl cysteine (C4) contrast agent marker for prostate brachytherapy”. In: *Phys Med Biol* 59.10 (2014), pp. 2505–16.

-
- [58] J. Christodouleas, J. Fox, T. DeWeese, and D. Song. “Radiation Therapy for Prostate Cancer”. In: *Early Diagnosis of Cancer: Prostate Cancer*. Ed. by L. M. Su. Philadelphia: Elsevier Publishers, 2009.
- [59] D. Petrik, C. Araujo, D. Kim, R. Halperin, and J. M. Crook. “Implications of CT imaging for postplan quality assessment in prostate brachytherapy”. In: *Brachytherapy* 11.6 (2012), pp. 435–40.
- [60] D. Beyersdorff, K. Taymoorian, T. Knosel, D. Schnorr, R. Felix, B. Hamm, and H. Bruhn. “MRI of prostate cancer at 1.5 and 3.0 T: comparison of image quality in tumor detection and staging”. In: *AJR Am J Roentgenol* 185.5 (2005), pp. 1214–20.
- [61] J. M. Albert, D. A. Swanson, T. J. Pugh, M. Zhang, T. L. Bruno, R. J. Kudchadker, and S. J. Frank. “Magnetic resonance imaging-based treatment planning for prostate brachytherapy”. In: *Brachytherapy* 12.1 (2013), pp. 30–7.
- [62] K. Tanderup, A. N. Viswanathan, C. Kirisits, and S. J. Frank. “Magnetic resonance image guided brachytherapy”. In: *Semin Radiat Oncol* 24.3 (2014), pp. 181–91.
- [63] M. Barkati, S. Van Dyk, F. Foroudi, and K. Narayan. “The use of magnetic resonance imaging for image-guided brachytherapy”. In: *J Med Imaging Radiat Oncol* 54.2 (2010), pp. 137–41.
- [64] Seungtaek Choi. “The Role of Magnetic Resonance Imaging in the Detection of Prostate Cancer”. In: *The Journal of Urology* 186.4 (2011), pp. 1181–1182.
- [65] C. F. Geraldles and S. Laurent. “Classification and basic properties of contrast agents for magnetic resonance imaging”. In: *Contrast Media Mol Imaging* 4.1 (2009), pp. 1–23.
- [66] P. R. Carroll, F. V. Coakley, and J. Kurhanewicz. “Magnetic resonance imaging and spectroscopy of prostate cancer”. In: *Rev Urol* 8 Suppl 1 (2006), S4–S10.
- [67] B. N. Bloch, R. E. Lenkinski, T. H. Helbich, L. Ngo, R. Oismueller, S. Jaromi, K. Kubin, R. Hawliczek, I. D. Kaplan, and N. M. Rofsky. “Prostate postbrachytherapy seed distribution: comparison of high-resolution, contrast-enhanced, T1- and T2-

- weighted endorectal magnetic resonance imaging versus computed tomography: initial experience”. In: *Int J Radiat Oncol Biol Phys* 69.1 (2007), pp. 70–8.
- [68] J. L. Wright, J. H. Newhouse, J. L. Laguna, D. Vecchio, and R. D. Ennis. “Localization of neurovascular bundles on pelvic CT and evaluation of radiation dose to structures putatively involved in erectile dysfunction after prostate brachytherapy”. In: *Int J Radiat Oncol Biol Phys* 59.2 (2004), pp. 426–35.
- [69] M. A. Moerland, H. K. Wijrdeman, R. Beersma, C. J. Bakker, and J. J. Battermann. “Evaluation of permanent I-125 prostate implants using radiography and magnetic resonance imaging”. In: *Int J Radiat Oncol Biol Phys* 37.4 (1997), pp. 927–33.
- [70] D. F. Dubois, B. R. Prestidge, L. A. Hotchkiss, Jr. Bice W. S., and J. J. Prete. “Source localization following permanent transperineal prostate interstitial brachytherapy using magnetic resonance imaging”. In: *Int J Radiat Oncol Biol Phys* 39.5 (1997), pp. 1037–41.
- [71] M. De Brabandere, B. Al-Qaisieh, L. De Wever, K. Haustermans, C. Kirisits, M. A. Moerland, R. Oyen, A. Rijnders, F. Van den Heuvel, and F. A. Siebert. “CT- and MRI-based seed localization in postimplant evaluation after prostate brachytherapy”. In: *Brachytherapy* 12.6 (2013), pp. 580–8.
- [72] M. D. Bridges. “Pelvis: male MRI Normal Variants and Pitfalls”. In: ed. by L. W. Bancroft and M. D. Bridges. Philadelphia: Lippincott Williams and Wilkins, 2009, pp. 450–67.
- [73] Melissa Lamberto. “A Feasibility Study of Ultra-short Echo Time MRI for Positive Contrast Visualization of Prostate Brachytherapy Permanent Seed Implants for Post-implant Dosimetry”. MA thesis. Louisiana State University, 2014.
- [74] D. Bowes, J. M. Crook, R. Rajapakshe, C. Araujo, and B. Parker. “Defining a magnetic resonance scan sequence for permanent seed prostate brachytherapy postimplant assessment”. In: *Brachytherapy* 12.1 (2013), pp. 25–9.
- [75] S. J. Frank, R. C. Tailor, R. J. Kudchadker, K. S. Martirosyan, R. J. Stafford, A. M. Elliott, D. A. Swanson, D. Sing, J. Choi, F. Mourtada, and G. S. Ibbott. “Anisotropy

- characterization of I-125 seed with attached encapsulated cobalt chloride complex contrast agent markers for MRI-based prostate brachytherapy”. In: *Med Dosim* 36.2 (2011), pp. 200–5.
- [76] C. S. Melhus, J. K. Mikell, S. J. Frank, F. Mourtada, and M. J. Rivard. “Dosimetric influence of seed spacers and end-weld thickness for permanent prostate brachytherapy”. In: *Brachytherapy* (2013).
- [77] S. J. Frank, M. J. Johansen, K. S. Martirosyan, M. Gagea, C. S. Van Pelt, A. Borne, Y. Carmazzi, and T. Madden. “A biodistribution and toxicity study of cobalt dichloride-N-acetyl cysteine in an implantable MRI marker for prostate cancer treatment”. In: *Int J Radiat Oncol Biol Phys* 85.4 (2013), pp. 1024–30.
- [78] R. J. Kudchadker, D. A. Swanson, D. A. Kuban, A. K. Lee, T. L. Bruno, and S. J. Frank. “Is a loose-seed nomogram still valid for prostate brachytherapy in a stranded-seed era?” In: *Int J Radiat Oncol Biol Phys* 72.2 (2008), pp. 623–7.
- [79] S. K. Dhanesar, T. Y. Lim, W. Du, T. L. Bruno, S. J. Frank, and R. J. Kudchadker. “Evaluation of the MIM Symphony treatment planning system for low-dose-rate prostate brachytherapy”. In: *J Appl Clin Med Phys* 16.5 (2015), pp. 62–75.
- [80] R. Tailor, G. Ibbott, S. Lampe, W. B. Warren, and N. Tolani. “Dosimetric characterization of a Cs131Cs131 brachytherapy source by thermoluminescence dosimetry in liquid water”. In: 35.12 (2008), pp. 5861–8.
- [81] M. S. Gossman, S. S. Hancock, R. J. Kudchadker, P. R. Lundahl, M. Cao, and C. S. Melhus. “Brachytherapy dose-volume histogram commissioning with multiple planning systems”. In: *J Appl Clin Med Phys* 15.2 (2014), p. 4620.
- [82] *VariSeedTM 8.0 User Test Procedures*.
- [83] *VariSeedTM 8.0: I-125 (6711) Source Specification/User Test Data*.
- [84] S. M. Shirvani, R. J. Kudchadker, T. L. Bruno, A. Likhacheva, D. A. Swanson, and S. J. Frank. “Impact of urinary catheterization on dosimetry after prostate implant brachytherapy with palladium-103 or iodine-125”. In: *Brachytherapy* 10.4 (2011), pp. 269–74.

-
- [85] Jerrold T. Bushberg. *The essential physics of medical imaging*. 3rd ed. Philadelphia: Lippincott Williams and Wilkins, 2012.
- [86] D. W. McRobbie, E. A. Moore, M. J. Graves, and M. R. Prince. *MRI: From picture to proton*. New York: Cambridge University Press, 2013.
- [87] R. B. Lauffer. “MRI contrast agents: basic principles”. In: *Clinical Magnetic Resonance Imaging*. Ed. by R. R. Edelman. Vol. 1. Philadelphia: W. B. Saunders, 1996, pp. 177–91.
- [88] Nahideh Gharehaghaji, Mohammad Ali Oghabian, Saeed Sarkar, Saeedeh Amir-mohseni, and Hossein Ghanaati. “Optimization of Pulse Sequences in Magnetic Resonance Lymphography of Axillary Lymph Nodes Using Magnetic Nanoparticles”. In: *Journal of Nanoscience and Nanotechnology* 9.7 (2009), pp. 4448–4452.
- [89] R. M. Henkelman, P. Hardy, P. Y. Poon, and M. J. Bronskill. “Optimal pulse sequence for imaging hepatic metastases”. In: *Radiology* 161.3 (1986), pp. 727–34.
- [90] W. R. Hendee and C. J. Morgan. “Magnetic resonance imaging. Part II—Clinical applications”. In: *West J Med* 141.5 (1984), pp. 638–48.
- [91] K. Levenberg. “A method for the solution of certain non-linear problems in least squares”. In: *Quart. Appl. Math.* 2 (1944), pp. 164–8.
- [92] D Marquardt. “An algorithm for least-squares estimation of nonlinear parameters”. In: *J. Appl. Math.* 11 (1963), pp. 431–41.
- [93] S. D. Thomas, K. Wachowicz, and B. G. Fallone. “MRI of prostate brachytherapy seeds at high field: A study in phantom”. In: *Medical Physics* 36.11 (2009), p. 5228.
- [94] J. R. Reichenbach, T. Hacklander, T. Harth, M. Hofer, M. Rassek, and U. Modder. “ ^1H T1 and T2 measurements of the MR imaging contrast agents Gd-DTPA and Gd-DTPA BMA at 1.5T”. In: *Eur Radiol* 7.2 (1997), pp. 264–74.
- [95] D. Hao, T. Ai, F. Goerner, X. Hu, V. M. Runge, and M. Tweedle. “MRI contrast agents: basic chemistry and safety”. In: *J Magn Reson Imaging* 36.5 (2012), pp. 1060–71.

-
- [96] T. Y. Lim, R. J. Kudchadker, J. Wang, R. J. Stafford, C. J. MacLellan, A. Rao, G. Ibbott, and S. J. Frank. “Effect of pulse sequence parameter selection on signal strength in positive-contrast MRI markers for MRI-based prostate post-implant assessment”. In: *Med Phys* 43.7 (2016).
- [97] E. L. Hahn. “Spin Echoes”. In: *Physical Review* 80.4 (1950), pp. 580–594.
- [98] A. D. Elster. “Gradient-echo MR Imaging: Techniques and Acronyms”. In: *Radiology* 186 (1993), pp. 1–8.
- [99] C. M. de Bazelaire, G. D. Duhamel, N. M. Rofsky, and D. C. Alsop. “MR imaging relaxation times of abdominal and pelvic tissues measured in vivo at 3.0 T: preliminary results”. In: *Radiology* 230.3 (2004), pp. 652–9.
- [100] R. H. Hashemi, W. G. Bradley, and C. J. Lisanti. *MRI: the basics*. Philadelphia: Lippincott Williams and Wilkins, 2010.
- [101] *Determination of Signal-to-Noise Ratio (SNR) in Diagnostic Magnetic Resonance Imaging*. 2008.
- [102] E. M. Haacke, R. W. Brown, M. R. Thompson, and R. Venkatesan. *Magnetic Resonance Imaging: Physical Principles and Sequence Design*. New York: John Wiley and Sons, Inc., 1999.
- [103] T. Y. Lim, R. J. Kudchadker, J. Wang, T. Bathala, J. Szklaruk, T. J. Pugh, U. Mahmood, G. S. Ibbott, and S. J. Frank. “Development of an MRI protocol to visualize encapsulated contrast agent markers in prostate brachytherapy recipients: Initial patient experience”. In: *J Contemp Brachytherapy* 8.3 (2016).
- [104] W. R. Hendee and C. J. Morgan. “Magnetic resonance imaging. Part I—physical principles”. In: *West J Med* 141.4 (1984), pp. 491–500.
- [105] *Healthcare Bluebook*. 2016. URL: https://healthcarebluebook.com/page_ConsumerFront.aspx.
- [106] R. J. Amdur, D. Gladstone, K. A. Leopold, and R. D. Harris. “Prostate seed implant quality assessment using MR and CT image fusion”. In: *Int J Radiat Oncol Biol Phys* 43.1 (1999), pp. 67–72.

-
- [107] P. L. Roberson, P. W. McLaughlin, V. Narayana, S. Troyer, G. V. Hixson, and M. L. Kessler. “Use and uncertainties of mutual information for computed tomography/magnetic resonance (CT/MR) registration post permanent implant of the prostate”. In: *Med Phys* 32.2 (2005), pp. 473–82.
- [108] H. Kunogi, H. Hojo, Y. Wakumoto, A. I. Saito, S. Ishikura, Y. Yamashiro, R. Kuwatsuru, and K. Sasai. “A new two-step accurate CT-MRI fusion technique for post-implant prostate cancer”. In: *J Contemp Brachytherapy* 7.2 (2015), pp. 117–21.
- [109] A. M. Tahmasebi, R. Sharifi, H. K. Agarwal, B. Turkbey, M. Bernardo, P. Choyke, P. Pinto, B. Wood, and J. Kruecker. “A statistical model-based technique for accounting for prostate gland deformation in endorectal coil-based MR imaging”. In: *Conf Proc IEEE Eng Med Biol Soc* 2012 (2012), pp. 5412–5.
- [110] D. B. Fuller, H. Jin, J. A. Koziol, and A. C. Feng. “CT-ultrasound fusion prostate brachytherapy: a dynamic dosimetry feedback and improvement method. A report of 54 consecutive cases”. In: *Brachytherapy* 4.3 (2005), pp. 207–16.
- [111] O. Tanaka, S. Hayashi, M. Matsuo, K. Sakurai, M. Nakano, S. Maeda, K. Kajita, T. Deguchi, and H. Hoshi. “Comparison of MRI-based and CT/MRI fusion-based postimplant dosimetric analysis of prostate brachytherapy”. In: *Int J Radiat Oncol Biol Phys* 66.2 (2006), pp. 597–602.
- [112] K. Wachowicz, S. D. Thomas, and B. G. Fallone. “Characterization of the susceptibility artifact around a prostate brachytherapy seed in MRI”. In: *Medical Physics* 33.12 (2006), pp. 4459–4467.
- [113] A. K. Robertson, P. S. Basran, S. D. Thomas, and D. Wells. “CT, MR, and ultrasound image artifacts from prostate brachytherapy seed implants: the impact of seed size”. In: *Med Phys* 39.4 (2012), pp. 2061–8.
- [114] N. Kuo, J. Lee, C. Tempany, M. Stuber, and J. Prince. “MRI-Based Prostate Brachytherapy Seed Localization”. In: *Proc IEEE Int Symp Biomed Imaging* 2010 (2010), pp. 1397–1400.

-
- [115] A. Fatemi-Ardekani and J. Borg. “Identifying prostate brachytherapy seeds at MRI: A study in phantom”. In: *Proc. Intl. Soc. Mag. Reson. Med.* 19 (2011).
 - [116] A. Elzibak, A. Fatemi-Ardekani, A. Soliman, S. Mashouf, H. Safigholi, D. Han, A. Ravi, G. Morton, and W. Y. Song. “Towards MR-only Image Guided Identification of Calcifications and Brachytherapy Seeds: Application to Prostate and Breast LDR Implant Dosimetry”. In: vol. 42. 2015, p. 3315.
 - [117] G. Varma, R. E. Clough, P. Acher, J. Senegas, H. Dahnke, S. F. Keevil, and T. Schaeffter. “Positive Visualization of Implanted Devices with Susceptibility Gradient Mapping using the Original Resolution”. In: *Magn Resonan Med* 65.5 (2011), pp. 1483–90.
 - [118] Y. Dong, Z. Chang, G. Xie, G. Whitehead, and J. Ji. “Susceptibility-based Positive Contrast MRI of Brachytherapy Seeds”. In: *Magn Reson Med* 74 (2015), pp. 716–726.
 - [119] Y. Dong and J. Ji. “Positive contrast MRI of prostate brachytherapy seeds by susceptibility mapping”. In: *Conf Proc IEEE Eng Med Biol Soc* (2012), pp. 392–5.
 - [120] Y. Dong, Z. Chang, G. Whitehead, and J. Ji. “Localization of brachytherapy seeds in MRI by deconvolution”. In: *Conf Proc IEEE Eng Med Biol Soc* (2013), pp. 2960–3.
 - [121] P. R. Seevinck, H. de Leeuw, C. Bos, and C. J. G. Bakker. “Highly Localized Positive Contrast of Small Paramagnetic Objects using 3D Center-out Radial Sampling with Off-resonance Reception”. In: *Magn Reson Med* 65 (2011), pp. 146–56.
 - [122] H. de Leeuw, P. R. Seevinck, and C. J. G. Bakker. “Center-out Radial Sampling with Off-resonant Reconstruction for Efficient and Accurate Localization of Punctuate and Elongated Paramagnetic Structures”. In: *Magn Reson Med* 65 (2011), pp. 1611–22.
 - [123] N. Schieda, L. Avruch, W. M. Shabana, and S. C. Malone. “Multi-echo gradient recalled echo imaging of the pelvis for improved depiction of brachytherapy seeds and fiducial markers facilitating radiotherapy planning and treatment of prostatic carcinoma”. In: *J Magn Reson Imaging* 41.3 (2015), pp. 715–20.

-
- [124] J. O. Barentsz, J. Richenberg, R. Clements, P. Choyke, S. Verma, G. Villeirs, O. Rouviere, V. Logager, and J. J. Futterer. “ESUR prostate MR guidelines 2012”. In: *Eur Radiol* 22.4 (2012), pp. 746–57.
- [125] A. Fransson, P. Andreo, and R. Potter. “Aspects of MR image distortions in radiotherapy treatment planning”. In: *Strahlenther Onkol* 177.2 (2001), pp. 59–73.
- [126] Y. Kim, I. C. Hsu, J. Pouliot, S. M. Noworolski, D. B. Vigneron, and J. Kurhanewicz. “Expandable and rigid endorectal coils for prostate MRI: impact on prostate distortion and rigid image registration”. In: *Med Phys* 32.12 (2005), pp. 3569–78.
- [127] D. H. Brinkmann and R. W. Kline. “Automated seed localization from CT datasets of the prostate”. In: *Med Phys* 25.9 (1998), pp. 1667–72.
- [128] Z. Li, I. A. Nalcacioglu, S. Ranka, S. K. Sahni, J. R. Palta, W. Tome, and S. Kim. “An algorithm for automatic, computed-tomography-based source localization after prostate implant”. In: *Med Phys* 28.7 (2001), pp. 1410–5.
- [129] R. J. Lee, H. S. Suh, K. J. Lee, S. Lim, Y. Kim, S. Kim, and J. Choi. “A magnetic resonance-based seed localization method for I-125 prostate implants”. In: *J Korean Med Sci* 22 Suppl (2007), S129–33.
- [130] E. J. Holupka, P. M. Meskill, E. C. Burdette, and I. D. Kaplan. “An automatic seed finder for brachytherapy CT postplans based on the Hough transform”. In: *Medical Physics* 31.9 (2004), p. 2672.
- [131] E. J. Holupka, P. M. Meskill, and I. D. Kaplan. “Automatic detection of linear artifacts in medical images”. In: *Medical Physics* 31.9 (2004), p. 2707.
- [132] Dragan Tubic and Luc Beaulieu. “Sliding slice: A novel approach for high accuracy and automatic 3D localization of seeds from CT scans”. In: *Medical Physics* 32.1 (2005), p. 163.
- [133] A. V. D’Amico, R. Cormack, C. M. Tempany, S. Kumar, G. Topulos, H. M. Kooy, and C. N. Coleman. “Real-time Magnetic Resonance Image-guided Interstitial Brachytherapy in the Treatment of Select Patients with Clinically Localized Prostate Cancer”. In: *Int J Radiat Oncol Biol Phys* 42.3 (1998), pp. 507–15.

- [134] R. A. Cormack, H. Kooy, C. M. Tempany, and A. V. D’Amico. “A clinical method for real-time dosimetric guidance of transperineal ^{125}I prostate implants using interventional magnetic resonance imaging”. In: *Int J Radiat Oncol Biol Phys* 46.1 (2000), pp. 207–14.
- [135] Alejandro F. Frangi, Wiro J. Niessen, Koen L. Vincken, and Max A. Viergever. “Multiscale vessel enhancement filtering”. In: *Medical Image Computing and Computer Assisted Interventions*. Ed. by W. M. Wells, A. Colchester, and S. L. Delp. Vol. 1496. Lecture Notes in Computer Science. Berlin, Germany: Springer-Verlag, 1998, pp. 130–137.
- [136] B. Pickett, R. K. Ten Haken, J. Kurhanewicz, A. Qayyum, K. Shinohara, B. Fein, and 3rd Roach M. “Time to metabolic atrophy after permanent prostate seed implantation based on magnetic resonance spectroscopic imaging”. In: *Int J Radiat Oncol Biol Phys* 59.3 (2004), pp. 665–73.
- [137] P. J. De Visschere, G. O. De Meerleer, J. J. Futterer, and G. M. Villeirs. “Role of MRI in follow-up after focal therapy for prostate carcinoma”. In: *AJR Am J Roentgenol* 194.6 (2010), pp. 1427–33.
- [138] R. S. Brame, M. Zaider, K. L. Zakian, J. A. Koutcher, A. Shukla-Dave, V. E. Reuter, M. J. Zelefsky, P. T. Scardino, and H. Hricak. “Regarding the focal treatment of prostate cancer: inference of the Gleason grade from magnetic resonance spectroscopic imaging”. In: *Int J Radiat Oncol Biol Phys* 74.1 (2009), pp. 110–4.
- [139] K. L. Zakian, K. Sircar, H. Hricak, H. N. Chen, A. Shukla-Dave, S. Eberhardt, M. Muruganandham, L. Ebor, M. W. Kattan, V. E. Reuter, P. T. Scardino, and J. A. Koutcher. “Correlation of proton MR spectroscopic imaging with gleason score based on step-section pathologic analysis after radical prostatectomy”. In: *Radiology* 234.3 (2005), pp. 804–14.
- [140] Aleksandra Zapotoczna, Giuseppe Sasso, John Simpson, and Mack Roach. “Current Role and Future Perspectives of Magnetic Resonance Spectroscopy in Radiation Oncology for Prostate Cancer”. In: *Neoplasia* 9.6 (2007), pp. 455–463.

- [141] F. Cornud, N. B. Delongchamps, P. Mozer, F. Beuvon, A. Schull, N. Muradyan, and M. Peyromaure. “Value of multiparametric MRI in the work-up of prostate cancer”. In: *Curr Urol Rep* 13.1 (2012), pp. 82–92.
- [142] H. Hricak, P. L. Choyke, S. C. Eberhardt, S. A. Leibel, and P. T. Scardino. “Imaging prostate cancer: a multidisciplinary perspective”. In: *Radiology* 243.1 (2007), pp. 28–53.
- [143] J. O. Deasy, C. S. Mayo, and C. G. Orton. “Treatment planning evaluation and optimization should be biologically and not dose/volume based”. In: *Med Phys* 42.6 (2015), pp. 2753–6.

Vita

Tze Yee Lim was born in Georgetown, Penang, Malaysia on November 21, 1989, the daughter of Kheng Kok Lim and Chan Dean Siew. She graduated from Penang Chinese Girls' High School in December 2006. She enrolled in Inti College's American Degree Transfer Program for 8 months before starting her bachelor's degree at Drexel University, Philadelphia in September 2007. She received the degree of Bachelor of Science with a major in physics and minor in mathematics from Drexel in May 2011. After the Med-Into-Grad Howard Hughes Medical Institute's fellowship over the summer, she entered The University of Texas MD Anderson Cancer Center Graduate School of Biomedical Sciences at Houston in September 2011.

Permanent address:

41, Jalan Kenari,
Sungai Ara,
11900 Bayan Lepas,
Pulau Pinang, Malaysia.